CONDITION HEALTH MONITORING AND ITS APPLICATION TO CAVITATION DETECTION/CHARACTERIZATION WITHIN HYDROPOWER TURBINES

by

Samuel J. Dyas

A thesis submitted to the Faculty and the Board of Trustees of the Colorado School of Mines in partial fulfillment of the requirements for the degree of Masters of Science (Mechanical Engineering).

Golden, Colorado

Date _____

Signed: _____
Samuel J. Dyas

Signed: _____
Dr. Michael A. Mooney
Thesis Advisor

Golden, Colorado

Date _____

Signed: _____
Dr. Greg Jackson
Professor and Head of
Department of Mechanical Engineering

ABSTRACT

Hydroelectric power has been the number one renewable energy source in the U.S. since the beginning of the industrial revolution and continues to be today. Hydroelectricity is a critical component in the power production grid to keep greenhouse gas emissions and pollution minimized. As such, it is crucial that unexpected shutdowns and unplanned maintenance of hydropower turbines be kept to a minimum, so as to maximize hydroelectricity production.

This thesis aims to investigate condition health monitoring (CHM) methods specifically designed for non-intrusive cavitation detection within hydropower turbines. Cavitation is a highly damaging phenomenon common within turbines. When allowed to continue undetected over an extended period of time, cavitation can lead to severe and crippling effects for efficient operation. The application of CHM will lead to less downtime and ultimately more electrical production from hydropower turbines, resulting in the maximization of the U.S.'s number one renewable energy source's potential.

An instrumented cavitation inducing apparatus was designed and built for laboratory testing. The goal of the cavitation inducing apparatus was to produce both non-cavitating and cavitating flows within the available flow range. Also, it was critical for the apparatus to be simple and allow the instrumentation utilized to be placed as close as possible to the cavitation within the flow. Instrumentation including pressure transducers, accelerometers and acoustic emission sensors were used to non-intrusively record cavitation signals from the cavitation apparatus. Multiple signal processing techniques, spanning both the time and frequency domains were utilized to develop methods and metrics to quantify the cavitation monitoring data. Most of

the techniques are well documented, including analyzing the root mean square values of the signals and utilizing the Fast Fourier Transform for frequency domain analysis. There were also some signal processing techniques developed throughout this project, specifically for cavitation monitoring.

The metrics and methods developed proved successful at identifying volatile flow rates and subsequently the onset of cavitation state change with the flow. It was also determined that time domain signal processing techniques were more successful at cavitation characterization than frequency domain techniques. There is confidence the methods developed for non-intrusive cavitation monitoring through this thesis could be easy transferred to on-site operational test data received from a cavitating turbine and successfully diagnose the onset of cavitation with the flow range.

TABLE OF CONTENTS

LIST OF FIGURES

LIST OF TABLES

ACKNOWLEDGMENTS

There are many people and organizations that made this project possible. Thank you to the Hydro Research Foundation for funding this work, and specifically Brenna Vaughn for all her organizational help. Thank you to the U.S. Bureau of Reclamation. The opportunity to intern with the Infrastructure Services Division from Fall 2012 to Spring 2013 allowed for many learning opportunities and access to what became this projects experimental set-up within the Hydraulics Research Laboratory. Specifically, I'd like to thank Warren Frizell, John Germann and James DeHaan of Reclamation for their input and guidance throughout the project.

Thanks to Bryan Walter, his guidance throughout this project and graduate school was immensely appreciated. Thank you to Dr. John Steel and Dr. Mike Wakin for their input on my data analysis and serving on my thesis committee. Finally, thank you to Dr. Mike Mooney for his role as my advisor throughout my time at Colorado School of Mines and guidance on this thesis project.

CHAPTER 1

INTRODUCTION

1.1 Background

In the early 1800's, hydropower helped start the industrial revolution, and by 1881 the first hydroelectric power was created in the US. In the early 1900's there were many large hydroelectric projects throughout the U.S. (e.g., Hoover - 1936, Grand Coulee - 1942) that at the time supplied a relatively large percentage of the US energy consumption. From 1950 to 2010, hydroelectric power fell from 30% to 6% of the US annual electric consumption [1]. This reduction is mainly due to the ever increasing demand for electricity combined with the near stoppage of new hydroelectric projects. Although no major hydroelectric power plants have been built since 1985, hydroelectricity remains the number one renewable energy source in the US today [2].

In order for hydroelectric power to stay competitive in today's electric production market, operational costs must be kept low and all non-scheduled repairs minimized. One way to help achieve this goal is through condition health monitoring (CHM) of hydro turbines, more specifically, non-intrusive cavitation detection monitoring. Cavitation within large scale hydropower turbines can and does cause severe damage to critical components in many of the leading hydropower production plants throughout the world. These cavitation inflicted damages are one of, if not the leading causes for unexpected shut-downs of hydropower turbines, resulting in lost revenue and increased/unplanned maintenance costs [3] [4]. If cavitation could be monitored during operation of the turbines through the application of CHM, electrical production

and profitability would increase, ultimately reducing the need for fossils fuel power based production.

1.2 Summary

This thesis is divided into seven chapters. Chapter 2 will provide a literature review of pertinent information relating to the project and the current state of non-intrusive cavitation detection within hydropower turbines.

Chapter 3 outlines the fundamental research questions, goals and purpose of this project. The ultimate goal of this project is to develop methods and metrics which can be applied to non-intrusive cavitation monitoring data which will efficiently and effectively identify volatile flow ranges and cavitating states within turbines. These methods and metrics will be developed on a simple cavitation inducing laboratory set-up where the cavitation states can be controlled and all methods can be validated.

Chapter 4 will present the experimental set-up conception, design and implementation. Due to the difficulty of access to large scale hydropower plants throughout the U.S., this project focuses around developing non-intrusive cavitation detection techniques and validating them on a controllable experimental set-up. A cavitation inducing tunnel was conceived, designed and implemented at the U.S. Bureau of Reclamation's (USBR) Denver Federal Center Hydraulics' Laboratory. The cavitation inducing tunnel could be easily controlled, allowing for cavitation signals to be collected with various types of sensors at known cavitation states.

Chapter 5 will present the data acquisition system and data analyses background used throughout the project. The project focused on utilizing accelerometers and acoustic emission (AE) sensors to characterize the cavitation signals from the outside of the cavitation inducing

tunnel. In addition, a pressure sensor was used to record gage pressure and validate predicted cavitation states at specific flow rates. A 16-bit A/D data acquisition system capable of recording up to 1 MHz was used for all data acquisition. The data analysis processes and metrics applied to the data ranged from simple, i.e. root-mean-square of signals, to complex, i.e. auto-correlation of signals to search for discernible and repeatable characteristics across the turbulent flows.

Chapter 6 will present the results of the methods and metrics developed applied to the non-intrusive monitoring data. Cavitation onset and state change were determined to be accurately identifiable phenomena. Chapter 7 presents conclusions and recommendations for future work based on the preceding chapters.

CHAPTER 2

LITERATURE REVIEW

2.1 Hydropower Plant Basics

Hydropower plants utilize the power of stored water and its potential energy to generate electricity. A typical hydropower plant is shown in Figure 2.1.

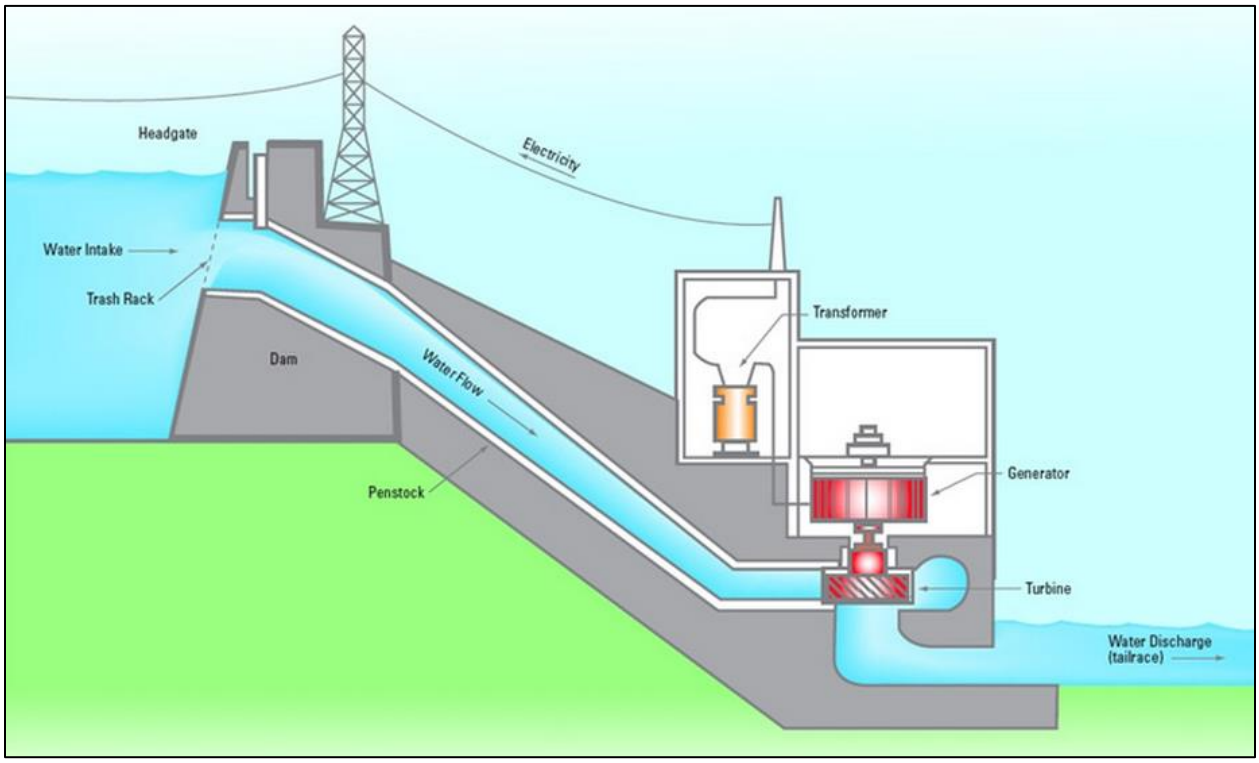

Figure 2.1 Typical Hydropower Plant Set-up [5]

As shown in Figure 2.1, water flows from high head storage downhill through a penstock where its potential energy is converted to kinetic energy. Near the bottom of the dam (to allow for maximum kinetic energy to be generated), a turbine is utilized to convert the water flow's kinetic

energy into mechanical energy. The mechanical energy is transported via a rotating shaft to the generator where it is then transformed into electrical energy. All electrical energy is then transformed into high voltage current to be transported away from the dam and to energy consumers via transmission wires.

2.2 Hydropower Turbine Basics

The most common hydropower turbine utilized in large scale hydropower plants is a Francis turbine. While there are other turbine options available, Francis turbines provide highly efficient energy transformation while offering wide head ranges. A Francis hydropower turbine diagram is shown in Figure 2.2.

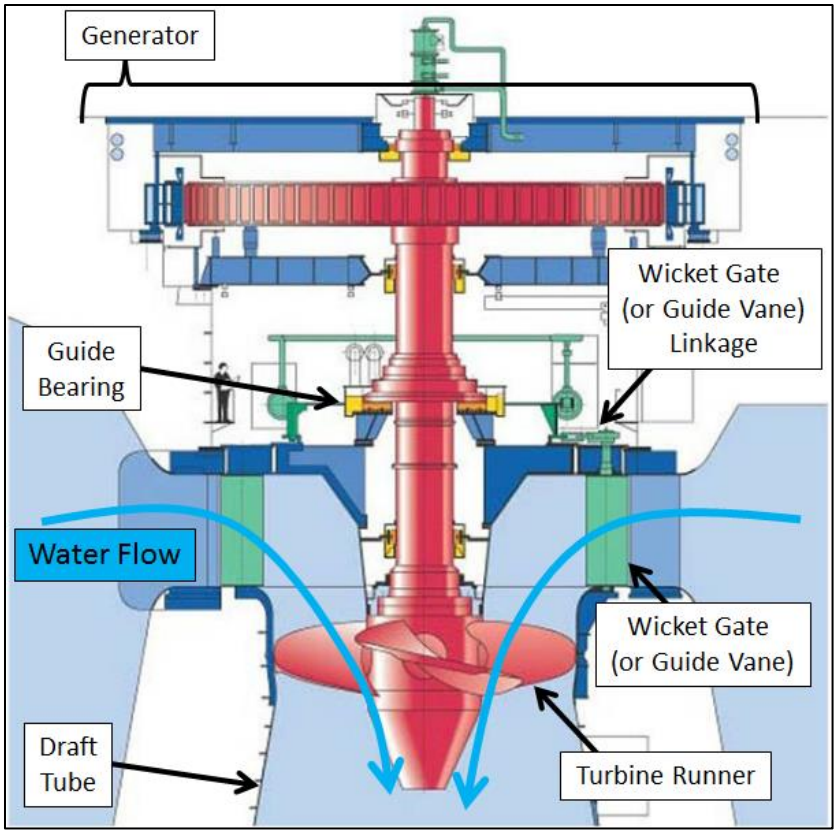

Figure 2.2 Francis Turbine Diagram [6]

As shown in Figure 2.2, a Francis turbine generates power by allowing water with high kinetic energy to pass through the turbine runner, spinning the shaft connected to the generator. The water flow through the turbine and subsequently the power output of the turbine is controlled via the wicket gates.

2.3 Cavitation Erosion

Cavitation is the formation of vapor cavities within a flow. The complex flows within a hydropower turbine can experience local pressure drops that fall below the liquid's vapor pressure, resulting in cavitation. The two main influences on the rate at which these vapor structures form and collapse is determined by (1) the static pressure at the runner's level and (2) the superimposed dynamic pressure pulsation of the liquid's flow associated with the hydro turbine's design, the active hydraulic conditions and operating point within the turbine. Consequently, the vapor structures size and formation are statistically random by nature [7] [8].

A consequence of cavitation in hydropower turbines is erosion of critical components. This erosion is due to the collapse of cavitation bubbles localized near the surfaces of these critical components. Figure 2.3 displays a visual of the process, while Figure 2.4 shows an example of the damage that cavitation may cause.

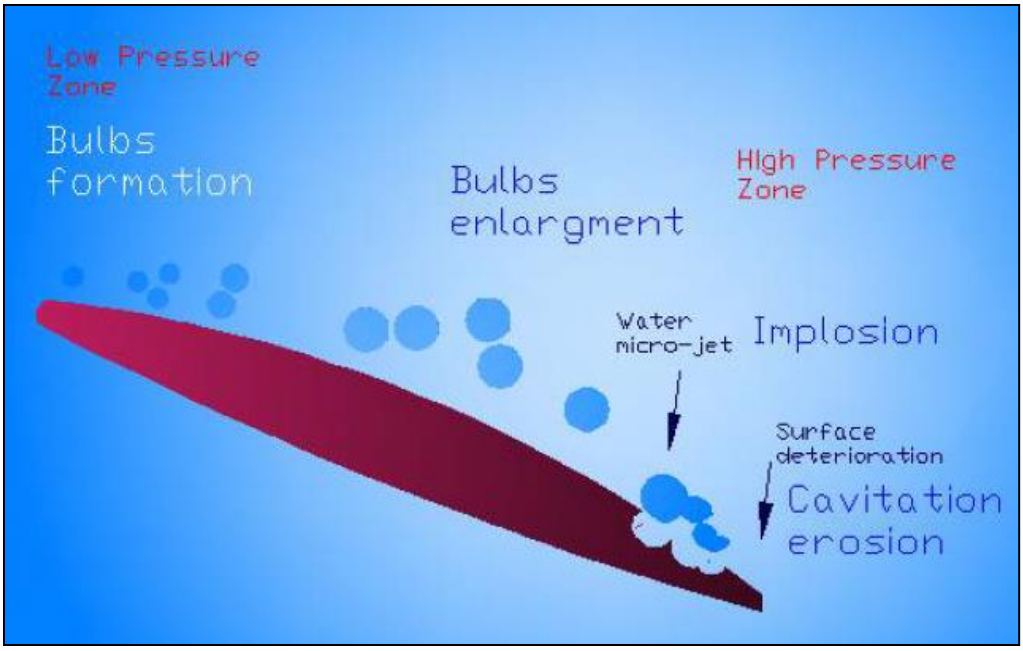

Figure 2.3 Diagram of Cavitation leading to Erosion of Critical Hydro Turbine Components [7]

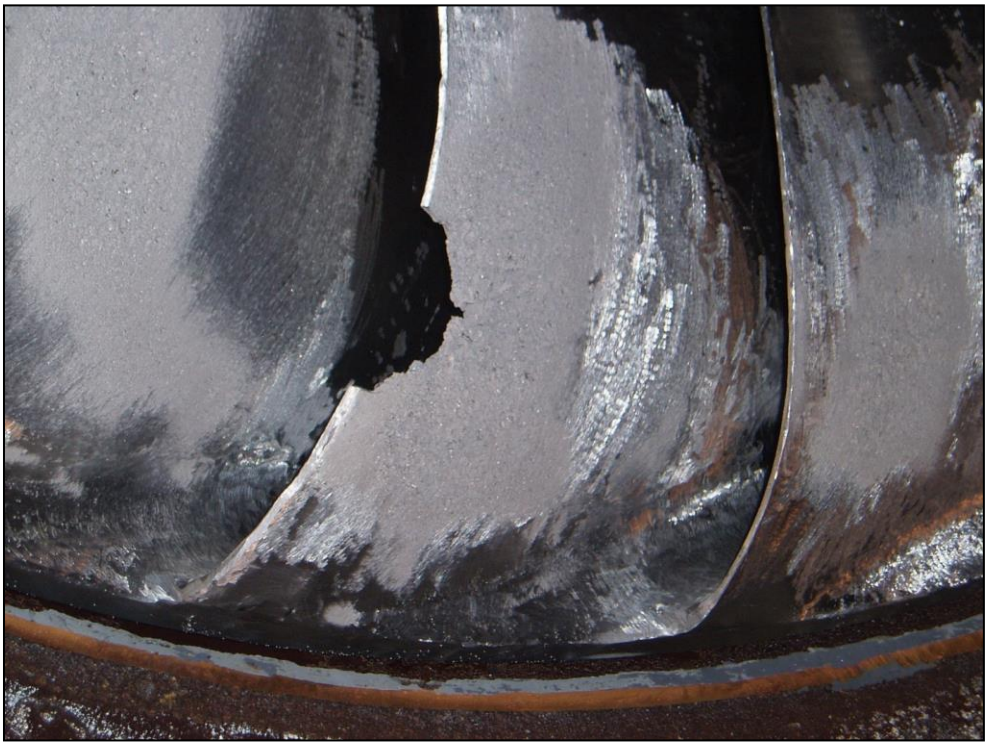

Figure 2.4 Cavitation Damage on a Turbine's Runner Blade at Fremont Canyon Power Plant in Wyoming (USBR facility)

As shown in Figure 2.3, cavitation bubbles move from a low-pressure zone to a high-pressure zone, at which point they implode causing a water micro-jet. Harrison in 1952 determined theoretically that cavitation bubble implosion entails an infinite inward radial velocity and thus an infinite pressure is developed local to the implosion site; it is practically interpreted that cavitation implosion causes localized pressures in the gigapascal range [9]. It is these localized impulses/micro-jets that lead to cavitation erosion areas where the vapor structures ultimately collapse. The erosion rate can be related to the energy carried in the vapor structures, their rate per unit time and the erosion resistance of the material.

When a new material is subjected to cavitation impacts, it first undergoes a plastic deformation period where there is no material loss; this is referred to as the incubation period. Over time, this plastic deformation turns to micro-cracks, which leads to loss of material. If cavitation impacts are allowed to continue on a material for an extended amount of time, material loss can become substantial and large cracks due to fatigue will ultimately occur. Figure 2.5 displays a typical material mass loss rate versus exposure time plot for materials exposed to cavitation over an extended period of time.

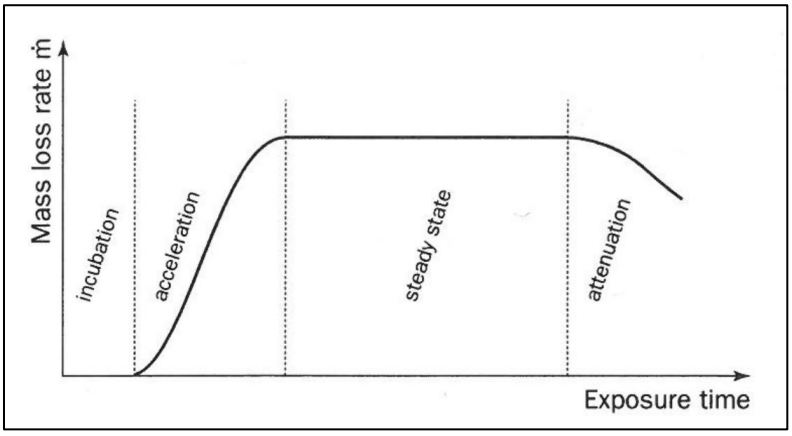

Figure 2.5 Typical Material Mass Loss versus Exposure Time due to Prolonged Cavitation [10]

2.4 Previous Research

Over the past three decades, there has been research on cavitation erosion and the development of cavitation detection for hydropower turbines. The major contributors include Hydro-Quebec (HQ), Tennessee Valley Authority (TVA), Swiss Federal Institute of Technology Lausanne (EPFL), Technical University of Catalonia (UPC), Korto Cavitation Services, and the USBR. Most of the research has been focused on the determination of damaging cavitation on hydropower turbine's runners. Turbine runners are the single most expensive component of a hydro turbine and the most frequent cavitation damaged component.

The majority of cavitation monitoring is performed using either accelerometers or AE sensors [11] [12]. The sensors are most commonly placed in one of three locations, namely wicket gates linkages, guide bearings or the draft tube of the hydro turbine (See Figure 2.2 for visual of locations) [13]. These three locations provide the most direct mechanical link from cavitation impact locations to available sensor locations [14].

The simplest cavitation monitoring method involves computing the root mean square amplitude (RMS) of the signal output from the instrumentation on the turbine and working to correlate RMS output to cavitation aggressiveness. More in-depth analysis has also been carried out; some examples of more involved analyses involve the following [15] [16] [17] [18] [19] [20] [21] [22] [23]:

- Identification from time traces of ‘bursts’ or peaks representative of the cavitation erosion.
- Amplitude demodulation of high frequency bands.

- Utilizing the Hilbert transform to process the cavitation signal, resulting in an analytical function from which harmonics are computed.

In addition, HQ, EPFL, and UPC have spearheaded two major advances in cavitation monitoring. The first is the characterization of the transfer functions from cavitation impact locations to the sensor locations. By using an instrumented impact hammer to impact a stationary dewatered turbine runner while measuring at the determined sensor locations, the absolute aggressiveness of the cavitation can be determined from the sensor outputs during in-field monitoring. Determining the transfer function is referred is often referred to as calibration of the cavitation detection system [21]. The transfer function is an amplitude ratio between the known or anticipated cavitation impact locations and the sensor locations. By determining the amplitude ratio, the Absolute Cavitation Aggressiveness, measured in Kg/10,000 Hrs can be determined [7]. This technique has the inherent unknown that all transfer function measurements are taken while the turbine is stationary and dewatered, thus leaving the question of how does the fluid interaction effect the transfer functions during operation [24].

The second advancement in cavitation detection monitoring was published by EPFL and UPC in 2003/2004 [24] [25]. They used accelerometers mounted directly to the rotating shaft of a turbine to record cavitation signatures. The data was then transmitted wirelessly back the acquisition system. Mounting the accelerometers directly to the shaft provides the most direct mechanical link from the impact locations on the runner to the sensors. A case study will be presented to demonstrate the advantages of rotating shaft mounted sensors versus stationary sensor locations and present the reader with an example of cavitation detection methodology.

2.4.1 Example Case Study

The case study is titled: “Cavitation Erosion Prediction in Hydro Turbines from Onboard Vibrations” and was completed by a team including engineers from EPFL and UPC [24]. The case study includes the most current state of the art in cavitation detection, both wireless data acquisition from a sensor located on the turbines shaft and transfer function determination used to determine the actual cavitation impact acceleration. Two similar Francis turbines were instrumented as shown in Figure 2.6; *FT1* is a Francis turbine that had no history of cavitation erosion, while *FT2* is a Francis turbine with extensive cavitation erosion problems. The turbines were chosen so that when identical sensors and data analyses were used, the results could be compared, revealing cavitation identifying techniques. There were five sensors used on both turbines, one mounted directly to the rotating shaft of the turbine (data wirelessly transmitted), two on guide bearing and two on the guide vane linkages. The turbine’s individual characteristics are shown in Table 2.1.

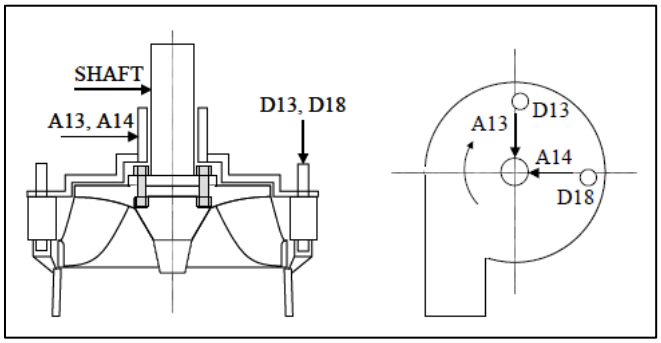

Figure 2.6 Outline of a Francis Turbine indicating the Location and Direction of the Accelerometers [22]

Table 2.1 Comparison of Francis Turbine 1 and 2 Characteristics [22]

Prototype	Erosive Cavitation	*N* [rpm]	Z_b	Z_v	Max. Power (MW)
FT1	*No*	*375*	*15*	*24*	*14*
FT2	*Yes*	*250*	*15*	*24*	*11*

Due to wireless transmission limitations, all shaft measurements were bandlimted to 6 kHz, while all other measurements had a bandwidth of 20 kHz. Figure 2.7 shows the signal RMS values from all sensors corresponding to the turbine's power output (all sensors were band filtered from 3-6 kHz). Power output of hydropower turbines is proportional to water flow through the turbines.

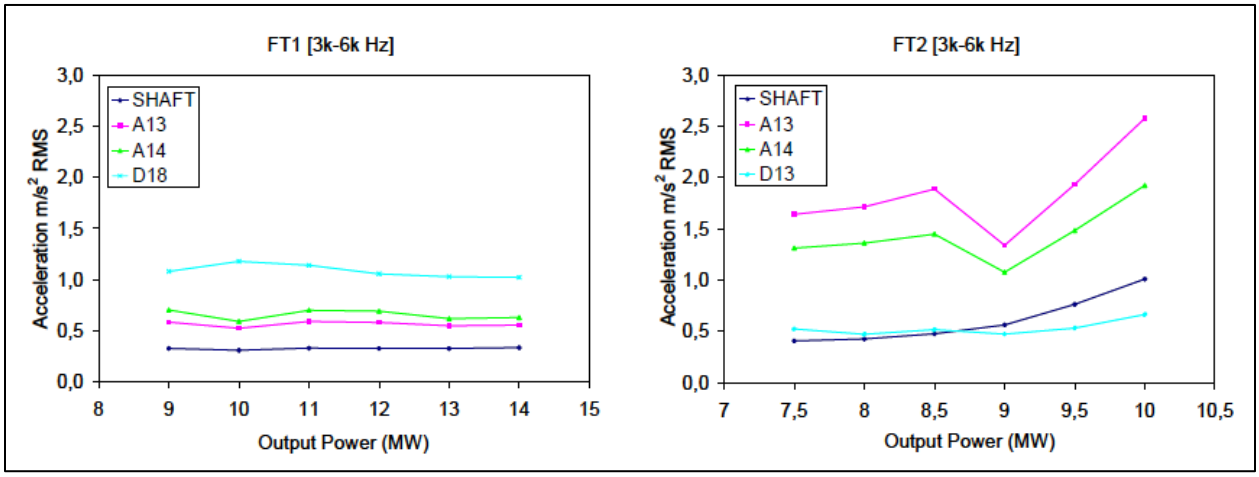

Figure 2.7 RMS Output of Vibrations Signals Filtered between 3-6 kHz as a Function of Output Power [22]

As Figure 2.7 demonstrates, a turbine with no cavitation does not experience an increase in RMS signal output as a result of changing power output (*FT1*). However, a turbine that does experience cavitation does experience changes in signal RMS outputs as a function of output power. The only ground truth known for *FT2* was that cavitation was taking place at some point during the operating range. Figure 2.7 suggests the cavitation starts low in the range at approximately 8 MW and increases at an exponential rate. It should be noted, that the only 'linear' increase on *FT2* came from the rotating shaft mounted accelerometer. In all other cases (turbine bearing and guide vane linkages) the RMS values dropped at 9 MW output power. The drop is RMS values at 9 MW for all stationary sensors could be for a number of reasons, including an anti-resonance within the structure or a temporary drop in cavitation aggressiveness.

Figures 2.8 – 2.10 present the raw data auto power spectra. The shaft mounted accelerometers data is presented from 1-6 kHz, while the guide bearing and guide vane accelerometers data is presented from 0-20 kHz.

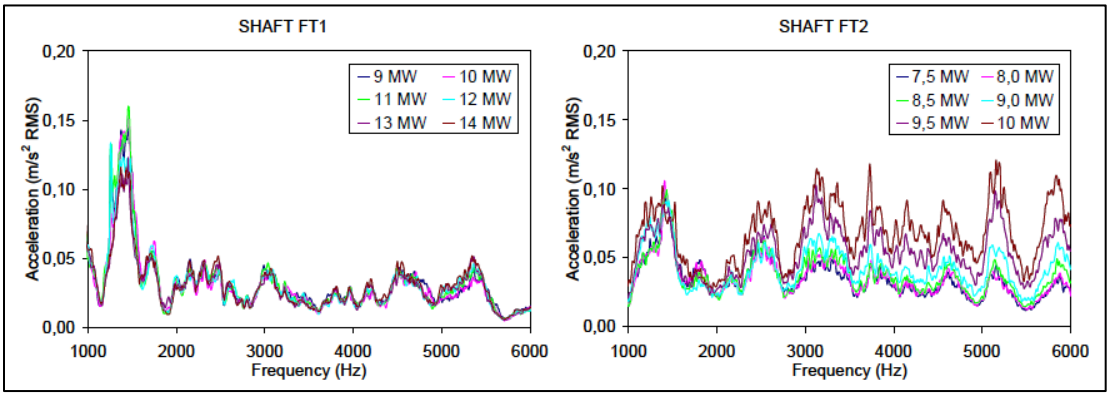

Figure 2.8 Auto Power Spectra from 1-6 kHz of Shaft Vibrations as a Function of Output Power [22]

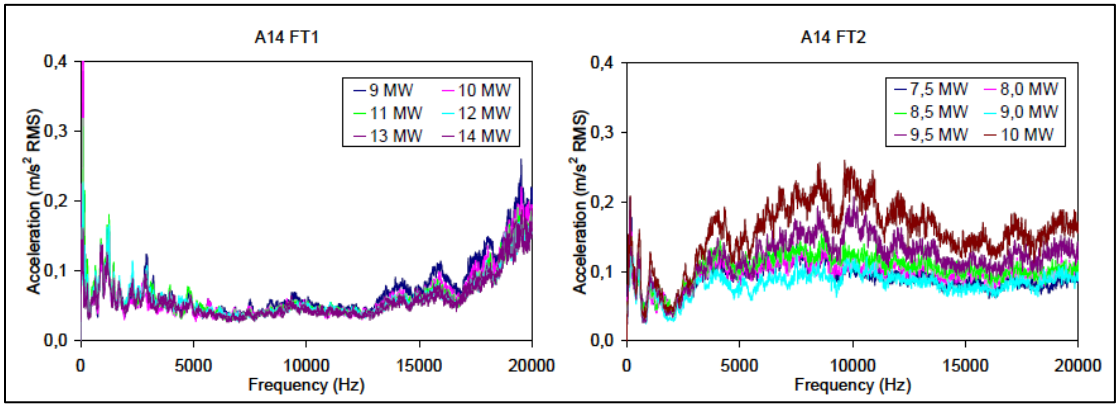

Figure 2.9 Auto Power Spectra up to 20 kHz of Guide Bearing Vibrations as a Function of Output Power [22]

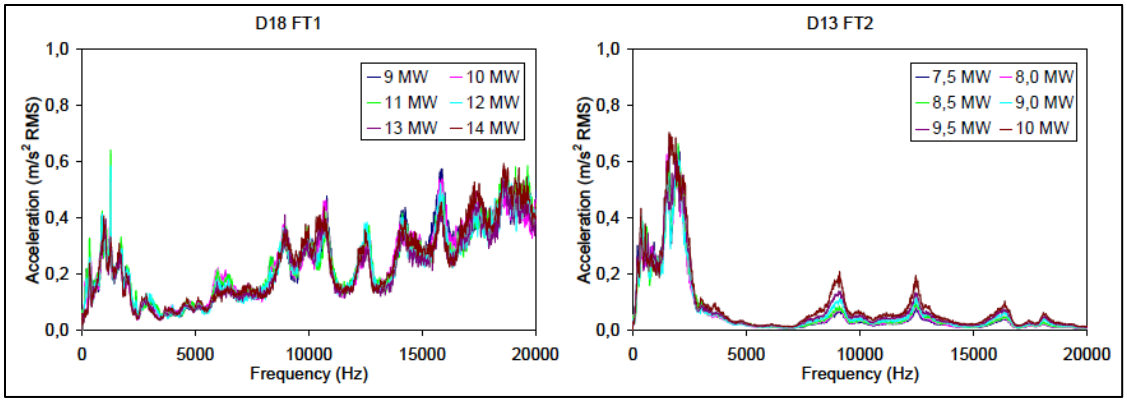

Figure 2.10 Auto Power Spectra up to 20 kHz of Guide Vane Vibrations as a Function of Output Power [22]

Figures 2.8 – 2.10 demonstrate that in a turbine without cavitation (*FT1*), frequency domain amplitude does not change with respect to output power; however, it does demonstrate that frequency content amplitude does change with respect to output power for a turbine experiencing cavitation (*FT2*).

Finally, amplitude demodulation was performed on the data to determine the main frequencies that modulate the signals. This analysis was completed by the use of the Hilbert transform in specific frequency envelopes. The main hydrodynamic frequencies of interest are:

- Fundamental Frequency: $f_f = \frac{N}{60}$
- Blade Passing Frequency: $f_b = f_f * Z_b$
- Guide Vane Passing Frequency: $f_v = f_f * Z_v$

Figures 2.11 – 2.13 present that demodulated signals for shaft, guide bearing and guide vane respectively. All signals were band filtered between 3-6 kHz.

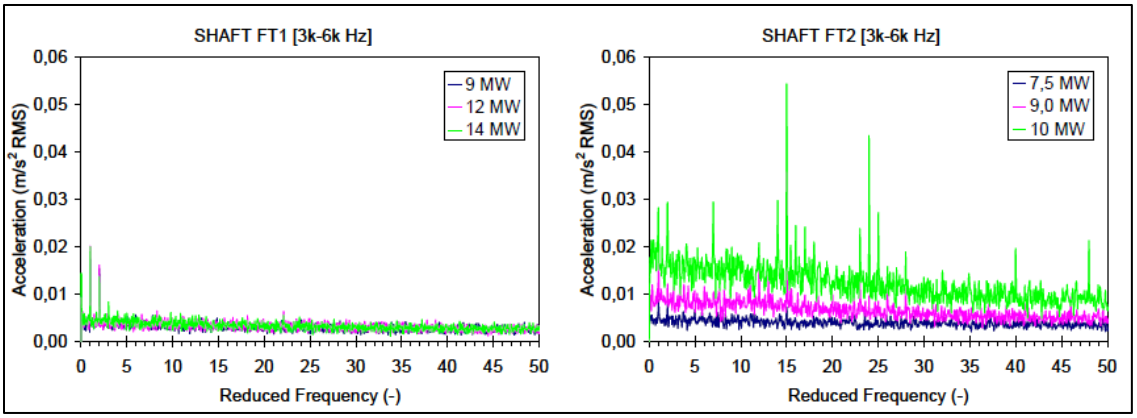

Figure 2.11 Auto Power Spectra of Demodulated Filtered Signal (3-6 kHz) for Shaft Vibrations as a Function of Output Power [22]

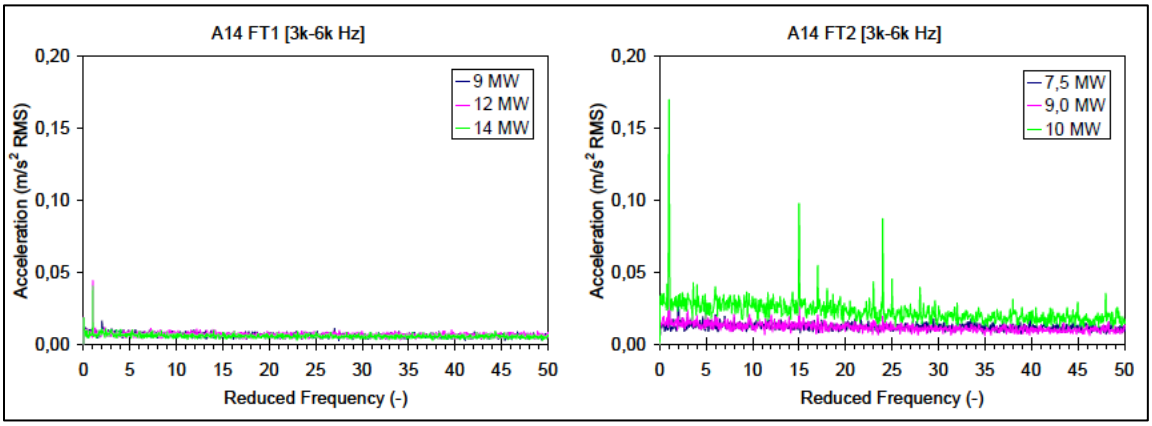

Figure 2.12 Auto Power Spectra of Demodulated Filtered Signal (3-6 kHz) for Guide Bearing Vibrations as a Function of Output Power [22]

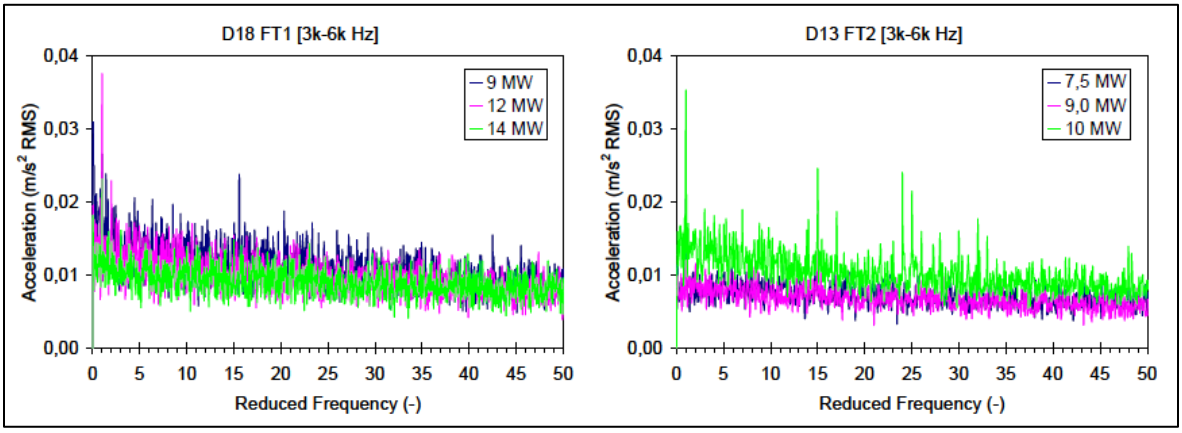

Figure 2.13 Auto Power Spectra of Demodulated Filtered Signal (3-6 kHz) for Guide Vane Vibrations as a Function of Output Power [22]

Figures 2.11 – 2.13 demonstrate that the results from the turbine experiencing cavitation are more informative than the results from the turbine not experiencing cavitation. In all measured positions, as *FT2* output increases, the main hydrodynamic frequencies (f_b and f_v) and their harmonics become evident.

The increase of RMS signal output, frequency content amplitude and modulated vibration harmonics indicate the appearance and development of erosive cavitation; these phenomena are demonstrated by Figure 2.7, Figures 2.8 – 2.10 and Figure 2.11 – 2.13 respectively. In addition, the results find both the guide bearing and guide vane measurements constantly contain noise that cannot be assumed to correspond to erosive cavitation activity. However, the rotating shaft mounted accelerometer with its direct mechanical link to the cavitation impact location provided less noisy measurements and ultimately more trustworthy results. For cavitation monitoring, it was determined that shaft measurement appears advantages due to its ability to shed noise from fluid/mechanical interactions, however further investigation is still necessary moving forward [24] [25].

CHAPTER 3

FUNDAMENTAL RESEARCH QUESTIONS, GOALS AND PURPOSE

The goal of this research is to further develop and validate tools and methods for on-site hydropower turbine cavitation characterization and detection. Before developing these tools and methods however, one must first ask, what are the fundamental research questions that need to be addressed?

3.1 Fundamental Research Questions

With the goal of designing and implementing a non-intrusive cavitation characterization/detection monitoring system, the following fundamental research questions must be addressed:

I. Can cavitation be characterized via repeatable and discernible inherent characteristics that are capable of being measured/monitored?
    - Is it advantageous to focus the analysis on the time domain over the frequency domain? Or vice versa?

II. Can the ability to 'listen' for damage within a hydropower turbine be demonstrated from a 'known' input? i.e. Can a turbine with known cavitation history be characterized?

3.2 Project Objectives

At the start of this project there was optimism access to Hydropower Plants would be possible between the Fall of 2012 and Spring of 2013 for onsite validation of methods developed. Quickly however, it was determined that this was outside of the projects budget and control. It was then determined that a simple cavitation inducing apparatus that could be controlled in a laboratory environment would be developed and all non-intrusive cavitation detection/characterization methods would be developed and validated on said apparatus. The project objectives were determined to be:

I. Design, build and make operational a simple cavitation-inducing apparatus instrumented to measure cavitation-induced vibration and acoustics.

II. The cavitation-induced vibroacoustical data will be analyzed to determine if there are repeatable and discernible characteristics of cavitation that can be used for characterization of the signal.

III. Develop metrics that clearly demonstrate volatility and cavitation onset within the flow.

CHAPTER 4

EXPERIMENTAL SET-UP

4.1 Design Conception

It was determined that a simple cavitation inducing apparatus would be designed and built to be utilized in a laboratory environment for non-intrusive cavitation detection and characterization. Working closely with a Senior Hydraulic Engineer of the USBR, it was determined that the simplest and most controllable cavitation inducing set-up would be a cavitation tunnel with an offset into the flow. The tunnel's water flow would be fed by the USBR Denver Federal Center Hydraulics' Laboratory High Head Pump (HHP). The Hydraulics' Laboratory HHP is comprised of a 250 hp variable speed drive motor and nine-stage pump. Two pipes are available with the HHP set-up:

- 12" Diameter round piping
- 4" Square piping

Figure 4.1 presents the HHP discharge curve while Figure 4.2 presents a simplified and generalized diagram of the HHP station standard set-up. It was determined from the available piping sizes, that a four inch square cavitation tunnel with an offset would be designed for inducing and studying cavitation.

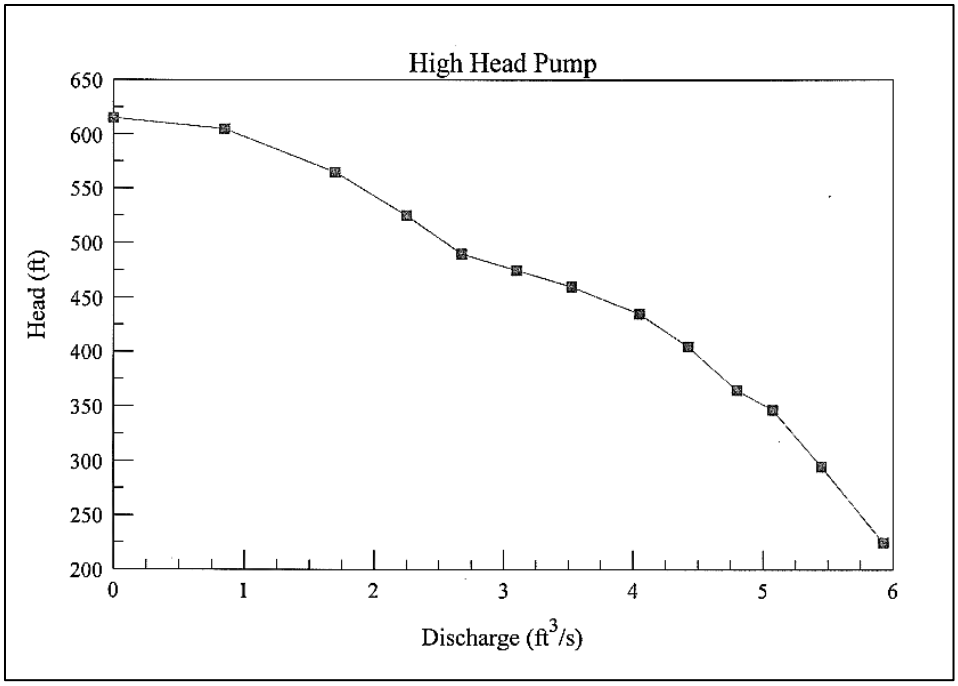

Figure 4.1 USBR Denver Federal Center Hydraulic Laboratory High Head Pump Discharge Curve

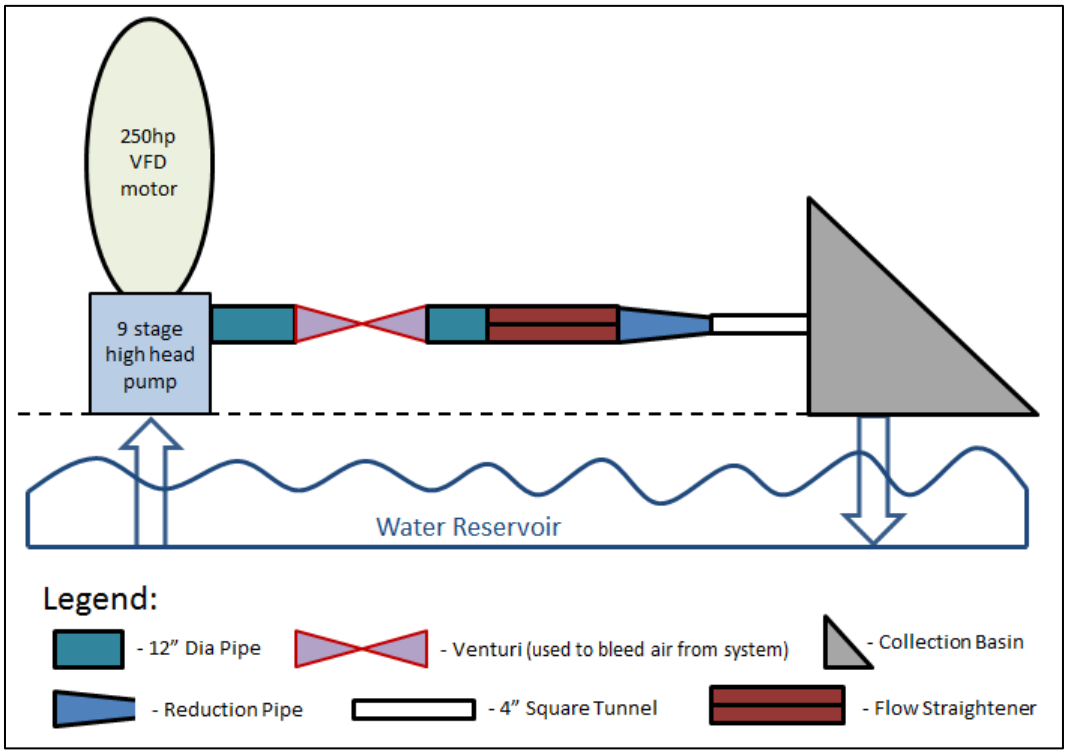

Figure 4.2 Simplified and Generalized Diagram of the USBR Denver Federal Center Hydraulic Laboratory HHP Station Standard Set-up

4.2 Design

The size of the tunnel (four inch square) was pre-determined by the standard size piping available. The next step was determining the proper offset into the flow to allow for flow ranging from non-cavitating to developed cavitation. In order to do this, the approximate minimum and maximum flow rates needed to be determined.

$$A_T = 16in^2 = {}^{1}/_{9}\ ft^2 \qquad Q_{min} = 1\ {}^{ft^3}/_{s} \qquad Q_{\max} = 6\ {}^{ft^3}/_{s}$$

$$V_{\min} = {}^{Q_{min}}/_{A_T} = 9\ {}^{ft}/_{s} \qquad V_{max} = {}^{Q_{max}}/_{A_T} = 54\ {}^{ft}/_{s}$$

Once the minimum and maximum flow rates were determined, Figure 4.3 was used to determine the offset into the flow. The curves presented in the nomograph in Figure 4.3 describe only the cavitation initiation points at specific misalignment offsets and corresponding fluid velocities and pressures. The test facility used to obtain the curves presented in the nomograph was 4.02 inches high by 6.00 inches wide, very similar dimensions to the cavitation tunnel to be designed for this project. There was an assumption of an extremely thin boundary layer. The curves presented in the nomograph can be compressed and represented in an equation form, see equation 4.2 for this underlying theory [26].

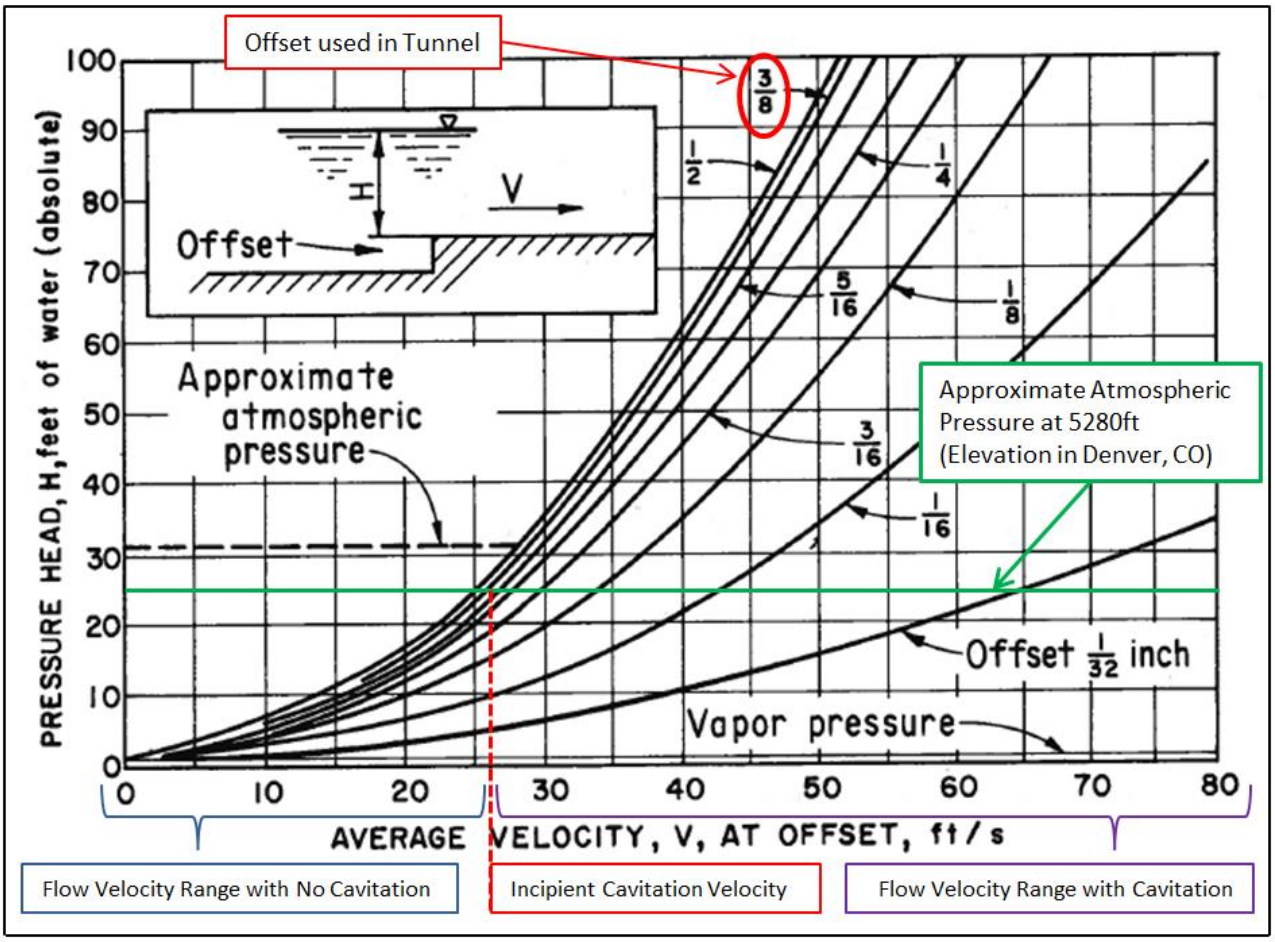

Figure 4.3 Incipient Cavitation Characteristics of Offsets into the Flow [9]

As shown in Figure 4.3, the use of a 3/8 inch offset would provide a flow range that would include both non-cavitating flow and developed flow. To confirm that the designed tunnel would range from a non-cavitating flow to a cavitating flow, Equations 4.1 and 4.2 were used to theoretically predict the cavitation indexes throughout the range of the high head pump [26].

$$P_o = P_a + P_g \tag{4.1}$$

$$\sigma = \frac{P_o - P_v}{\frac{\rho {V_o}^2}{2}} \tag{4.2}$$

Where:

σ: Cavitation Index
P_o: Reference pressure – Pressure in free stream flow at offset
P_a: Atmospheric pressure
P_g: Gage pressure
ρ: Density
V_o: Average fluid velocity in free stream flow at offset

The predicted cavitation indexes are provided in Table 4.1 (calculations shown in Appendix A).

Table 4.1 Theoretical Cavitation Index Calculations

Cavitation Index Prediction Calculations assuming constant low head		
Gage Pressure assumed to be 0.5ft of head / Atmospheric Pressure = 11.25psi (test site in Denver, CO)		
Pump Discharge (ft^3/s)	Mean Velocity (ft/s)	Cavitation Index (unitless)
1.0	9.93	*16.70*
2.0	19.86	*4.18*
3.0	29.79	*1.86*
4.0	39.72	*1.04*
5.0	49.66	*0.67*
6.0	59.59	*0.46*

A constant low head of 0.5 ft was assumed for the gage pressure as the cavitation inducing offset into the flow will be taking place near the end of the tunnel where the tunnel opens to atmosphere. To quantify the cavitation indexes, reference [26] provides general cavitation index responses for offsets into the flow, Table 4.2 provides the corresponding cavitation with the cavitation index (see Appendix B for visual).

Table 4.2 Cavitation Index Range

Cavitation Index Range	Cavitation In-Flow
$\sigma \geq 3$	No Cavitation
$1.8 \leq \sigma < 3$	Incipient Cavitation
$0.3 \leq \sigma < 1.8$	Developed Cavitation
$\sigma < 0.3$	Super Cavitation

Table 4.2 presents four separate cavitation states. No cavitation describes a flow devoid of vapor cavities. Incipient cavitation describes a flow with intermittent small vapor cavities, a flow where cavitation is starting. Developed cavitation describes a flow with many individual bubbles, constantly forming from the cavitation inducing offset. To the naked eye, developed cavitation appears to be a fuzzy white cloud within a flow. Super cavitation describes a flow where the cloud suddenly forms larger bubbles or supercavitating pockets and the bubbles/pockets move downstream a substantial distance further then during developed cavitation.

As Table 4.1 shows, given the available pump discharge, flows ranging from non-cavitating to near super cavitation will be achievable. While it was desired for the minimum flow rates to be laminar, there were expectations that even the minimum flows would be turbulent given the high velocities and small tunnel (turbulence does not imply cavitation). To check for turbulence, the Reynolds Number (Re) was determined for each flow rate. Re is a dimensionless number which provides the ratio of the inertial forces to the viscous forces. Low Re represent laminar flow, flow in which viscous forces are dominant, these fluid processes are generally smooth or quiet flows (Re < 2300). High Re represent flows dominated by inertial forces, these fluid processes are generally chaotic and contain flow instabilities (Re > 2300). Equations 4.3 and 4.4 present the formula to calculate the Re, Table 4.3 presents the calculated Re throughout the pumps discharge range (calculations shown Appendix C).

$$D_H = \frac{4A_s}{P} \tag{4.3}$$

$$Re = \frac{QD_H}{\nu A_s} \tag{4.4}$$

Where:

Re: Reynolds Number
D_H: Hydraulic diameter
A_S: Cross-Section area of Cavitation Tunnel at offset
P: Perimeter
v: Kinematic viscosity
Q: Flow rate

Table 4.3 Reynolds Number Calculations

Pump Discharge (ft^3/s)	Reynolds Number (Re)
1.0	2.80E+05
2.0	5.60E+05
3.0	8.40E+05
4.0	1.12E+06
5.0	1.40E+06
6.0	1.68E+06

As shown in Table 4.3, all Re are in the $10^5 – 10^6$ range, thus showing even the minimum flow rates are turbulent. While the turbulence may provide some baseline noise, this turbulent state cannot be avoided to obtain flows with near super cavitation at the near maximum flow range.

As Figure 4.3 and Table 4.1 demonstrate, a tunnel of size four-by-four inch with an offset of 3/8 inch will provide the necessary cavitation range to study the phenomenon. The tunnel was designed using the CAD software package, SolidWorks©. Both the CAD model rendering and actual cavitation tunnel are shown in Figure 4.4 (see Appendix D for technical drawings and supplemental isometric CAD model final renderings).

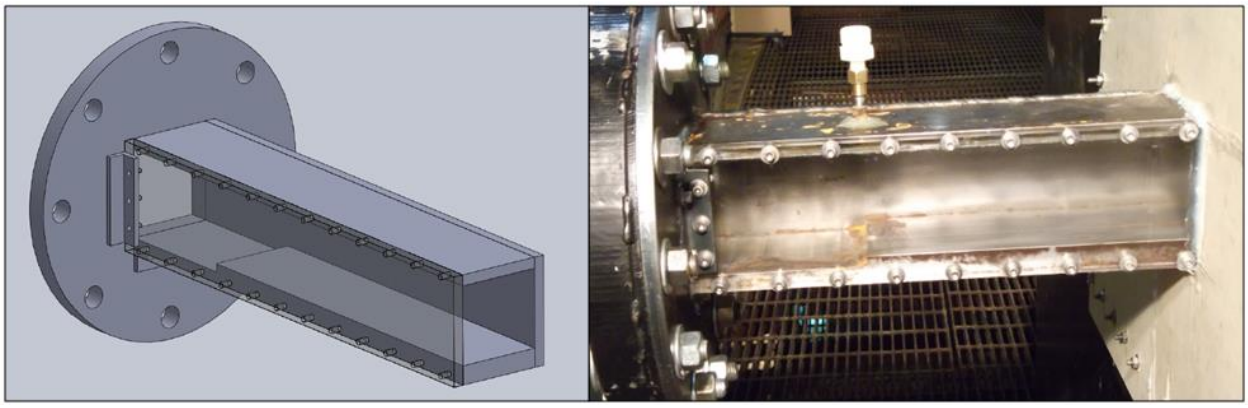

Figure 4.4 Isometric View of Final Rendering of Cavitation Tunnel and Photo of Cavitation Tunnel In-situ

Cavitation will take place roughly within an inch downstream of the offset within the cavitation tunnel. Both AE sensors and accelerometers were placed close to the cavitation to record the phenomenon's signature. Figure 4.5 shows a diagram of the sensors placement. A configuration utilizing two accelerometers and two AE sensors was deemed ideal. This would allow for signal coherence analysis across the turbulent and cavitating flows.

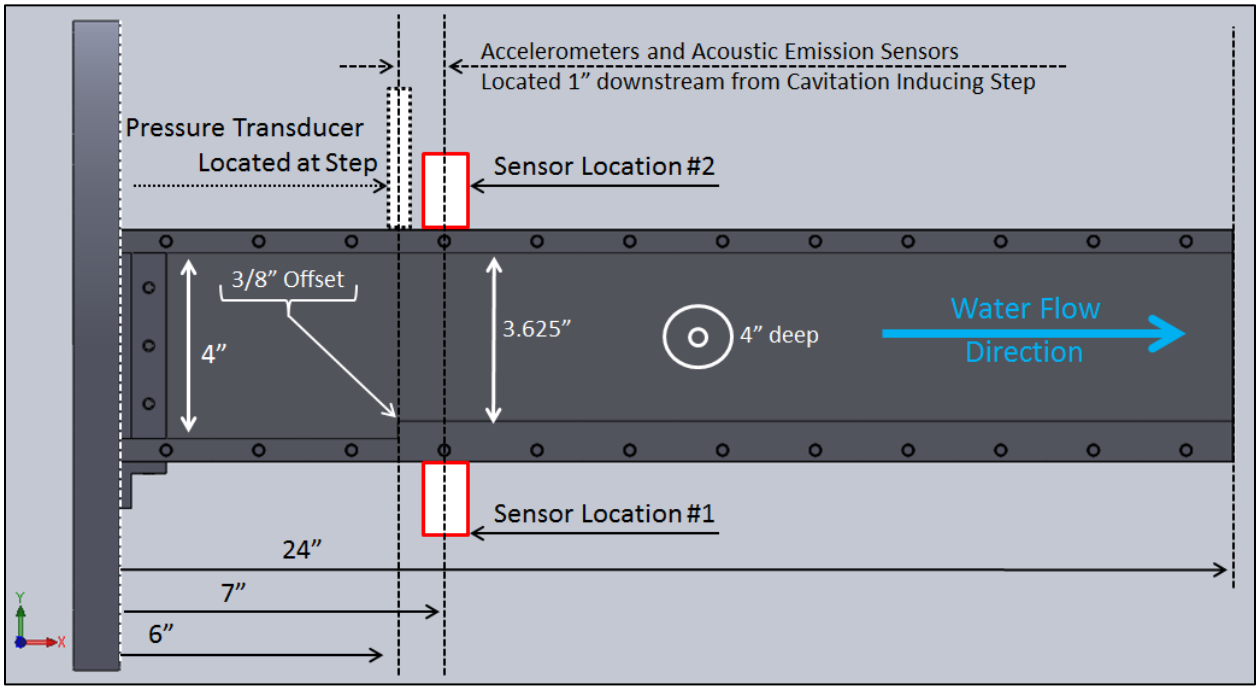

Figure 4.5 Side View of Sensor Locations in Cavitation Tunnel

Figure 4.6 presents the final experimental set-up at the USBR HHP station (refer to Appendix E for supplemental photos).

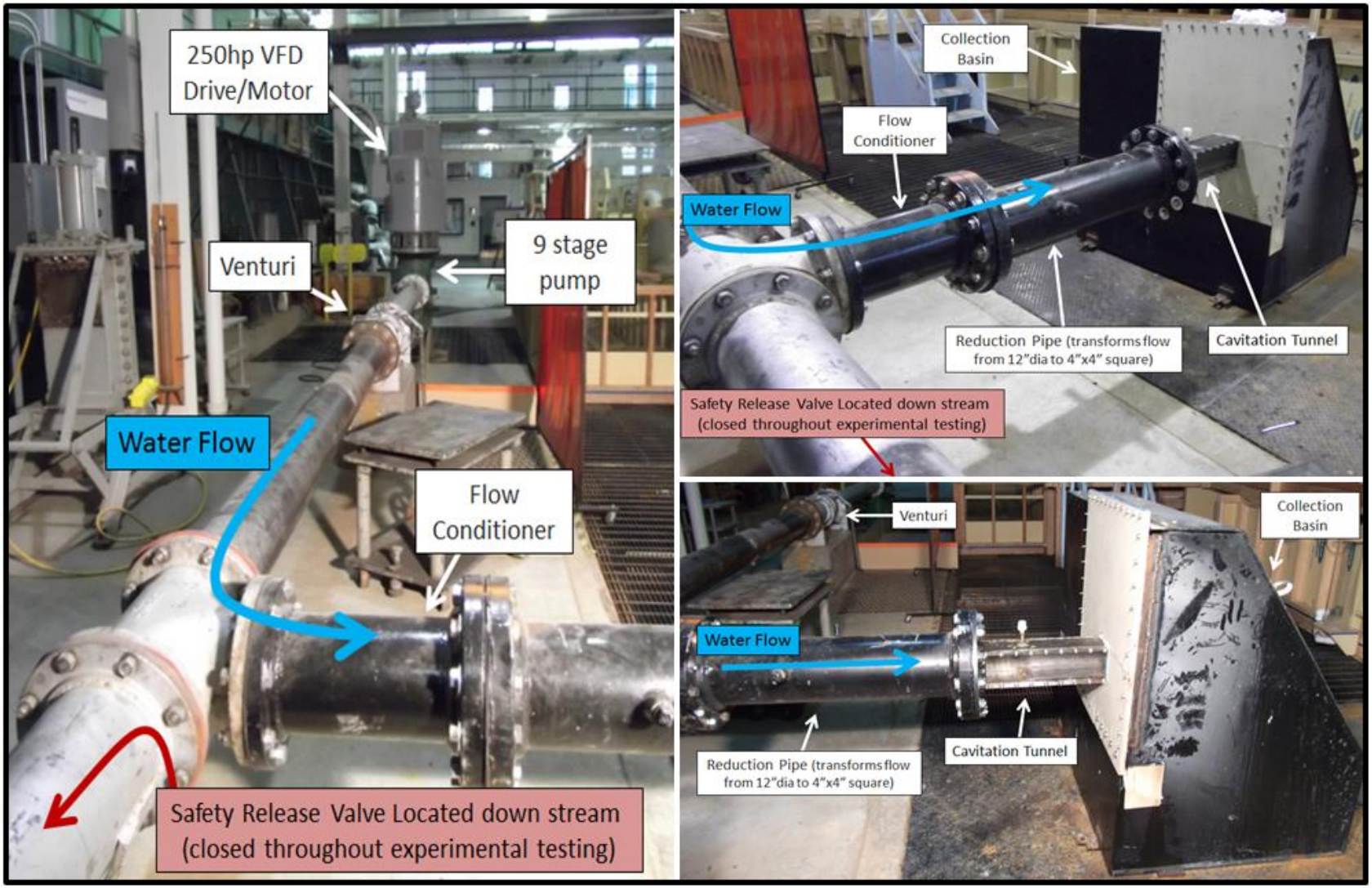

Figure 4.6 Pictures of Final Experimental Set-up

CHAPTER 5

INSTRUMENTATION AND DATA ANALYSIS METHODS

5.1 Sensors

There were three types of sensors used throughout the analysis; pressure sensors, accelerometers and AE sensors. Figure 5.1 shows the sensors in place on the cavitation tunnel during a test. As shown, the final test set-up included one pressure transducer, two accelerometers and one AE sensor.

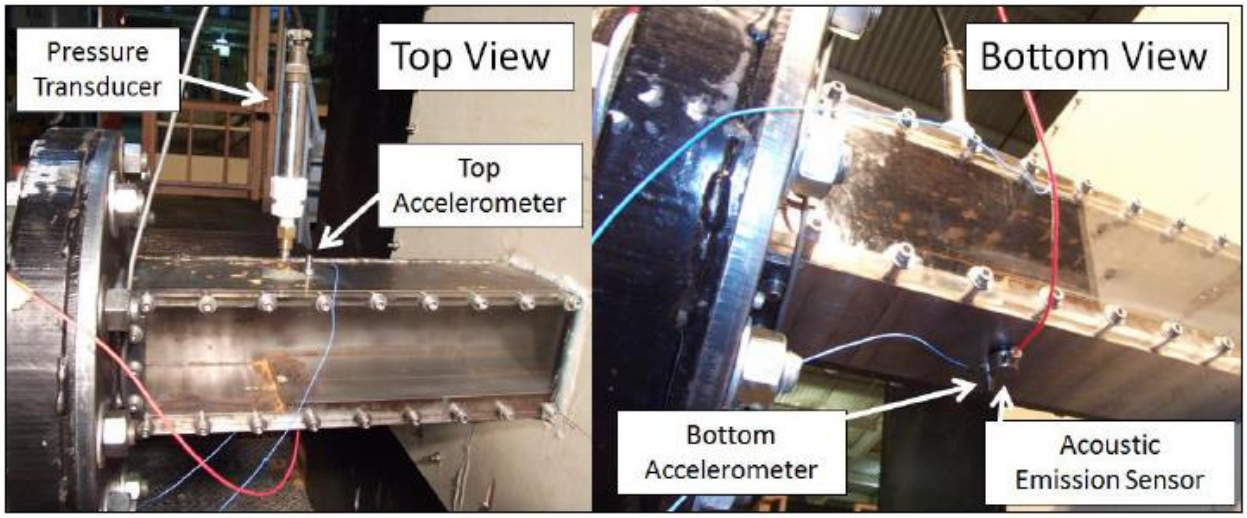

Figure 5.1 View of Cavitation Tunnel with Sensors in Place during Operational Testing

5.1.1 Pressure Sensor

A pressure sensor was placed directly over the offset of the cavitation inducing tunnel (refer to Figure 4.5 for dimensioned visual of placement). The pressure transducer used is made by Honeywell© Data Instruments, Model BL. The working range of the pressure transducer is

0-10 psi with accuracy to 0.25% [27]. The pressure transducers calibration curve is presented is Figure 5.2.

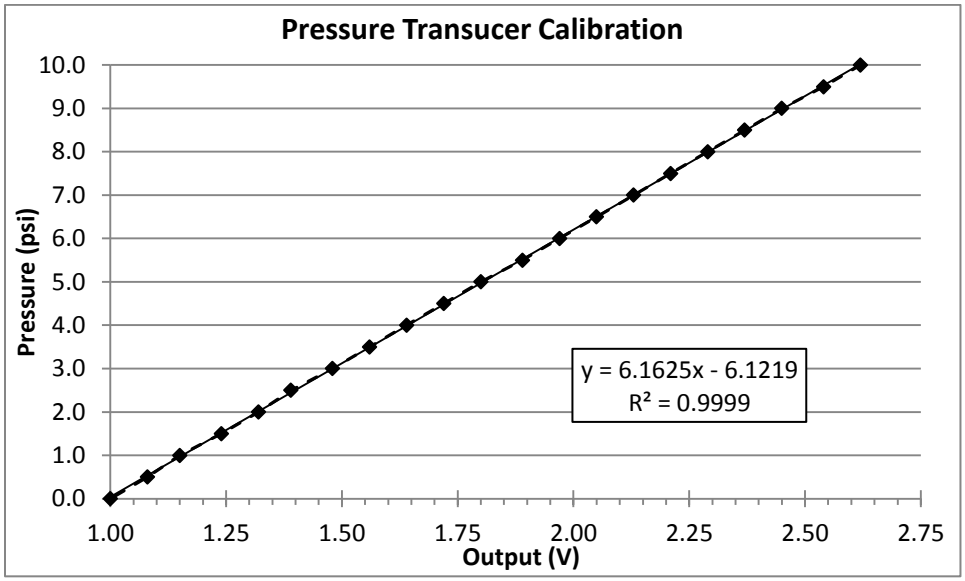

Figure 5.2 Pressure Transducer Calibration Curve

5.1.2 Accelerometers

Two piezoelectric miniature accelerometers with broad frequency ranges were chosen for recording the vibration of the cavitation tunnel. The accelerometers chosen were VibroMetrics© Model 1000 Series with a sensitivity of 10 mV/g. The accelerometers were chosen for their broad range (1 Hz-40 kHz) and sensitivity [28]. Both accelerometers were calibrated using a handheld1g_{rms} shaker. The calibrated sensitivities are shown in Table 5.1, while the accelerometers sensitivity curve is presented in Figure 5.3.

Table 5.1 Accelerometer Calibration Check – VibroMetrics© Model 1000

Serial Number	Stated Sensitivity (mV/g)	Calibrated Sensitivity (mV/g)	Percent Difference
9566	10.00	10.01	0.10%
9567	10.00	10.01	0.10%

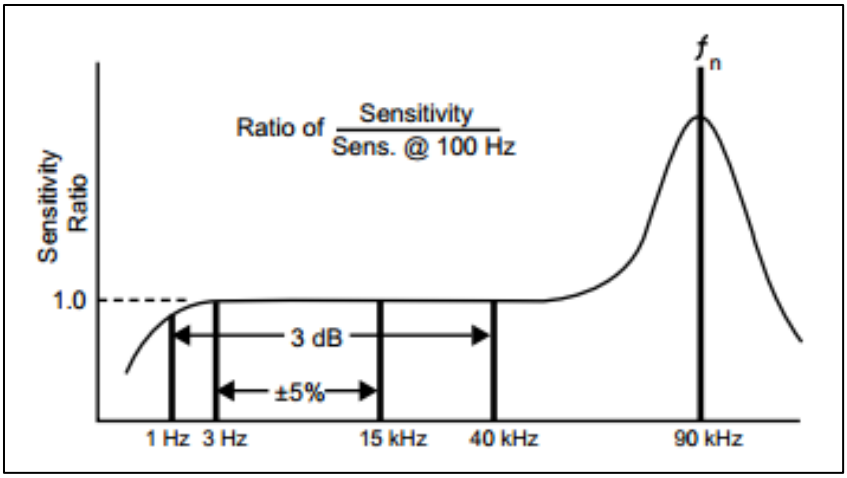

Figure 5.3 Accelerometer Sensitivity Curve [28]

5.1.3 Acoustic Emission Sensor

The AE sensor chosen is sensitive to both in-plane and out-of-plane plate waves. The AE sensor is made by DECI©, model number SE9125-MI, unit 650. The sensor's frequency range is approximately 30-200kHz with a sensitivity ranging from 57-78 dB re-1V/µM across the frequency range (calibration curve is presented in Figure 5.4) [29]. Due to the range of sensitivities across the frequency range, it was decided to keep all data from the AE sensor in raw voltage for analysis.

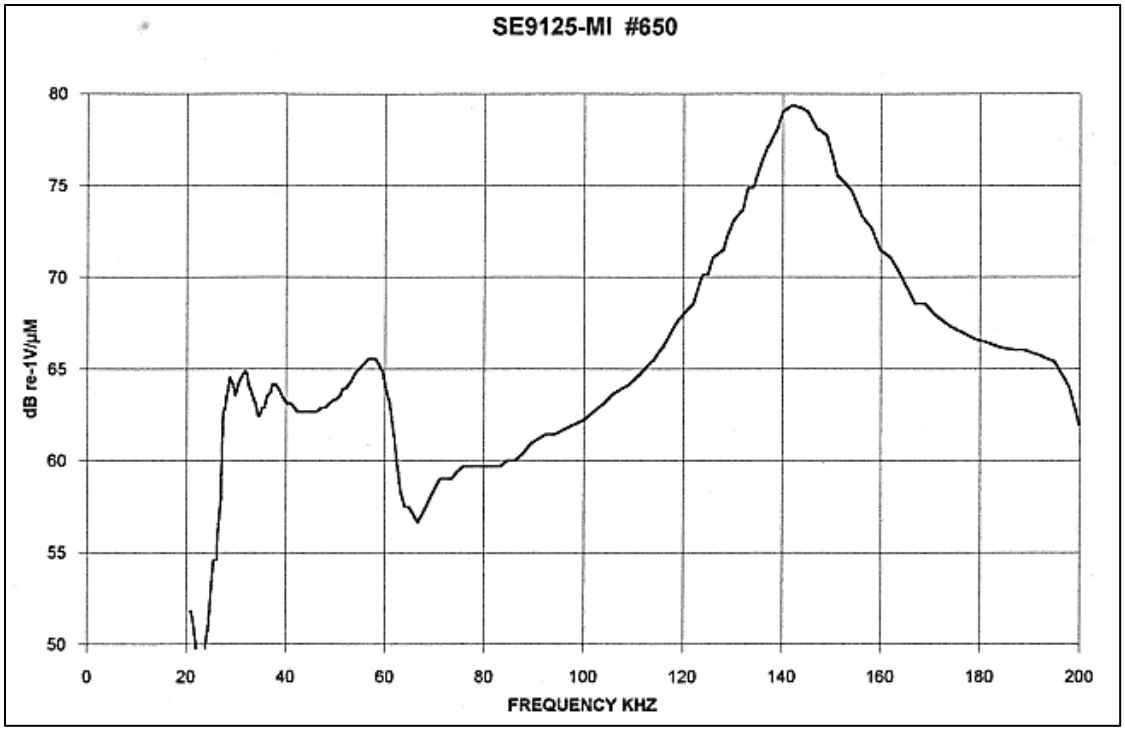

Figure 5.4 DECI AE Sensor Sensitivity Curve [29]

5.2 Hardware

An iOtech Wavebook/516E in combination with an extension WBk18 was used for all data acquisition. The system can record at up to 1 MHz utilizing a 16-bit A/D converter. In addition, the system could act as the power supply to the VibroMetrics© accelerometers which require a power source. There was a constraint however, any channel acting dually as a recording channel and power source has a limit of 0.333 MHz recording ability [30].

5.3 Software

All data acquisition was performed using DASYLab© software. DASYLab has a graphical user interface (GUI) which allows for easy manipulation of the incoming data [31]. Generally however, data was simply imported via DASYLab and the raw data was stored in the

American Standard Code for Information Exchange (ASCII). ASCII is a common format used to exchange information between different software.

5.4 Data Acquisition Parameters

All testing and data acquisition was performed by using the following parameters:

- Pressure transducer recorded at 1 kHz and RMS of signal calculated over one second interval and recorded.
- Accelerometers recorded simultaneously at 333 kHz for 14 seconds.
- AE sensor recorded at 1 MHz for 9 seconds.

Samples rates and recording length were chosen based on sampling high enough to prevent aliasing while keeping the ASCII files to a manageable size. Typical file sizes were on the order of 10^2 megabytes.

5.5 Band-Pass Filtering

The first step in post-processing was to apply appropriate band-pass filters to the accelerometer and acoustic emission data. The high pass filters will efficiently remove any DC bias and low frequency noise which falls below the sensors effective sensing range. The low pass filters will remove high frequency noise from the recorded data between the sensor's effective range limit and Nyquist frequency. Table 5.2 presents the filters used throughout the signal processing.

Table 5.2 Butterworth Band Pass Filter Parameters Applied to All Data Prior to Post-Processing

Data Type	High Pass Filter		Low Pass Filter	
	Cut-off (Hz)	Number of Poles	Cut-off (Hz)	Number of Poles
Accelerometer	1	2	56,474	8
Acoustic Emission	21,249	8	282,371	8

All filters were designed to keep data taken within the sensors frequency range to be reduced to a maximum of 0.998 magnitude. Also, any energy located at the Nyquist frequency (Accelerometers: 167 kHz & AE Sensor: 500 kHz), was reduced to -75 dB and -40 dB respectively. See Appendix F for confirming calculations. It is important to note that the ideal high pass filter for the accelerometer data was not a two pole Butterworth with a cut-off frequency equal to 1 Hz. However, the ideal high pass filter for the accelerometer data could not be implemented due to resolution restrictions within the frequency domain. Due to this, the high pass filter shown in Table 5.2 was implemented.

5.6 Data Analysis Background

There were many different analysis methods and metrics applied to the cavitation monitoring data. Section 5.6 will explain the theoretical background and how the analysis methods may be able to be used to characterize the cavitation signals. Chapter 6 will present the results and characterization of the cavitation using the methods and metrics outlined. The general data analysis flow is presented in Figure 5.5.

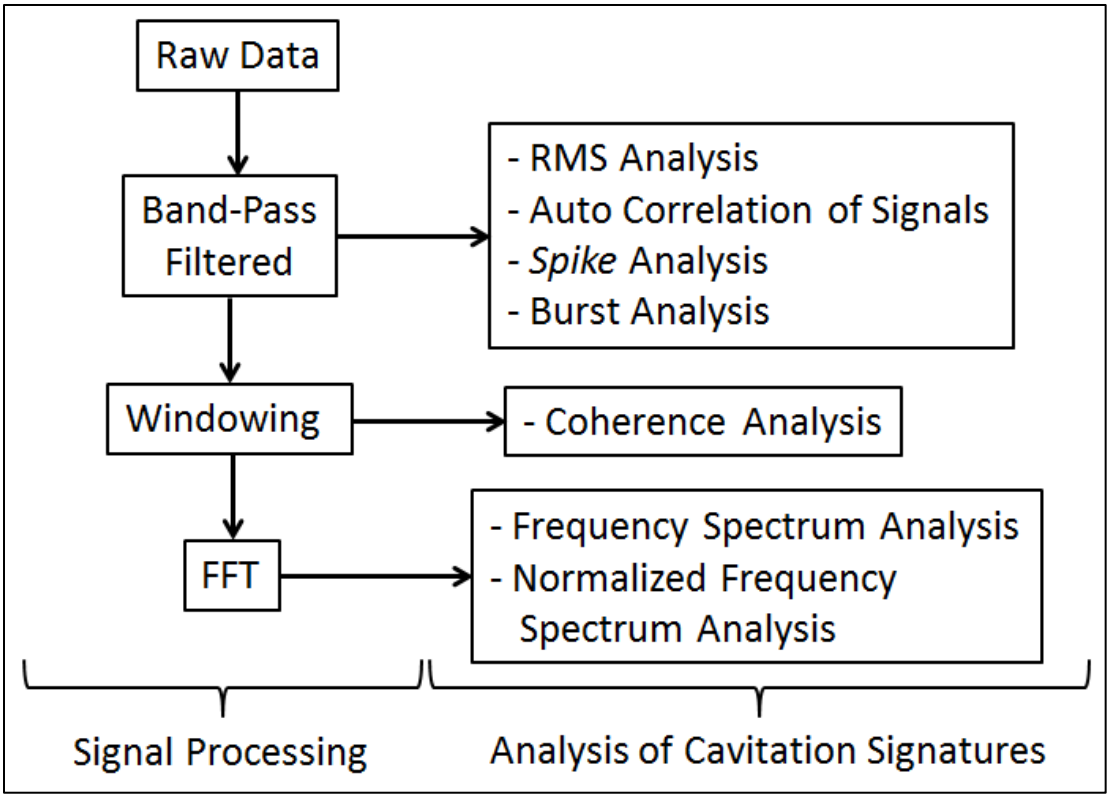

Figure 5.5 General Data Analysis Flow Chart

5.6.1 Root-Mean-Square Signal Analysis

The root-mean-square (RMS) value of a signal is a statistical measure of the magnitude of a varying signal. For a discrete signal, the equation

$$x_{rms} = \sqrt{\frac{1}{n}\left(x_1^2 + x_2^2 + \cdots + x_n^2\right)} \tag{5.1}$$

is used to determine RMS value. Determining the RMS value is one of the more simplistic ways of quantifying a signal. However, tracking the RMS value can provide indication of the strength of the phenomenon being investigated. The RMS value of the cavitation signal will be investigated at all attainable flow rates and cavitation indexes.

5.6.2 Auto-Correlation

Auto-correlation is a cross-correlation of a signal with itself. Cross-correlations are generally used for searching large signals for repeatable/identifiable time domain characteristics. This is done by convolving a shorter signal, which is the repeatable time domain characteristic being searched for, over the longer signal. Identification of the repeatable characteristics of interest are easily identified within the cross-correlation. As auto-correlation is a cross-correlation of a signal with itself, the signal is convolved front to back with itself. If repeatable patterns exist, they will be identified with an autocorrelation. For a discrete signal, equation

$$R_{xx}(j) = \sum_n x_n \bar{x}_{n-j} \tag{5.2}$$

is used to determine the autocorrelation of the signal. Auto-correlations will be used to investigate if the observed cavitation signals have repeatable/identifiable characteristics.

Equation

$$\bar{R}_{xx}(j) = \frac{R_{xx}(j)}{\max(abs(R_{xx}(j)))} \tag{5.3}$$

will be used to plot the auto-correlations. Equation 5.3 facilitates easily quantifiable comparisons between different flow rates/cavitation indexes for all auto-correlation results.

5.6.3 *Spike* Analysis

Spike analysis is a technique that was fabricated by myself throughout the course of this project. *Spike* analysis consists of dividing the absolute maximum value observed (the *spike*) in a time series sample by the RMS value of the signal.

$$x_{spike} = \frac{\max\{abs(x(t))\}}{x_{rms}(t)} \tag{5.4}$$

It was determined that the most basic *spike* analysis, presented in equation 5.4, was inherently susceptible to noise. To reduce the method's susceptibility to noise, it was decided to average the top ten absolute maximum values of the signal prior to dividing by the RMS value of the signal.

$$x_{spike10} = \frac{mean[\sum_{i=1}^{10} \max_i\{abs(x(t))\}]}{x_{rms}(t)} \tag{5.5}$$

Spike analysis can be used to determine the volatility of a phenomenon's current state based on magnitude. If the current state has a low *spike* value, the state is most likely steady and not on the verge of changing. If the current state has a high *spike* ratio value, the state is most likely on the verge of changing, i.e. from an incipient to a developed cavitation state or from a developed to a super cavitation state.

5.6.4 Burst Analysis

Burst analysis is a method consisting of determining a time domain value, and counting each time the signal in the time domain breaches that value. For this project, the burst count threshold was always set at multiples of the signals standard deviation. Throughout the analysis, this multiplier would change, and based on iterative approach, the most well suited burst count threshold was determined for different signals. An example of an ideal signal for burst analysis is shown in Figure 5.6.

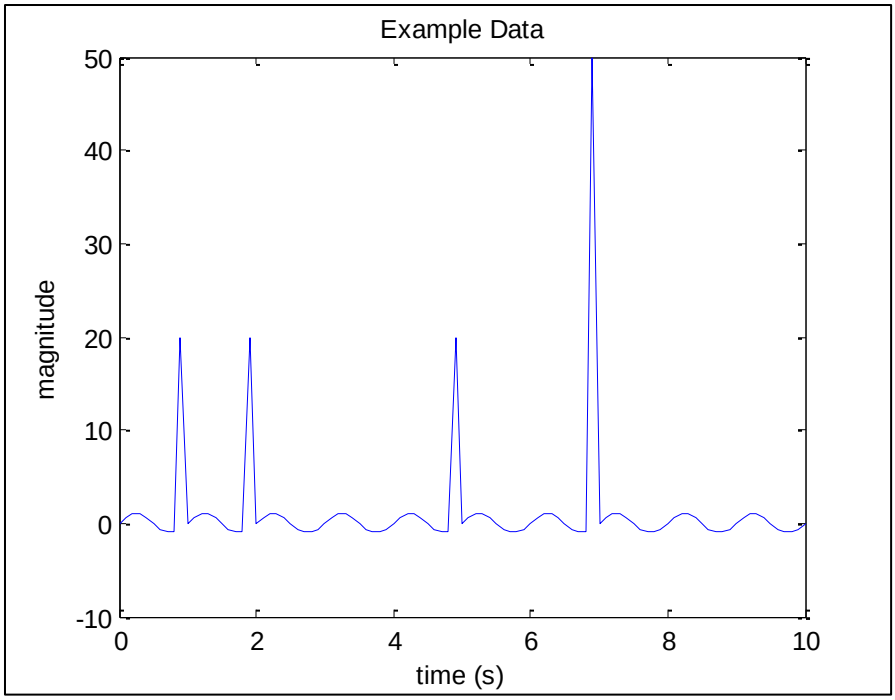

Figure 5.6 Example of Ideal Data to be Quantified by Burst analysis

The standard deviation of the data shown in Figure 5.6 is 6.02. Using the standard deviation as the burst counter threshold, four spikes are counted accurately. On nosier data however, it is recommended to use a multiple of the standard deviation. One must be careful though, for the example data shown in Figure 5.6, if the threshold is set to three times the standard deviation, the algorithm still returns a count of four spikes. However, if the burst count threshold is set to four times the standard deviation, the algorithm only returns a count of one. The process of determining the burst count threshold will be determined iteratively on the cavitation data. See Appendix G for example Burst analysis code.

5.6.5 Coherence Analysis

Coherence in signal processing refers to the agreement between two signals at specific frequencies. For this project, coherence between the top and bottom accelerometers will be

analyzed. Coherence between two real-valued signals, *x(t)* and *y(t)*, is determined from equation 5.6.

$$C_{xy} = \frac{|G_{xy}|^2}{G_{xx}G_{yy}} \tag{5.6}$$

Where:

C_{xy}: Coherence between two real-valued signals
G_{xy}: Cross spectral density of two real valued signals
G_{xx}: Auto-spectral density of *x*
G_{yy}: Auto-spectral density of *y*

The use of a Hanning window greatly reduces noise and allows for easier observation of important characteristics revealed from the coherence. Coherence between the top and bottom accelerometers could reveal natural frequencies of the system, common frequencies generated from impacts and/or turbulent flow effects within the cavitation tunnel.

5.6.6 Frequency Spectrum Analysis

The use of the Fast Fourier Transform (FFT) is well known and a common analysis technique used in signal processing. All data will be windowed and transformed into the frequency domain utilizing the FFT and searched for prominent frequencies and frequency bands. Figure 5.7 shows the basic technique demonstrated through a visual example.

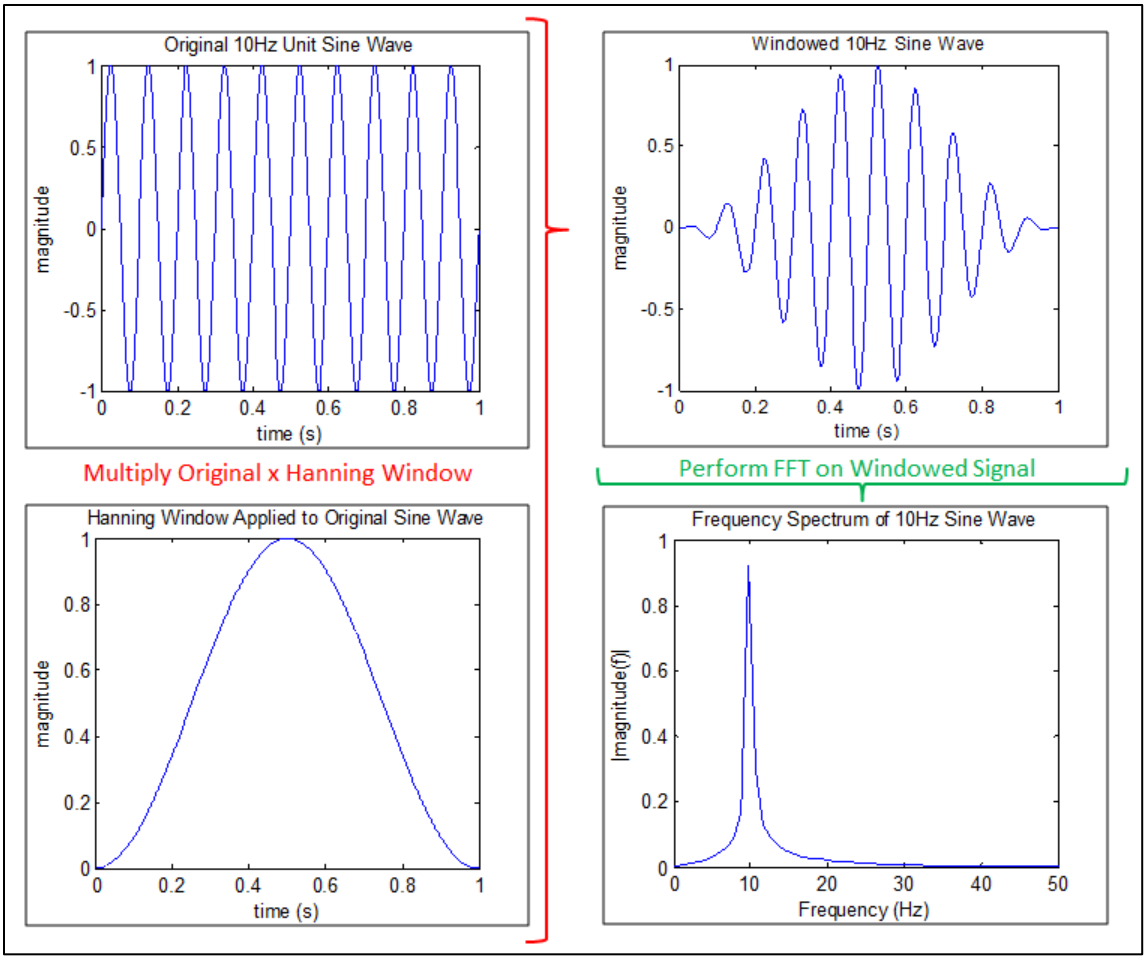

Figure 5.7 Fast Fourier Transform Example

Frequency spectra will be analyzed to check for changing frequency spectra across flow ranges. This is a common technique used to identify cavitation onset.

5.6.7 Normalized Frequency Spectrum Analysis

Frequency spectrum normalization is a way of suppressing non-critical frequency spectrum content while amplifying content of interest. The idea is to obtain initial frequency spectrum measurements of an apparatus without the phenomenon of interest occurring. Then to use that frequency spectrum to normalize other frequency spectrums which were taken while the phenomenon was taking place. This normalization will reduce the non-phenomenon frequencies

while pronouncing the phenomenon of interest frequencies [16] [17]. Figure 5.8 provides a visual of the technique. Refer to Appendix H for example frequency spectrum normalization code.

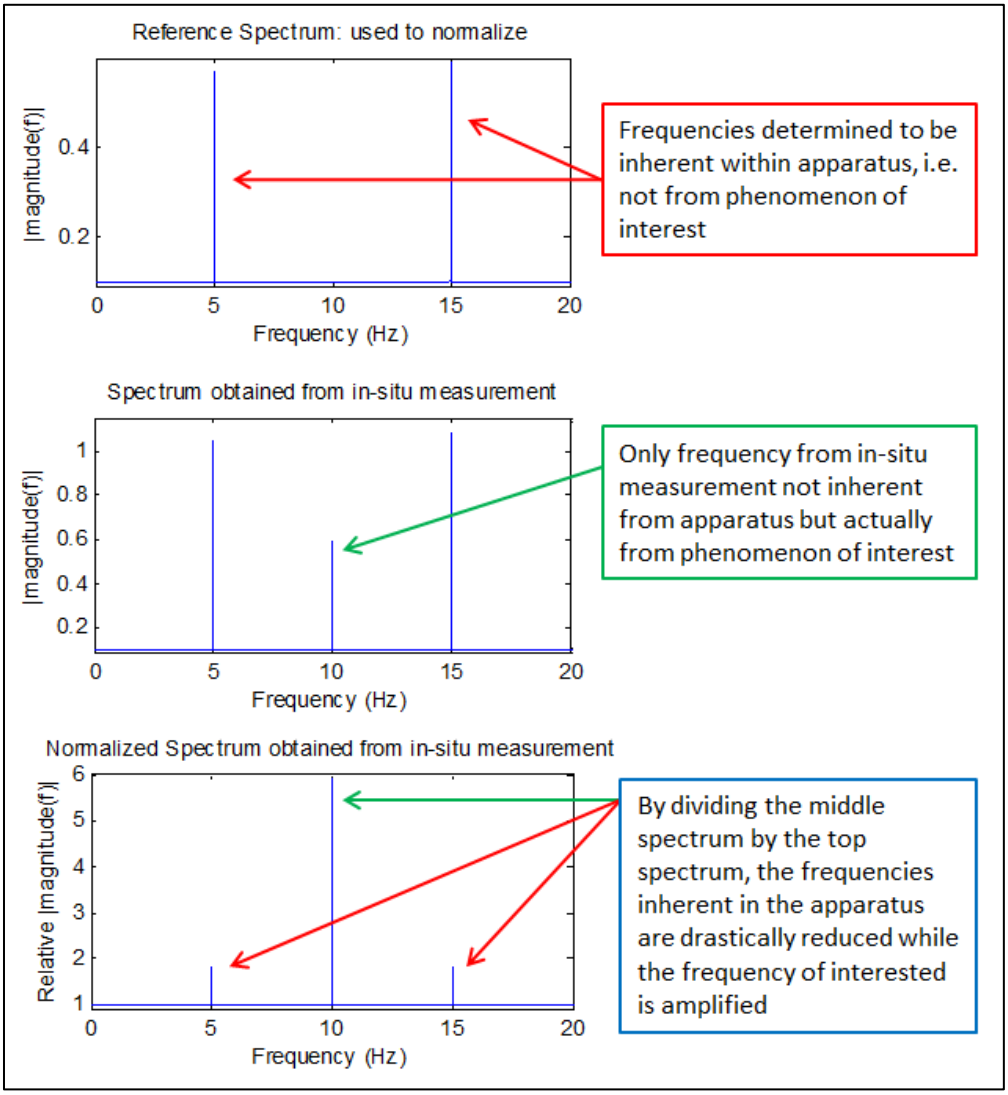

Figure 5.8 Spectrum Normalization Visual

CHAPTER 6

RESULTS

6.1 Testing Procedure and Testing Days

All operational tests were performed using the same method. An outline of the method followed is presented below:

a) Start test by recording barometric pressure at USBR High Head Pump station
b) Start High Head Pump at minimum flow rate
c) Take sensor measurements at flow rate
    - All flow rates were allowed to settle into a steady state. After the flow rate was increased or decreased, the set-up was generally allowed to settle for 20-60 seconds.
d) Increase flow rate by 0.25 ft^3/s
e) Repeat (c) – (d) – (e) until maximum flow rate is reached
f) Decrease flow rate by 0.25 ft^3/s
g) Repeat (c) – (f) – (g) until minimum flow rate is reached
h) Turn off High Head Pump

A full-test took between 20-40 minutes. The time was dependent on if there were multiple people running the experiment or a single person as the flow adjustment dial was remotely located from the data acquisition equipment. There were three full-tests taken for final data analysis, along with numerous spot checks, half tests and incomplete tests performed on the experimental set-up. The major milestone tests and corresponding atmospheric pressures are presented in Appendix I.

All data presented in this results section was taken on February 1st, 2012 when the atmospheric pressure was recorded to be 11.75 psi. Figures 6.1 and 6.2 present some example bottom acceleration and acoustic emission data taken on February 1st, 2012.

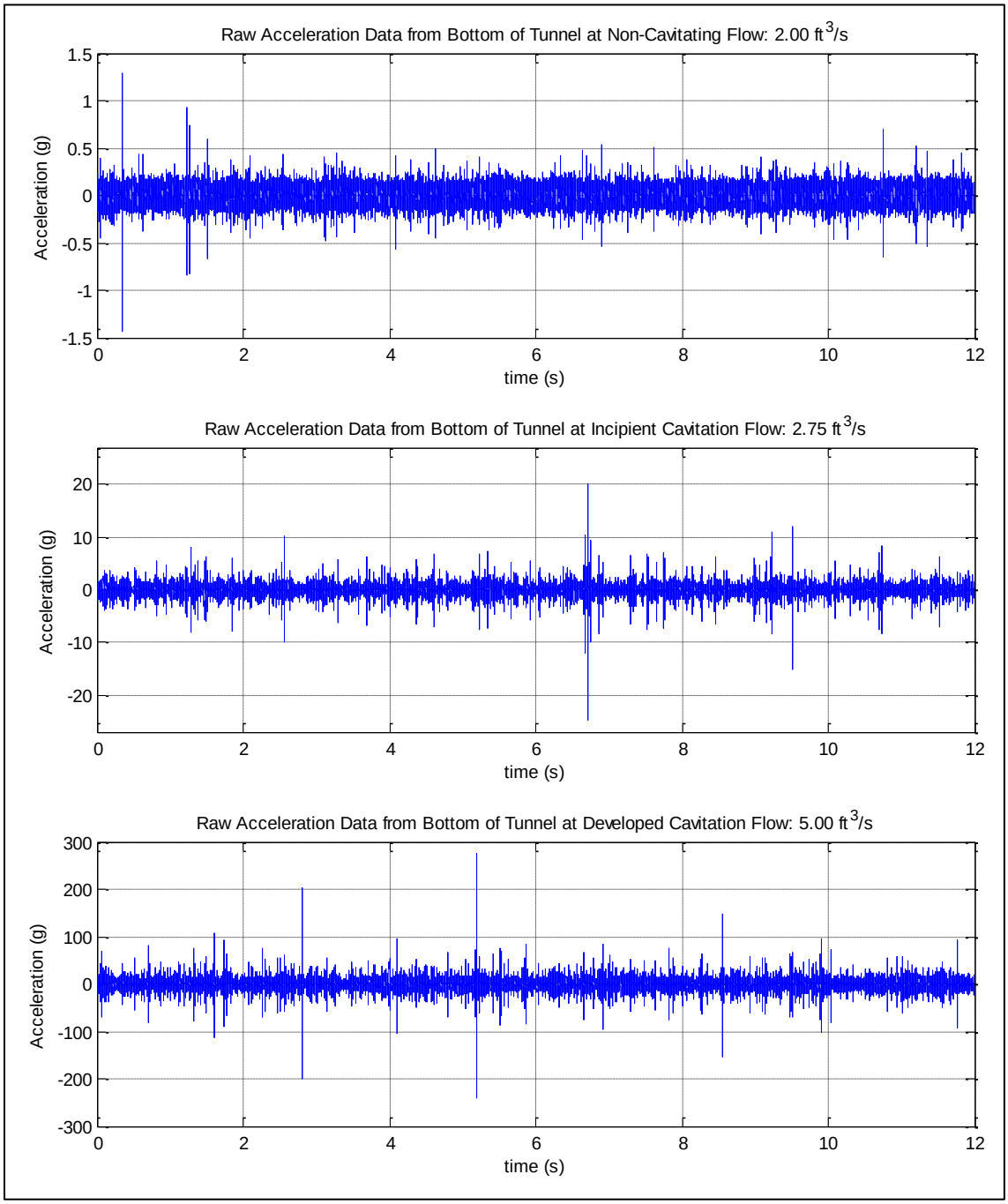

Figure 6.1 Raw Acceleration Data from Bottom of Cavitation Tunnel for Non-Cavitating, Incipient Cavitation and Developed Cavitating Flow

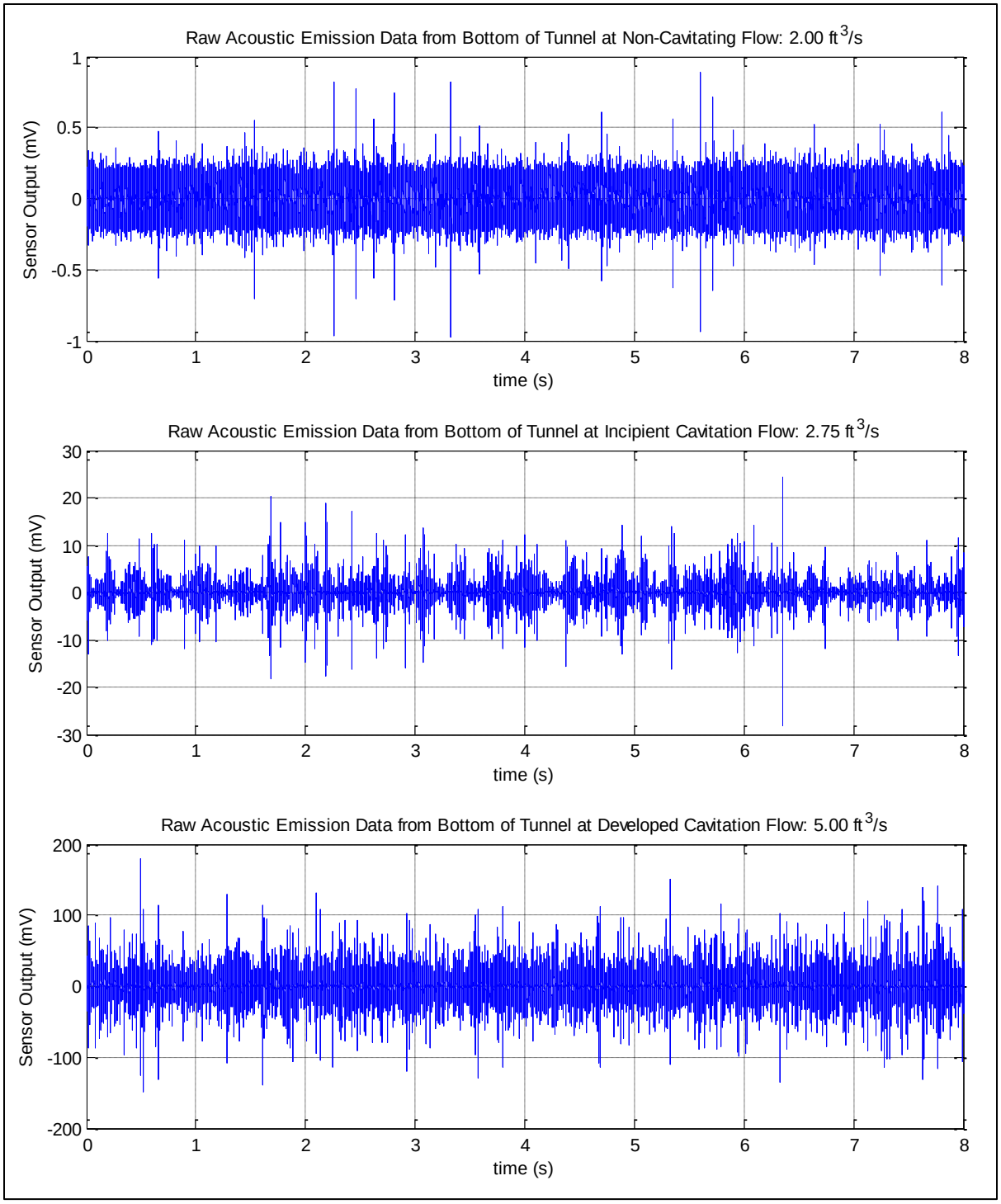

Figure 6.2 Raw Acoustic Emission Data from Bottom of Cavitation Tunnel for Non-Cavitating, Incipient Cavitation and Developed Cavitating Flow

6.2 Gage Pressure and Cavitation Index versus Flow Rate

The cavitation index was predicted at each flow rate (shown in Table 4.1) however the prediction utilized an estimated atmospheric pressure and constant gage pressure (details in Appendix A). Using the atmospheric pressure measured at the testing site and gage pressure determined from the operational testing, which is presented in Figure 6.3, the cavitation index was calculated for each flow rate. The cavitation indexes were calculated using Equation 4.2 and are presented in Figure 6.4.

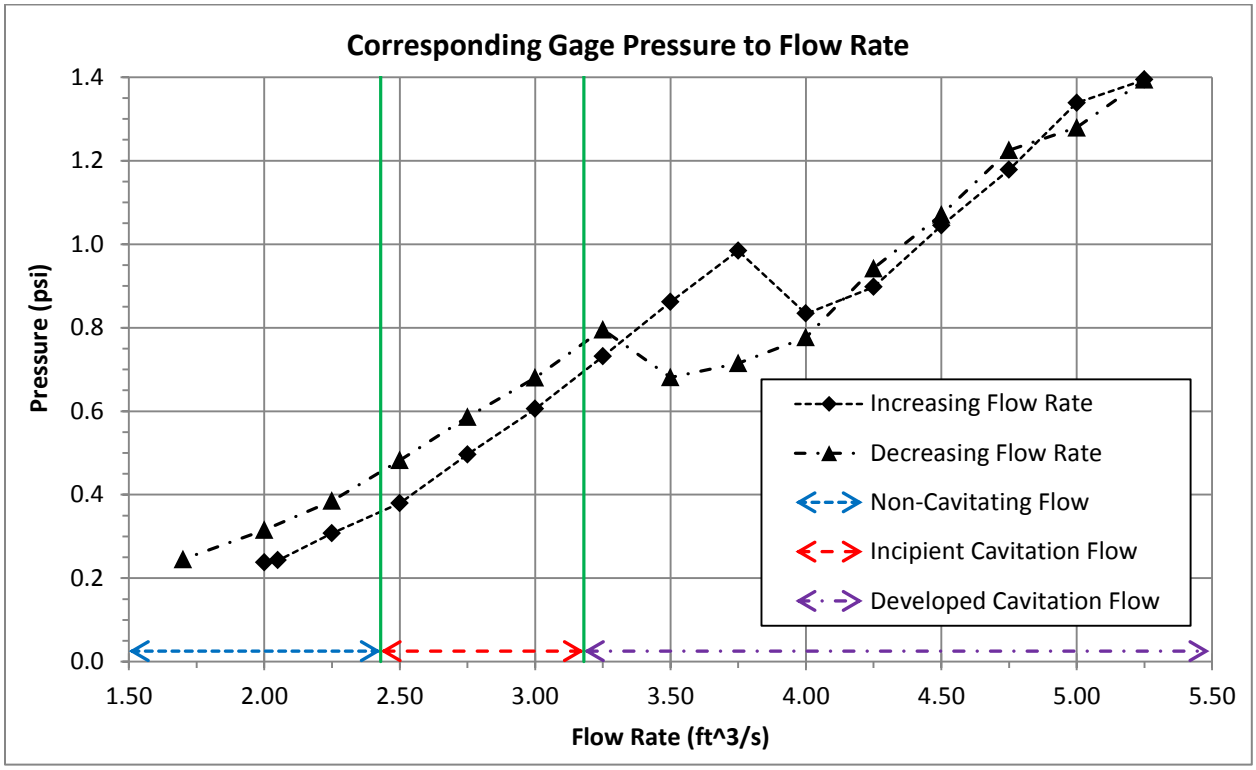

Figure 6.3 Gage Pressure recorded at Cavitation Inducing Offset into the Flow

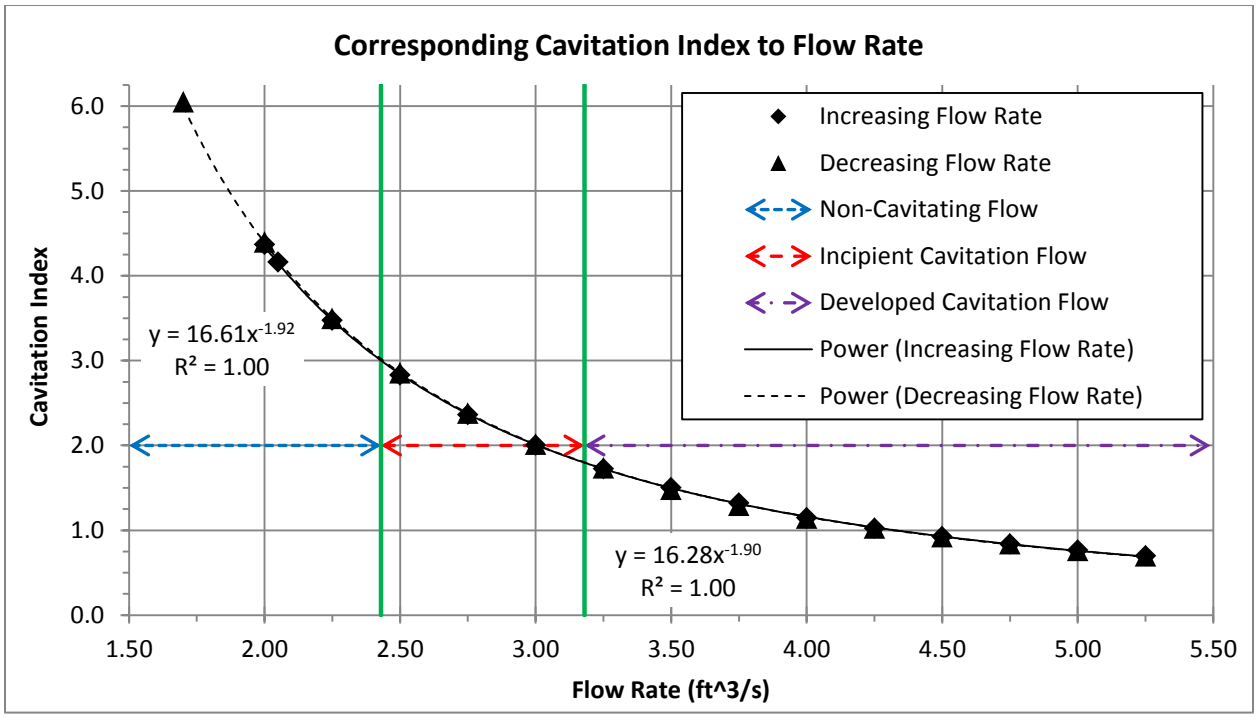

Figure 6.4 Corresponding Cavitation Index to Flow Rate

The gage pressures observed during increasing flow rates were found to be different than the gages pressure observed during decreasing flow rates. While the gage pressures are low enough values relative to atmospheric pressure (see how they relate in determining σ by referring to Equation 4.2) so they do not drastically alter the cavitation index versus flow rate determinations, the disagreement between the increasing and deceasing flow rates gage pressure readings do however foreshadow trends presented later. Power regression fits presented in Figure 6.4 are:

$$\sigma = 16.3Q^{-1.90} \tag{6.1}$$

$$\sigma = 16.6Q^{-1.92} \tag{6.2}$$

Where:

Q: Flow Rate (ft^3/s)

Equation 6.1 represents the relationship between cavitation index and increasing flow rate, while Equation 6.2 represents the relationship between cavitation index and decreasing flow rate. These equations are practically identical as shown in Figure 6.4. The flow range during testing was from 1.70 ft^3/s to 5.25 ft^3/s. Although the pump curve provided in Figure 4.1 shows a range from 1.00 ft^3/s to 6.00 ft^3/s, the minimum and maximum flows could not be reached during operation. Equations 6.1 and 6.2 provide an average error of 0.73% when predicting the cavitation index from the flow rate over the range 1.70-5.25 ft^3/s (error code presented in Appendix J). Using the cavitation index quantifications provided in Appendix B, critical flows and ranges were determined in relation to the cavitation index. Table 6.1 presents the flow ranges corresponding to cavitation activity.

Table 6.1 Flow Ranges Corresponding to Cavitation Index

Cavitation Index Range	Cavitation Intensity	Flow Range (ft^3/s)
$\sigma \geq 3$	No Cavitation	$Q \leq 2.43$
$1.8 \leq \sigma < 3$	Incipient Cavitation	$2.43 < Q \leq 3.18$
$0.3 \leq \sigma < 1.8$	Developed Cavitation	$3.18 < Q \leq 8.12$
$\sigma < 0.3$	Super Cavitation	$Q > 8.12$

Figure 6.5 provides a visual of various levels of cavitation within the tunnel. Video of the cavitation within the flow was used to validate the predicted cavitation states. The video shot was at 60 fps at 1080 pixels.

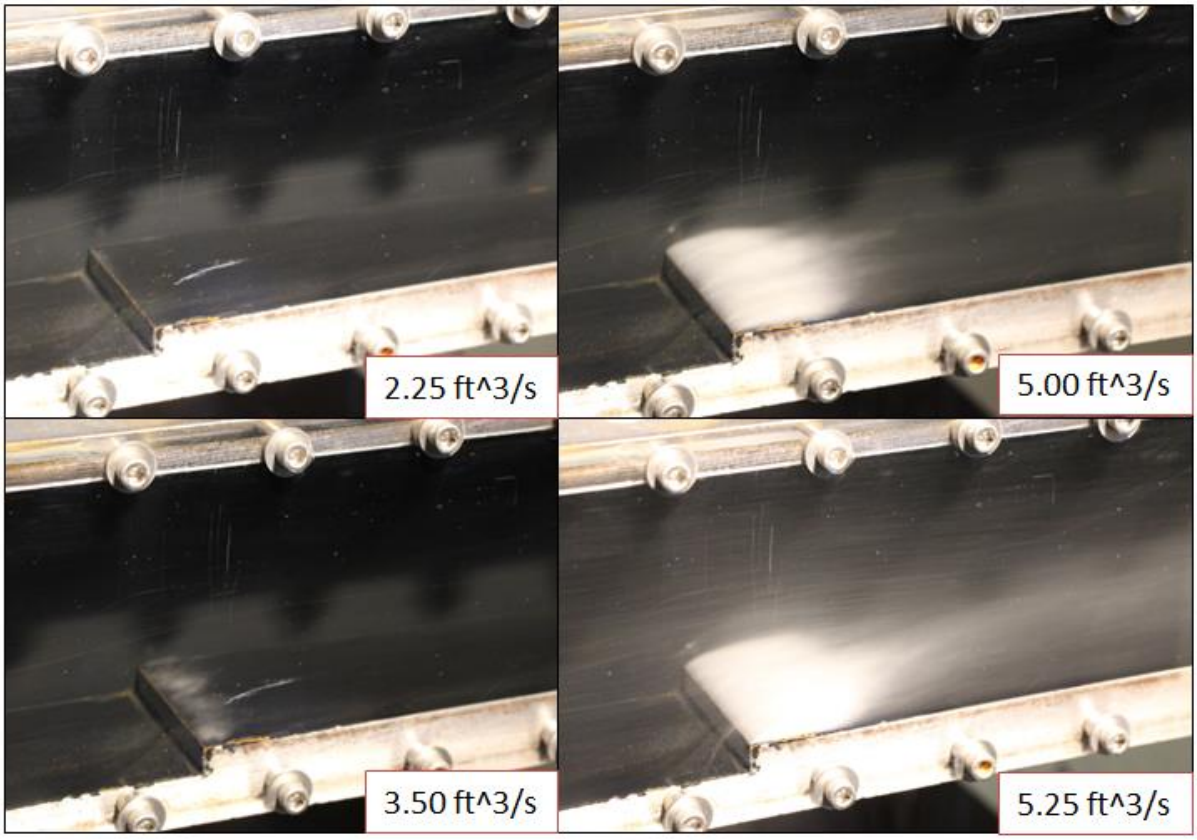

Figure 6.5 Visual of Cavitation within Tunnel at Various Flow Rates

From the video, it was clear that incipient cavitation had begun by 2.75 ft^3/s and possible as early has 2.50 ft^3/s. It was apparent that developed cavitation began at 3.25 ft^3/s. This visual inspection confirmed what was determined and presented in Table 6.1. Cross-over flows within the flow range available are 2.43 ft^3/s and 3.18 ft^3/s. However, it is important to note the visual difference shown between 5.00 ft^3/s and max flow 5.25 ft^3/s shown in Figure 6.5. At a flow rate of 5.00 ft^3/s the cavitation cavity appears to reattached to the bottom plate of the tunnel roughly 1.5 inches downstream of the offset. At a flow rate of 5.25 ft^3/s the cavitation cavity does not appear to reattached to the bottom plate of the tunnel, instead the cavity become a super-cavity with no absolute measureable reattachment point. Refer to Appendix K for supplemental cavitation flow photos. In addition to the visual difference, there was a discernible audible decrease in cavitation

noise from 5.00 to 5.25 ft^3/s. It is believed that 5.25 ft^3/s was audibly quieter than 5.00 ft^3/s due to the cavitation cavity which developed from 2.50 ft^3/s to 5.00 ft^3/s broke loose from the bottom plate. Once the cavity broke free, the bubbles were no longer collapsing 1.0-1.5 inches past the offset local to the bottom plate but simply collapsing in the flow stream. This visual and audible difference between 5.00 and 5.25 ft^3/s was foreshadowing what would be confirmed later, that maximum flow was actually the beginning of super cavitation. As such, two specific flow ranges were to be scrutinized throughout the results analysis, 2.25-3.50 ft^3/s for incipient cavitation and 5.00-5.25 for the transition from developed to super cavitation.

6.3 Root-Mean-Square Signal Strength Analysis

The simplest cavitation detection signal processing method is to correlate the strength of the recorded signals to flow rate/cavitation index. Equation 5.1 was used to determine the RMS value of all signals at recorded flow rates. Figures 6.6 – 6.8 present the RMS values of the recorded signals for the top accelerometer, bottom accelerometer and AE sensor, respectively. Refer to Appendix L for analysis code for both accelerometers and AE Sensor data. All acceleration RMS values were determined from a 12 second time history, while all acoustic emission RMS values were determined from an 8.5 second time history. Also, recorded signals were from steady state measurements.

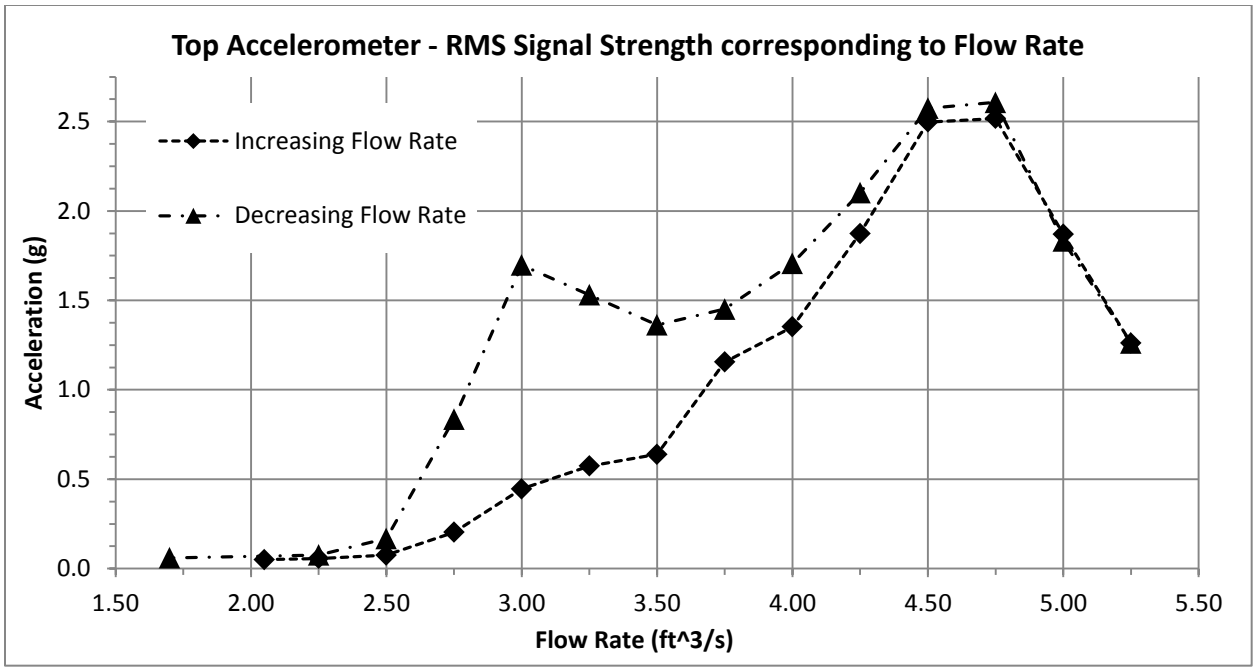

Figure 6.6 RMS of Acceleration from Top of Tunnel corresponding to Flow Rate

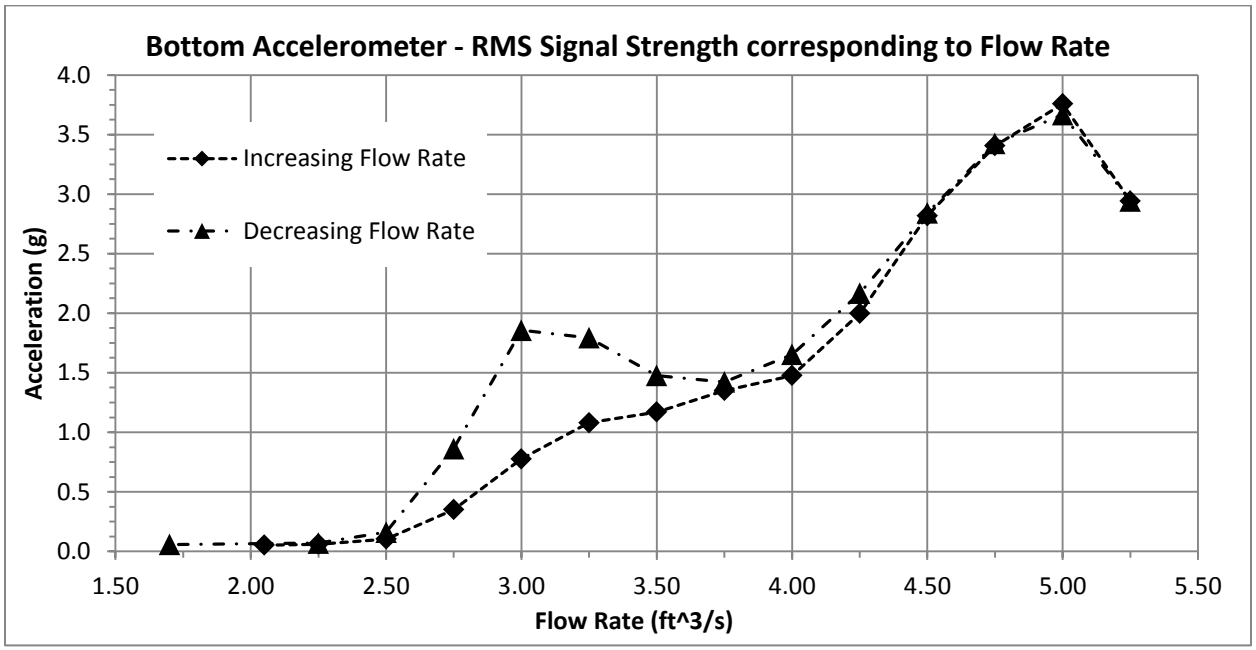

Figure 6.7 RMS of Acceleration from Bottom of Tunnel corresponding to Flow Rate

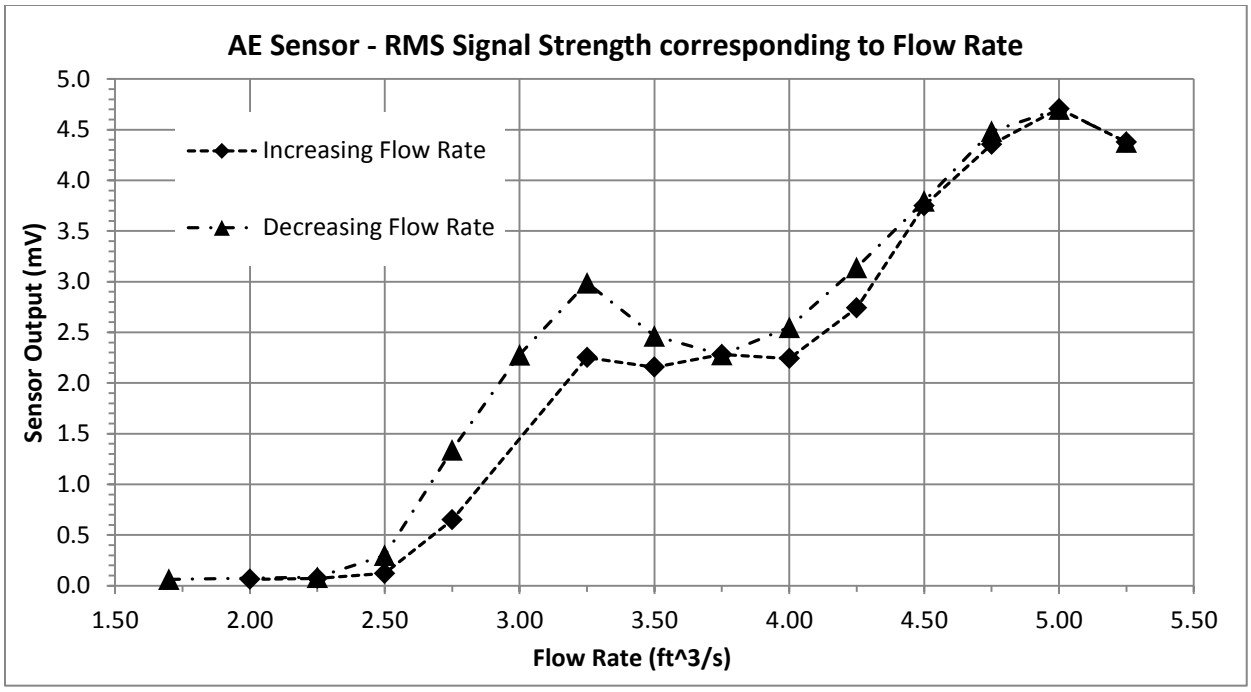

Figure 6.8 RMS of AE Sensor Signal corresponding to Flow Rate

There were a few consistent trends between all three of the sensor responses. RMS values consistently started to increase between 2.50 and 2.75 ft^3/s during increasing flow rates, suggesting incipient cavitation. The second was a consistent drop in signal strength between near maximum and maximum flow rates. The consistent drop from near maximum to maximum flow rates confirms the notion of super cavitation taking place at maximum flow rate. This confirmed what was audibly observed during initial testing of the tunnel. Third a consistent increase in signal strength was observed during decreasing flow rates starting at 3.75/3.50 ft^3/s and continuing to 3.25/3.00 ft^3/s. The third trend would infer an increase of cavitation while decreasing the flow rate, a trend not intuitive.

As observed in Figure 6.3, the pressure trends recorded during increasing and decreasing flow rates did not agree. This trend is also consistent with the RMS analyses. It should also be noted, that the acceleration readings of the phenomenon disagree much greater than the AE

sensors in regards to the increasing versus decreasing flow rates. The disagreement between increasing and decreasing flows suggest a hysteresis effect or a latent energy remaining in the system during decreasing flow rates.

6.4 Auto-Correlation of Signals

The next step in the analysis was to confirm if the recorded signals had repeatable characteristics. This was accomplished through the use of an auto-correlation, shown in equation 5.2. Figures 6.9 – 6.11 present the results of the auto correlations of the top acceleration, bottom acceleration and acoustic emissions respectively. Each figure contains three separate flows, 2.00 ft^3/s demonstrates a quiet non-cavitating flow, 2.75 ft^3/s demonstrates an incipient cavitation and 5.00 ft^3/s demonstrates a developed cavitation flow. Each auto-correlation has been normalized via equation 5.3. Refer to Appendix L for analysis code for both accelerometers and AE Sensor data.

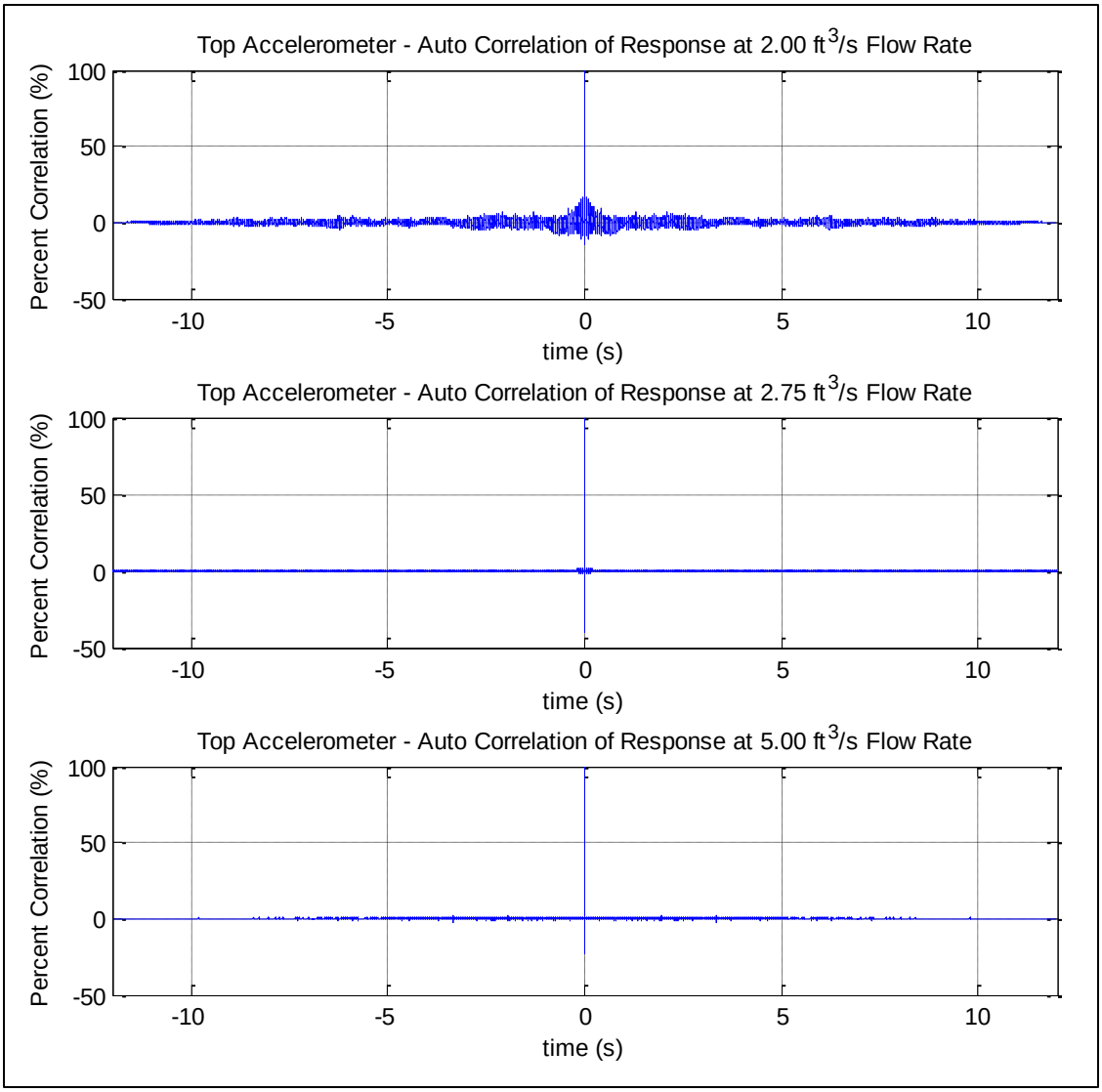

Figure 6.9 Auto-Correlation of Top Acceleration at Non-Cavitating, Incipient Cavitation and Developed Cavitation Flow Rates

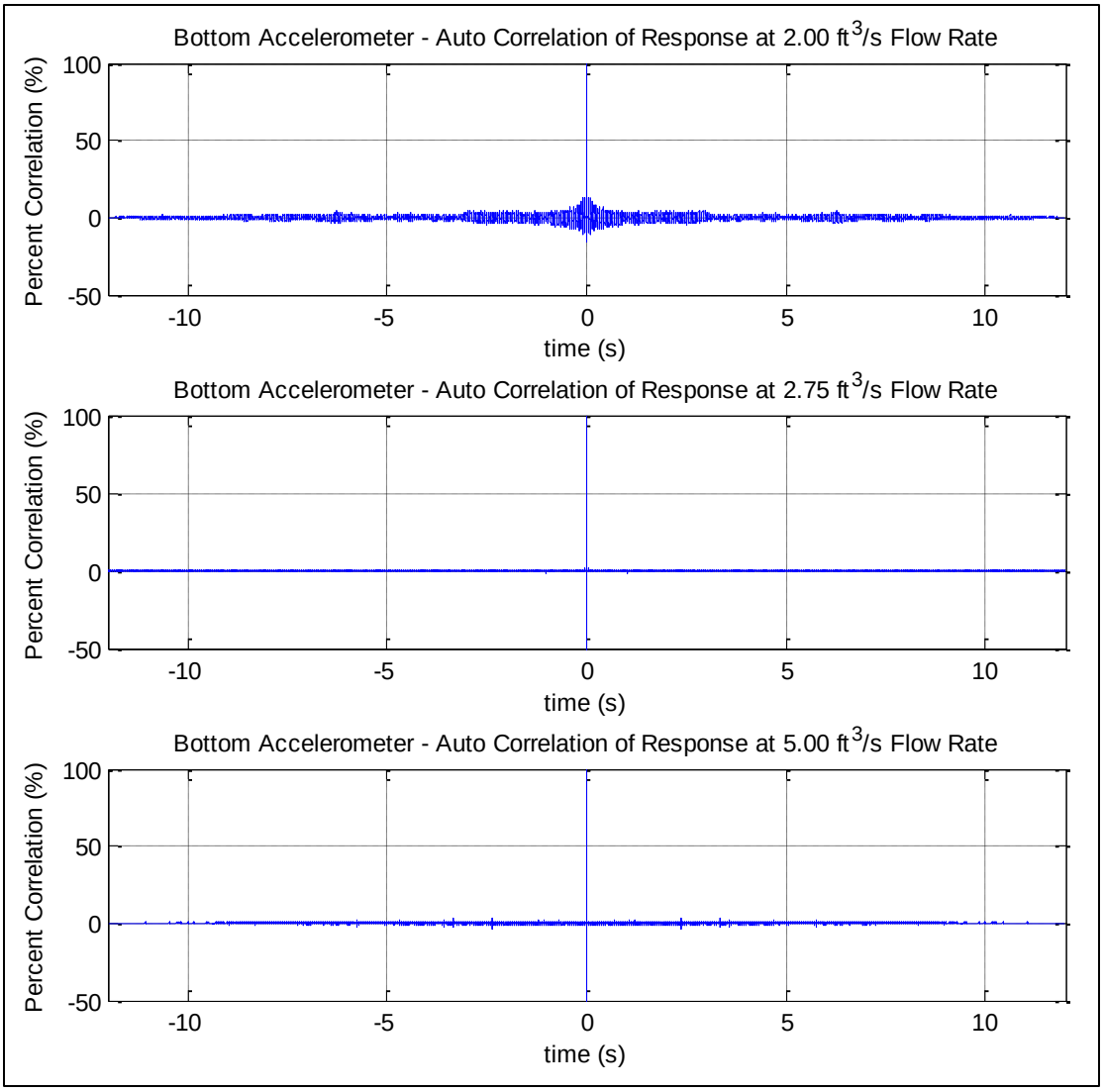

Figure 6.10 Auto-Correlation of Bottom Acceleration at Non-Cavitating, Incipient Cavitation and Developed Cavitation Flow Rates

As shown in Figures 6.9 and 6.10, there is almost zero repeatability within the incipient and developed cavitation flows. There is however, slight repeatability within the non-cavitating flow. This is most likely due to non-cavitating flow results have little to none turbulent flow data being recorded. The only data being recorded is that due to the structural movement of the apparatus. It is assumed the structural movement is linear and repeatable, hence the slight increase in auto-correlation at minimum flows.

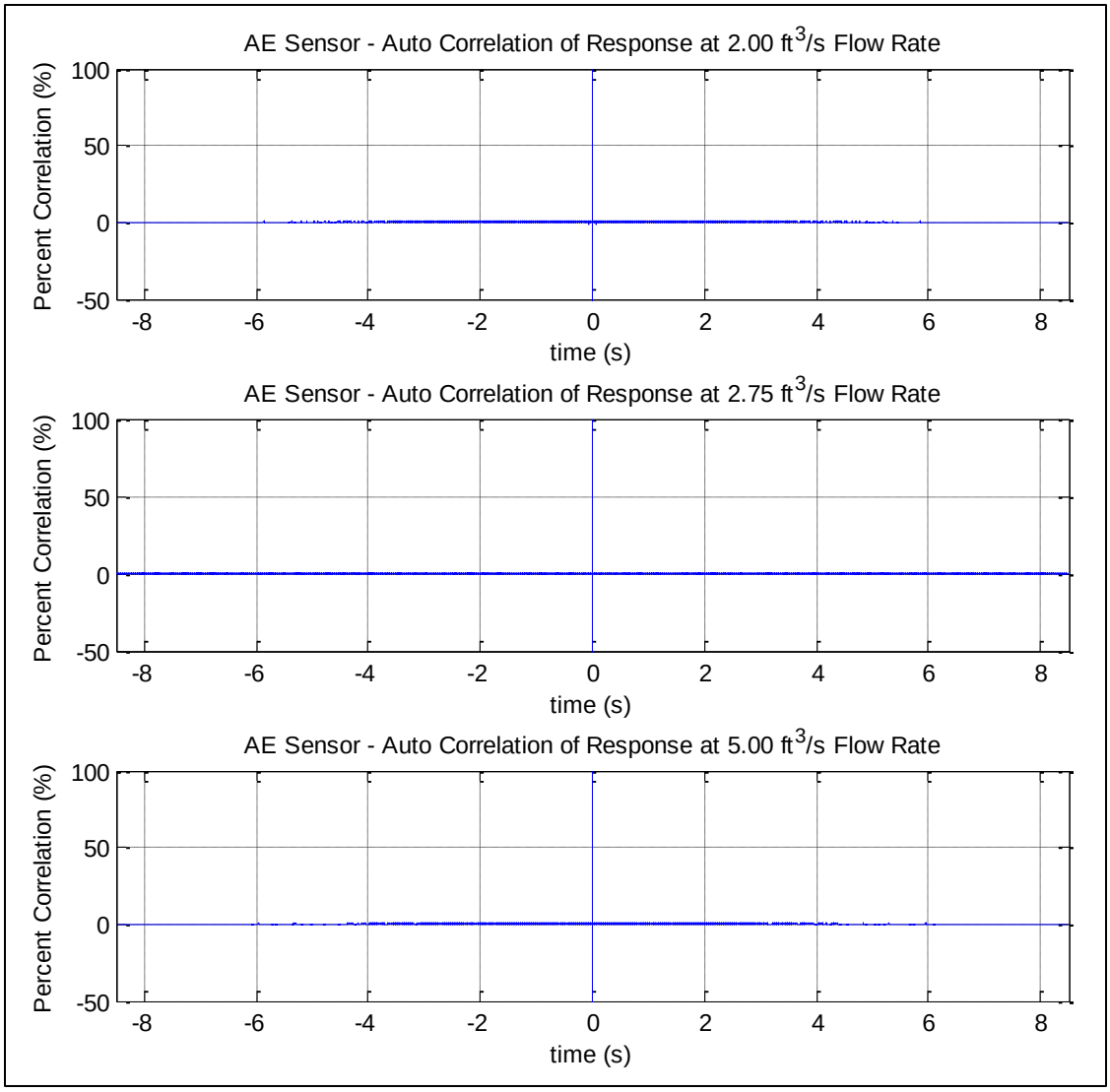

Figure 6.11 Auto-Correlation of Acoustic Emission at Non-Cavitating, Incipient Cavitation and Developed Cavitation Flow Rates

As shown in Figure 6.11, since the AE Sensor exclusively detects shear waves within the bottom plate of the cavitation tunnel (hence no structure movement), there was close to zero repeatability found within the signals. The auto-correlation analysis of the cavitation signals reveals an unfortunate truth, cavitation is a difficult signal to quantify. Refer to Appendix M for supplemental Auto Correlation plots. The autocorrelations did however provide confirmation that at flow rates ($Q < 2.25$ ft^3/s), the majority of energy recorded in the signals was from

structural movement and not cavitation. This confirmed that the goal of designing a cavitation inducing apparatus with a flow ranging from non-cavitating to cavitating was achieved.

6.5 Frequency Spectrum Analysis

All time domain data was transformed into the frequency domain utilizing the Fast Fourier Transform (FFT). The method used is outlined in Section 5.6.6. The goal of analyzing the frequency domain data was to search the data for common frequencies of interests between flows and cavitation states and observe if frequency spectra changed throughout the flow range. Figures 6.12 – 6.14 show the frequency spectra for the top accelerometer, bottom accelerometer and AE sensor for non-cavitating, incipient and super cavitation flows respectively. Increasing and decreasing flows are shown for non-cavitating and incipient flows while only the maximum flow rate is shown for super cavitation. Refer to Appendix L for all FFT MATLAB code.

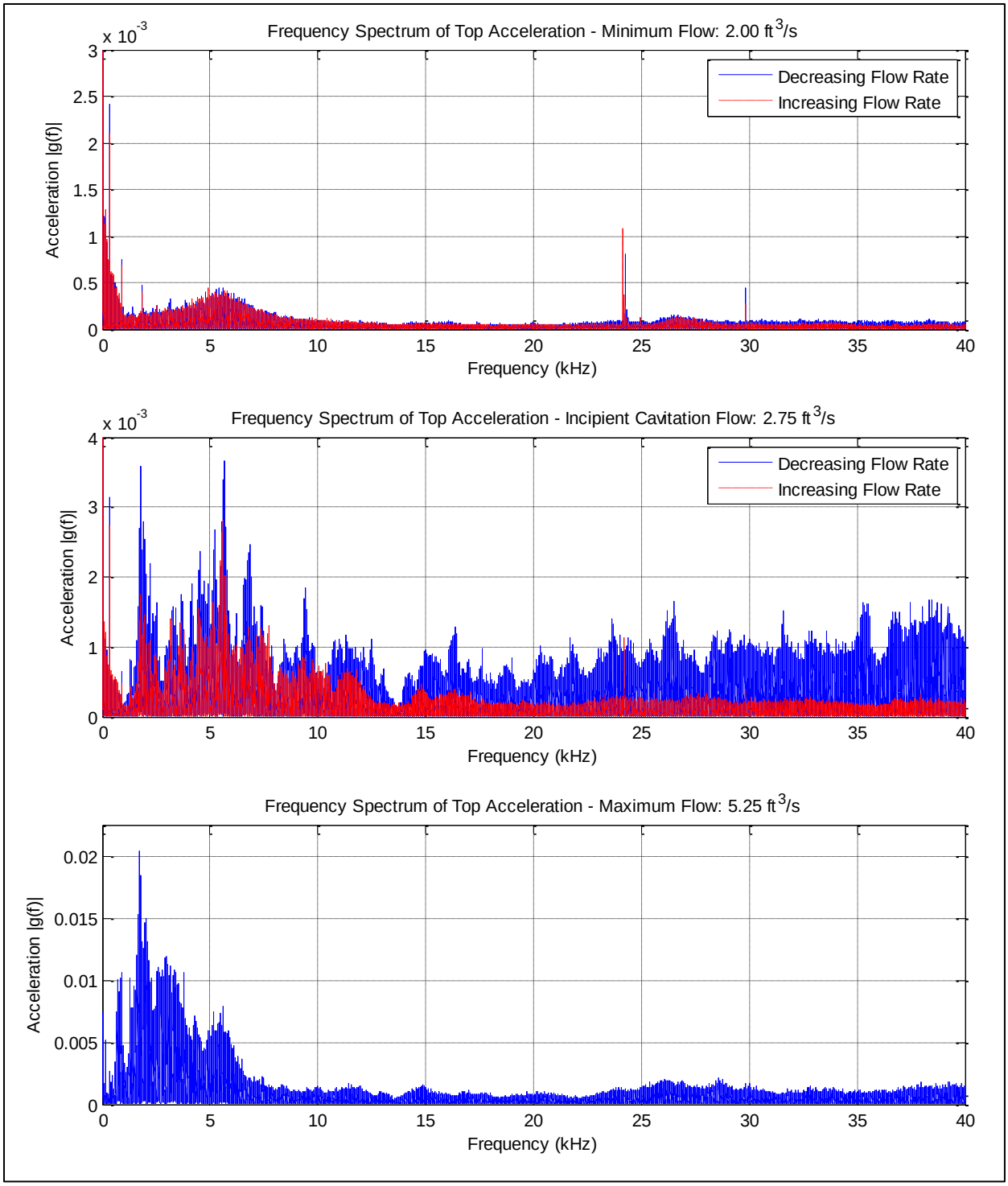

Figure 6.12 Frequency Spectrum of Acceleration Signal recorded from Top of Cavitation Tunnel during Non-Cavitating, Incipient Cavitation and Developed Cavitation Flow Rates

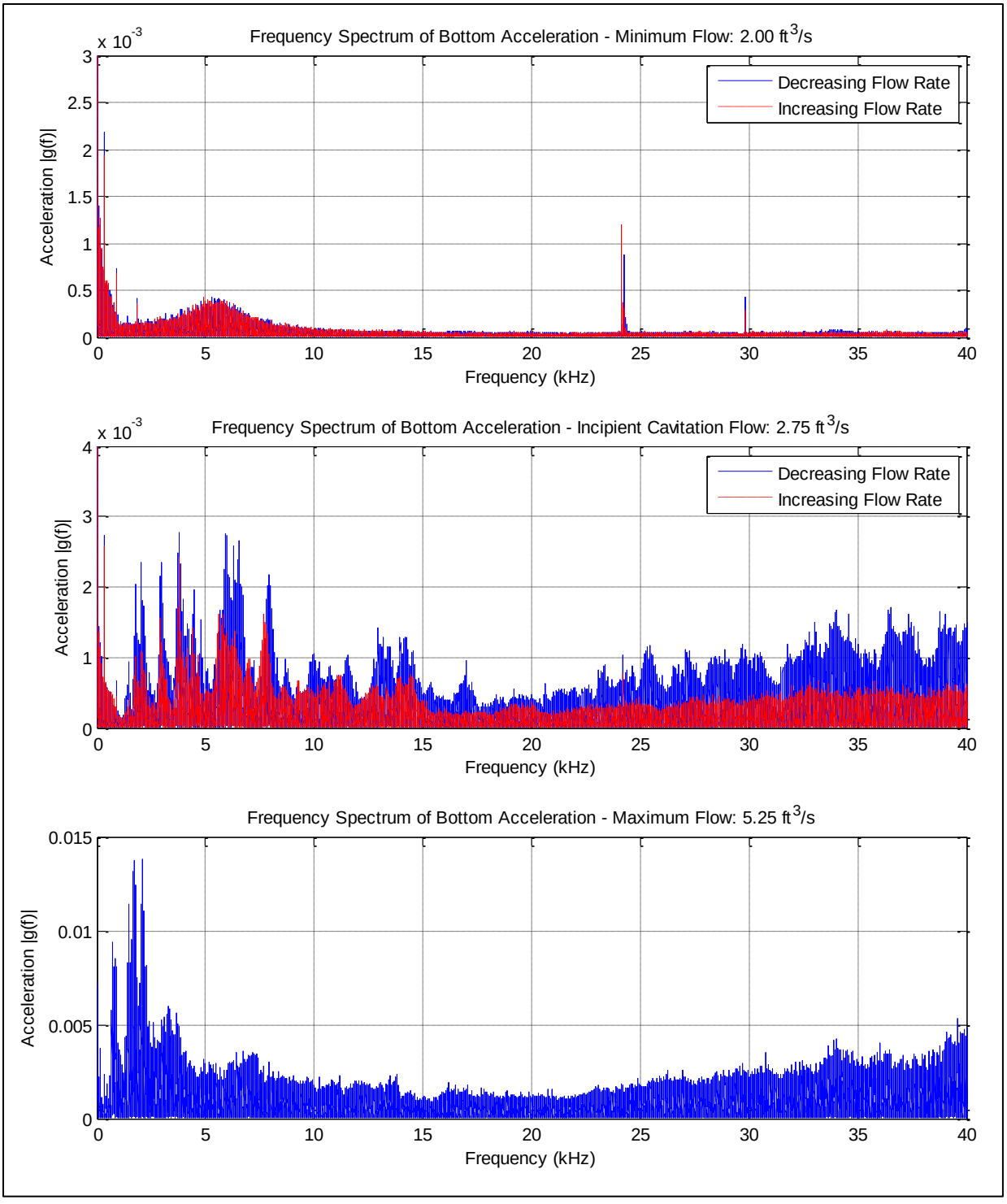

Figure 6.13 Frequency Spectrum of Acceleration Signal recorded from Bottom of Cavitation Tunnel during Non-Cavitating, Incipient Cavitation and Developed Cavitation Flow Rates

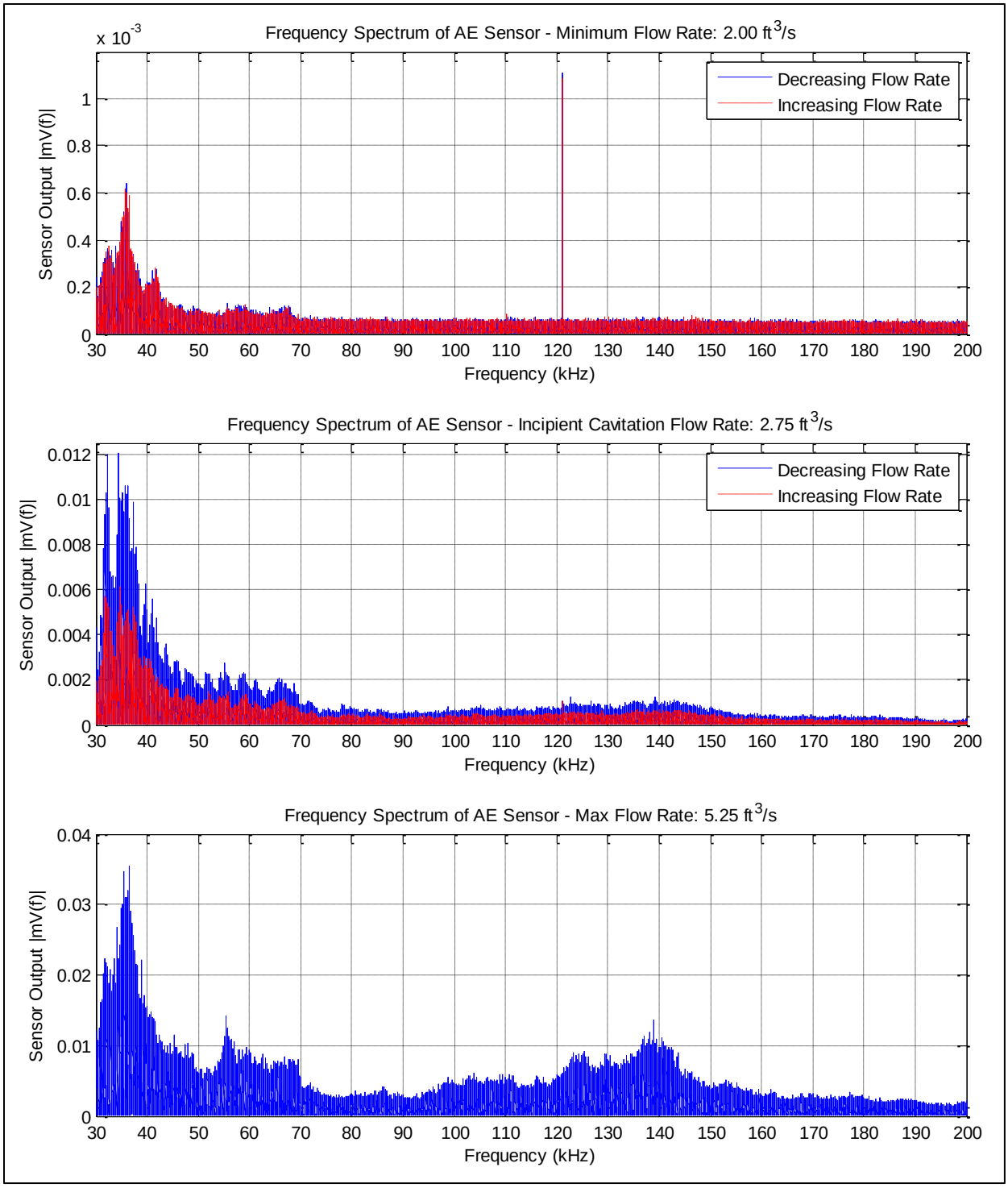

Figure 6.14 Frequency Spectrum of Acoustic Emission Signal Recorded from Top of Cavitation Tunnel during Non-Cavitating, Incipient Cavitation and Developed Cavitation Flow Rates

As shown in Figures 6.12 and 6.13, during minimum flow rates, the top and bottom acceleration frequency spectrums look very similar. The majority of energy is located below 10 kHz. This consistently between the top and bottom acceleration at minimum flow rates is most likely due the sensors only recording the structural movement of the set-up. In addition, natural frequencies of the structure appear at 24.5 kHz and 29.85 kHz.

As flow increases, cavitation takes place and enacts a random series of impacts on the cavitation tunnel bottom plate. This in turn returns frequency spectrums with broadband noise as demonstrated in the flow rates 2.75 ft^3/s and max flow frequency spectrums of Figures 6.12 – 6.14. Note the consistently higher frequency spectrums in the deceasing flow rates. This confirms what was seen prior in the RMS analysis, a latent energy within the system during the decreasing flows.

Also, take note of the difference between the maximum flow rate frequency spectrums between Figures 6.12 and 6.13, the top and bottom acceleration. The bottom acceleration frequency spectrum is consistently higher across all frequencies > 10 kHz. Based on the minimum flow rates, the majority of energy < 10 kHz is from the structural movement of the set-up, this with consistently higher magnitudes across frequencies 10-40 kHz, confirms that the cavitation impacts are taking place local to the bottom accelerometer.

As seen prior in the case study presented in Section 2.4.1, the changing of spectral content of signals as the flow rates increase, can be an indication of cavitation within the flow. Throughout Figures 6.12 – 6.14, the frequency spectra consistently change throughout the flow rates, providing validation cavitation is taking place. Refer to Appendix N for supplemental frequency spectrums of different flow rates.

6.6 Normalized Frequency Spectrum Analysis

For low flow rates ($Q < 2.25$ ft^3/s), the energy within the recorded signals is primarily due to the structure and background noise from the non-cavitating flow. It was decided to average the frequency spectrums of flow rates 2.00 ft^3/s and 2.25 ft^3/s and use this spectrum to normalize all the frequency spectrums. A detailed description of how the *normalizing* spectrum was obtained is provided in Appendix O. The process of frequency spectrum normalization outlined in Section 5.6.7 was followed. Figures 6.15 – 6.17 provide the normalized frequency spectrums for the top accelerometer, bottom accelerometer and AE sensor for non-cavitating, incipient and super cavitation respectively. Refer to Appendix L for normalized FFT MATLAB code.

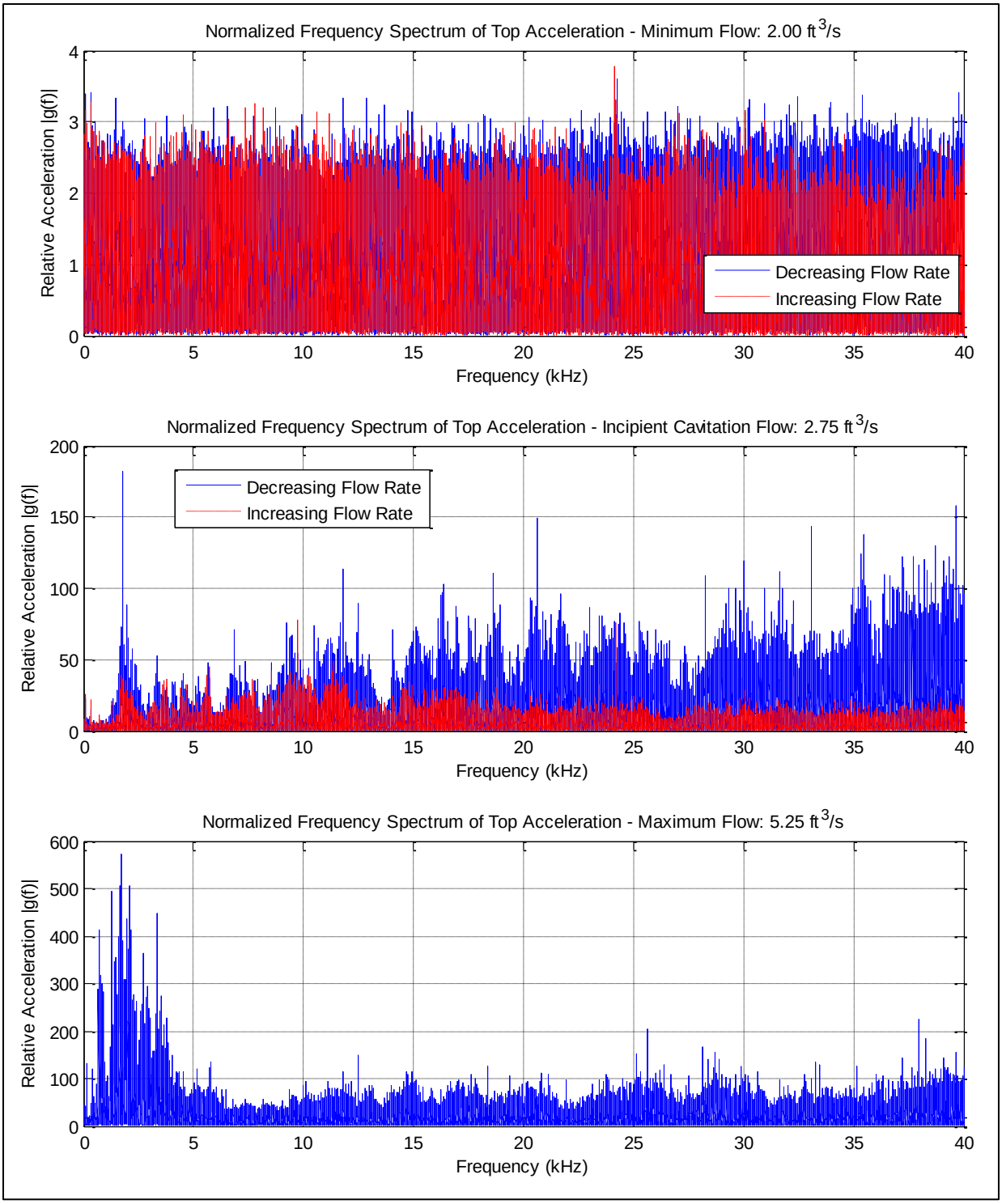

Figure 6.15 Normalized Frequency Spectrum of Acceleration Signal recorded from Top of Cavitation Tunnel during Non-Cavitating, Incipient Cavitation and Developed Cavitation Flow Rates

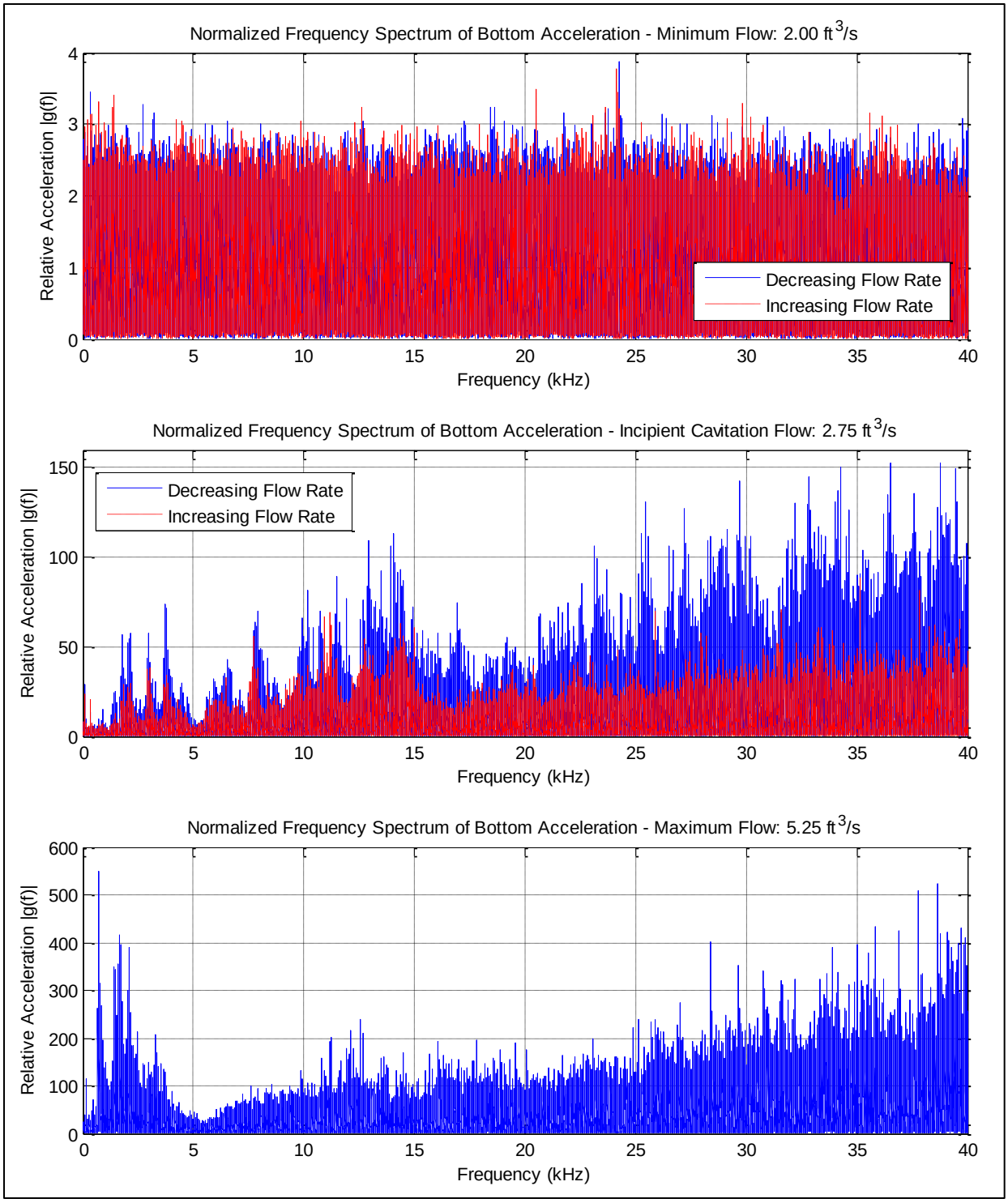

Figure 6.16 Normalized Frequency Spectrum of Acceleration Signal recorded from Bottom of Cavitation Tunnel during Non-Cavitating, Incipient Cavitation and Developed Cavitation Flow Rates

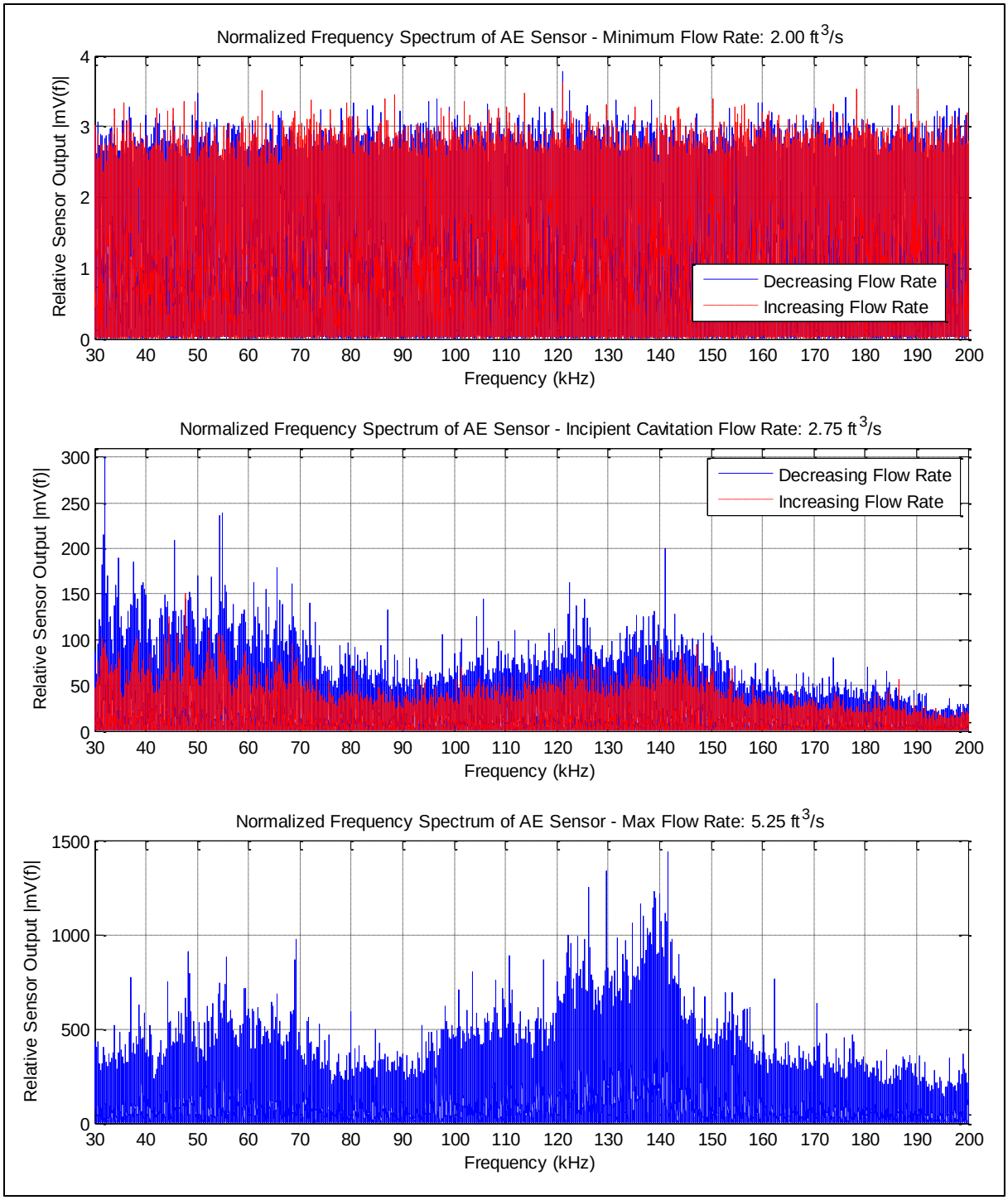

Figure 6.17 Normalized Frequency Spectrum of Acoustic Emission recorded from Bottom of Cavitation Tunnel during Non-Cavitating, Incipient Cavitation and Developed Cavitation Flow Rates

As shown in Figures 6.15 – 6.17, the minimum flow rates frequency spectrums are flat (consistent amplitude across the spectrum). It was the flow rates 2.00 – 2.25 ft^3/s which were used to normalize all the frequency spectrums, thus the minimum flows relative frequency spectrums being flat provides confirmation the normalization has worked effectively to remove non-cavitation influences on the spectrums. It is important to notice the y-axis on Figures 6.15 – 6.17. The y-axis are not |*magnitude(f)*|, but *relative* |*magnitude(f)*|. This *relative* |*magnitude(f)*| unit is due to the resulting magnitude being dependent on the low flow frequency spectrums but as all frequency spectrums were normalized by the same low flow frequency spectrum, comparing different flows and observing specific frequencies with particularly high magnitudes is still a valid metric for analysis. It important however to not use normalized spectrums in absolute terms.

As shown in the prior Figures 6.15 – 6.17, the normalized frequency spectrums reinforced the fact that broadband noise is being introduced into the system from cavitation impacts on the bottom plate. As seen in prior, its important to note that the bottom accelerometer consistently recorded higher acceleration that the top accelerometer at non-cavitating flows. Finally, the changing of frequency spectra and amplitude throughout the with cavitation states is clearly demonstrated. Refer to Appendix P for supplemental normalized frequency spectrums.

6.7 Coherence between Top and Bottom Acceleration

The first step when utilizing equation 5.6 to determine the coherence between two signals is to determine the type, length and overlap of the window applied to the data. For all results presented in this section, a Hanning window of length 2^{15} was used with an overlap of 2^{14}. For a detailed explanation of how this window, length and overlap were chosen and how these choices influence the coherence results, refer to Appendix Q. Figure 6.18 presents the coherence of the top and bottom acceleration readings at flow rates 2.00 ft^3/s, 2.75 ft^3/s and 5.25 ft^3/s. Refer to Appendix L for coherence MATLAB code.

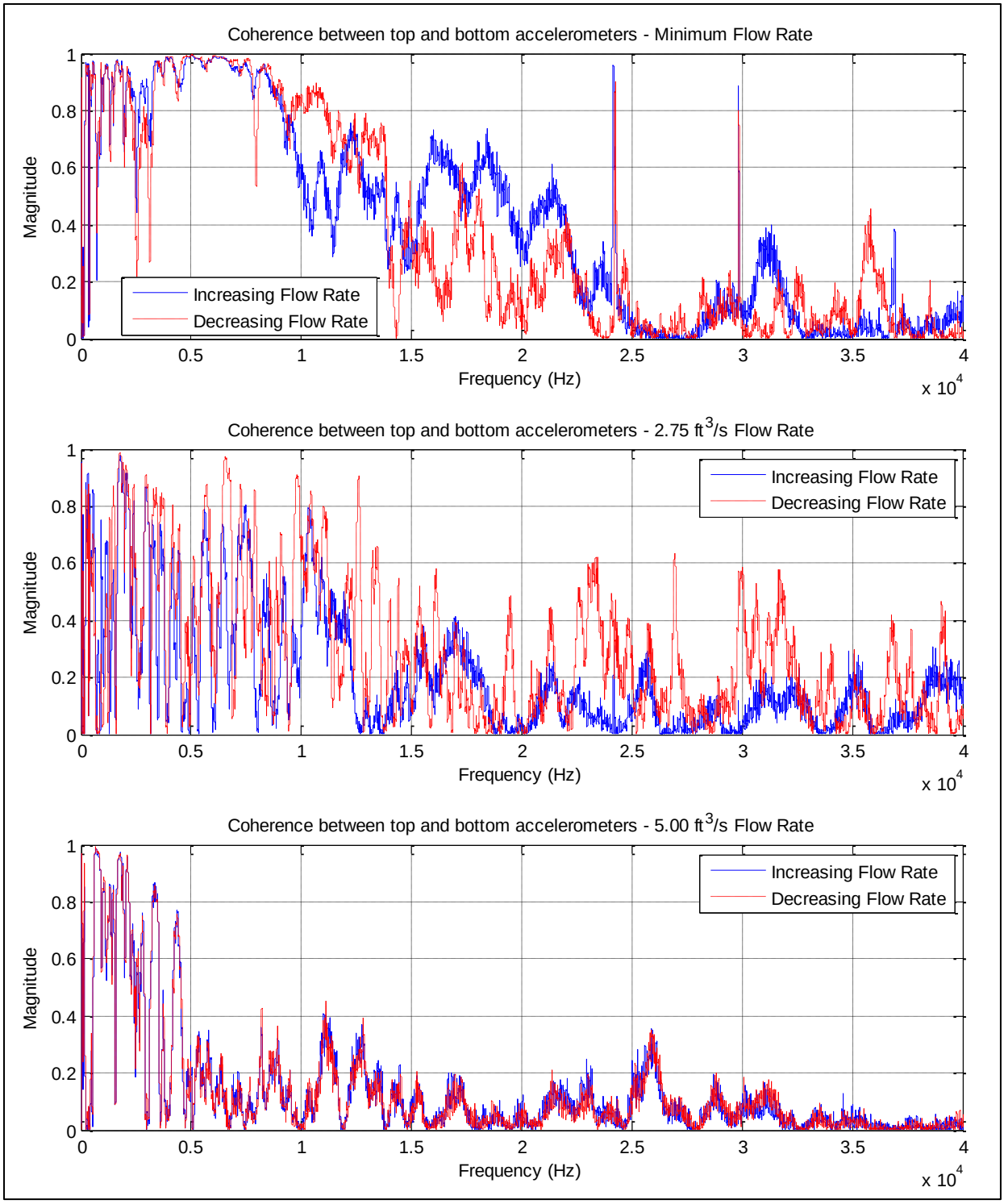

Figure 6.18 Coherence of Top and Bottom Acceleration Readings at Non-Cavitating, Incipient Cavitation and Developed Cavitation Flow Rates

There are two important characteristics to look for in Figure 6.18. The first is for frequencies with a magnitude close to one. Any frequency with coherence close to one demonstrates that that frequency exists in both signals. Notice the highest coherence region is below 10 kHz at the minimum flow rate. As the minimum flow rate data is primary filled with energy coming from structural movement, it can be inferred that this agreement within the coherence is due to structure resonance. In addition there appears to be a structural frequency at 24.5 kHz and 29.85 kHz.

The second phenomenon to take note of is repeatability in the data at high flow rates. High flow rates are dominated by cavitation impulses. When looking at increasing and decreasing flows, there is a high repeatability within the data at high flow rates. The non-repeatability demonstrated by the incipient flow rates (2.75 ft^3/s shown), confirms the disagreement between the increasing and decreasing flow rates seen in the RMS signal analysis in Section 6.3. The high repeatability between increasing and decreasing flow rates in the flow range 4.00 – 5.00 ft^3/s and the low repeatability between increasing decreasing flow rates in the flow range 2.50 – 3.75 ft^3/s can be seen in further detail in Appendix R.

6.8 *Spike* Analysis

The main idea behind *spike* analysis is to assess the magnitude of erratic impacts relative to the RMS value of the signal. This is accomplished by dividing the absolute maximum value of a signal by the RMS value (see equation 5.4). This metric allows for the volatility of the fluid to be assessed from the magnitude stand point. Figures 6.19 – 6.21 provide the *spike* analysis results corresponding to flow rate for the top acceleration, bottom acceleration and acoustic emission. Refer to Appendix L for *spike* analysis MATLAB code.

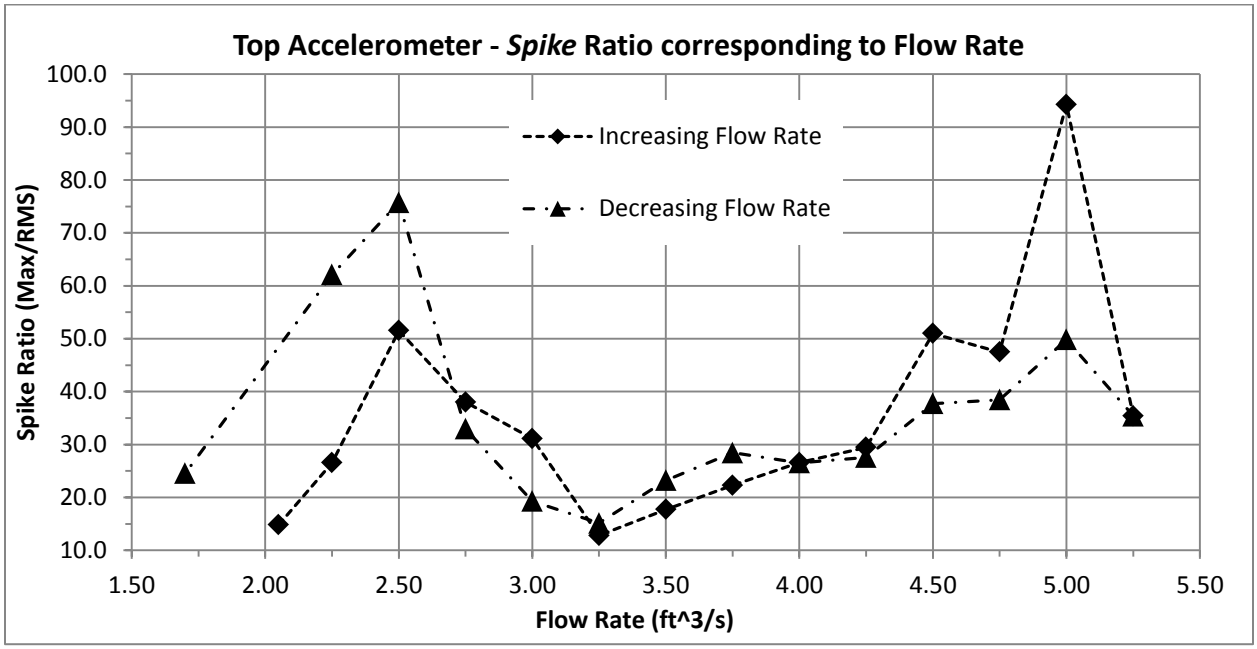

Figure 6.19 *Spike* Analysis of Acceleration Signal Collected from Top of Cavitation Tunnel

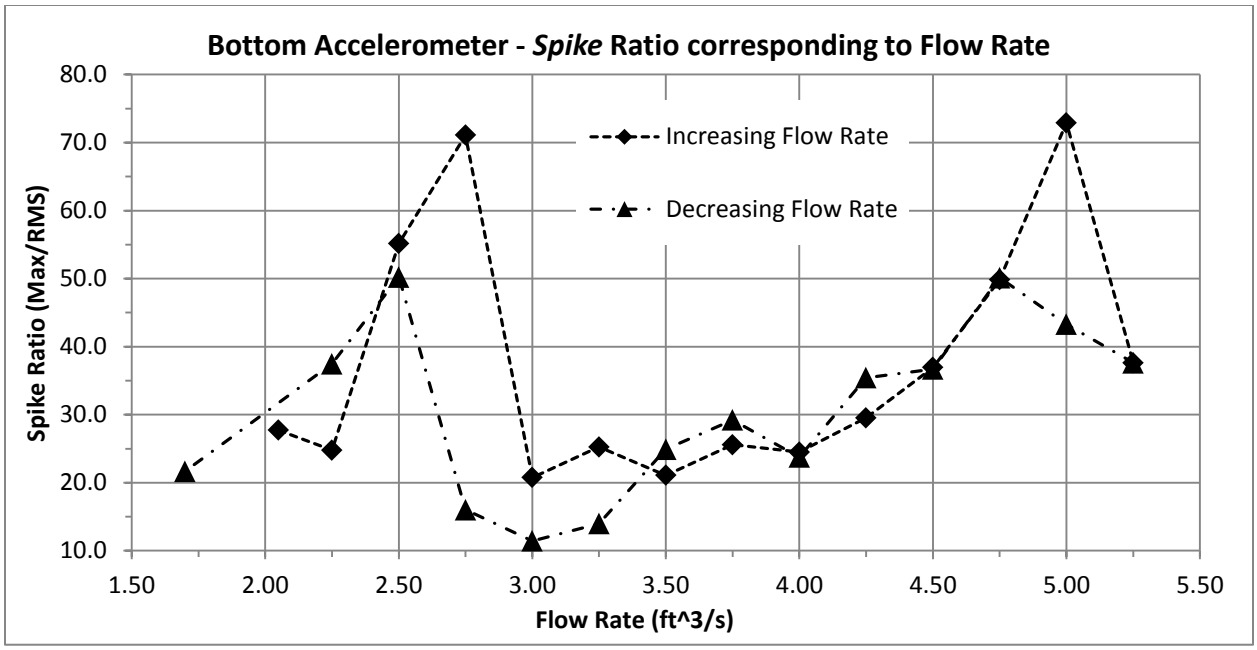

Figure 6.20 *Spike* Analysis of Acceleration Signal Collected from Bottom of Cavitation Tunnel

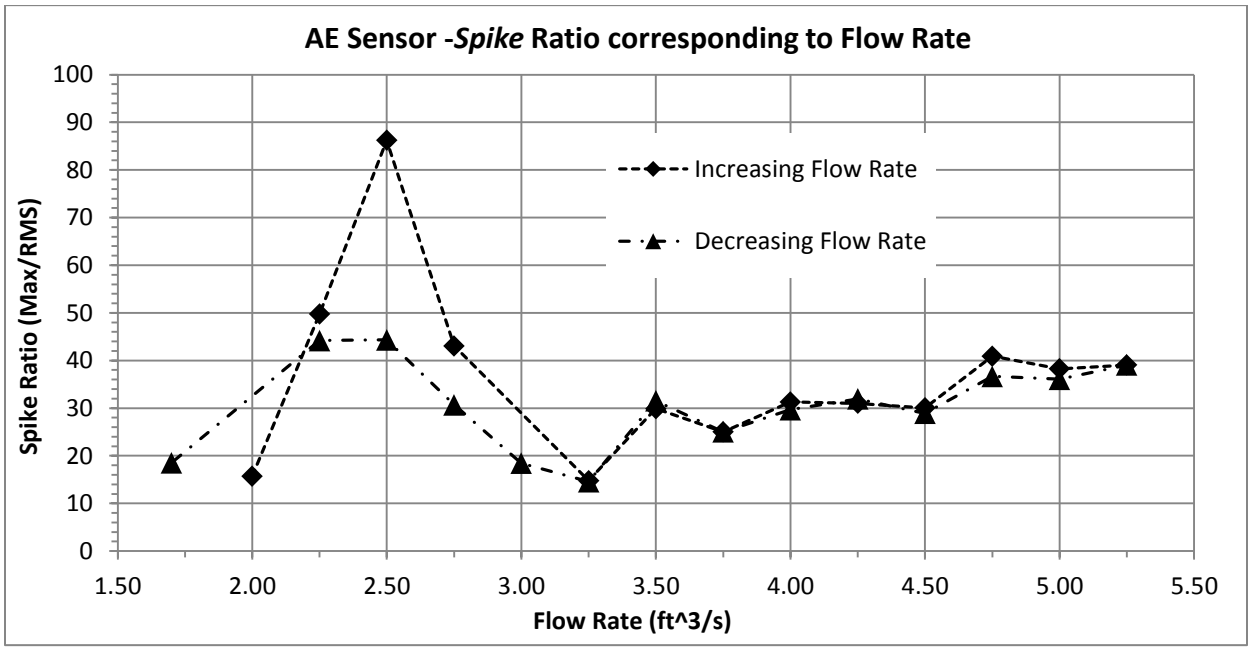

Figure 6.21 *Spike* Analysis of Acoustic Emission Signal Collected from Bottom of Cavitation Tunnel

Figures 6.19 – 6.21 were all calculated using equation 5.4. To confirm the *spike* analysis used in equation 6.4 was not too susceptible to noise, Equation 5.5 was used to determine

average spike analysis. The trends seen from *spike* analysis and *average spike* analysis are extremely similar, to the point where no different conclusions could be drawn from either. All *average spike* analysis plots are presented in Appendix S. *Spike* analysis proved to be a very capable time domain metric, it consistently identified volatile states within the flow and confirmed notions found in prior analysis.

Spike analysis accurately characterized three critical areas of flow, the first was incipient flow. In Figures 6.19 – 6.21 it is clear that through spike analysis, flow 2.50/2.75 ft^3/s is identified as a highly volatile state, or incipient flow. The consistent spike at 2.50/2.75 ft^3/s provides a warning some critical transition is about to take place. *Spike* analysis monitored in time with RMS value could provide a warning for cavitation onset. Note that at 2.50 ft^3/s, the RMS values of the signals (shown in Figures 6.6 – 6.8) has not yet increased, however the *Spike* value has increased, indicating the onset of cavitation.

In addition, both accelerometers identified the volatile flow just before the flow transitions from developed to super cavitation at 5.00 ft^3/s. Unfortunately the absolute maximum values of the AE signals increased correspondingly to the RMS values. As such, the AE sensor did not confirm the volatile flow at 5.00 ft^3/s as the accelerometers did. It's also important to note that with the acceleration data, incipient cavitation flow and the transition from developed to super cavitation are characterized to have the same volatility.

Also, it is important to note that *spike* analysis equates non-cavitating flow to developed cavitation flow. Using this metric in combination with RMS values may provide an accurate way of quantifying developed cavitation. An increase in RMS that correlates with a non-increase in *spike* analysis could identify a cavitation state change from non-cavitating to cavitating flow.

6.9 Burst Analysis

Burst analysis is a time domain metric similar to *spike* analysis, in that both methods are trying to quantify volatile states within the flow. The difference is that *spike* analysis utilizes a metric quantifying the magnitude of volatile impacts, where Burst analysis utilizes a metric quantifying the number of volatile impacts over a time period. The method described in Section 6.5.4 was followed for all Burst analysis. Burst thresholds were always set to a multiplier of the signals standard deviation. There were five separate Burst thresholds used, 5x, 10x, 15x, 20x, and 25x the standard deviations of the signals. For the body of this thesis, all results were normalized and averaged, refer to Appendix T for all Burst analysis plots and a detailed description on how the plots were normalized and averaged. Figures 6.22 – 6.24 present the normalized and averaged Burst analysis with thresholds of 5x, 10x, 15x, 20x, and 25x for the top acceleration, bottom acceleration and acoustic emission recorded data. The normalized plots range from zero to one, zero meaning no volatility within the flow and one meaning maximum volatility within the flow. Refer to Appendix L for Burst analysis MATLAB code.

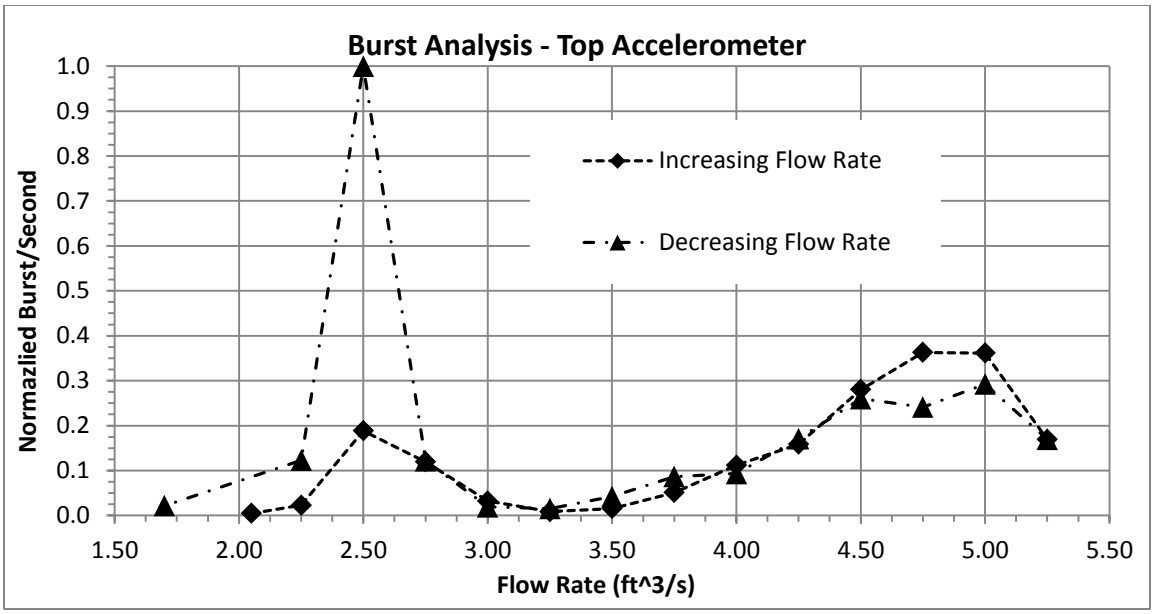

Figure 6.22 Burst Analysis of Acceleration Signal Collected from Top of Cavitation Tunnel

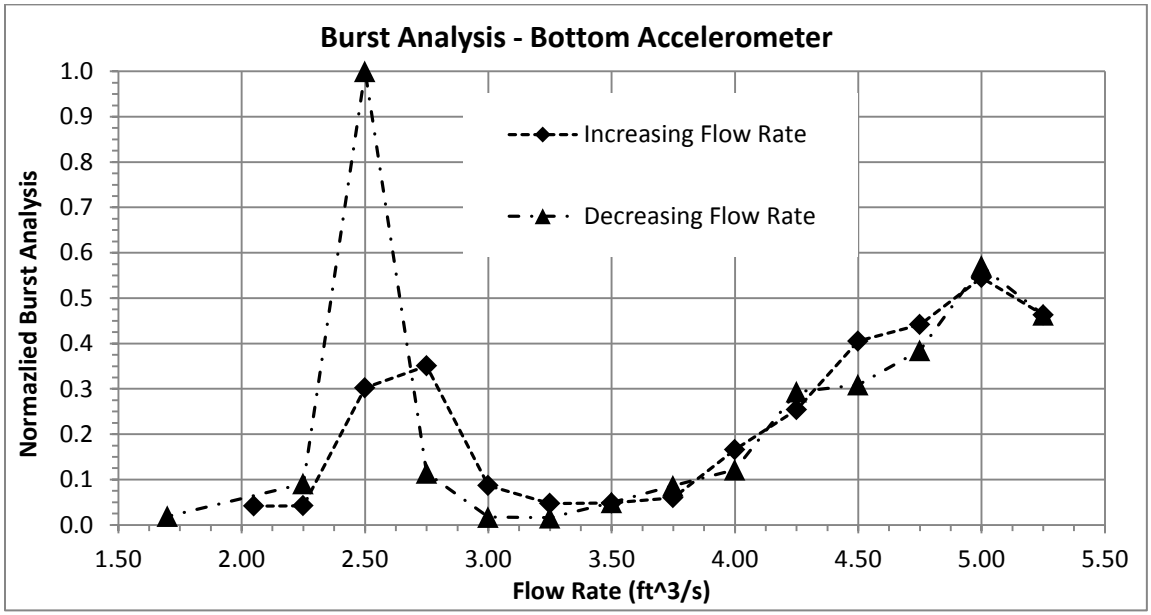

Figure 6.23 Burst Analysis of Acceleration Signal Collected from Bottom of Cavitation Tunnel

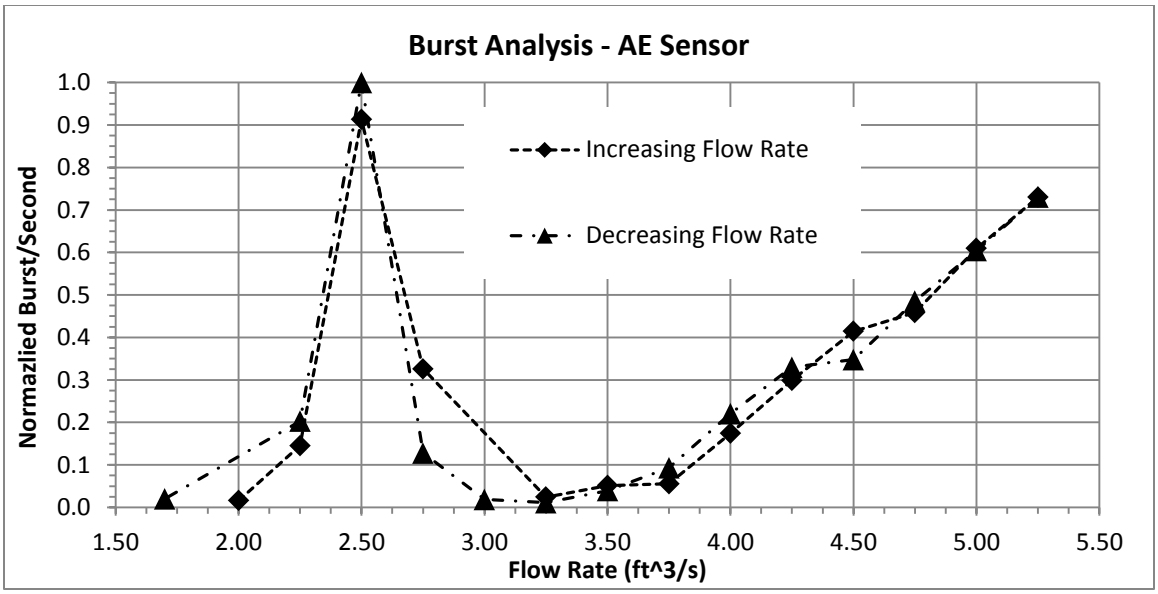

Figure 6.24 Burst Analysis of Acoustic Emission Collected from Bottom of Cavitation Tunnel

Burst analysis consistently identified, with increasing flow, volatility at 2.50 ft^3/s. As identified in many prior metrics, 2.50 ft^3/s is the start of incipient cavitation flow. In addition, the accelerometers identified much higher volatility in the decreasing flow rate, inferring cavitation continuing to further down the flow range. This phenomenon which has also been identified in multiple prior metrics was not confirmed with the acoustic emission recordings. The AE sensor however provided data inferring the increasing and decreasing flow rates had the same volatility at 2.50 ft^3/s. This is an anomaly among all the metrics utilized.

Also, both of the acceleration readings provided confirmation of the flow state change from 5.00 – 5.25 ft^3/s from developed to super cavitation. However, the acoustic emission sensor did not identify this state change. The AE sensor did however accurately depict the increasing volatility in the flow from 3.50 – 5.00 ft^3/s.

CHAPTER 7

CONCLUSIONS AND RECOMMENDATIONS FOR FUTURE WORK

7.1 Conclusions

A controllable laboratory experiment consisting of a cavitation inducing tunnel was conceived, designed and built for characterization of cavitation signals. Instrumentation to confirm cavitation and record vibroacoustic activity included a pressure transducer, two accelerometers and an AE sensor. The flow range of the laboratory set-up provided non-cavitating flow (quiet) at the low end of the range, and super cavitating flow (loud) at the maximum flow.

Initial characterization of the signals included correlating RMS values to specific flow rates and cavitation indexes. The RMS analysis revealed several characteristics of the flow. These included, incipient cavitation taking place at approximately 2.50 ft^3/s and super cavitation taking place at maximum flow, 5.25 ft^3/s. RMS signal analysis also revealed that once cavitation begins within a flow at a certain threshold during increasing flow, cavitation can then happen lower than the initial threshold when decreasing flow.

All signals were checked for repeatability via autocorrelations. It was determined that cavitation is a non-repeatable signal. However, the autocorrelations did provide confirmation that at flow rates ($Q < 2.25\ ft^3/s$), the majority of energy recorded in the signals was from structural movement and not cavitation; thus the goal of designing a cavitation inducing apparatus with a flow range ranging from non-cavitating to cavitating was achieved. This was further substantiated by the results of the coherence between the top and bottom accelerometers. At low

flow rates, there was a high degree of coherence agreement in the low frequency range, confirming the repeatability in the signals and the notion that the majority of energy in the signals recorded at low flow rates was primarily due to structural movement.

All signals were transformed into the frequency domain to check for changes in frequency spectra at different flow rates. As demonstrated in prior cavitation monitoring work, the frequency spectra changed throughout the cavitation states, inferring cavitation taking place within the apparatus. This was further substantiated by frequency normalization analysis, which removed structural influence on the frequency spectra. The results of frequency normalization again confirm that the frequency spectra changed throughout the flow range and subsequently cavitation changed throughout the flow range.

Spike and Burst time domain metrics were further developed due to difficulty in quantifying frequency domain results. Both time domain metrics developed were designed to quantify volatility within the flow. Volatility is a useful metric to quantify when cavitation states are going to change (i.e. incipient cavitation). Both metrics were able to identify incipient cavitation, the transition from developed to super cavitation and confirm the notion that cavitation takes place lower in the flow range with decreasing flow rate versus increasing flow rate.

The combination of RMS signal analysis, autocorrelation of signals, coherence of top and bottom accelerometer signals, frequency domain analysis, *spike* analysis and Burst analysis provides a validated framework for non-intrusive cavitation detection. Within the cavitation inducing apparatus developed for this project, it was predicted and validated that incipient cavitation took place at 2.50ft^3/s. In addition, it was experimentally determined that the transition

from developed to super cavitation takes place from 5.00 ft^3/s to 5.25 ft^3/s, when the cavitation cavity developed from 2.50 – 5.00 ft^3/s breaks loose from the bottom plate.

7.2 Future Work

The accomplishments of this project are a small step in the long term goals of real-time CHM of large scale hydropower turbines. This project's developed metrics for non-intrusive cavitation detection were proven on a simple and quantifiable cavitation inducing apparatus. The next step in the process is to apply the metrics to data taken from a known cavitating hydropower turbine. Such an opportunity may exist in the Summer/Fall of 2013 at the Judge Francis Carr Hydro Power Plant in Northern California. Carr Power Plant consists of two Francis turbine generators units with a total capacity of 154.4 MW [32]. The turbine runners are currently experiencing severe cavitation. There is a site-visit currently being planned for a team of engineers from the U.S. Bureau of Reclamation office in Denver to travel to the site and record accelerometer and acoustic emission readings from the turbine at various flow rates and generator load levels. A wireless data acquisition system will be used to collect data from the rotating shaft which connects the runner of the turbine to the generator, much in the same fashion as the case study presented in Section 2.4.1. All data collected from the site will be analyzed using the metrics created, validated and outlined in Chapter 5.

There is confidence the metrics here will lead to conclusions as to which operating conditions at Carr Powerplant are causing the cavitation. The use of these metrics will ultimately lead to restrictions on flow rates and generator loading. These restrictions however will lead to less downtime, less unplanned maintenance and ultimately higher electrical production and profit margins for Carr Powerplant.

LIST OF ABBREVIATIONS AND SYMBOLS

Abbreviations

CHM: Condition Health Monitoring
HQ: Hydro-Quebec
TVA: Tennessee Valley Authority
EPFL: Swiss Federal Institute of Technology, Lausanne
UPC: Technical University of Catalonia
USBR: U.S. Bureau of Reclamation
FT1: Francis Turbine 1
FT2: Francis Turbine 2
HHP: High Head Pump
AE: Acoustic Emission
GUI: Graphical User Interface
ACSII: American Standard Code for Information Exchange
RMS: Root Mean Square
FFT: Fast Fourier Transform
fps: frames per second

Symbols

Z_b: Number of turbine runner blades
Z_v: Number of turbine Guide Vanes
N: Turbine rotational speed (rpm)
f_f: Turbine fundamental frequency
f_b: Blade passing frequency
f_v: Guide vane passing frequency
σ: Cavitation Index
A_T: Cross-Sectional area of Cavitation Tunnel (before offset)
A_S: Cross-Section area of Cavitation Tunnel at offset
Q: Flow rate
Q_{min}: Minimum flow rate
Q_{max}: Maximum flow rate
V: Velocity
V_{min}: Minimum Velocity
V_{max}: Maximum Velocity
P_o: Reference pressure – Pressure in free stream flow at offset
P_a: Atmospheric pressure
P_g: Gage pressure
ρ: Density

Symbols (continued)

V_o: Average fluid velocity in free stream flow at offset
Re: Reynolds Number
D_H: Hydraulic diameter
v: Kinematic viscosity
P: Perimeter
x(t): Real valued time domain signal
y(t): Real valued time domain signal
C_{xy}: Coherence between two real-valued signals
G_{xy}: Cross spectral density of two real valued signals
G_{xx}: Auto-spectral density of *x*
G_{yy}: Auto-spectral density of *y*

REFERENCES

[1] "U.S. Energy Information Administration – EIA – Independent Statistics and Analysis."*Electric Power Monthly*. N.p., n.d. Web. 05 Nov. 2012. <http://www.eia.gov/electricity/monthly/>.

[2] "HydroResearchFoundation." *Hydro Research Foundation*. N.p., n.d. Web. 05 Nov. 2012. <http://www.hydrofoundation.org/hydropower-education.html>.

[3] Bourdon P., Farhat M., Mossoba Y., Lavigne P., "Hydro Turbine Profitability and Cavitation Erosion", Hydro-Quebec. Montreal, Quebec, Canada

[4] Mossoba, Y., "Efficient Cavitation Detection Technology for Optimizing Hydro Turbines Operation and Maintenance", Hydro-Quebec Generation. Montreal, Quebec, Canada

[5] "How Waterpower Works." How Waterpower Works. N.p., n.d. Web. 14 Mar. 2013. <http://www.xeneca.com/benefits/how_hyrdro_power_works.html>.

[6] "What Is Kaplan Turbine? Propeller Turbine. Types of Hydraulic Turbines." Brighthub Engineering. N.p., 27 Nov. 2009. Web. 14 Mar. 2013. <http://www.brighthubengineering.com/fluid-mechanics-hydraulics/27426-hydraulic-turbines-kaplan-turbine/>.

[7] Mossoba Y. (Principal Investigator), Wilson A. (Technology Cooridator), 2009, "Technology Review On-Line Cavitation Monitoring", Hydro-Quebec. Montreal, Quebec, Canada

[8] Mossoba Y., Bourdon P., October 1999, "Sharing Experience with Cavitation Repair, Monitoring", Hydro Review, pp. 16-22

[9] Harrison M., 1952, "An Experimental Study of Single Bubble Cavitation Noise", The Journal of the Acoustical Society of America, Volume 24, No.6, November 1952, pp. 776-782

[10] Franc, Jean-Pierre, and Jean-Marie Michel. Fundamentals of Cavitation. Dordrecht: Kluwer Academic, 2004. Print.

[11] Bajic, B., 2008 , "Multidimensional Method and Simple Methods for Cavitation Diagnostics and Monitoring", Seminar on the State of the Art Monitoring Systems applied to Rotating Machines, November 2008

[12] D. Mba and Raj B. K. N. Rao, 2006, "Development of Acoustic Emission Technology for Condition Monitoring and Diagnosis of Rotating Machines: Bearings, Pumps, Gearboxes,

Engines, and Rotating Structures", The Shock and Vibration Digest, Vol. 38, No.1, Jan 2006, pp.3-16

[13] Escaler X., Egusquiza E., Mebarki T., *Technical University of Catalonia-UPC*, Farhat M., Avellan F., *Swiss Federal Institute of Technology-EPFL*, 2002, "Field Assessment of Cavitation Detection Methods in Hydropower Plants", Proceedings of the XXIst IAHR Symposium on Hydraulic Machinery and Systems. Lausanne, Switzerland

[14] March P., Jones K., 1991, "Laboratory and Field Experience with Cavitation Monitoring of Hydroturbines", Waterpower Conference 1991

[15] Abbot, P.A., Gedney C.J., Greeley D.S., "Cavitation Monitoring of Two Axial-Flow Hydroturbines using Novel Acoustic and Vibration Methods", Atlantic Applied Research Corportation, Burlington, MA, 01803, U.S.

[16] Bajic, B., 2003, "Methods for Vibro-Acoustic Diagnostics of Turbine Cavitation", Journal of Hydraulic Research. Vol 41, 2003, No.1, pp. 87-96

[17] Bajic B., Keller A., 1996, "Spectrum Normalization Method in Vibro-Acoustical Diagnostic Measurements of Hydroturbine Cavitation", Journal of Fluids Engineering, Vol.118, December 1996, pp. 756-761

[18] Bourdon P., Farhat M., 1998, "Extending Repair Intervals of Hydro Turbines by Mitigating Cavitation Erosion", CEA Electricity Conference & Exposition. Toronto, Canada

[19] Farhat M., Bourdon P., Lavigne P., Simoneau R., 1997, "The Hydrodynamic Aggressiveness of Cavitating Flows in Hydro Turbines", ASME Fluids Engineering Division Summer Meeting

[20] Wenjie C., "Acoustic Method for Measuring Cavitation and Impulse Counting of it's Noise", Dailian Institute of Technology, Translated by: U.S. Bureau of Reclamation 1983.

[21] Bourdon P., Farhat M., Simoneau R., *Hydro-Quebec*, Pereira F., Dupont P., Avellan F., *IMHEF/EPFL*, Dorey J.M., *Electricite de France*, 1996, "Cavitation Erosion Prediction on Francis Turbines-Part 1 Measurements on the Prototype", Hydraulic Machinery and Cavitation, pp. 534-543

[22] Bourdon P., Simoneau R., Avellan F., June 1993, "Hydraulic Turbine Cavitation Pitting Detection by Monitoring Runner Vibration", Report for: Canadian Electrical Association, Prepared by: Hydro-Quebec

[23] Mossoba Y., *Hydro Quebec*, Bourdon P., Farhat M., Simoneau R., *Institut de Recherche d'Hydro-Quebec*, "Solutions dealing with the Cavitation Erosion Damages in Hydro Turbines".

[24] Escaler X., Egusquiza E., *Technical University of Catalonia-UPC*, Farhat M., Avellan F., *Swiss Federal Institute of Technology-EPFL*, 2004, "Cavitation Erosion Prediction in Hydro Turbines from Onboard Vibrations", 22nd IAHR Symposium on Hydraulic Machinery and Systems. Stockholm, Sweden

[25] Escaler X., Egusquiza E., *Technical University of Catalonia-UPC*, Farhat M., Avellan F., *Swiss Federal Institute of Technology-EPFL*, 2003, "Vibration Cavitation Detection using Onboard Measurements", Fifth International Symposium on Cavitation. Osaka, Japan

[26] United States of America. Department of the Interior. Bureau of Reclamation. Cavitation in Chutes and Spillways. By Henry T. Falvey. N.p.: Water Resources Technical Publication, n.d. Print. Engineering Monograph No.42.

[27] "Pressure Transmitter Honeywell Data Instruments Model BL." Pressure Transmitter Honeywell Data Instruments Model BL. N.p., n.d. Web. 14 Mar. 2013. <http://www.intertechnology.com/Honeywell_Data_Inst/Honeywell_BL.html>.

[28] "MODEL 1000/A/BMINIATURE PREMIUM 10 OR 1.5 MV/G ACCELEROMETER."MISTRAS NDT Products & Systems. N.p., n.d. Web. 14 Mar. 2013. <http://www.mistrasgroup.com/products/solutions/vibration/accelerometers/1000.aspx>.

[29] "SE9125-M." DECI. N.p., n.d. Web. 14 Mar. 2013. <http://www.deci.com/se9125m.pdf>.

[30] "WaveBook/516E." Ethernet-Based Portable High-Speed Waveform Acquisition. N.p., n.d. Web. 14 Mar. 2013. <http://www.mccdaq.com/products/wavebook516e.htm>.

[31] "Data Acquisition System Laboratory." DASYLab. N.p., n.d. Web. 14 Mar. 2013. <http://www.dasylab.com/>.

[32] "Judge Francis Carr Powerplant." U.S. Bureau of Reclamation. N.p., 13 May 2009. Web. 14 Mar. 2013. <http://www.usbr.gov/projects/Powerplant.jsp?fac_Name=Judge+Francis+Carr+Powerplant>.

APPENDIX A

PREDICTIVE CAVITION INDEX MATLAB© CODE

```
%% Cavitation Tunnel Cavitation Index Prediction Calculations
%    Denver Federal Center
%    Hydraulics Research Laboratory

% By: Samuel Dyas
clc, clear, close all

%% Calculating Cavitation Index
% Cavitation Index: sigma
% sigma = (Pres_a + Pres_g - Pres_v)/(rho*(Vo^2/2))
% Pres_a: atmospheric pressure (in Denver Pa = 75-80kPa)
Pres_a = 77500; % Pa
% Pres_g: gauge pressure  (assume very low as offset is placed only 18"
% from end of tunnel (0.5 ft of head = 1500 Pa)
Pres_g = 1500; % Pa
% Pres_v: vapor pressure of water (2500 Pa)
Pres_v = 2500; % Pa
% rho = density of water (1000 kg/m^3)
rho = 1000; % kg/m^3
% Flow Rate Taken in (ft^3/s)
Flow_Rate = [1.0 1.5 2 2.5 3 3.5 4 4.5 5 5.5 6 6.5 7]'
% Changing Flow Rate to Mean Velocity at Tunnel Step
% Area in tunnel at offset is 4"x(4-(3/8))" inches^2
Step_Area_in2 = 4*(4-(3/8)); % Inch^2
Step_Area_ft2 = (Step_Area_in2)/144; % ft^2
Mean_Vel_fts = Flow_Rate/Step_Area_ft2 % ft/s
% Transforming Mean Vel from ft/s to m/s:   1ft/s = 0.3048m/s
Mean_Vel_ms = Mean_Vel_fts*0.3048; % m/s
% Vo: Average Velocity at Offset (m/s)
Vo = Mean_Vel_ms;

sigma = (Pres_a+Pres_g-Pres_v)./(rho.*(Vo.^2)./2)

%% Estimated Pump Discharge vs. Cavitation Index
figure(1); plot(Flow_Rate, sigma)
title('Estimated Cavitation Index as function of Pump Discharge')
xlabel('Pump Discharge (ft^3/s)')
ylabel('Cavitation Index (unitless)')

disp('Cavitation Index at 1.00 - 2.00 - 3.00 - 4.00 - 5.00 - 6.00')
disp([sigma(1) sigma(3) sigma(5) sigma(7) sigma(9) sigma(11)])
```

Cavitation Index at 1.00 - 2.00 - 3.00 - 4.00 - 5.00 - 6.00

16.6983 4.1746 1.8554 1.0436 0.6679 0.4638

APPENDIX B

VISUAL OF CAVITION INDEXES

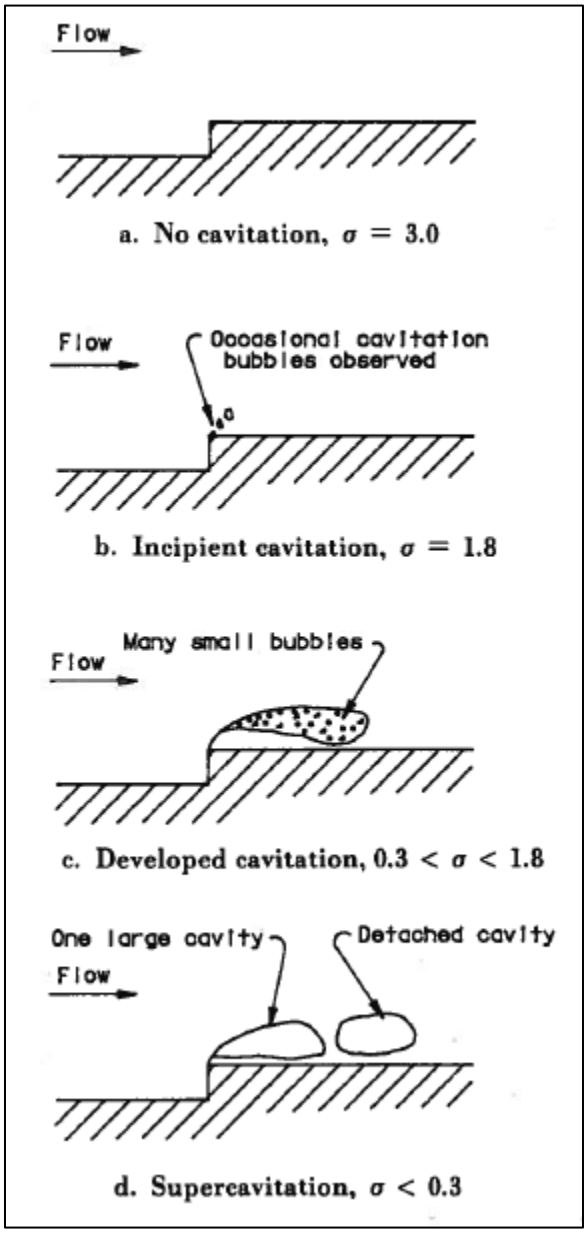

Figure B.1 Visual of Cavitation Index Implications

APPENDIX C

REYNOLDS NUMBER CALCULATIONS

$$Re = \frac{Q D_H}{\nu A}$$

Q: flow rate – varies

$D_H = \frac{4A}{P}$ $\quad D_H$: hydraulic diameter.

$A = 4" \times (4" - 3/8") = 14.5\ inch^2 = 0.00936\ m^2$

↑ area at step

$P = 4"(2) + (4" - 3/8")(2) = 15.25\ inch = 0.38735\ m$

$D_H = 0.0966\ m$

ν: kinematic viscosity $\quad \nu = 1.16 \times 10^{-6}\ m^2/s$

Example Calculations:

$Q_{max} = 6.0\ ft^3/s = 0.1698\ m^3/s$
$Q_{min} = 1.0\ ft^3/s = 0.0283\ m^3/s$

$$Re_{min} = \frac{(0.0283\ m^3/s)(0.0966 m)}{(1.16 \times 10^{-6}\ m^2/s)(0.00936 m^2)} = 2.80 \times 10^5$$

$$Re_{max} = \frac{(0.1698 m^3/s)(0.0966 m)}{(1.16 \times 10^{-6}\ m^2/s)(0.00936 m^2)} = 1.68 \times 10^6$$

Figure C.1 Reynolds Number Calculations

APPENDIX D

FINAL TECHNICAL DRAWINGS AND ISOMETRIC VIEWS OF CAD MODEL OF CAVITION TUNNEL

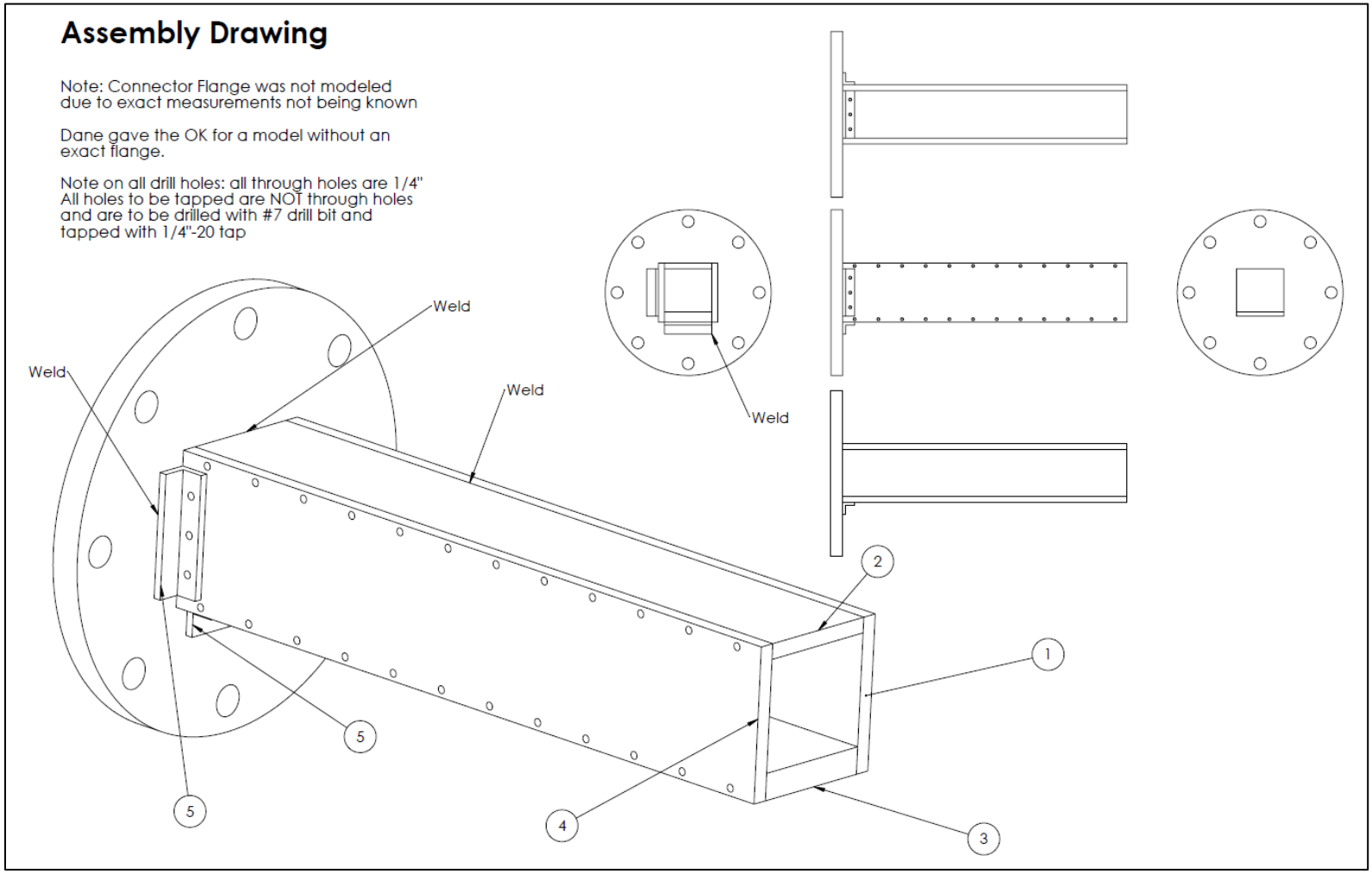

Figure D.1 Technical Assembly Drawing of Final Cavitation Tunnel Design

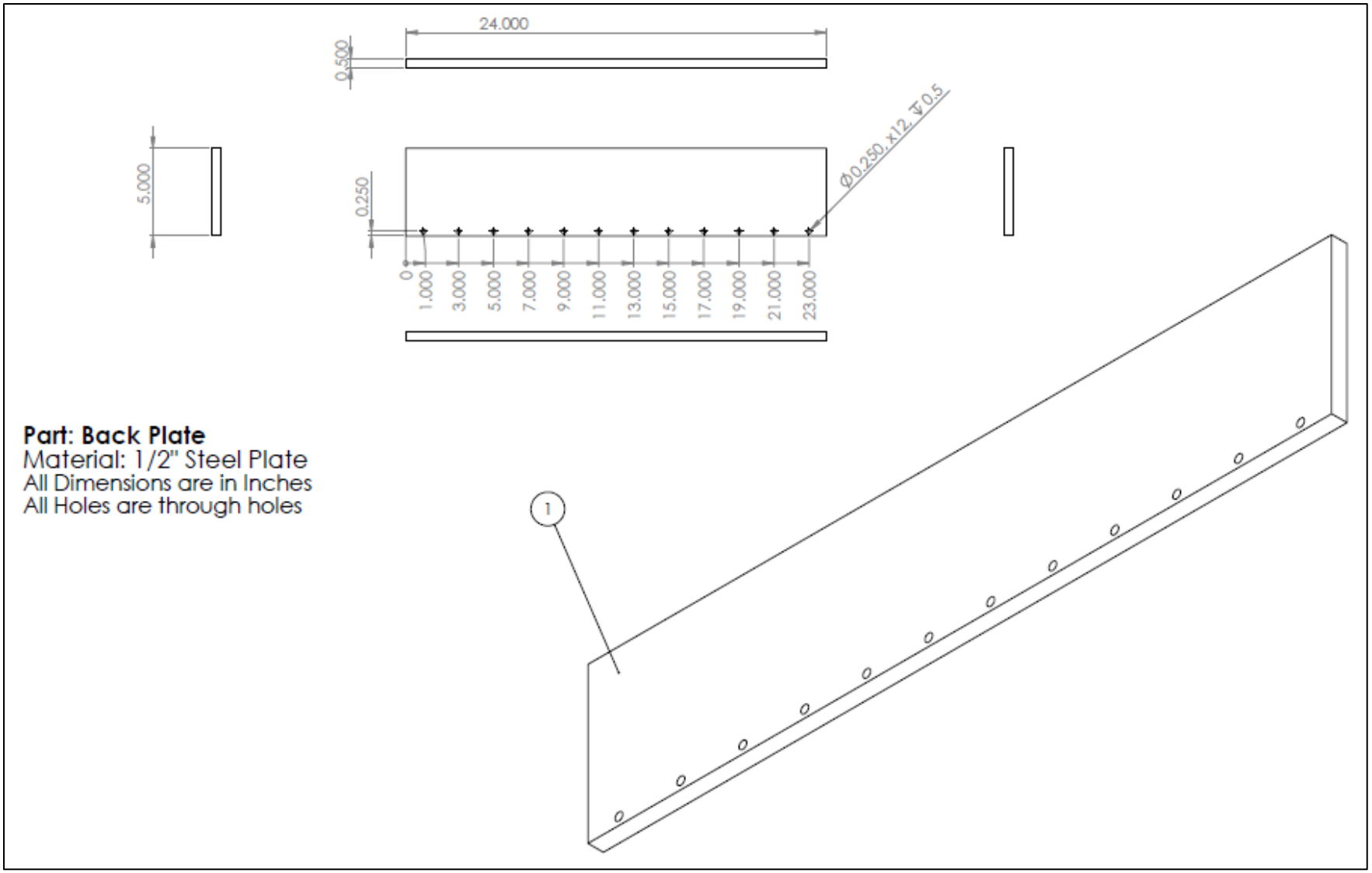

Figure D.2 Final Back Plate Design Technical Drawing for Cavitation Tunnel

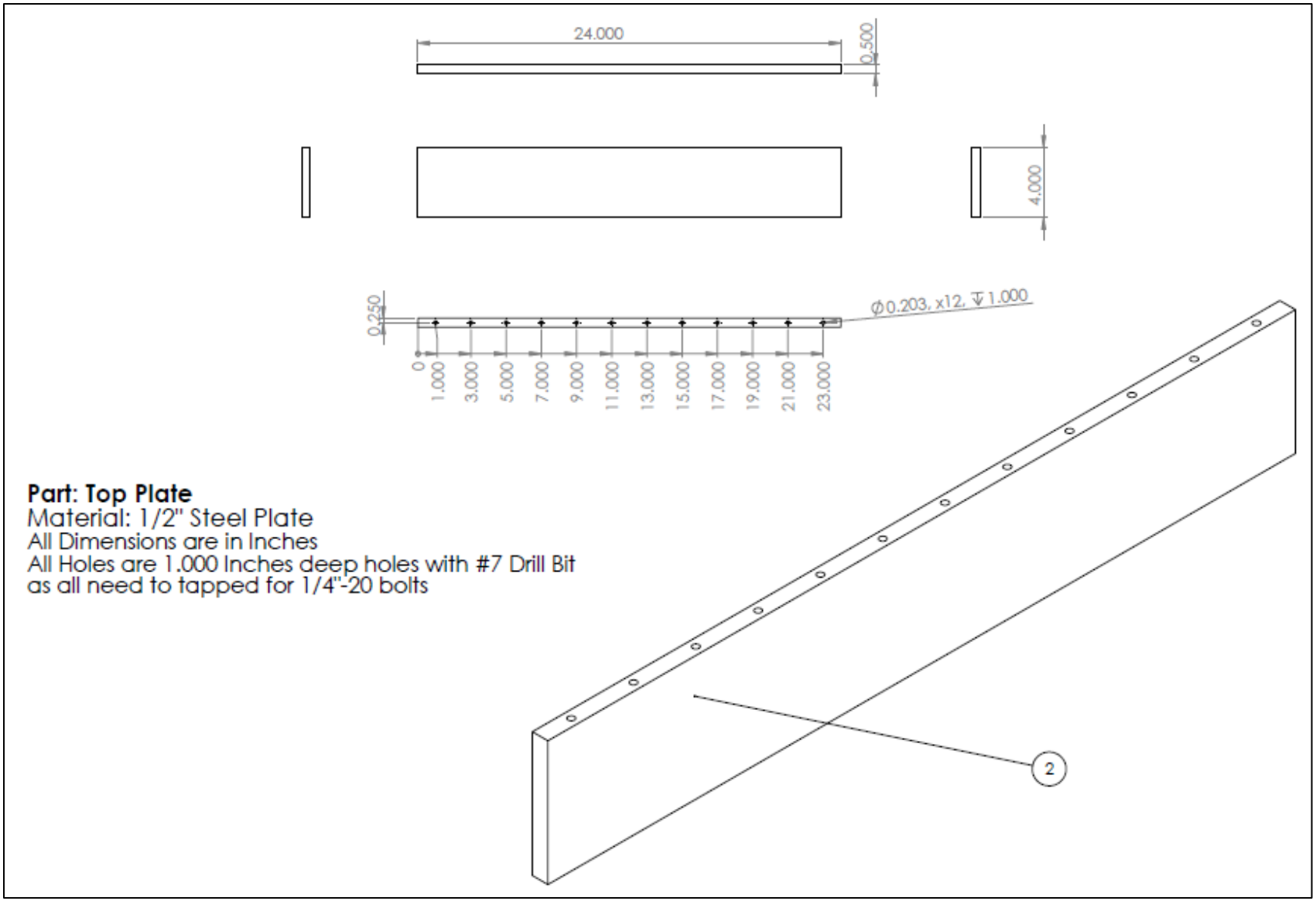

Figure D.3 Final Top Plate Design Technical Drawing for Cavitation Tunnel

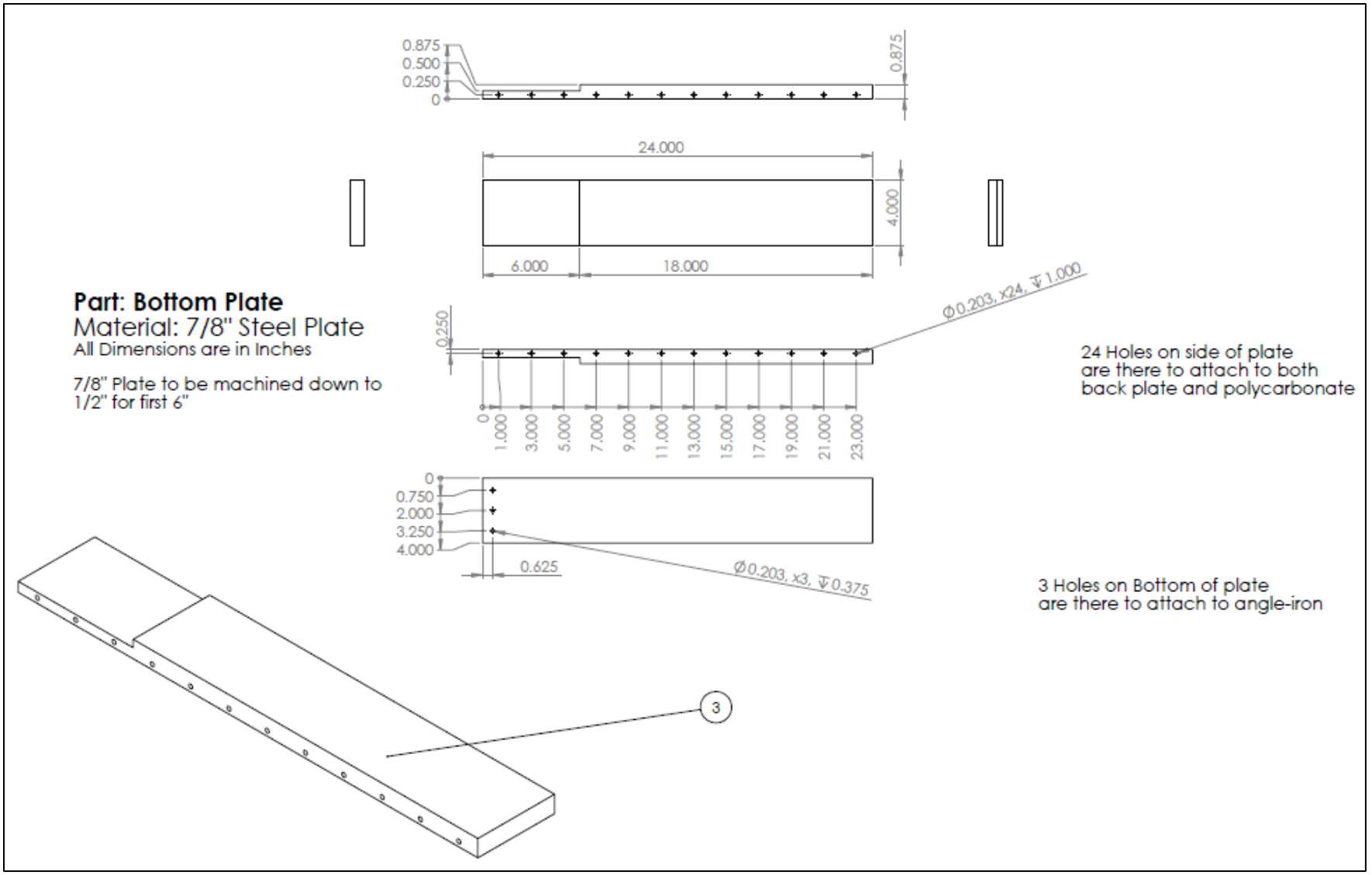

Figure D.4 Final Bottom Plate Design Technical Drawing for Cavitation Tunnel

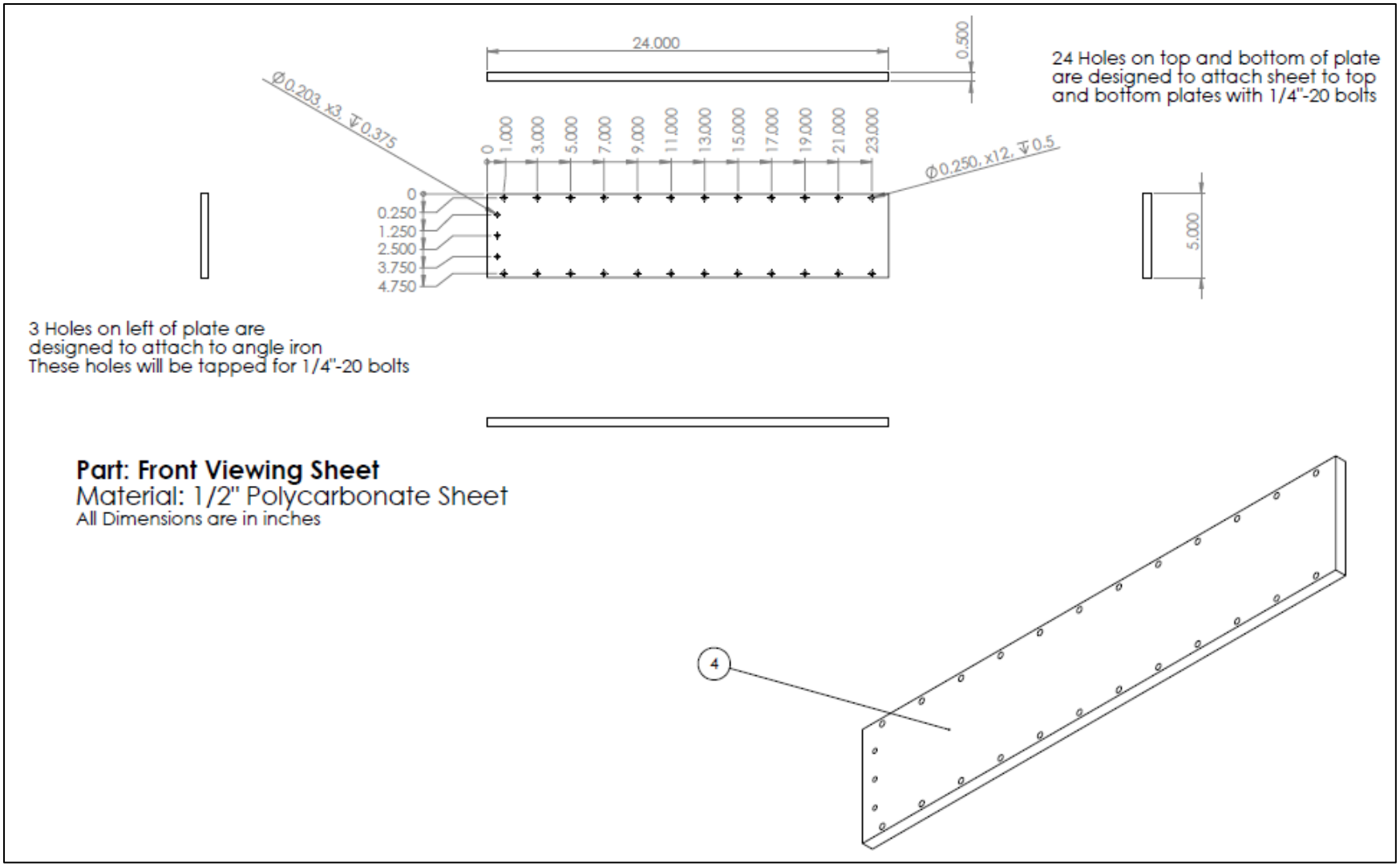

Figure D.5 Final Front Plate Design Technical Drawing for Cavitation Tunnel

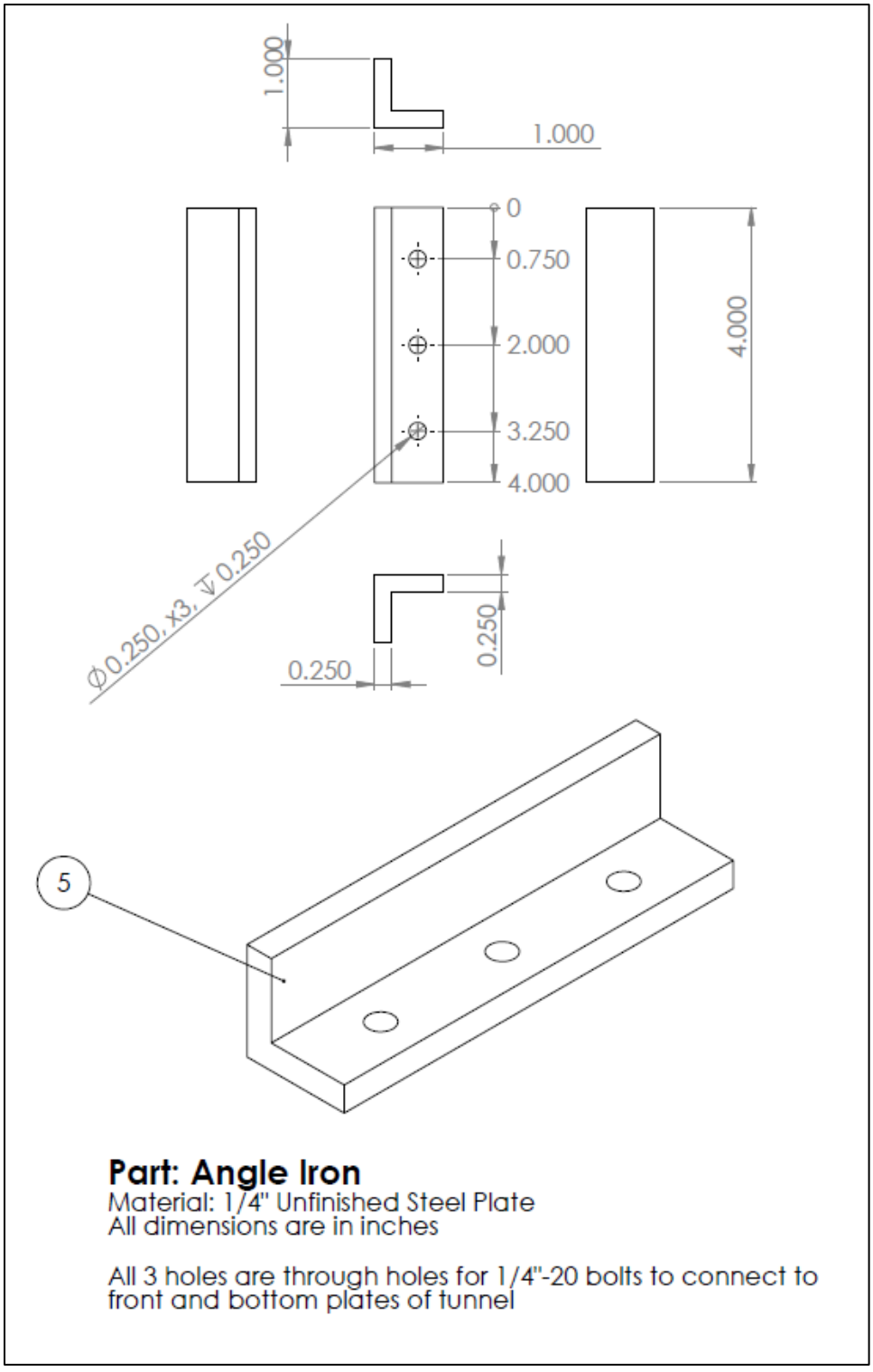

Figure D.6 Final Angle Iron Design Technical Drawing for Cavitation Tunnel

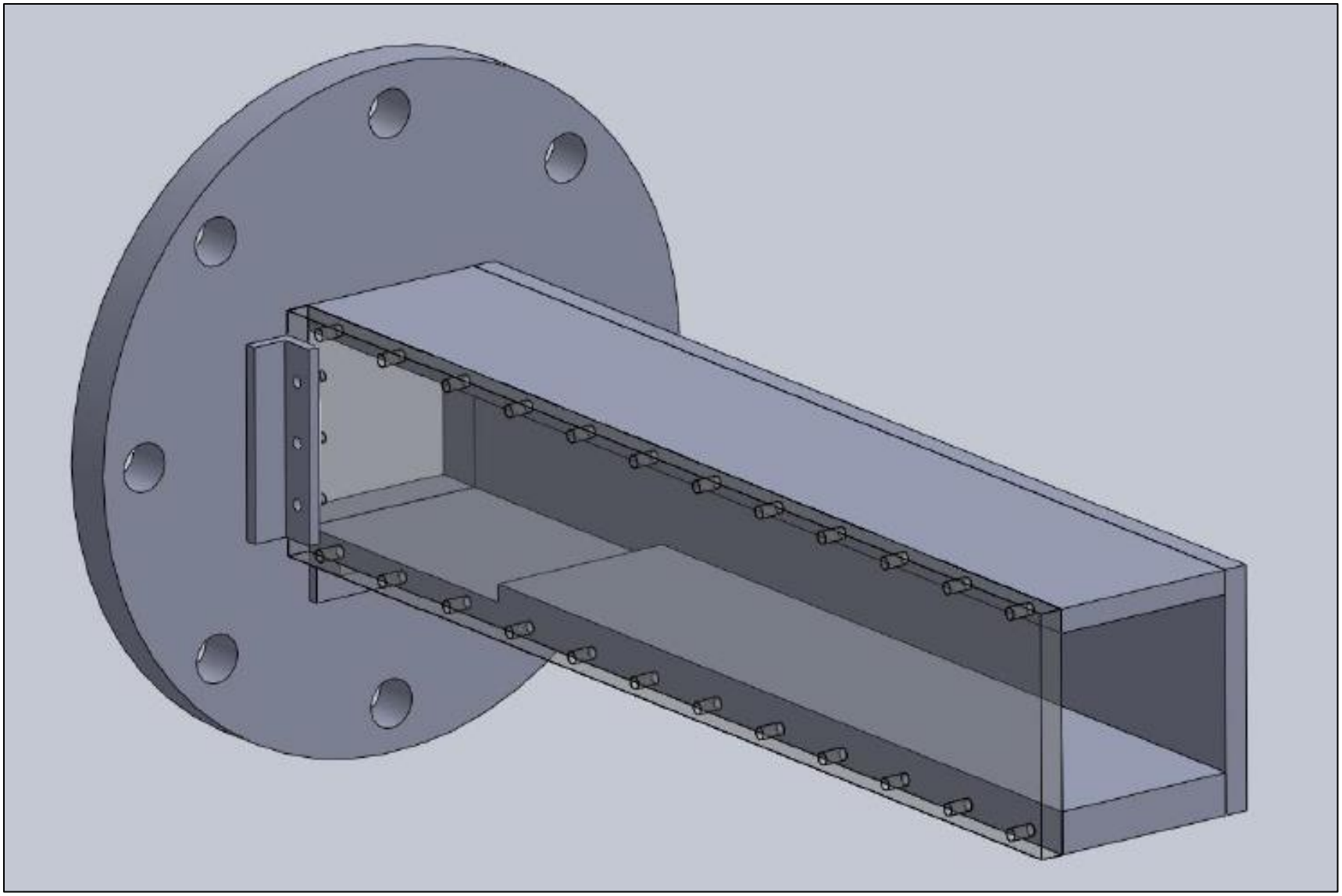

Figure D.7 Top Isometric View of Final CAD Model of Cavitation Tunnel

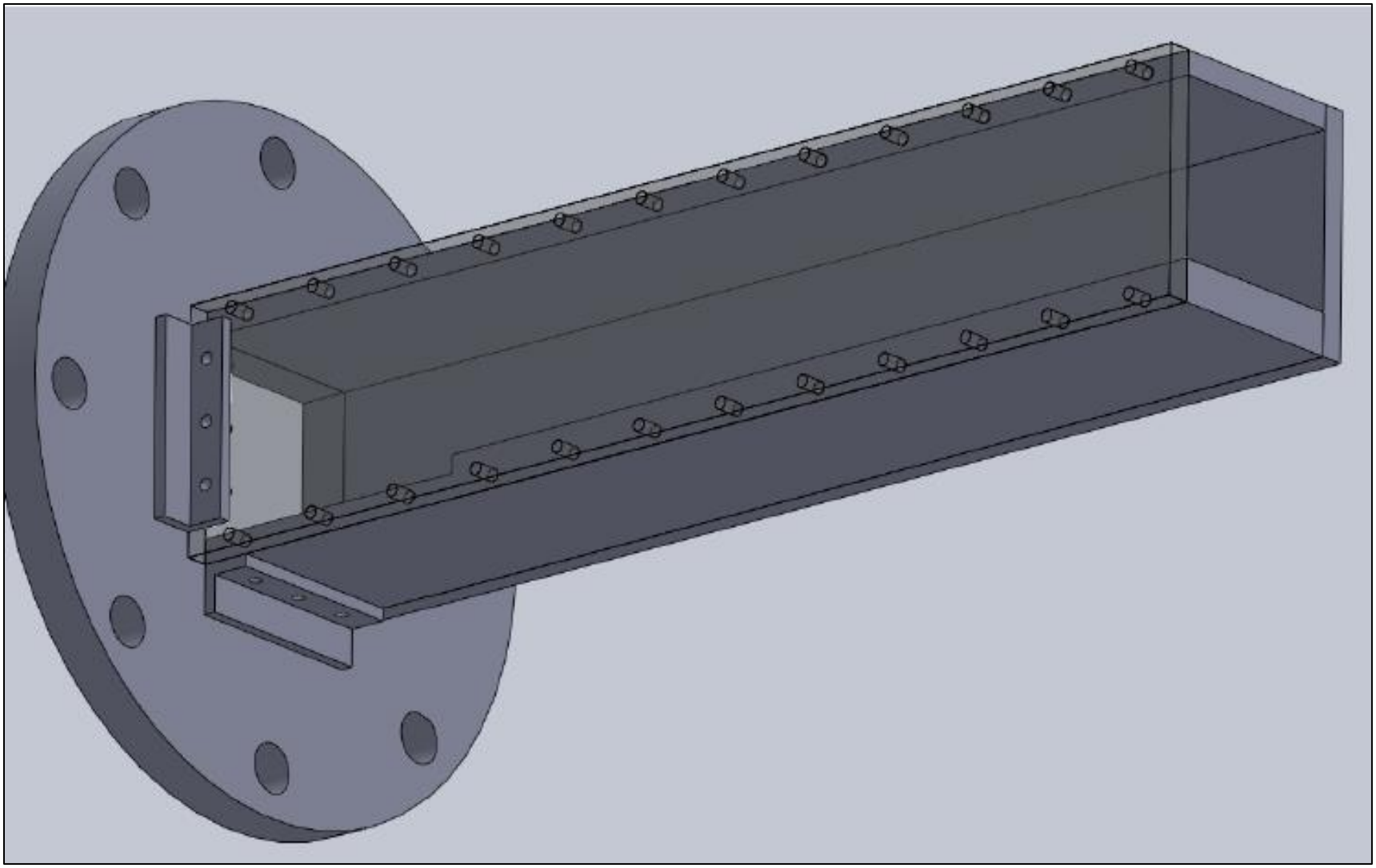

Figure D.8 Bottom Isometric View of Final CAD Model of Cavitation Tunnel

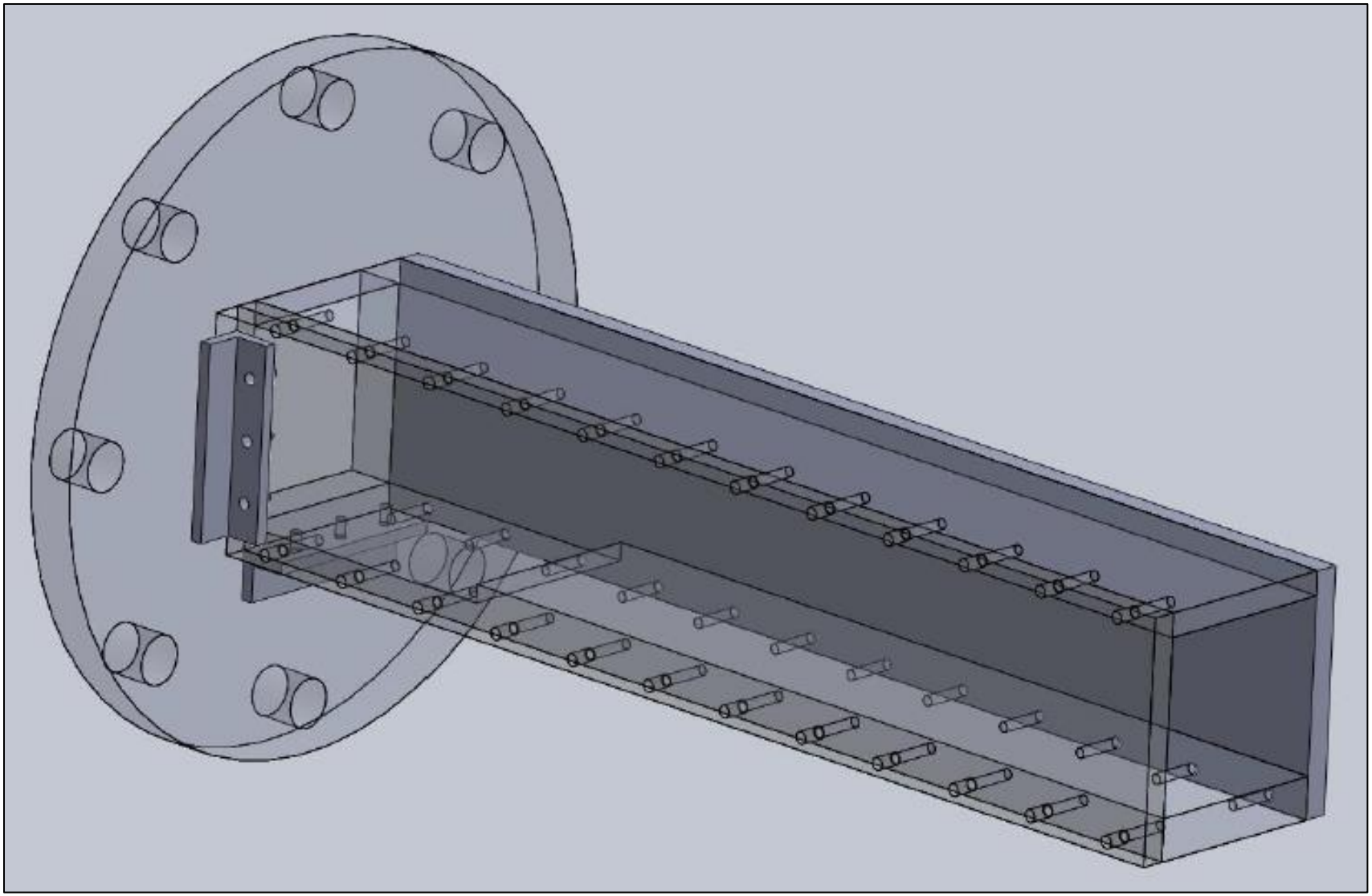

Figure D.9 Transparent Isometric View of Final Cavitation Tunnel CAD Model

APPENDIX E

DETAILED PHOTOS OF FINAL EXPERIMENTAL SET-UP

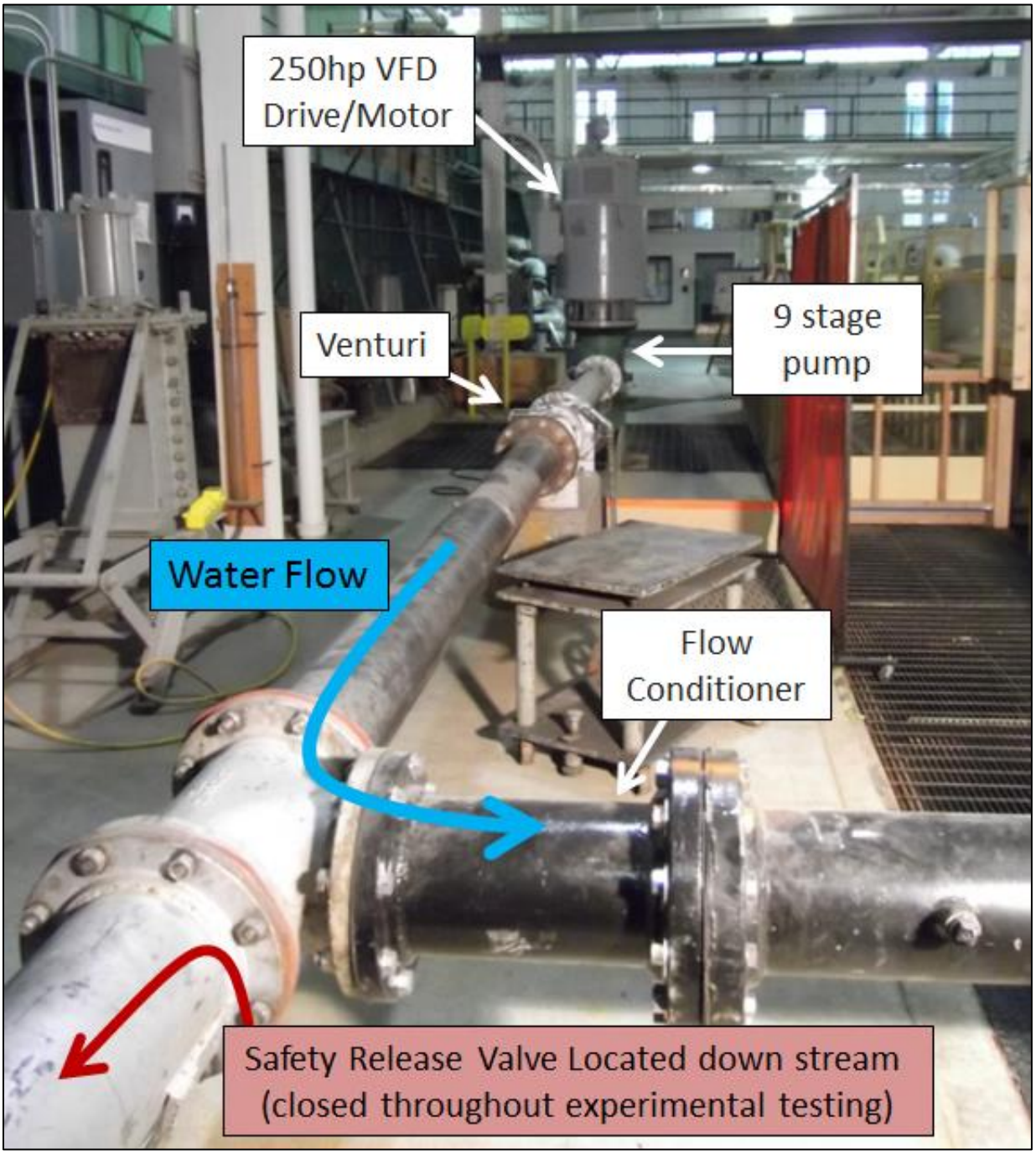

Figure E.1 Photo of Experimental Set-up 1

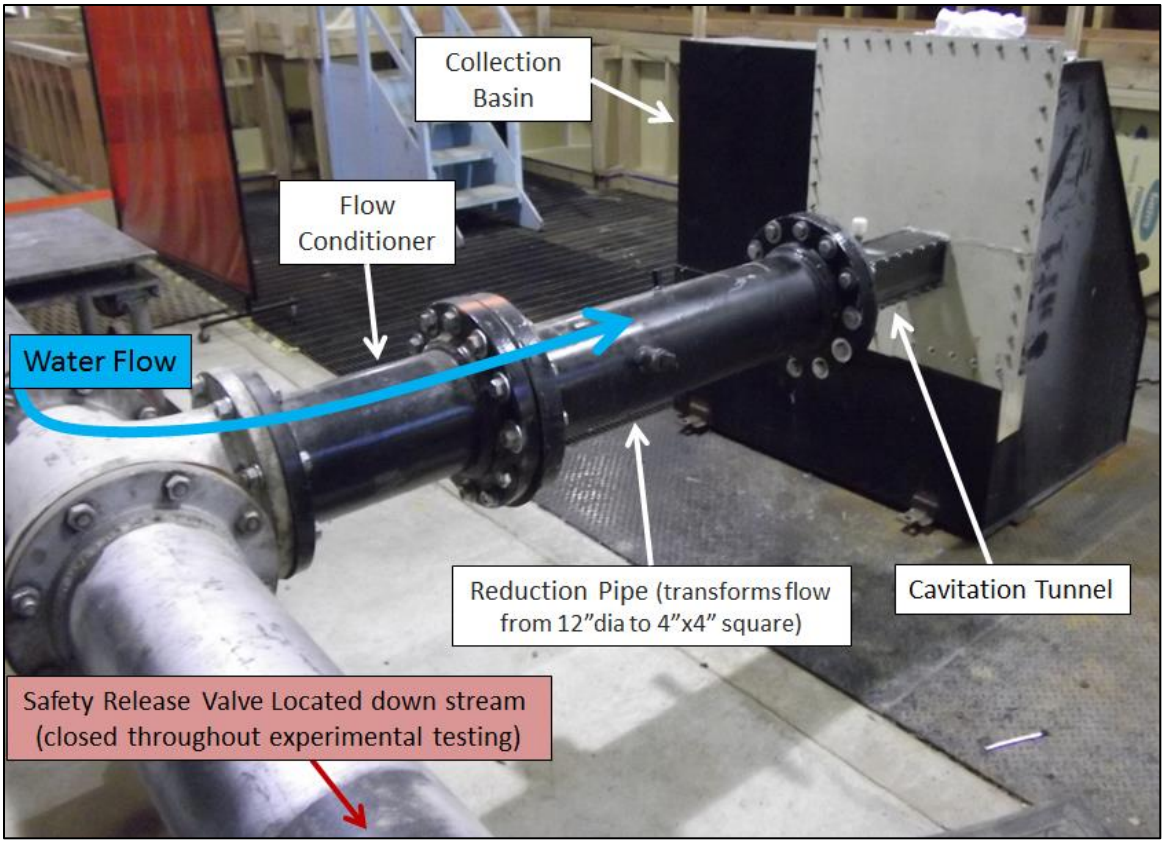

Figure E.2 Photo of Experimental Set-up 2

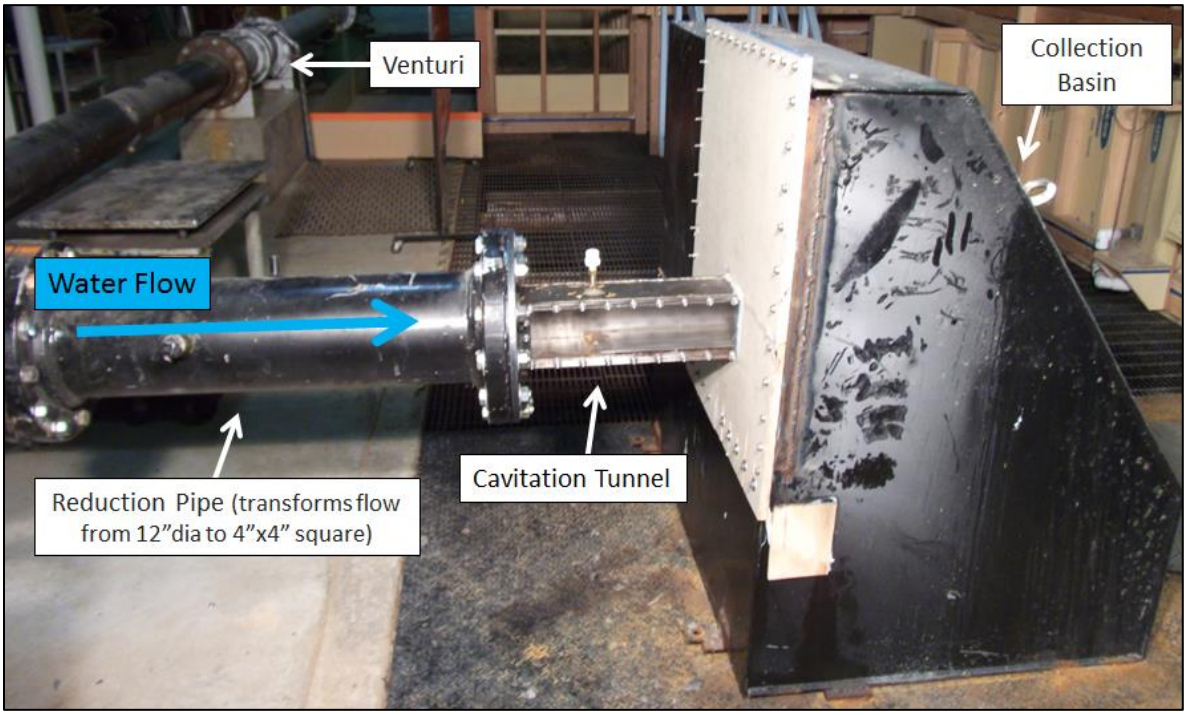

Figure E.3 Photo of Experimental Set-up 3

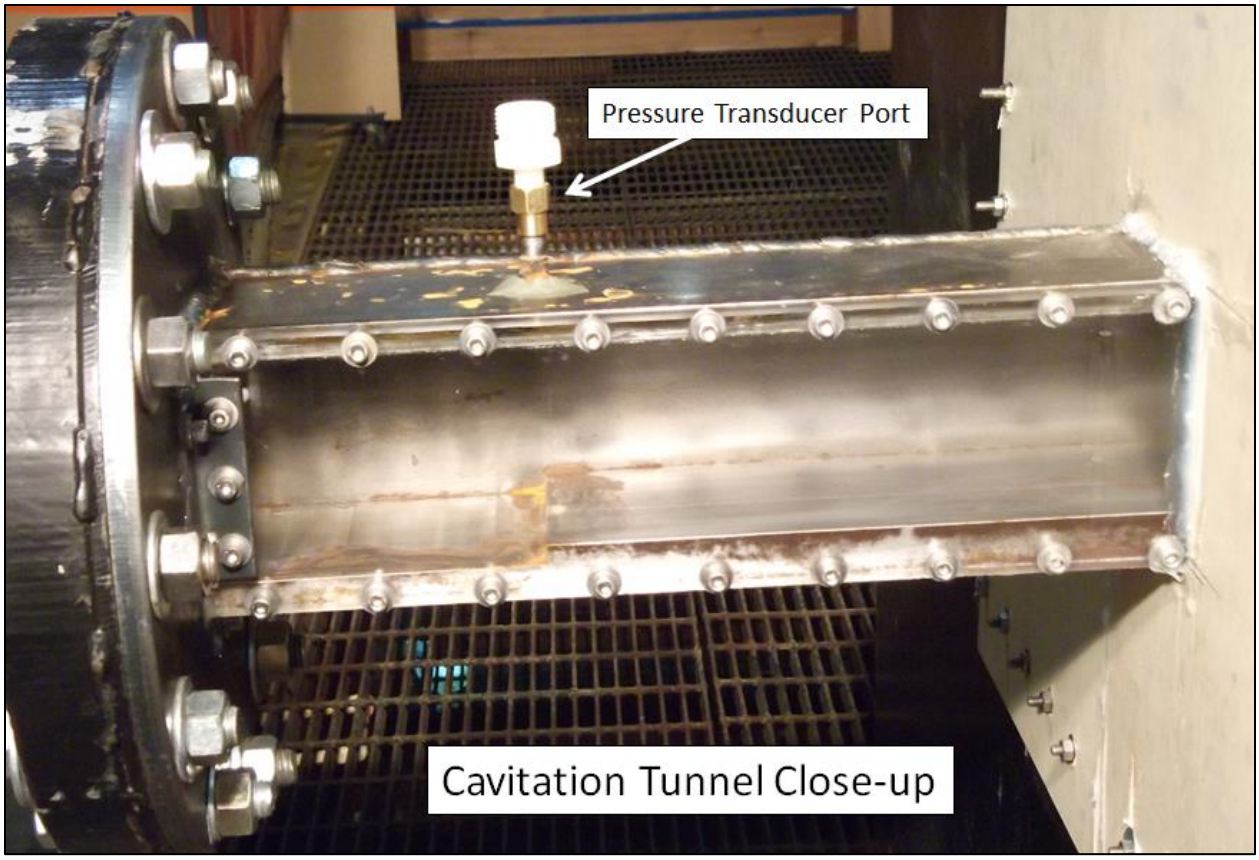

Figure E.4 Photo of Cavitation Tunnel In-Situ

Figure E.5 Close-up of Venturi within Experimental Set-up

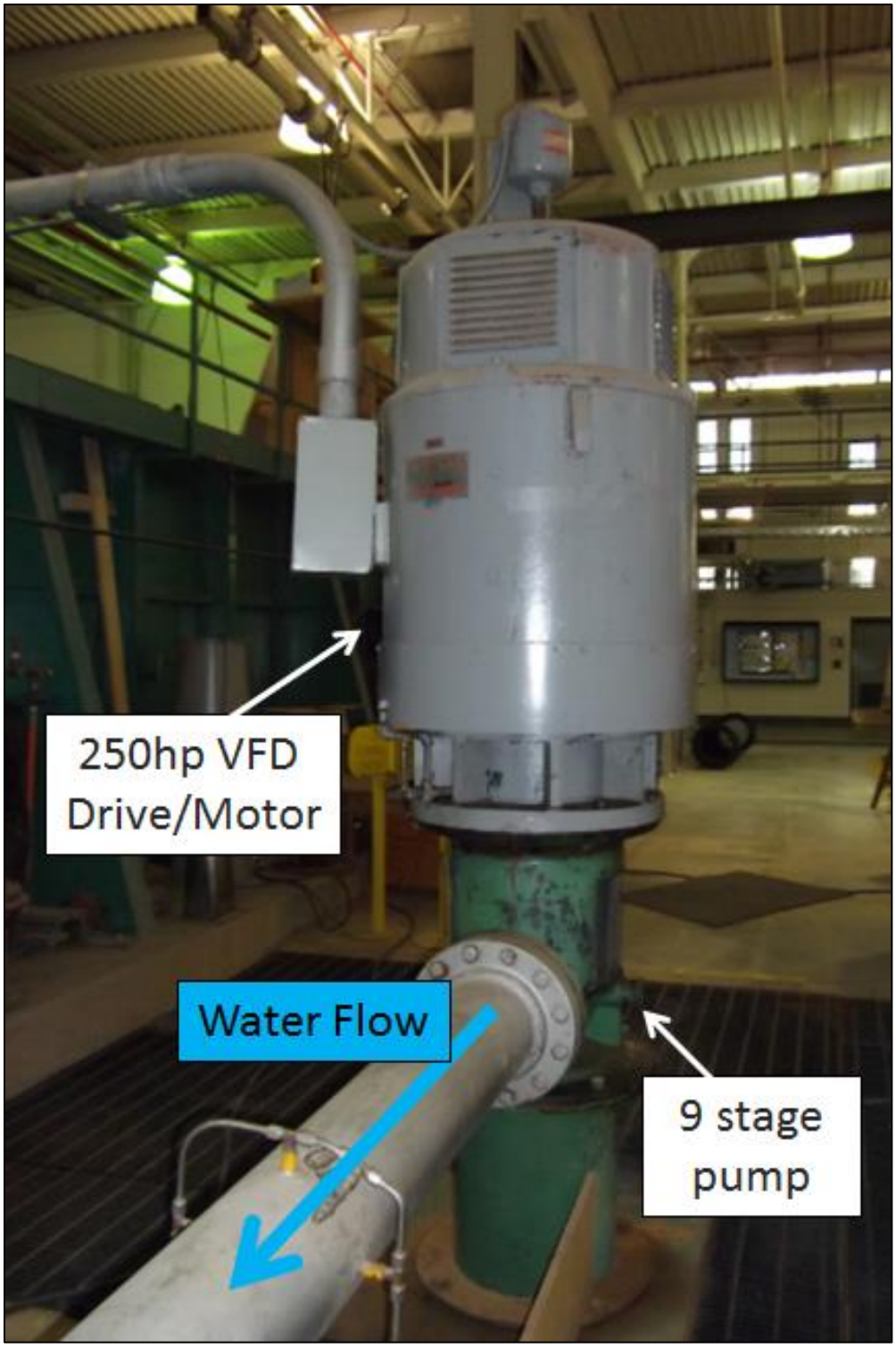

Figure E.6 Close-up of Variable Frequency Drive Motor and High Head Pump

APPENDIX F

BAND-PASS FILTER DESIGN FOR POST SIGNAL PROCESSING

Figures F.1 and F.2 present the supporting hand calculations behind the band pass filter cut-off frequencies.

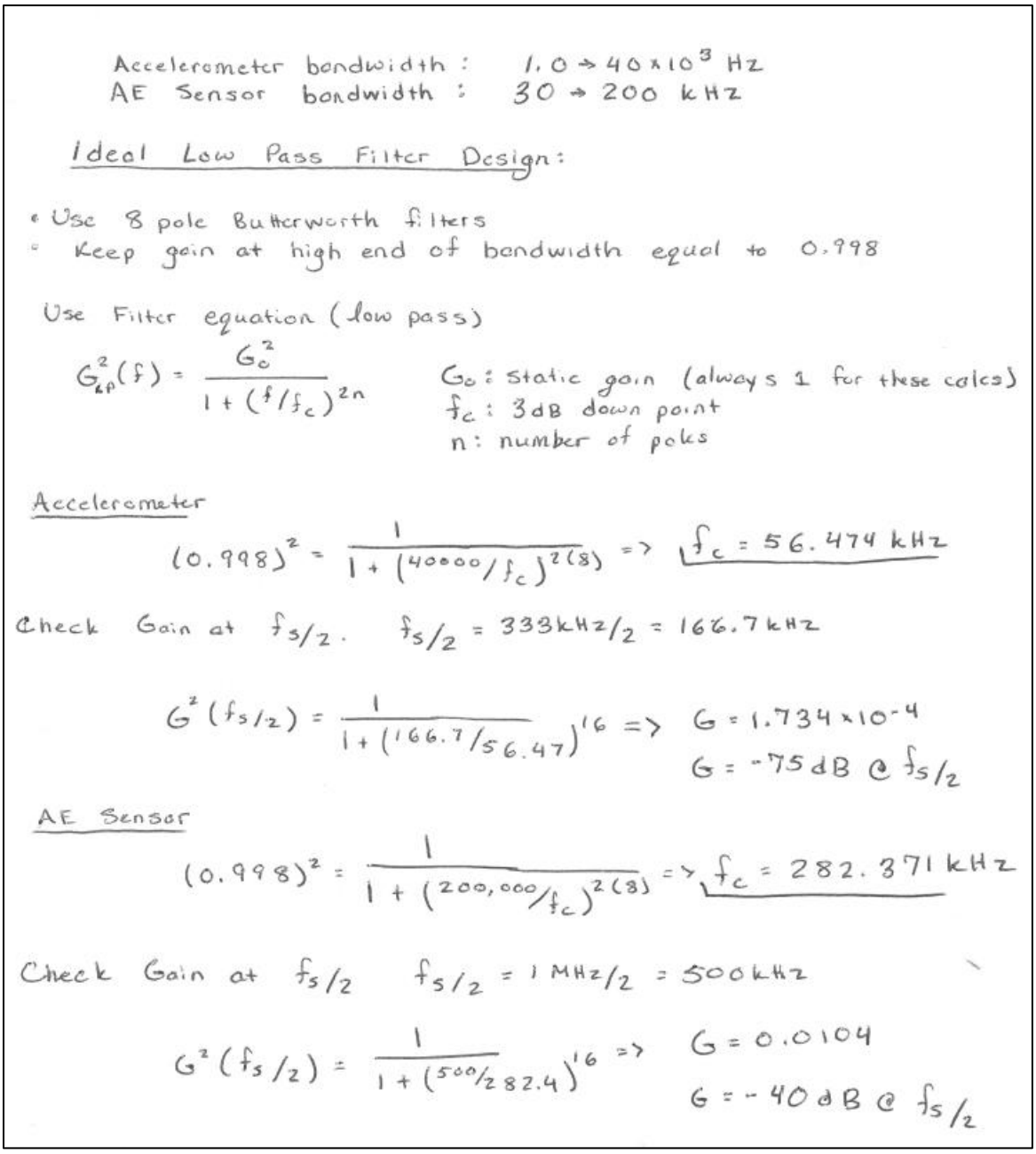

Figure F.1 Ideal Low Pass Filter Design Supporting Calculations

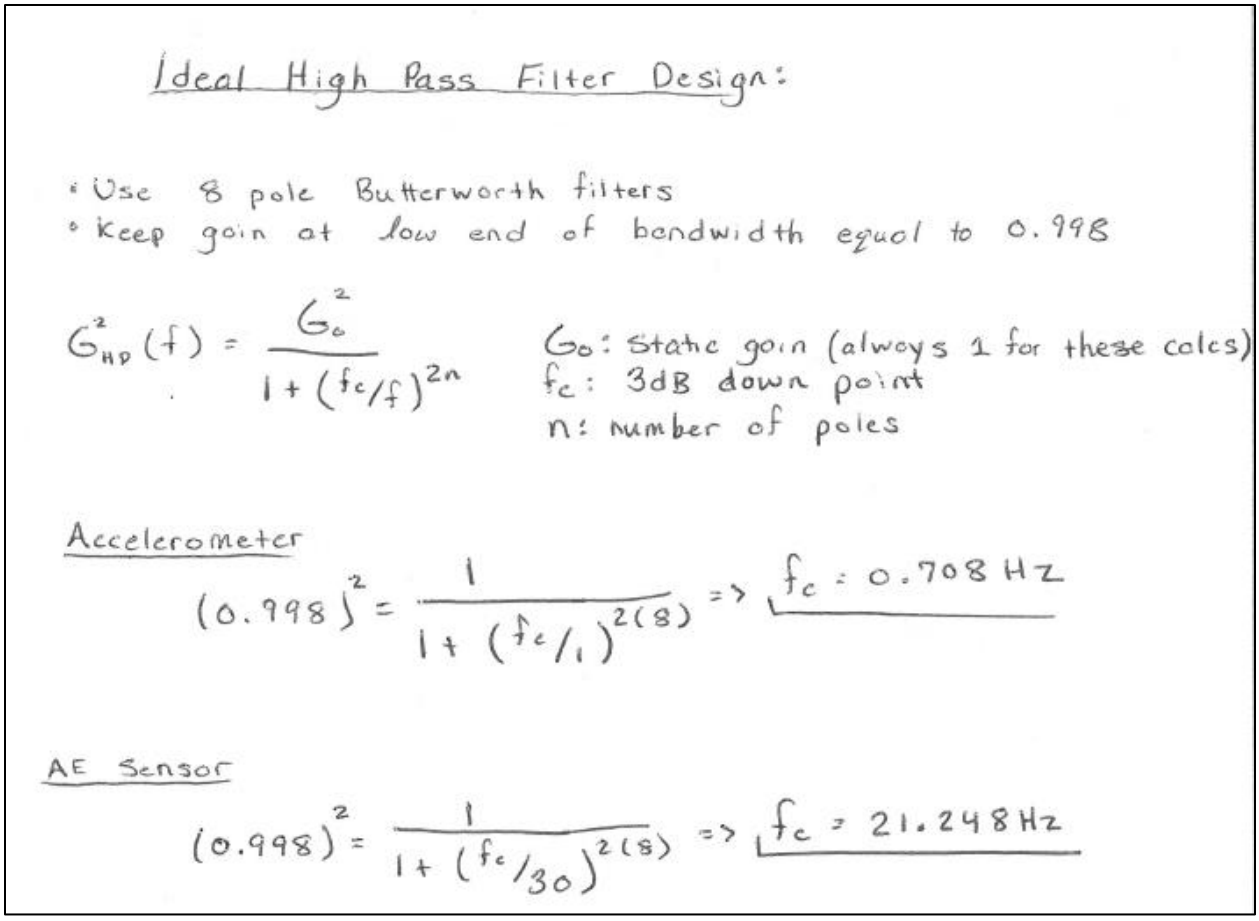

Figure F.2 Ideal High Pass Filter Design Supporting Calculations

The determined ideal cut-off frequencies were used for both the high and low pass filters for the AE Sensor and the low pass filter for the accelerometers. The ideal filter high pass filter for the accelerometers could not be implemented due to low frequency resolution within the filter design in MATLAB©. Hence the ideal high pass filter for accelerometers was not able to be implemented; instead a two pole high pass Butterworth a 3 dB down point at 1 Hz was implemented.

APPENDIX G

EXAMPLE BURST ANALYSIS MATLAB© CODE

```
% Example Burst Counter
clear, clc, close all

% Define time
t = 0:0.01:3;

% Create Sine Wave
y = sin(2*2*pi*t);

% Spike 1
y(100) = 7;
y(101) = 8;
y(102) = 7;
% Spike 2
y(200) = 6;
% Spike 3
y(249) = 4;
y(250) = 6;
y(251) = 5;

% Plot Data
plot(t,y)
xlabel('time (s)'), ylabel('magnatude')
title('Example Burst Counter Data')

% Determine Standard Deviation
st_y = std(y);

% Burst Counter
count = 0;
for i = 2:1:length(t)-1
    if y(i) >= st_y && y(i-1)< std(y)
        count = count+1;
        end
end

disp('Number of Bursts'), disp(count)
```

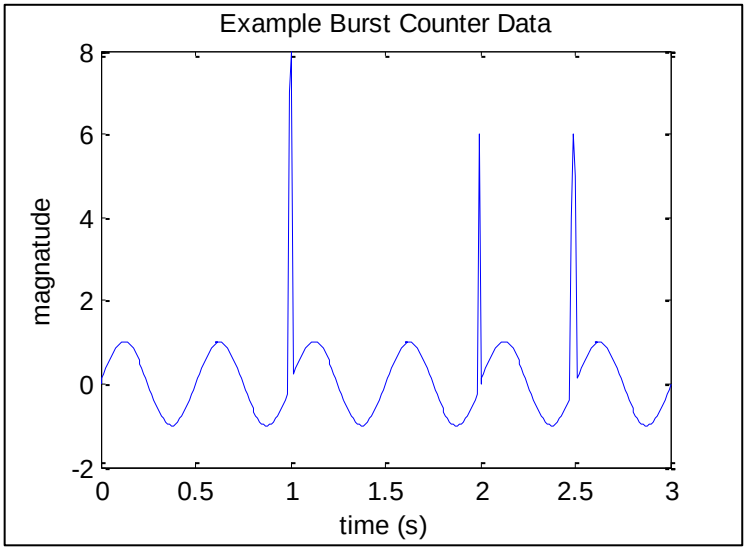

```
Number of Bursts
     3
```

APPENDIX H

EXAMPLE FREQUENCY SPECTRUM NORMALIZATION MATLAB© CODE

```
% Example of Spectrum Normalization
clear, clc, close all

fs = 100; % Hz
dt = 1/fs;

t = 0:dt:10;

y1 = sin(5*2*pi*t)+sin(15*2*pi*t);
y2 = 2*sin(5*2*pi*t)+2*sin(15*2*pi*t)+sin(10*2*pi*t);

h = hann(length(t));

% Determine FFT
nfft = 2^nextpow2(length(t));
x_freq = fs/2*linspace(0,1,nfft/2+1);
% Single Sided FFT
% Bottom Accelerometer
f1 = fft(y1.*h',nfft)/length(y1);
f2 = fft(y2.*h',nfft)/length(y2);


freq_1 = 2*abs(f1(1:nfft/2+1))+0.1; % 0.1 added for demonstration purposes
freq_2 = 2*abs(f2(1:nfft/2+1))+0.1;

figure(1), plot(x_freq,freq_1)
title('Reference Spectrum: used to normalize'), xlabel('Frequency (Hz)'),
ylabel('|magnitude(f)|')
axis([0 20 0.1 0.6])

figure(2), plot(x_freq,freq_2)
title('Spectrum obtained from in-situ measurement'), xlabel('Frequency
(Hz)'), ylabel('|magnitude(f)|')
axis([0 20 0.1 1.2])

figure(3), plot(x_freq,freq_2./freq_1)
title('Normalized Spectrum obtained from in-situ measurement')
xlabel('Frequency (Hz)'), ylabel('|magnitude(f)|')
axis([0 20 1 6])
```

Figure 1

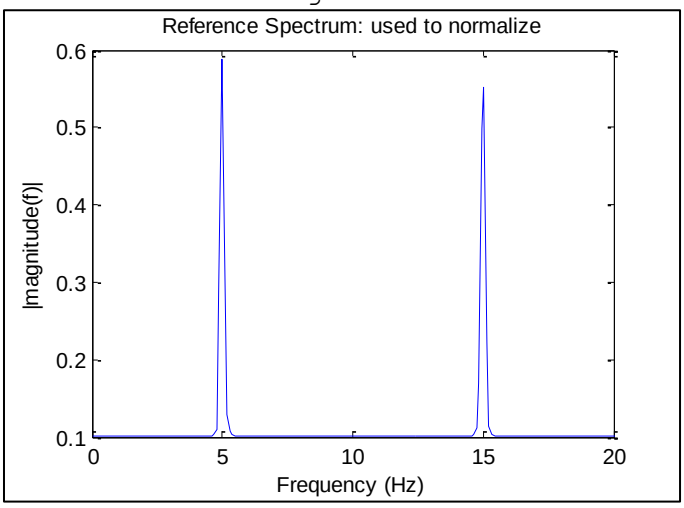

Figure 2

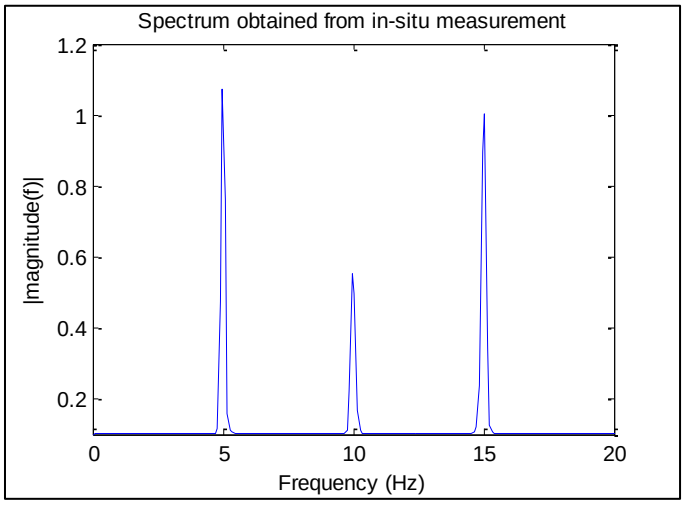

Figure 3

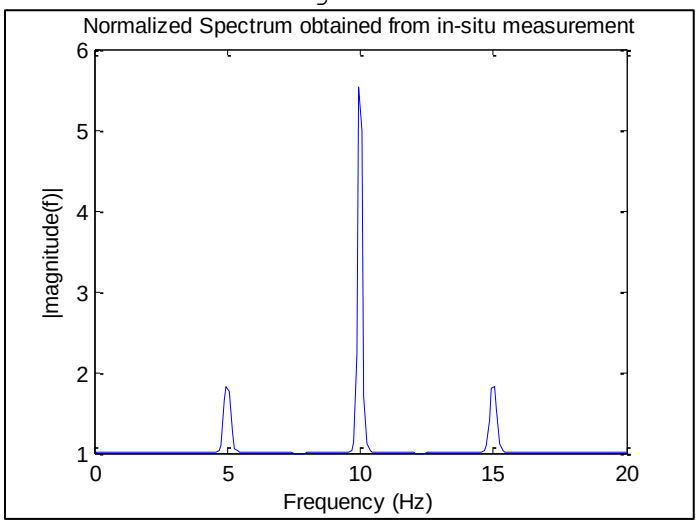

APPENDIX I

LIST OF TESTING DAYS AND CORRESPONDING ATMOSPHERIC PRESSURES

Table I.1 List of Days using Experimental Set-up and Corresponding Atmospheric Pressure

Date	Test Performed	Atmospheric Pressure	
		mmHg	psi
10/17/12	1st leak test - only ran up to 60% max - lots of leaks - needed to seal up before instrumentation could introduced into set-up	602.9	11.66
10/29/12	2nd leak test - ran up to 100% - very water tight - felt comfortable with applying instrumentation	608.5	11.77
11/14/12	Full Test Completed	609.7	11.79
12/12/12	Attempted to shoot high speed video, no success - Incomplete data set recorded	600.6	11.61
01/29/13	Final Test Set-up - Incomplete data set recorded	600.4	11.61
01/30/13	Full Test Completed	603	11.66
02/01/13	Full Test Completed and 60fps 1080p Video Shot	607.8	11.75

APPENDIX J

MATLAB© CODE FOR DETERMING AVERAGE ERROR BETWEEN INCREASING AND DECREASING FLOW RATE VERSUS CAVITATION INDEX POWER REGRESSION

```
% Determine Average Percent Error between Sigma vs. Flow Rate Power Fits

% Flow Range: 1.70 - 5.25 ft^3/s
Q = 1.7:0.01:5.25;

% Power Fits
% Increasing Flow Rate
pi = 16.3*(Q.^-1.90);
% Decreasing Flow Rate
pd = 16.6*(Q.^-1.92);

% Determine Difference between fits
pdiff = abs(pi-pd);

a = pdiff./pi;
b = pdiff./pd;

am = mean(a);
bm = mean(b);

disp('Average Percent Difference in Sigma vs. Flow Rate Power Fits')
disp(mean([am bm])*100)
Average Percent Difference in Sigma vs. Flow Rate Power Fits
    0.7325
```

```
Average Percent Difference in Sigma vs. Flow Rate Power Fits
    0.7325
```

APPENDIX K

CAVITATION AT FLOW - PHOTOS

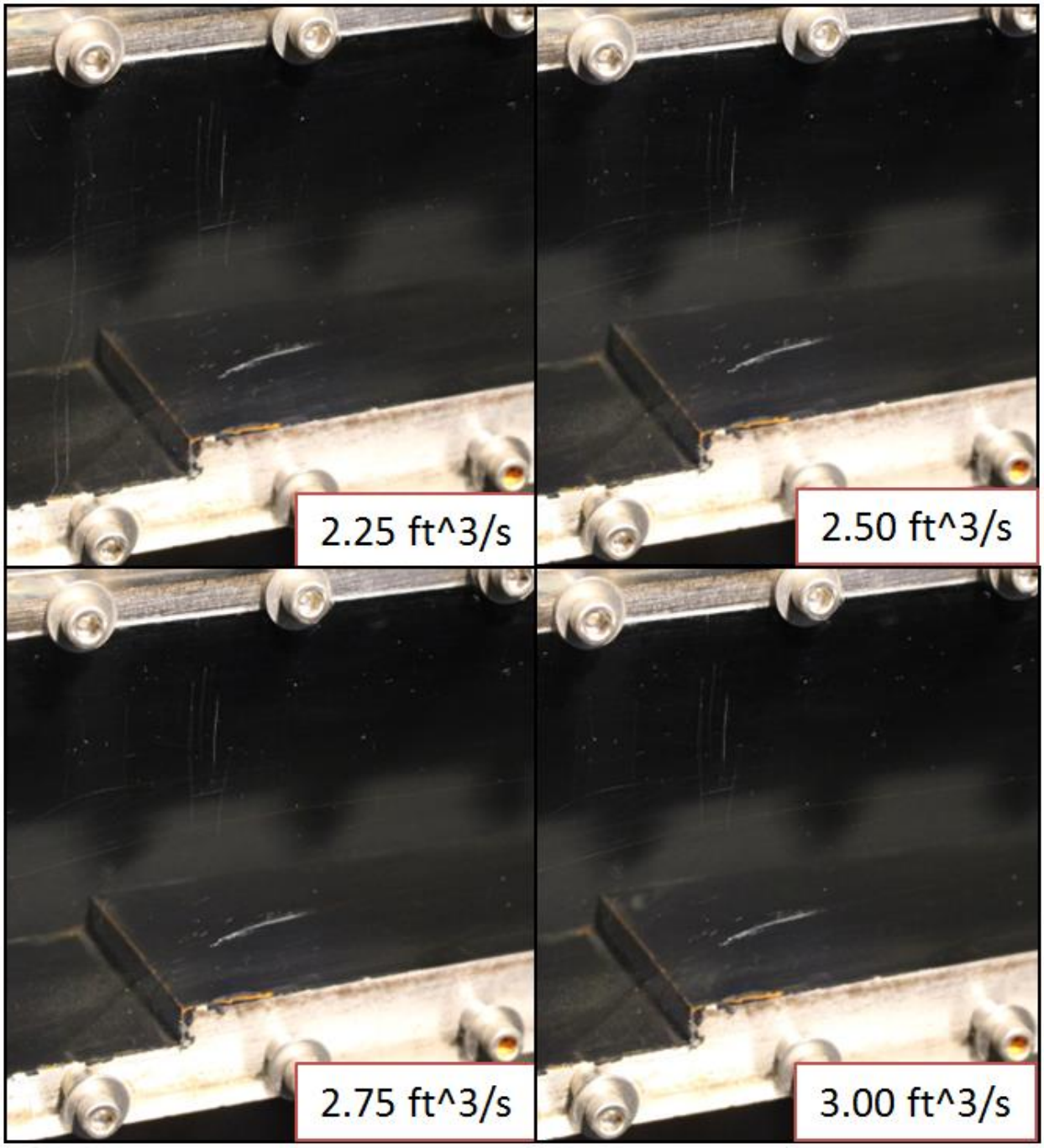

Figure K.1 Cavitation at Offset into the Flow at Flow Rates 2.25-3.00 ft^3/s

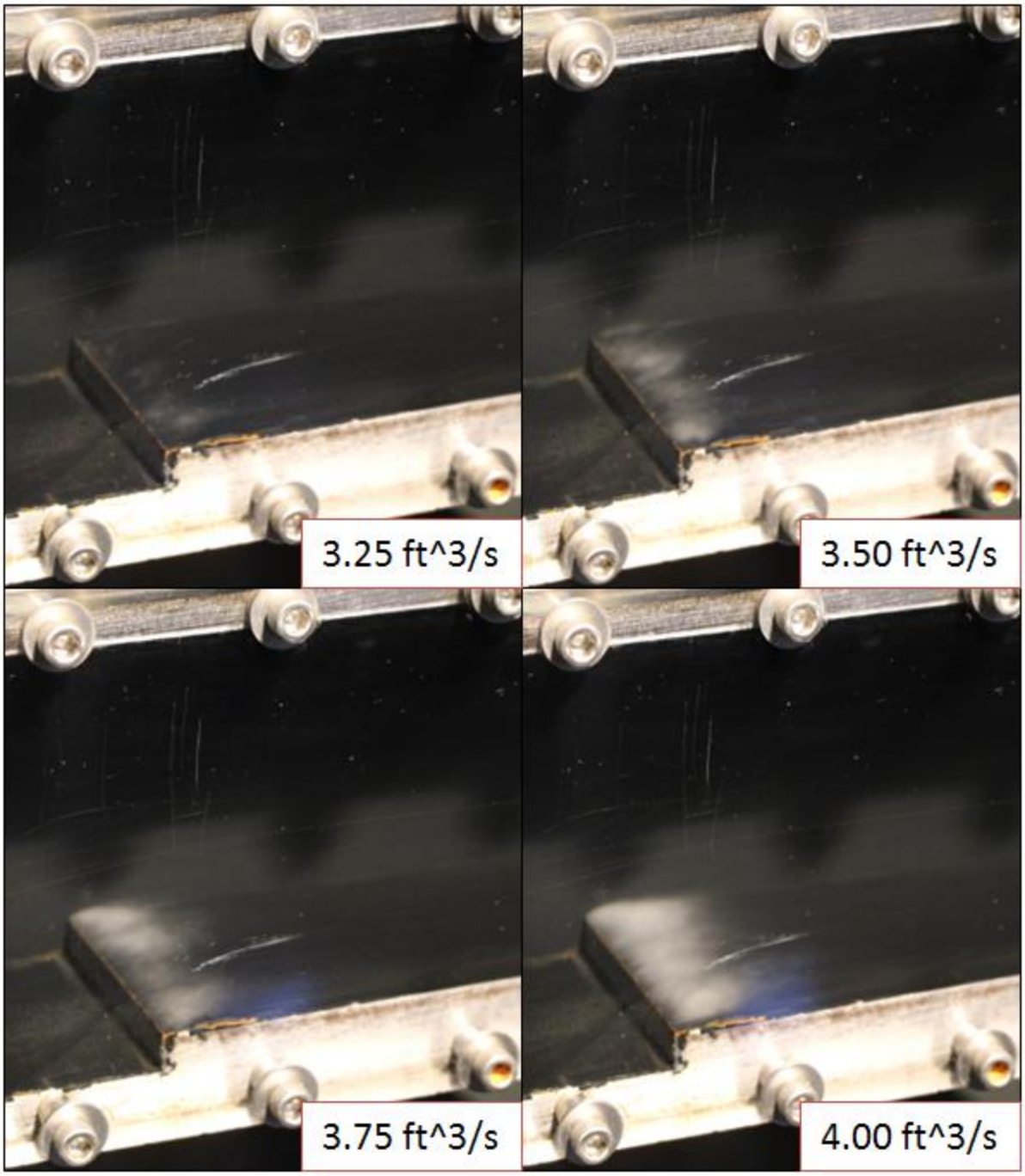

Figure K.2 Cavitation at Offset into the Flow at Flow Rates 3.25-4.00 ft^3/s

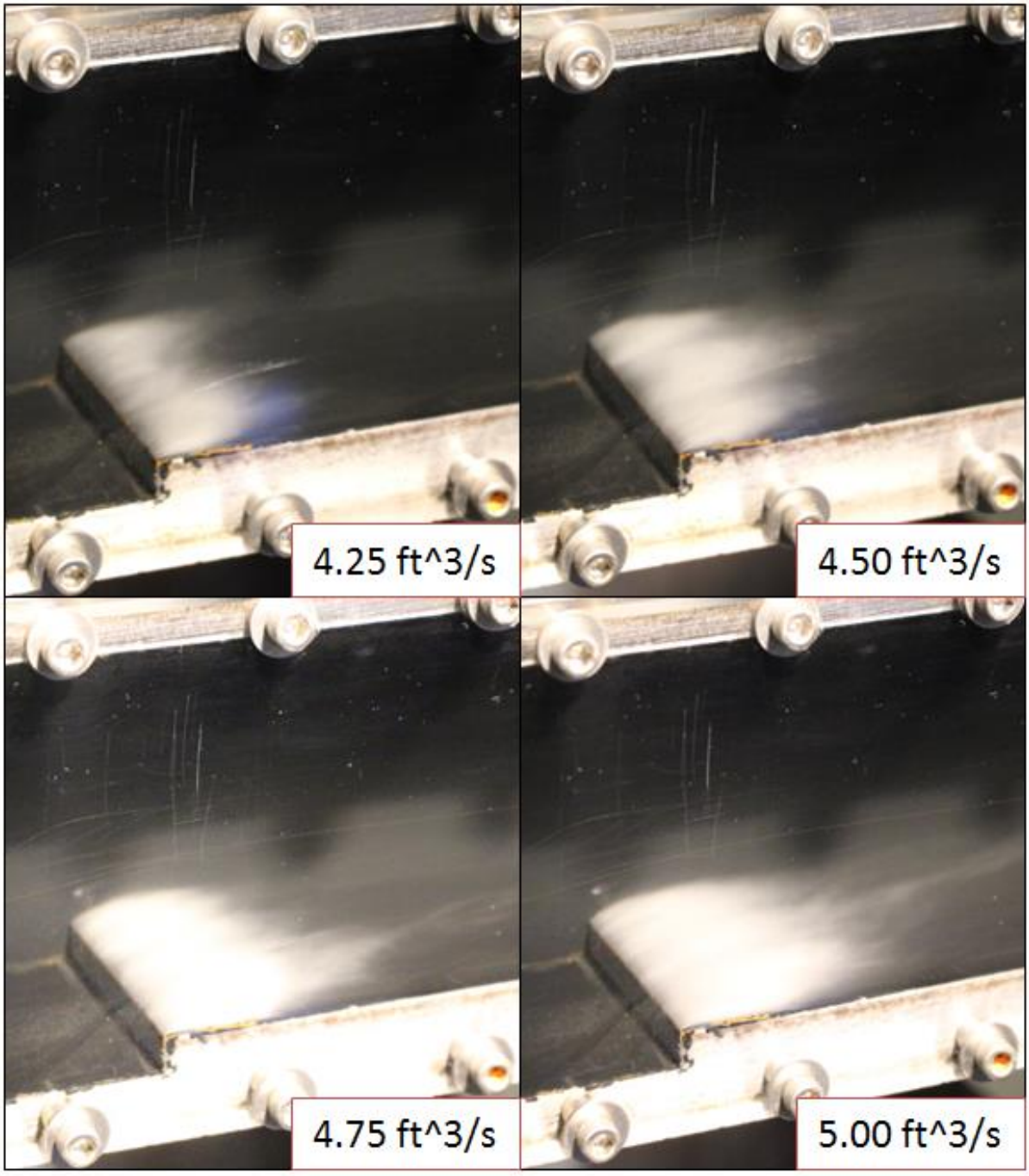

Figure K.3 Cavitation at Offset into the Flow at Flow Rates 4.25-5.00 ft^3/s

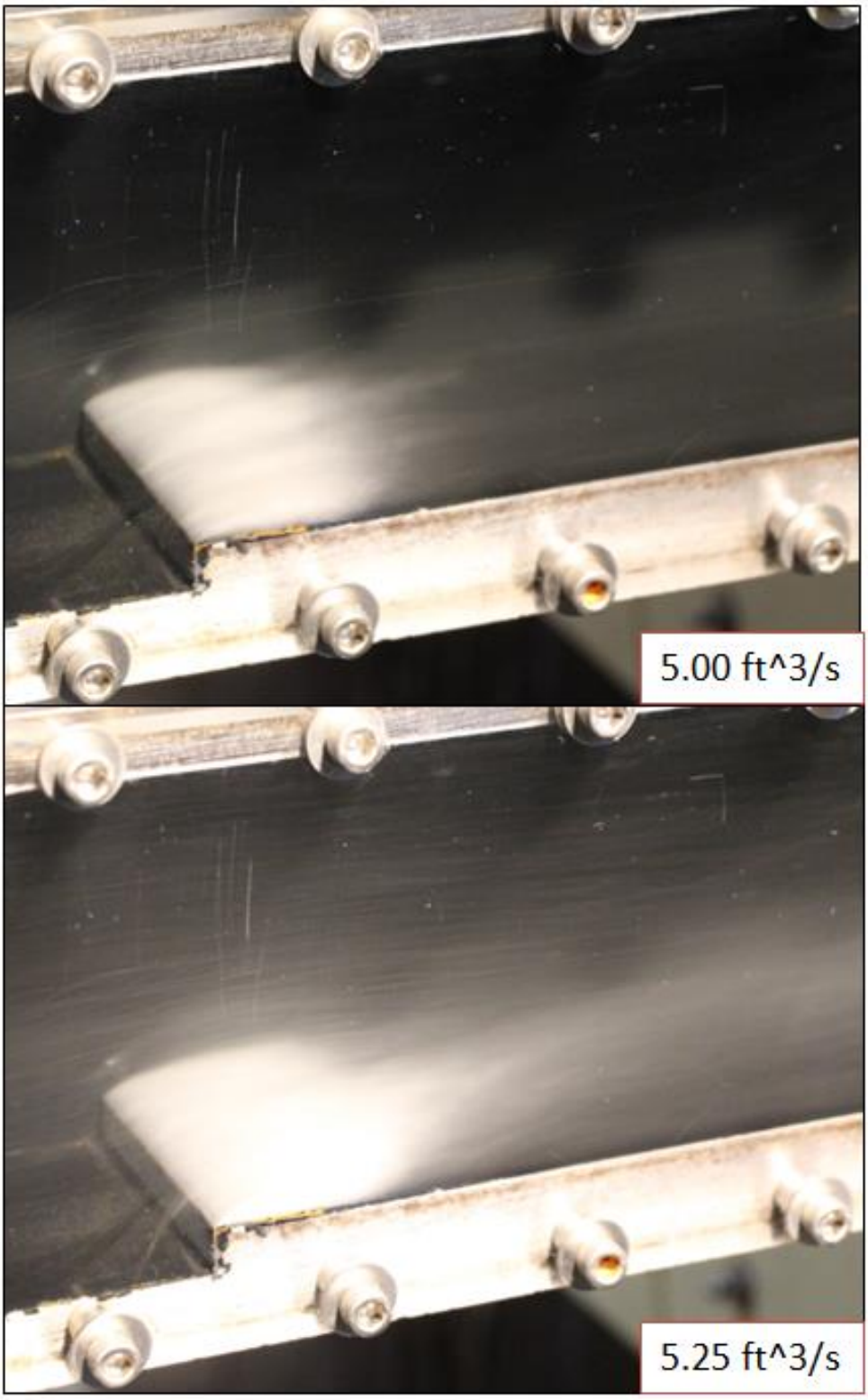

Figure K.4 Cavitation at Offset into the Flow at Flow Rates 5.00-5.25 ft^3/s

APPENDIX L

PRIMARY MATLAB© CODE FOR SIGNAL ANALYSIS

```
% Signal Analysis of Cavitation Data - ACCELERATION

% All Data taken from experimental set-up at Hydraulics Research Lab
% at Denver Federal Center in Lakewood, CO

clc, close all
%% Read in Data
% Sampling Frequency
fs = 333*10^3;
dt = 1/fs;

% Read-in Raw Data
ac = dlmread('Accel_Signals_4.00.ASC',';',7,1);

% Take only columns 1-2
% Column 1 = bottom accelerometer
% Column 2 = top accelerometer
% And standardize sample length - 12s
a1o = ac(1:12*fs,1); % mV
a2o = ac(1:12*fs,2); % mV
% Take care of 1000 gain in acquisition system and
% convert from v to g: 0.0101 v/g
a1g = (a1o./1000)/0.0101; % g
a2g = (a2o./1000)/0.0101; % g

%% Bandpass Filter Data
high_pass = 1; % high pass w = 1Hz
low_pass = 56474; % low pass w = 56.474kHz
[Bh, Ah] = butter(2,high_pass/(fs/2),'high'); % develop high pass filter
characteristics
[Bl, Al] = butter(8,low_pass/(fs/2),'low'); % develop low pass filter
characteristics

a1f = filter(Bh,Ah,a1g); % bottom accel passing through high pass filterff
a1 = filter(Bl,Al,a1f); % bottom accel with low pass filter (complete band
pass)
a1_keep = a1;

a2f = filter(Bh,Ah,a2g); % top accel passing through high pass filter
a2 = filter(Bl,Al,a2f); % top accel passing through low pass filter (complete
band pass)
a2_keep = a2;

%% Plot Time History
t = 0:dt:length(a1)/fs-dt; % Time axis
figure(1)
subplot(211), plot(t,a2), title('Top Accelerometer')
xlabel('time (s)'), ylabel('acceleration (g)')
```

```
subplot(212), plot(t,a1), title('Bottom Accelerometer')
xlabel('time (s)'), ylabel('acceleration (g)')

a1_max = max(abs(a1));
a2_max = max(abs(a2));

disp('Maximum Top Acceleration (g)'), disp(a1_max)
disp('Maximum Bottom Acceleration (g)'), disp(a2_max)

%% Determine RMS of Original Signal
a1_rms = sqrt((1/length(a1))*(sum(a1.^2)));
a2_rms = sqrt((1/length(a2))*(sum(a2.^2)));
disp('RMS of Top Accelerometer (g)'), disp(a2_rms)
disp('RMS of Bottom Accelerometer (g)'), disp(a1_rms)

%% Determine Spike Ratio of Signal
a1_spike = a1_max/a1_rms;
a2_spike = a2_max/a2_rms;

disp('Spike Ratio of Top Accelerometer'), disp(a2_spike)
disp('Spike Ratio of Bottom Accelerometer'), disp(a1_spike)

%% Spike Analysis Average (top 10 spike)
n = 10;
a1_sort = sort(abs(a1),'descend');
a2_sort = sort(abs(a2),'descend');
a1_S = mean(a1_sort(1:n))/a1_rms;
a2_S = mean(a2_sort(1:n))/a2_rms;
disp('Average Spike Analysis Ratio - Top Accelerometer'), disp(a2_S)
disp('Average Spike Analysis Ratio - Bottom Accelerometer'), disp(a1_S)


%% Burst Analysis
st_dv_a1 = std(a1);
st_dv_a2 = std(a2);
stn = [15]; % number of standard deviations before cut-off
for j = 1:1:length(stn)
cutff_a1 = st_dv_a1*stn(j);
cutff_a2 = st_dv_a2*stn(j);

count_a1(j) = 0;
count_a2(j) = 0;
for i = 2:1:length(t)-1
    if abs(a1(i)) >= cutff_a1 && abs(a1(i-1)) < cutff_a1
        count_a1(j) = count_a1(j)+1;
    end
    if abs(a2(i)) >= cutff_a2 && abs(a1(i-1)) < cutff_a2
        count_a2(j) = count_a2(j)+1;
    end
end

end
disp('Number of Bursts Detected Top Accelerometer'), disp(count_a2/12)
disp('Number of Bursts Detected Bottom Accelerometer'), disp(count_a1/12)
```

```
%% Determine Auto-Correlation of signals
% Auto Correlation of Bottom Accelerometer
X_1 = xcorr(a1,a1);
% Auto Correlation of Top Accelerometer
X_2 = xcorr(a2,a2);

figure(2)
subplot(211), plot((X_2./(max(X_2)))*100), title('Auto-Correlation of Top
Accelerometer')
ylabel('Percent Correlation (%)')
subplot(212), plot((X_1./(max(X_1)))*100), title('Auto-Correlation of Bottom
Accelerometer')
ylabel('Percent Correlation (%)')
%
%% Apply Hanning Window Prior to Further Analysis
whann = hann(length(t));
a1 = a1.*whann;
a2 = a2.*whann;

%% Determine FFT of Signals
nfft = 2^nextpow2(length(t));
x_freq = fs/2*linspace(0,1,nfft/2+1);
% Single Sided FFT
% Bottom Accelerometer
y1 = fft(a1,nfft)/length(a1);
freq_1 = 2*abs(y1(1:nfft/2+1));
% Top Accelerometer
y2 = fft(a2,nfft)/length(a2);
freq_2 = 2*abs(y2(1:nfft/2+1));

y_max_1 = max(freq_1(250:length(freq_1)));
y_max_2 = max(freq_2(250:length(freq_2)));
y_max =(max([y_max_1 y_max_2]));
figure(3)
subplot(211), plot(x_freq,freq_2), title('FFT of Top Accelerometer')
xlabel('Frequency (Hz)'), ylabel('|g(f)|'), axis([high_pass low_pass 0
y_max*1.025]), % axis 'auto y'
subplot(212), plot(x_freq,freq_1), title('FFT of Bottom Accelerometer')
xlabel('Frequency (Hz)'), ylabel('|g(f)|'), axis([high_pass low_pass 0
y_max*1.025]), % axis 'auto y'

for i = 1:1:length(x_freq)
    if freq_1(i) == y_max_1
        freq_c_1 = x_freq(i);
    end
    if freq_2(i) == y_max_2
        freq_c_2 = x_freq(i);
    end
end

disp('Maximum Top Acceleration in Frequency domain - max|g(f)|'),
disp(y_max_2)
disp('Maximum Top Acceleration Corresponding Frequency (Hz)'), disp(freq_c_2)
disp('Maximum Bottom Acceleration in Frequency domain - max|g(f)|'),
disp(y_max_1)
```

```
disp('Maximum Bottom Acceleration Corresponding Frequency (Hz)'),
disp(freq_c_1)

%% Normalized FFT
load FFT_Spectrum_Normalization_Accels
% normalized with original averaged FFT
freq1_n = freq_1./B_FFT_norm';
freq2_n = freq_2./T_FFT_norm';
% normalized with 1Hz average FFT
freq1_n1 = freq_1./B_FFT_norm_1;
freq2_n1 = freq_2./T_FFT_norm_1;
% normalized with 1Hz average FFT
freq1_n2 = freq_1./B_FFT_norm_2;
freq2_n2 = freq_2./T_FFT_norm_2;
% normalized with 1Hz average FFT
freq1_n5 = freq_1./B_FFT_norm_5;
freq2_n5 = freq_2./T_FFT_norm_5;
figure(4)
subplot(211), plot(x_freq,freq_2_norm), title('Normalized FFT of Top
Accelerometer')
xlabel('Frequency (Hz)'), ylabel('|g(f)| - normalized'), axis([0 40000 0 1]),
axis 'auto y'
subplot(212), plot(x_freq,freq_1_norm), title('Normalized FFT of Bottom
Accelerometer')
xlabel('Frequency (Hz)'), ylabel('|g(f)|-normalized'), axis([0 40000 0 1]),
axis 'auto y'

%% Determine Power Spectral Density (PSD)
% Bottom Accelerometer PSD
Pxx_1 = abs(fft(a1,nfft)).^2/length(a1)/fs;
Hpsd_1 = dspdata.psd(Pxx_1(1:length(Pxx_1)/2),'Fs',fs);
% Top Accelerometer PSD
Pxx_2 = abs(fft(a2,nfft)).^2/length(a2)/fs;
Hpsd_2 = dspdata.psd(Pxx_2(1:length(Pxx_2)/2),'Fs',fs);

figure(5)
subplot(211), plot(Hpsd_2), title('PSD of Top Accelerometer')
axis([0 40000 -100 100]), axis 'auto y'
subplot(212), plot(Hpsd_1), title('PSD of Bottom Accelerometer')
axis([0 40000 -100 100]), axis 'auto y'


%% Determine Coherence of Signals
% size of Hanning window (power to be applied to 2)
h = 15;
[Cxy,W] = mscohere(a1_keep,a2_keep,hanning(2^h),2^(h-1),nfft);
figure(5), plot(x_freq,Cxy), title('Coherence of Top and Bottom
Accelerometers')
xlabel('Frequency (Hz)'), ylabel('Coherence'), axis([0 40000 0 1])
```

```
% Signal Analysis of Cavitation Data - ACOUSTIC EMISSION

% All Data taken from experimental set-up at Hydraulics Research Lab
% at Denver Federal Center in Lakewood, CO

clc, clear, close all
%% Read in Data
% Sampling Frequency
fs = 1*10^6;
dt = 1/fs;

% Read-in Raw Data
aer = dlmread('AE_Signal_4.00.ASC',';',7,1);
% Raw Data - V
aeo = aer(1:8.5*fs,1); % Remove extra column of zeros and only take 1st 8.5s
% Reduce Data - due to 40db (100x) gain on instrumentation
aeg = (aeo/100)*1000; % mv

%% Bandpass Filter Data
high_pass = 21249; % high pass w = 30kHz
low_pass = 282371; % low pass w = 200kHz
[Bh, Ah] = butter(8,high_pass/(fs/2),'high'); % develop high pass filter
characteristics
[Bl, Al] = butter(8,low_pass/(fs/2),'low'); % develop low pass filter
characteristics

aef = filter(Bh,Ah,aeg); % Acoustic Emission high pass filter
ae = filter(Bl,Al,aef); % Acoustic Emission low pass filter (complete band
pass)

%% Plot Time History
t = 0:dt:length(ae)/fs-dt; % Time axis
figure(1)
plot(t,ae), title('Acoustic Emission')
xlabel('time (s)'), ylabel('Voltage output (mV)')

ae_max = max(abs(ae));
disp('Maximum AE Reading (mV)'), disp(ae_max)

%% Determine RMS of Signals
ae_rms = sqrt((1/length(ae))*(sum(ae.^2)));
disp('RMS of AE Sensor (mV)'), disp(ae_rms)

%% Determine Spike Ratio of Signal
ae_spike = ae_max/ae_rms;

disp('Spike Ratio of AE Sensor'), disp(ae_spike)

%% Spike Analysis Average (top 10 spike)
n = 10;
ae_sort = sort(abs(ae),'descend');
ae_S = mean(ae_sort(1:n))/ae_rms;
disp('Average Spike Analysis Ratio - AE Sensor'), disp(ae_S)
```

```
%% Burst Analysis
st_dv_ae = std(ae);

stn = [5]; % number of standard deviations before cut-off
for j = 1:1:length(stn)
cutff_ae = st_dv_ae*stn(j);

count_ae(j) = 0;

for i = 2:1:length(t)-1
    if abs(ae(i)) >= cutff_ae && abs(ae(i-1)) < cutff_ae
        count_ae(j)= count_ae(j)+1;
    end
end

end

disp('Number of Bursts Detected Per Second - AE Sensor'), disp(count_ae/8.5)


%% Determine Auto-Correlation of signals
% Auto Correlation of AE Sensor
X = xcorr(ae,ae);
figure(2)
plot((X./(max(X)))*100), title('Auto-Correlation AE Sensor')
ylabel('Percent Correlation (%)')

%% Apply Hanning Window Prior to Further Analysis
whann = hann(length(t));
ae = ae.*whann;

%% Determine FFT of Signals
nfft = 2^nextpow2(length(t));
x_freq = fs/2*linspace(0,1,nfft/2+1);
% Single Sided FFT
y = fft(ae,nfft)/length(ae);
freq = 2*abs(y(1:nfft/2+1));

y_max = max(freq);
figure(3)
plot(x_freq,freq), title('FFT of AE Sensor')
xlabel('Frequency (Hz)'), ylabel('|mV(f)|'), axis([high_pass low_pass 0 1]),
axis 'auto y'

for i = 1:1:length(x_freq)
    if freq(i) == y_max
        freq_c = x_freq(i);
    end
end

disp('Maximum Top Acceleration in Frequency domain - max|g(f)|'), disp(y_max)
disp('Maximum Top Acceleration Corresponding Frequency (Hz)'), disp(freq_c)

%% Normalized FFT
```

```
load FFT_Spectrum_Normalization_AE

freq_normed = freq./freq_n';
freq_normed1 = freq./freq_n1;
freq_normed2 = freq./freq_n2;
freq_normed5 = freq./freq_n5;

figure(4), plot(x_freq,freq_normed), title('Normalized FFT of AE Sensor')
xlabel('Frequency (Hz)'), ylabel('|mV(f)|'), axis([high_pass low_pass 0 1]),
axis 'auto y'

ave_f_n = mean(freq_normed(high_pass:low_pass));
disp('Average Value of Normalized FFT'), disp(ave_f_n)
ave_f = mean(freq(high_pass:low_pass));
disp('Average Value of FFT'), disp(ave_f)


%% Determine Power Spectral Density (PSD)
% AE Sensor PSD
Pxx = abs(fft(ae,nfft)).^2/length(ae)/fs;
Hpsd = dspdata.psd(Pxx(1:length(Pxx)/2),'Fs',fs);
figure(5)
plot(Hpsd), title('PSD of AE Sensor')
```

APPENDIX M

SUPPLEMENTAL AUTO-CORRELATION PLOTS

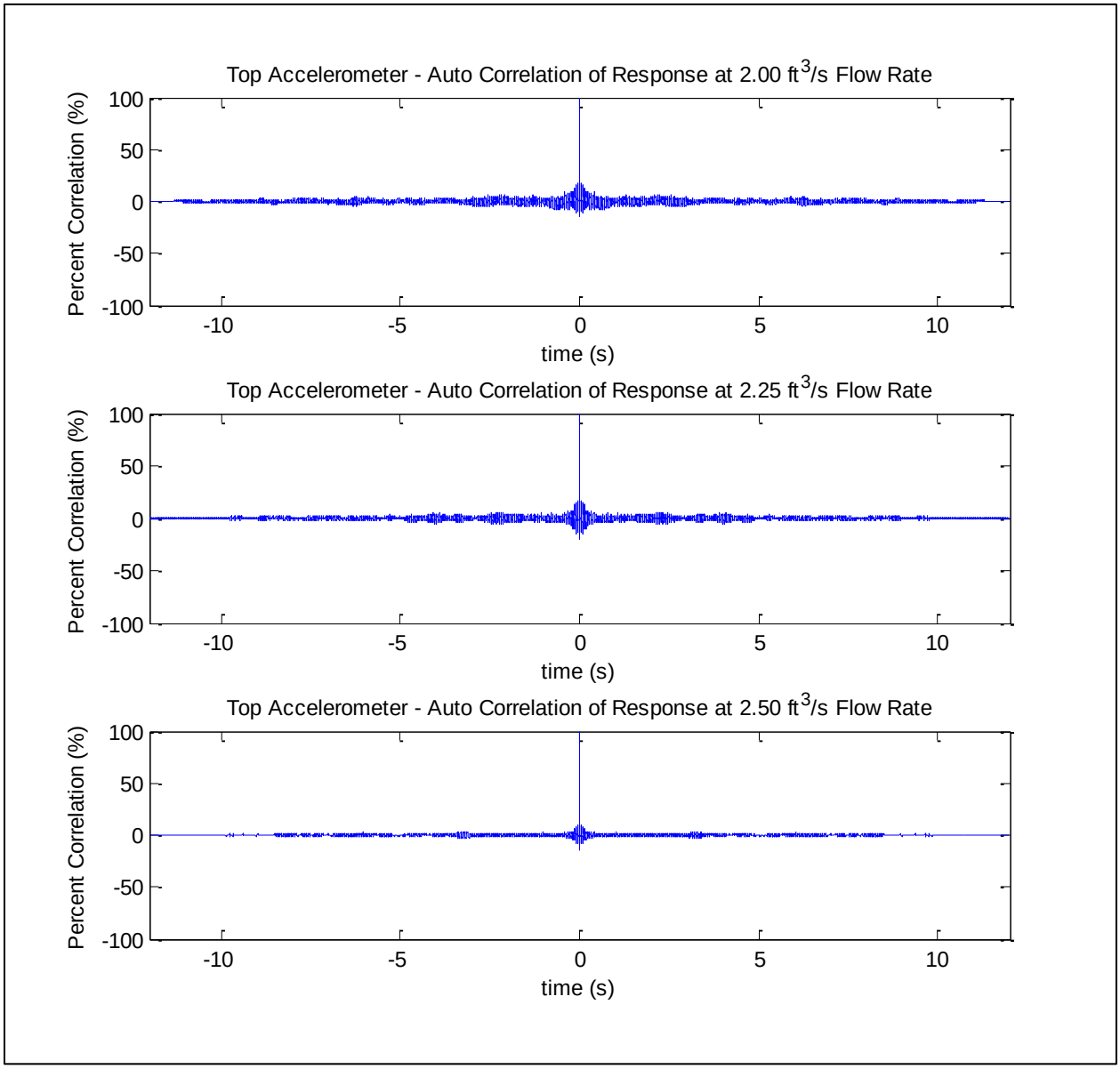

Figure M.1 Auto-Correlation of Top Acceleration at Flow Rates 2.00-2.50 ft^3/s

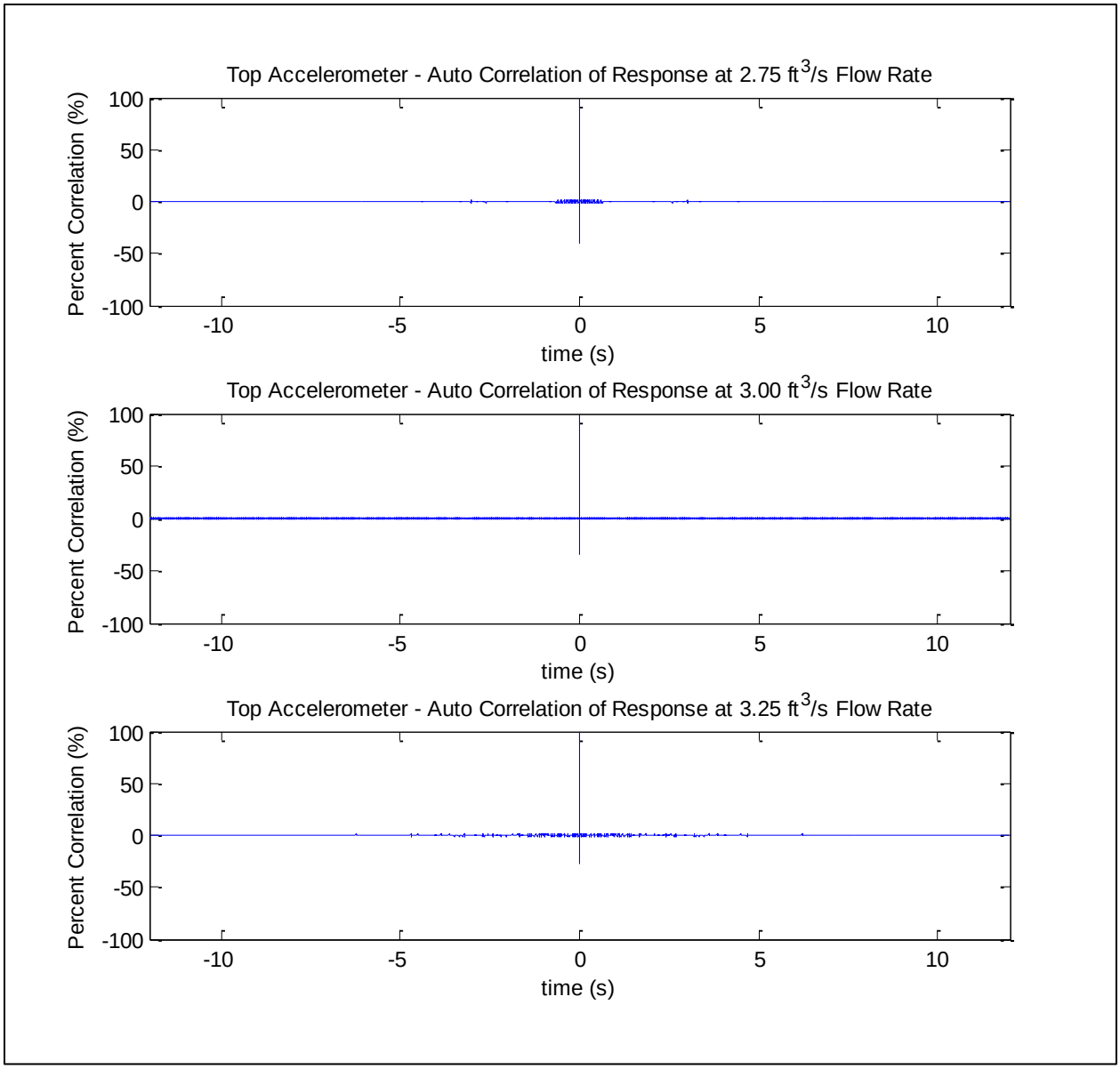

Figure M.2 Auto Correlation of Top Acceleration at Flow Rates 2.75-3.25 ft^3/s

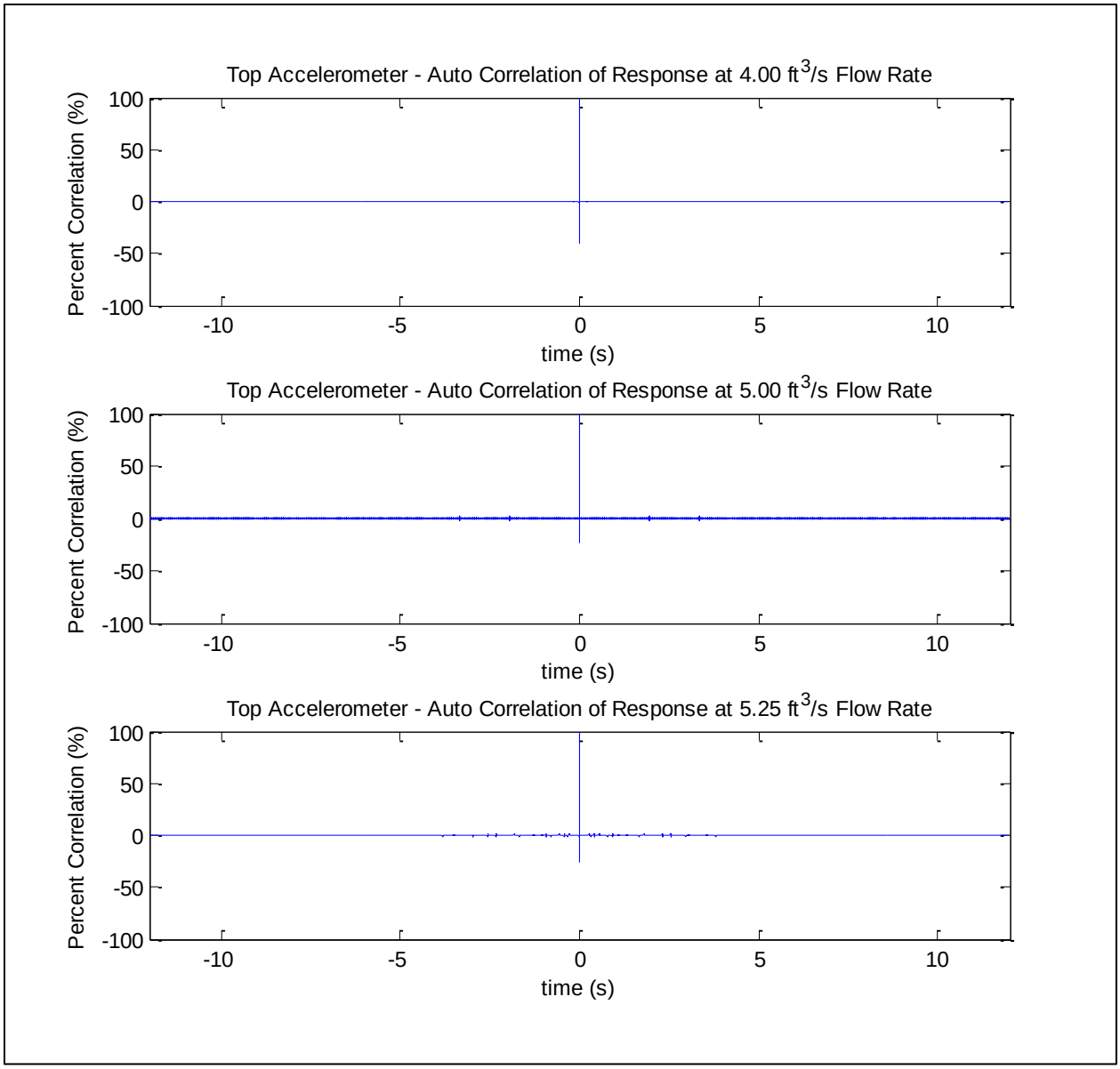

Figure M.3 Auto Correlation of Top Acceleration at Flow Rates 4.00, 5.00, 5.25 ft^3/s

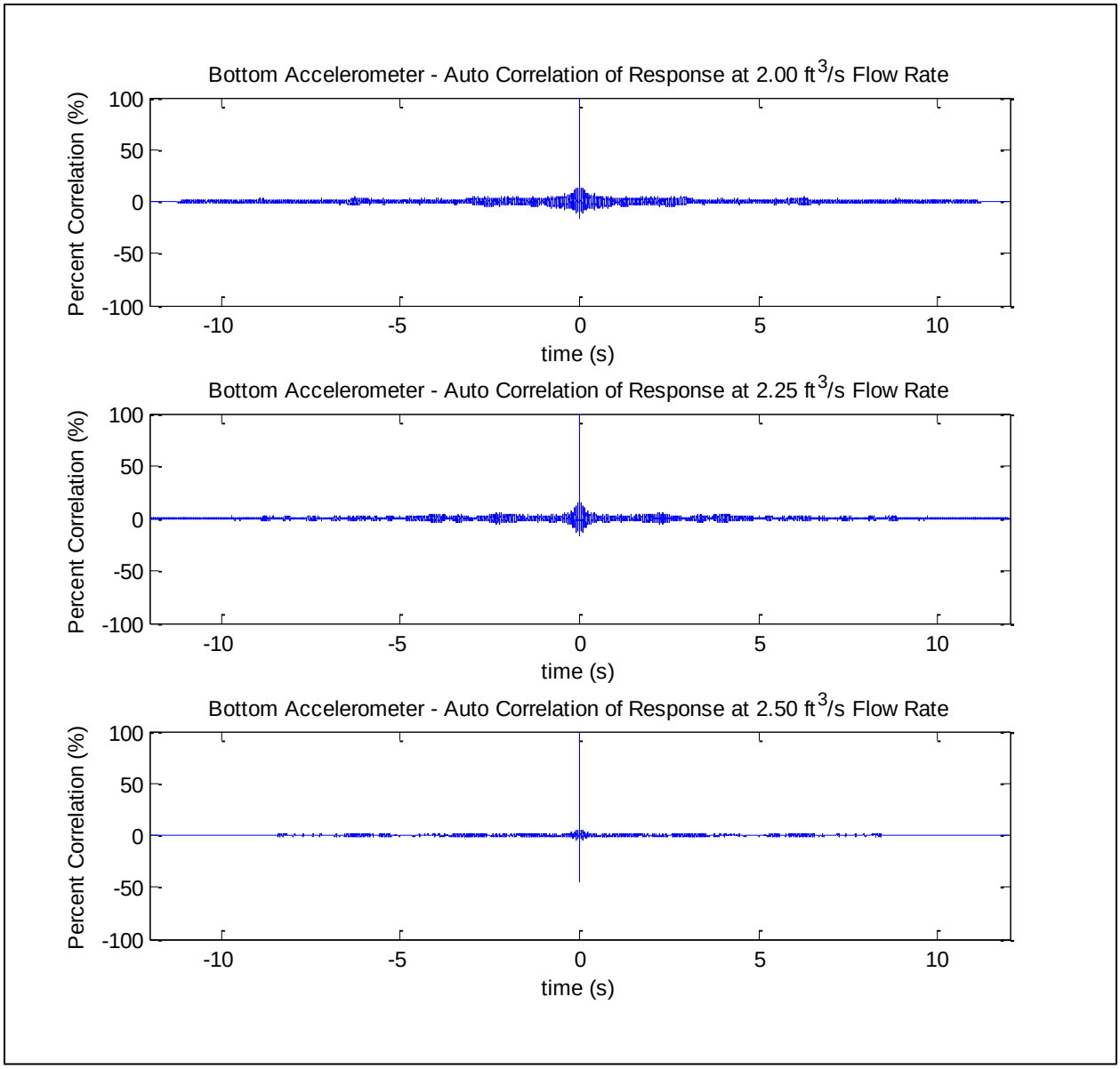

Figure M.4 Auto Correlation of Bottom Acceleration at Flow Rates 2.00-2.50 ft^3/s

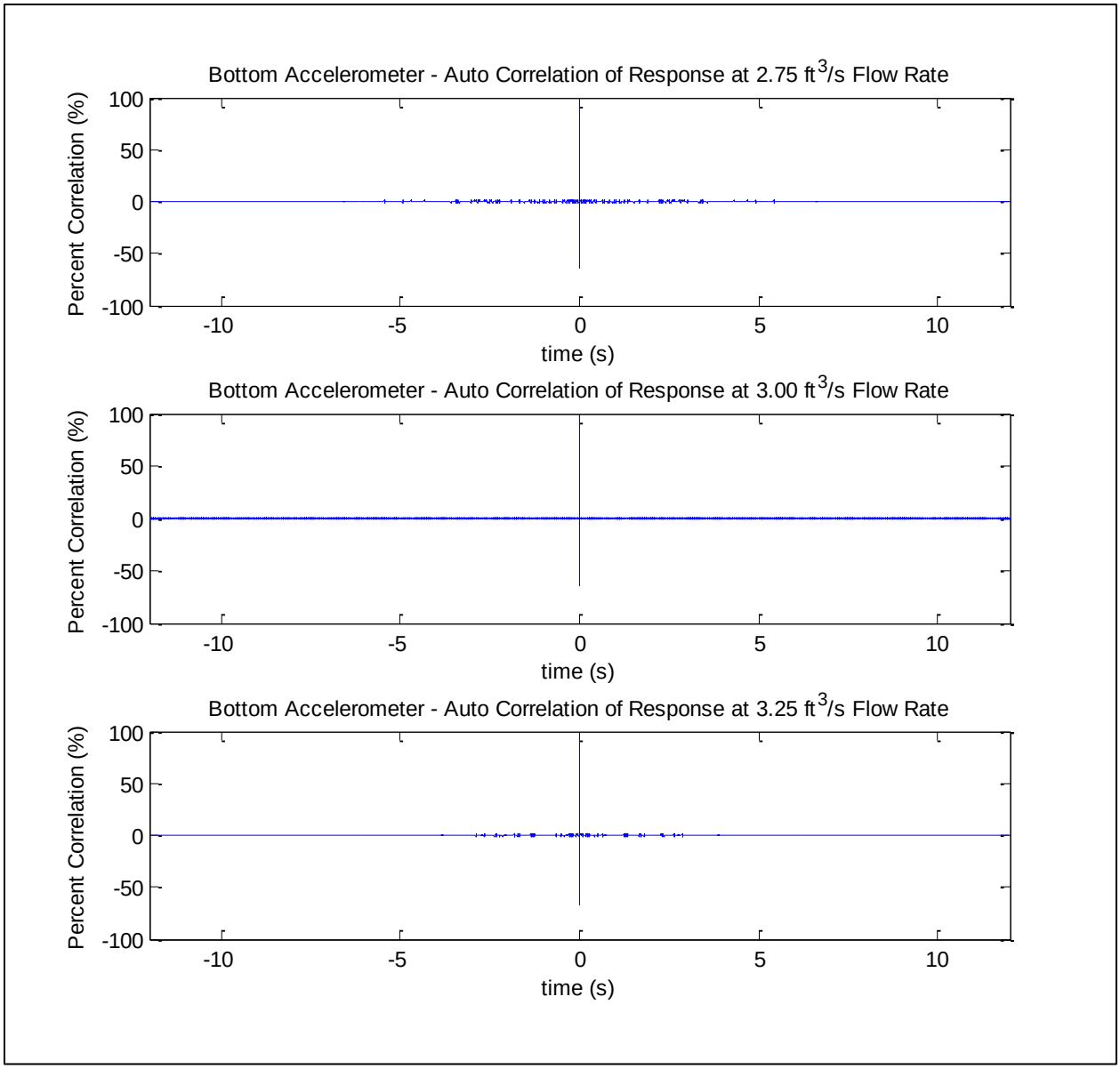

Figure M.5 Auto Correlation of Bottom Acceleration at Flow Rates 2.75-3.25 ft^3/s

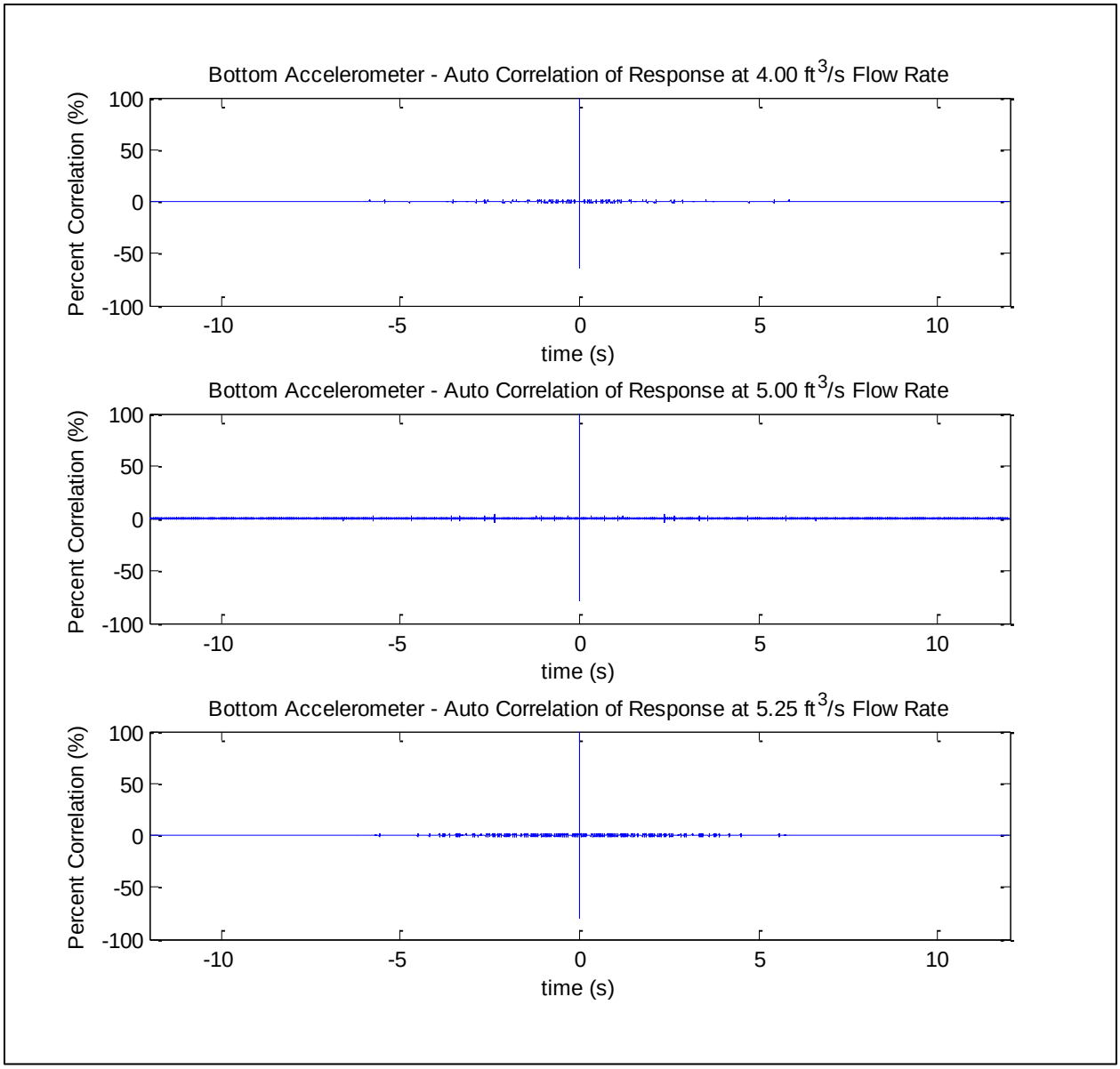

Figure M.6 Auto Correlation of Bottom Acceleration at Flow Rates 4.00, 5.00, 5.25 ft^3/s

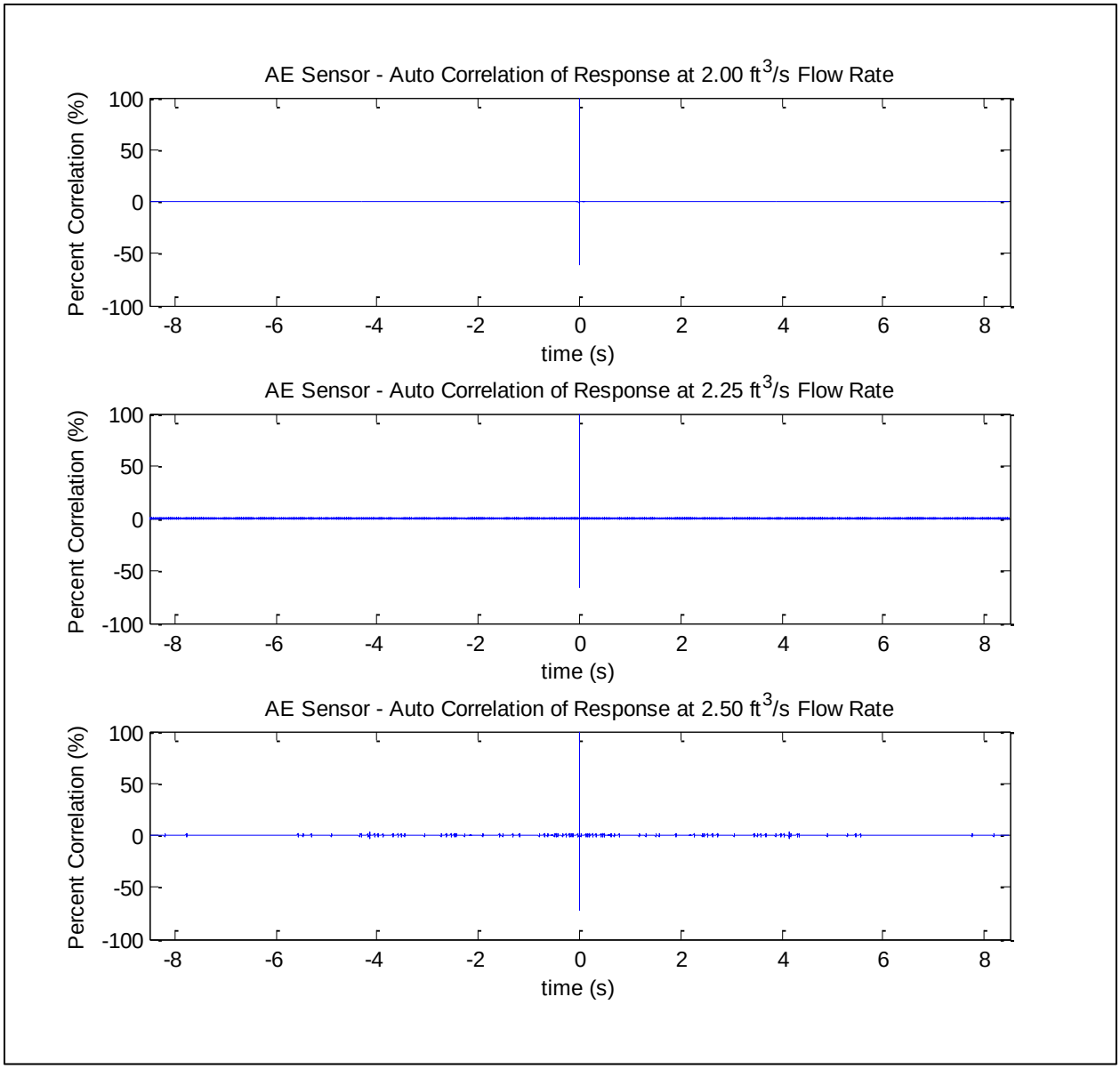

Figure M.7 Auto Correlation of Acoustic Emission at Flow Rates 2.00-2.50 ft^3/s

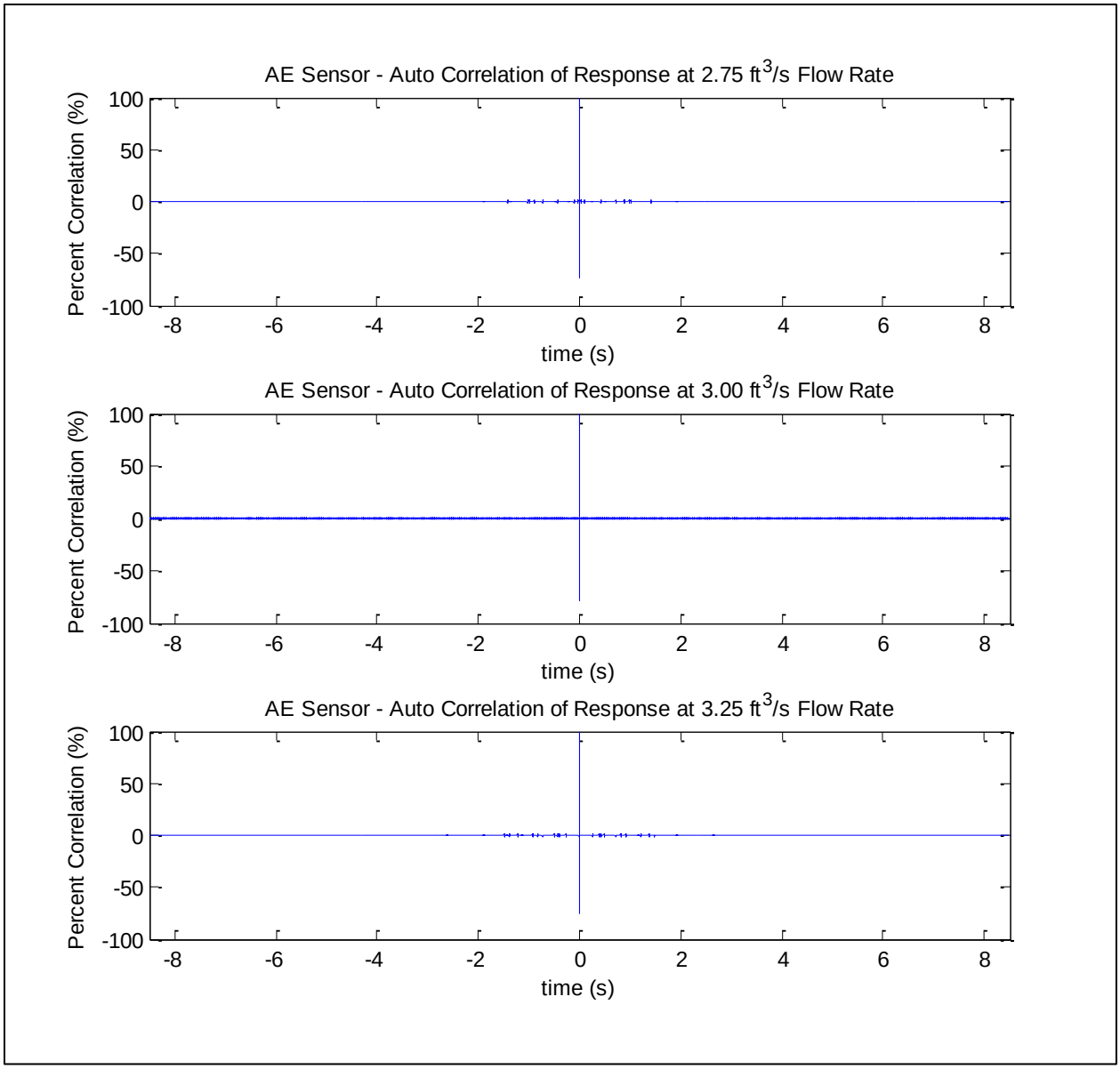

Figure M.8 Auto Correlation of Acoustic Emission at Flow Rates 2.75-3.25 ft^3/s

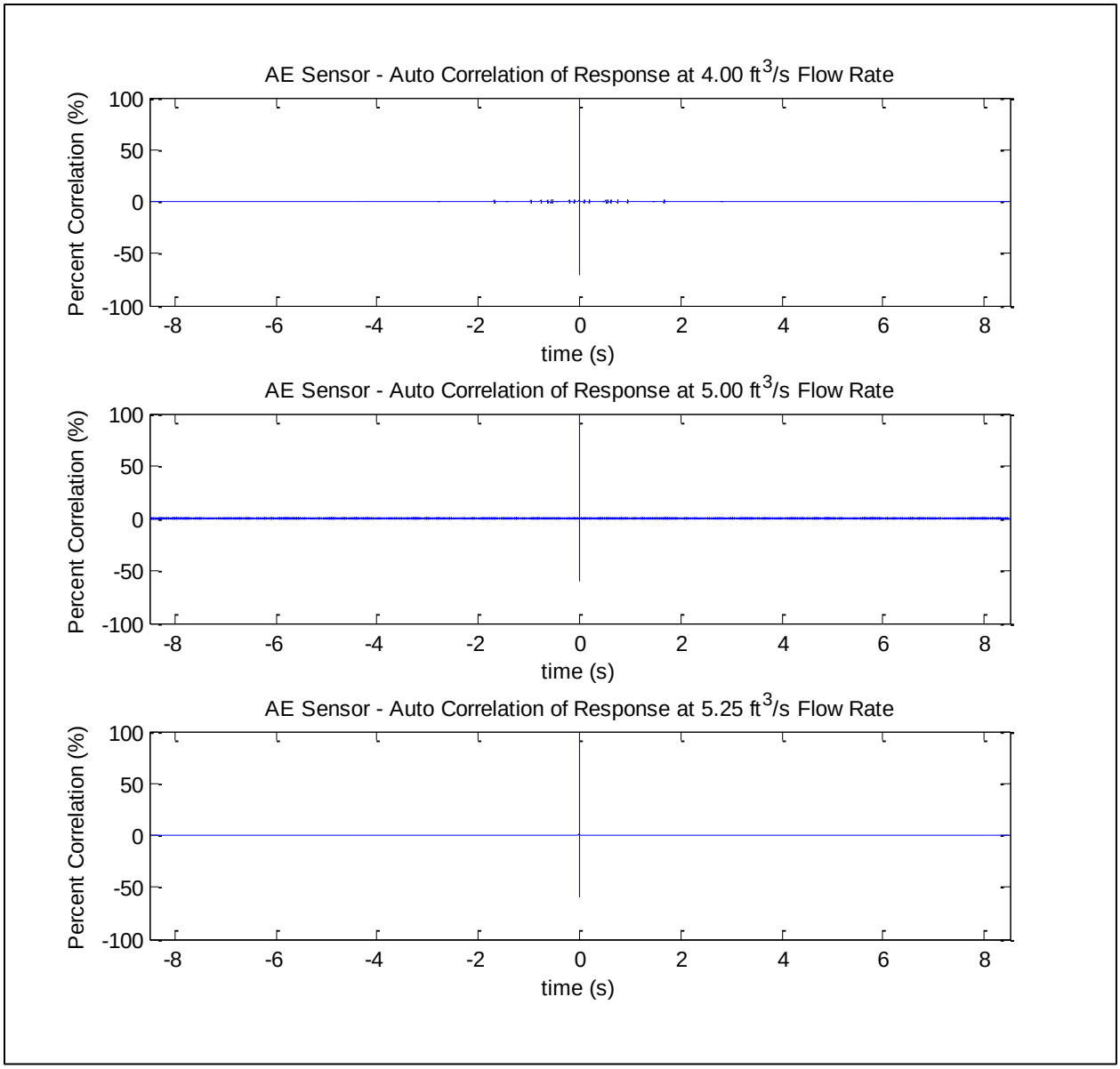

Figure M.9 Auto Correlation of Acoustic Emission at Flow Rates 4.00, 5.00, 5.25 ft^3/s

APPENDIX N

SUPPLEMENTAL FREQUENCY SPECTRUM PLOTS

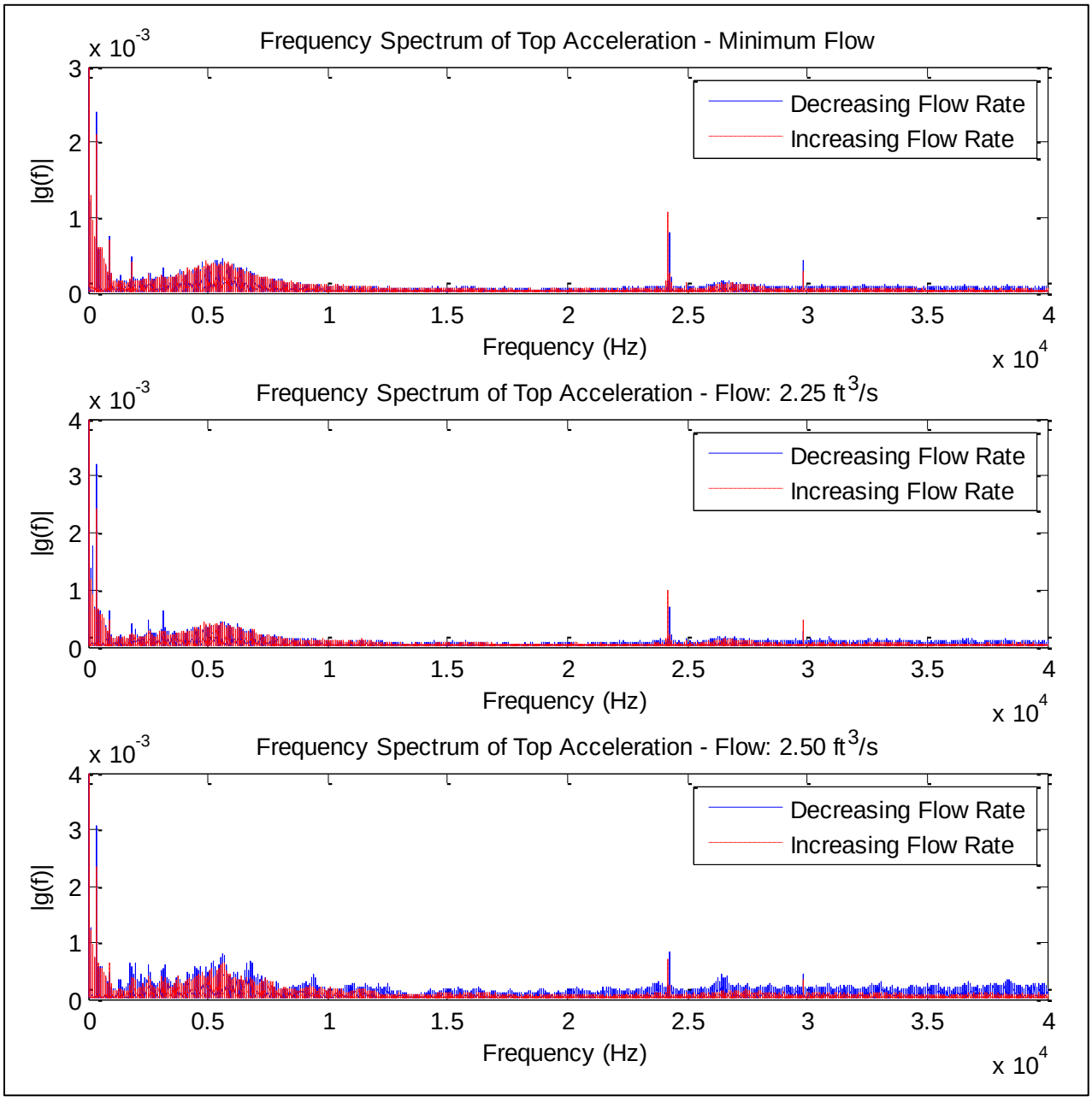

Figure N.1 Frequency Spectrum of Top Acceleration – Flow Range 2.00 – 2.50 ft^3/s

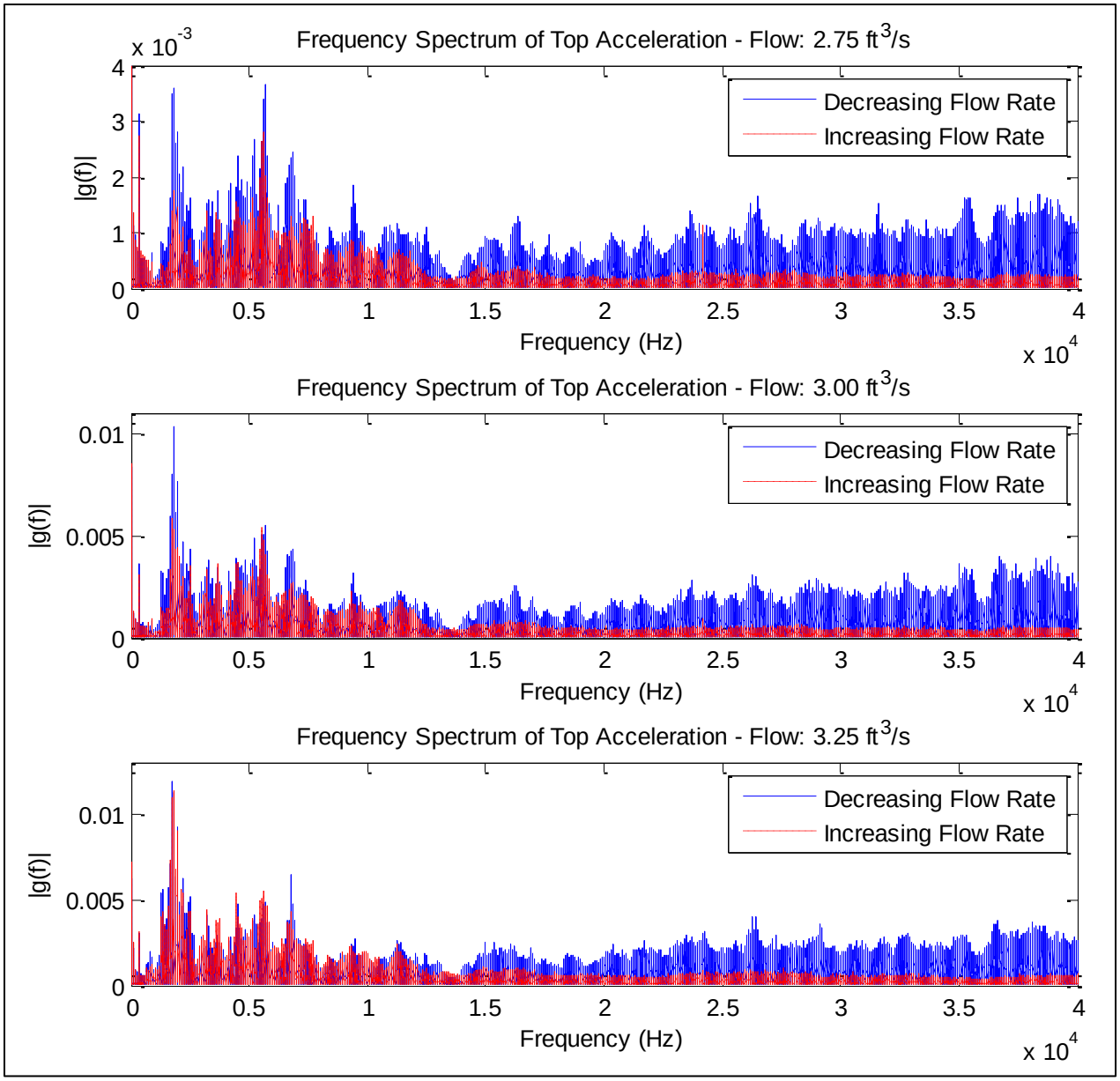

Figure N.2 Frequency Spectrum of Top Acceleration – Flow Range 2.75 – 3.25 ft^3/s

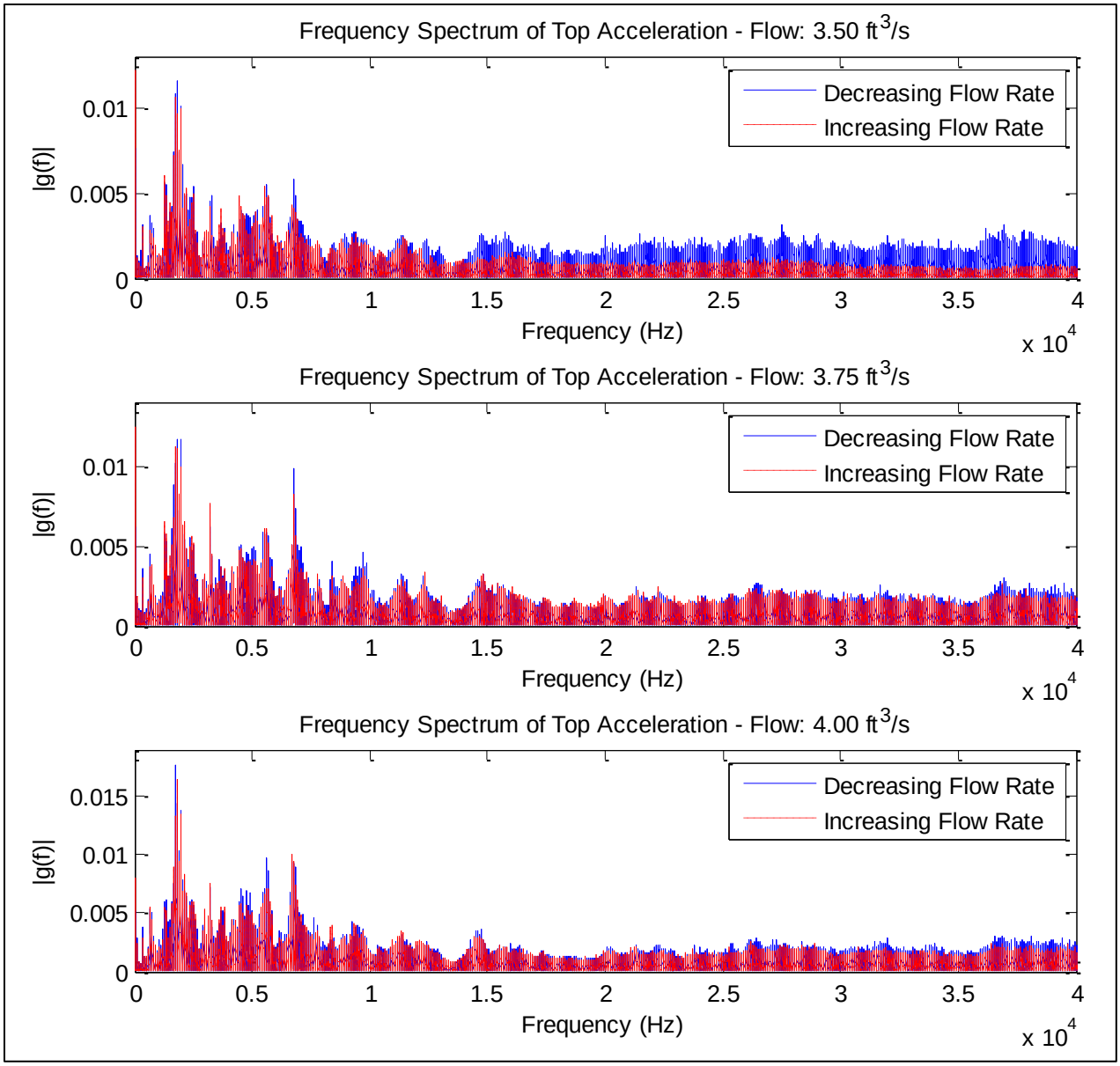

Figure N.3 Frequency Spectrum of Top Acceleration – Flow Range 3.50 – 4.00 ft^3/s

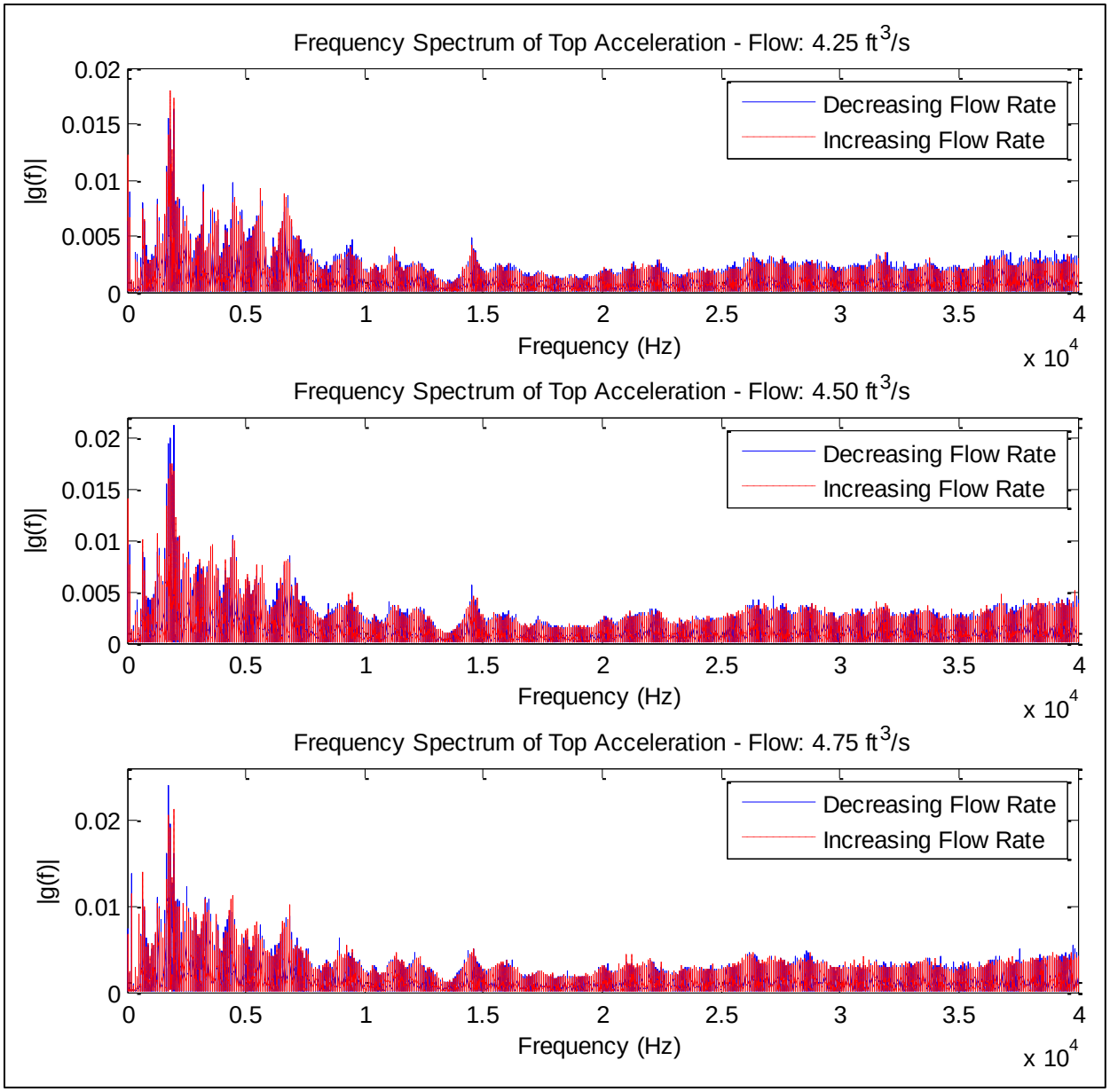

Figure N.4 Frequency Spectrum of Top Acceleration – Flow Range 4.25 – 4.75 ft^3/s

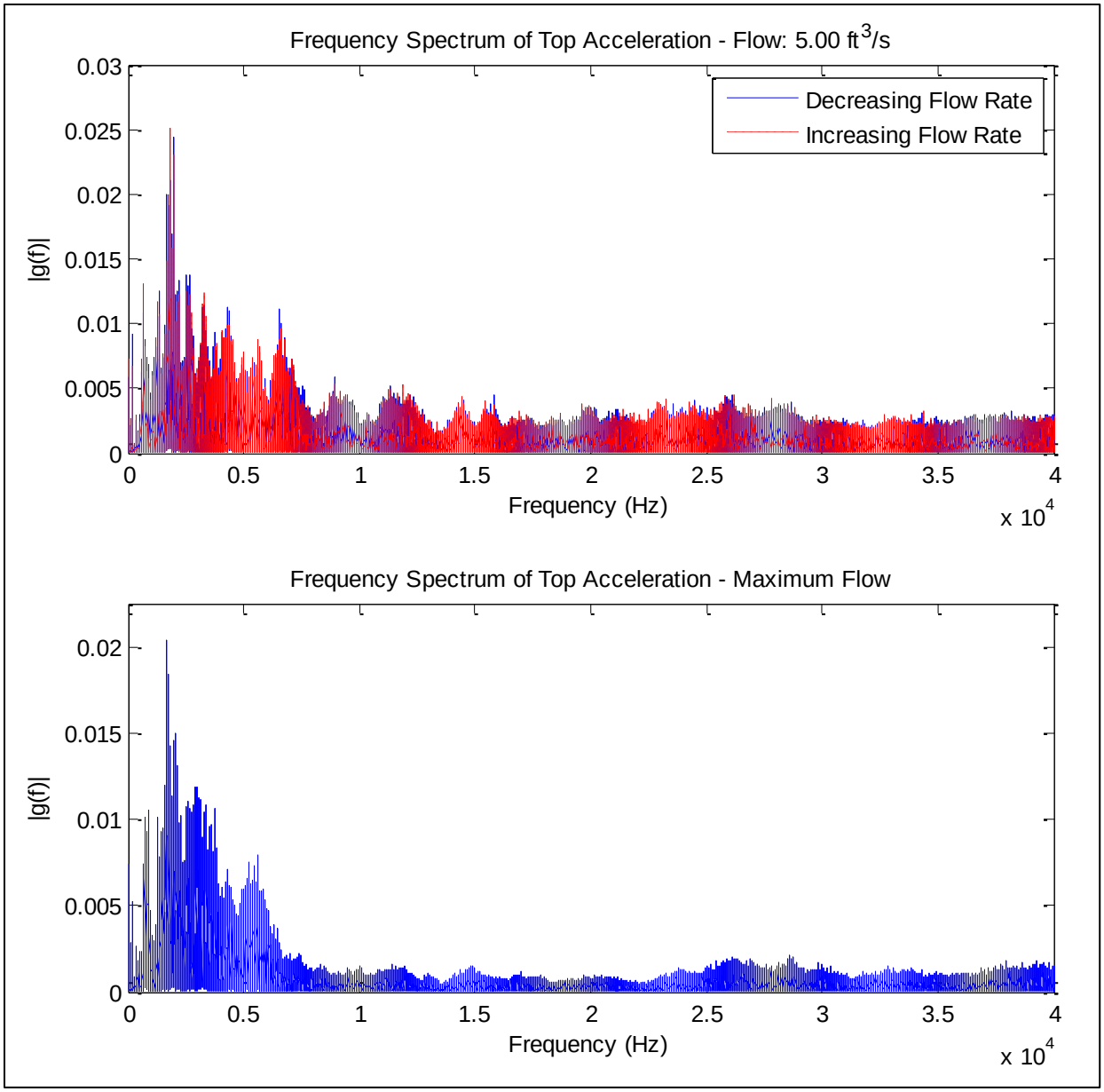

Figure N.5 Frequency Spectrum of Top Acceleration – Flow Range 5.00 – 5.25 ft^3/s

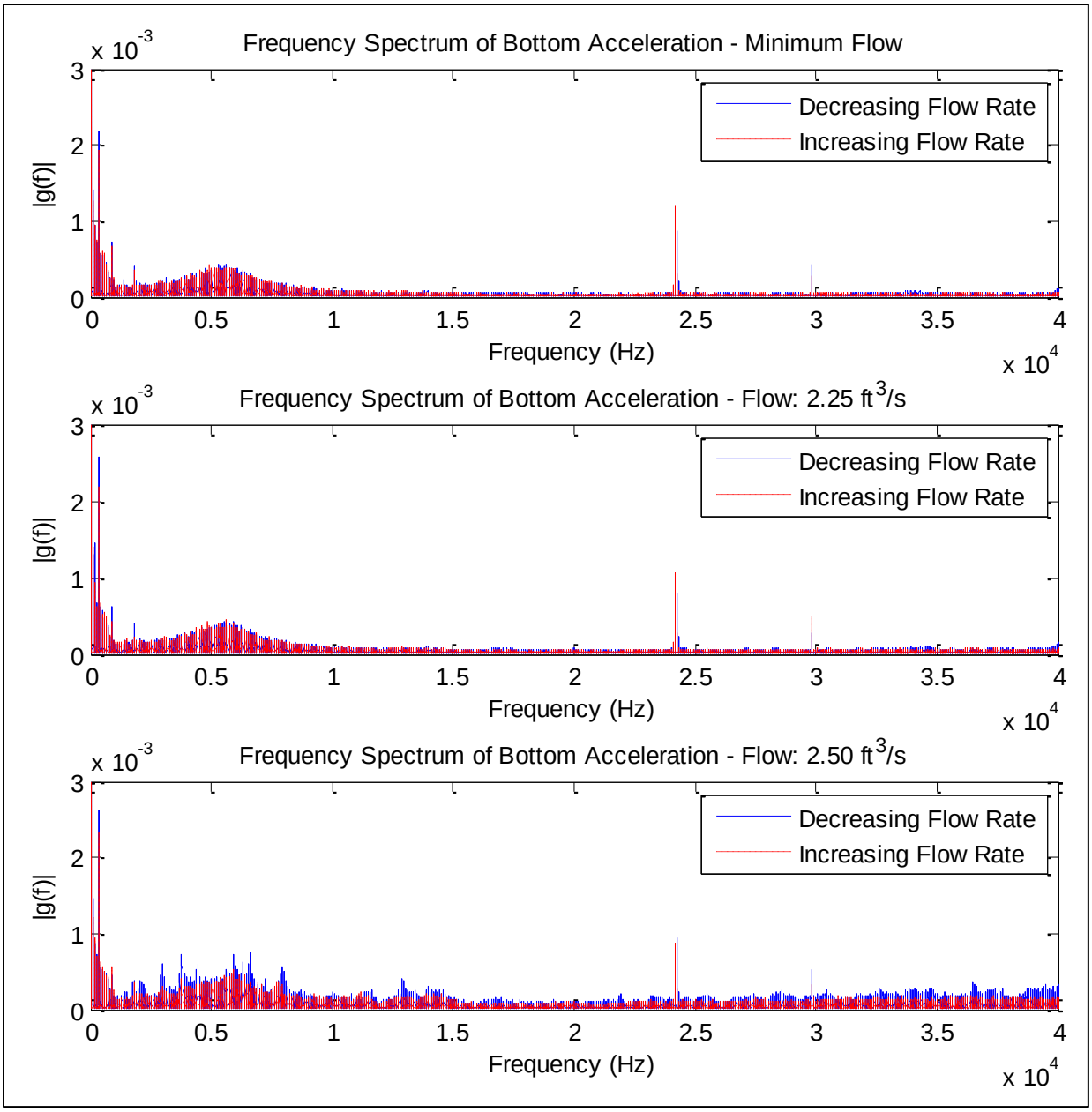

Figure N.6 Frequency Spectrum of Bottom Acceleration – Flow Range 2.00 – 2.50 ft^3/s

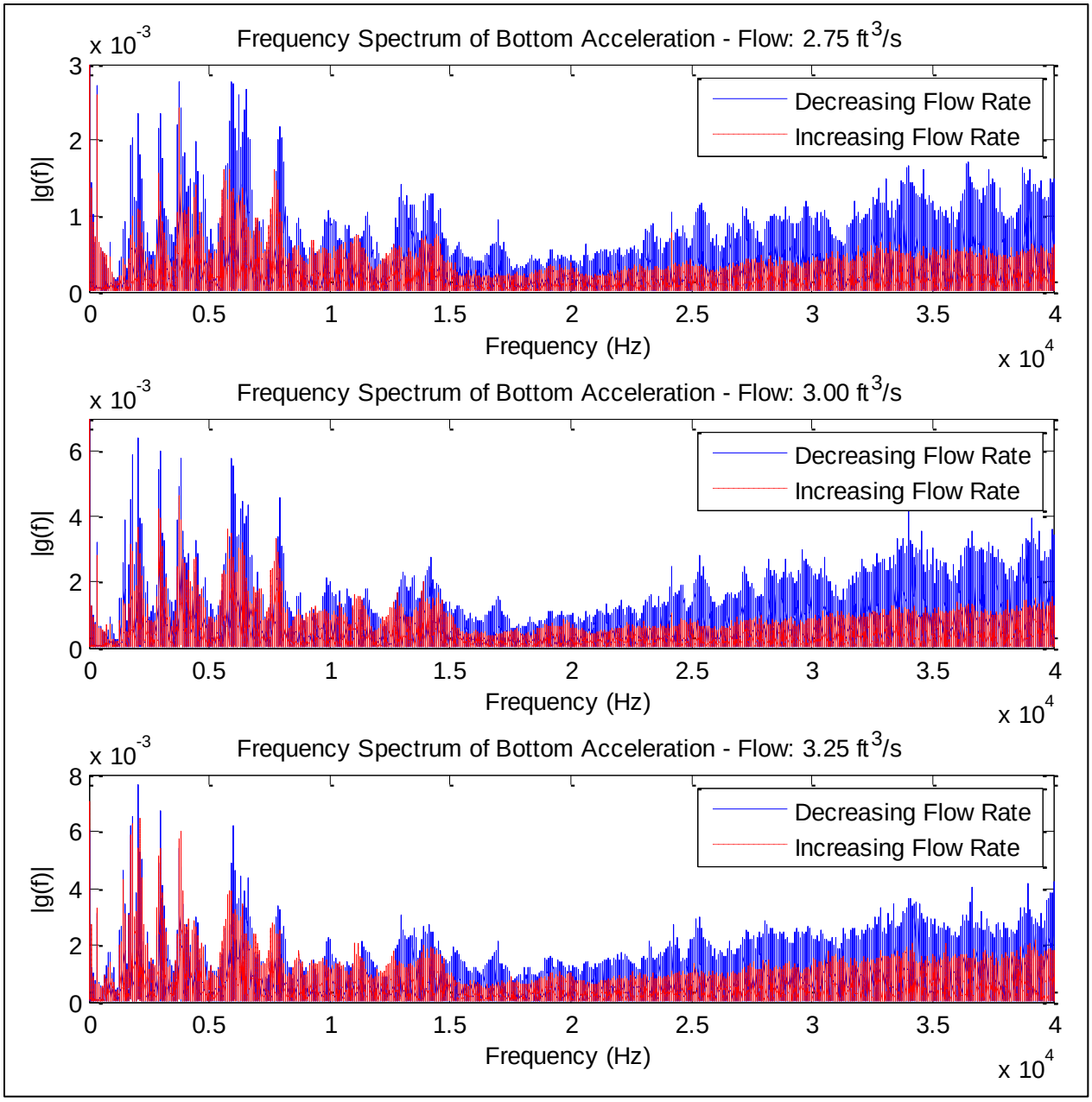

Figure N.7 Frequency Spectrum of Bottom Acceleration – Flow Range 2.75 – 3.25 ft^3/s

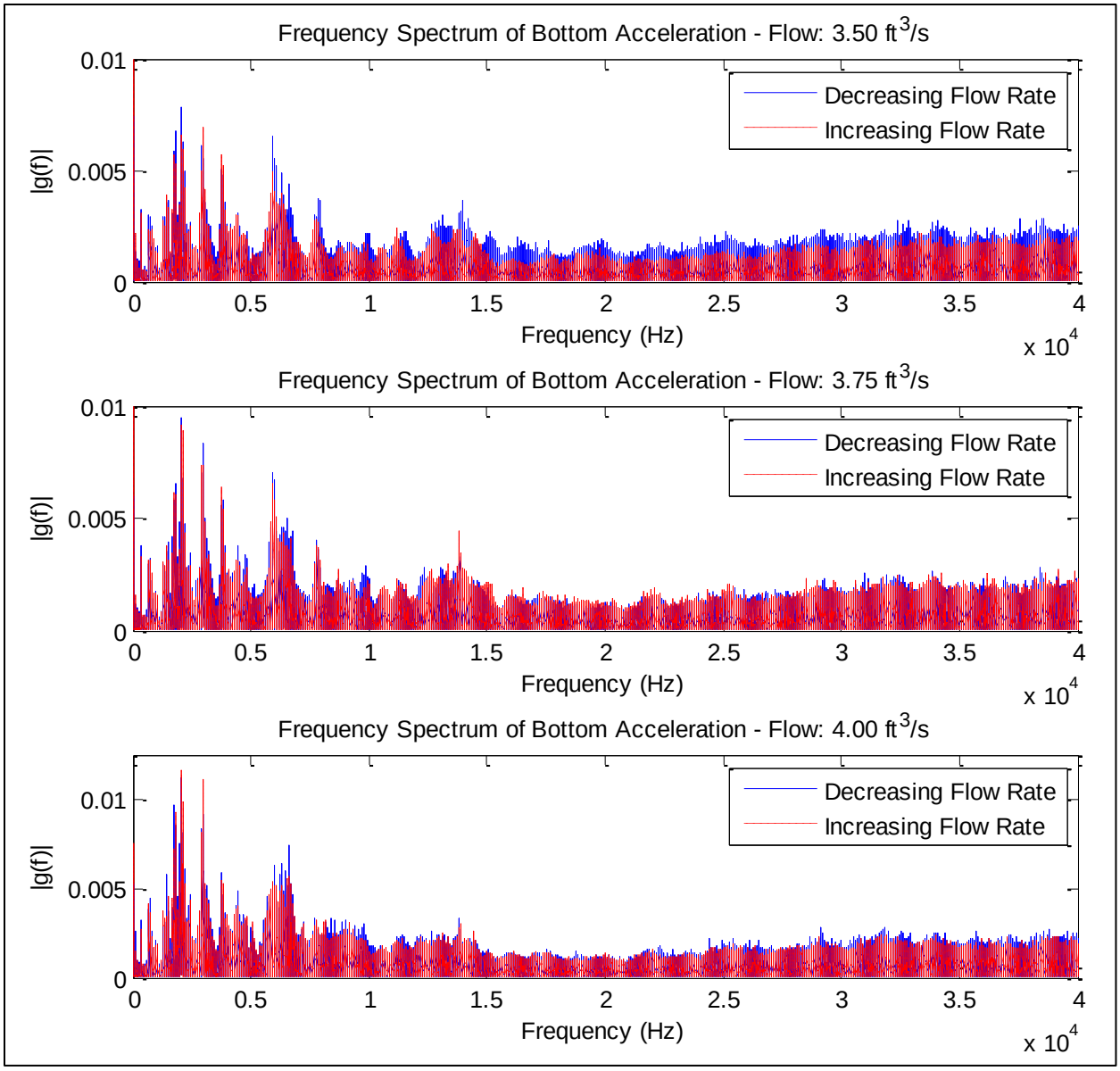

Figure N.8 Frequency Spectrum of Bottom Acceleration – Flow Range 3.50 – 4.00 ft^3/s

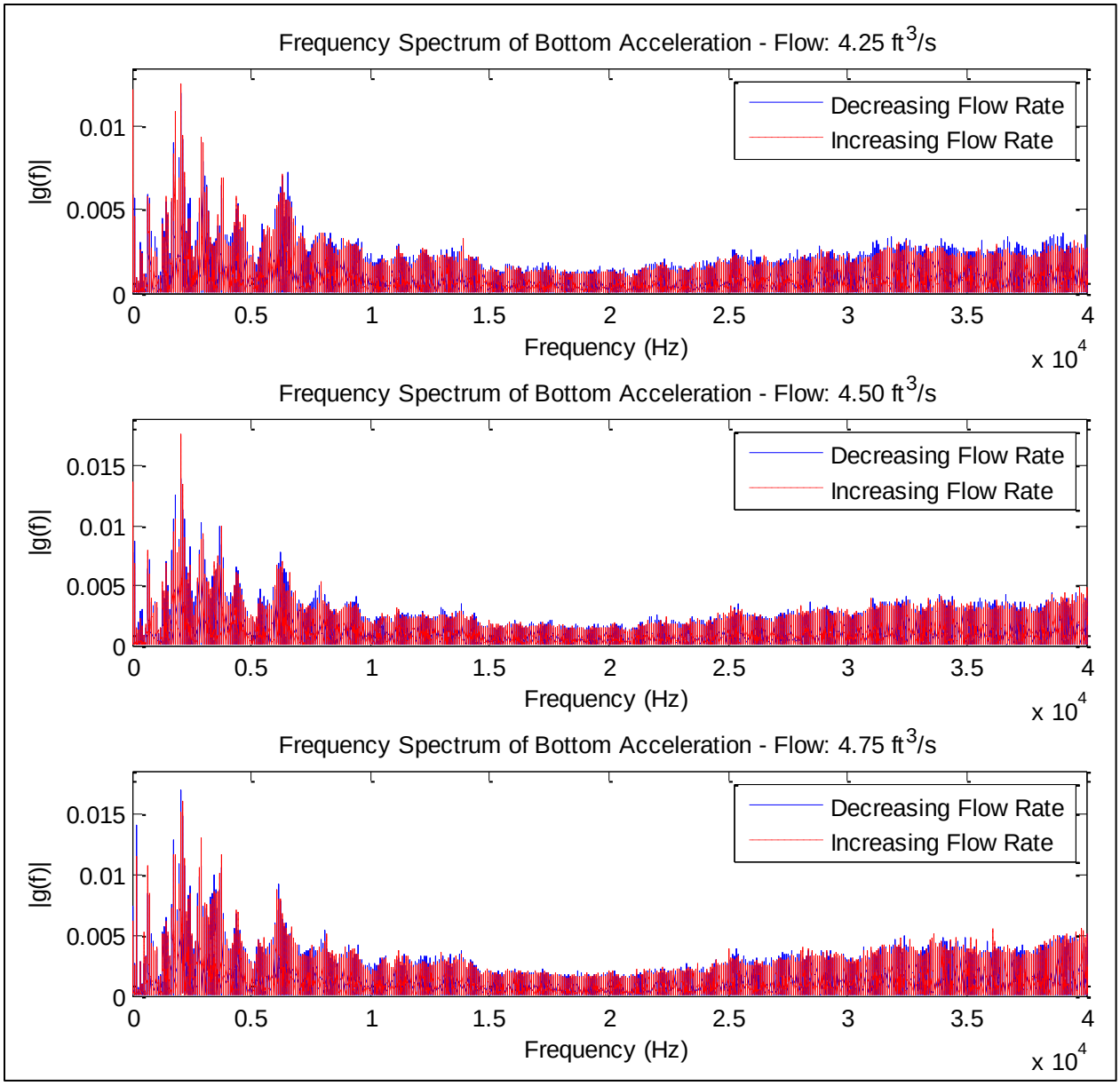

Figure N.9 Frequency Spectrum of Bottom Acceleration – Flow Range 4.25 – 4.75 ft^3/s

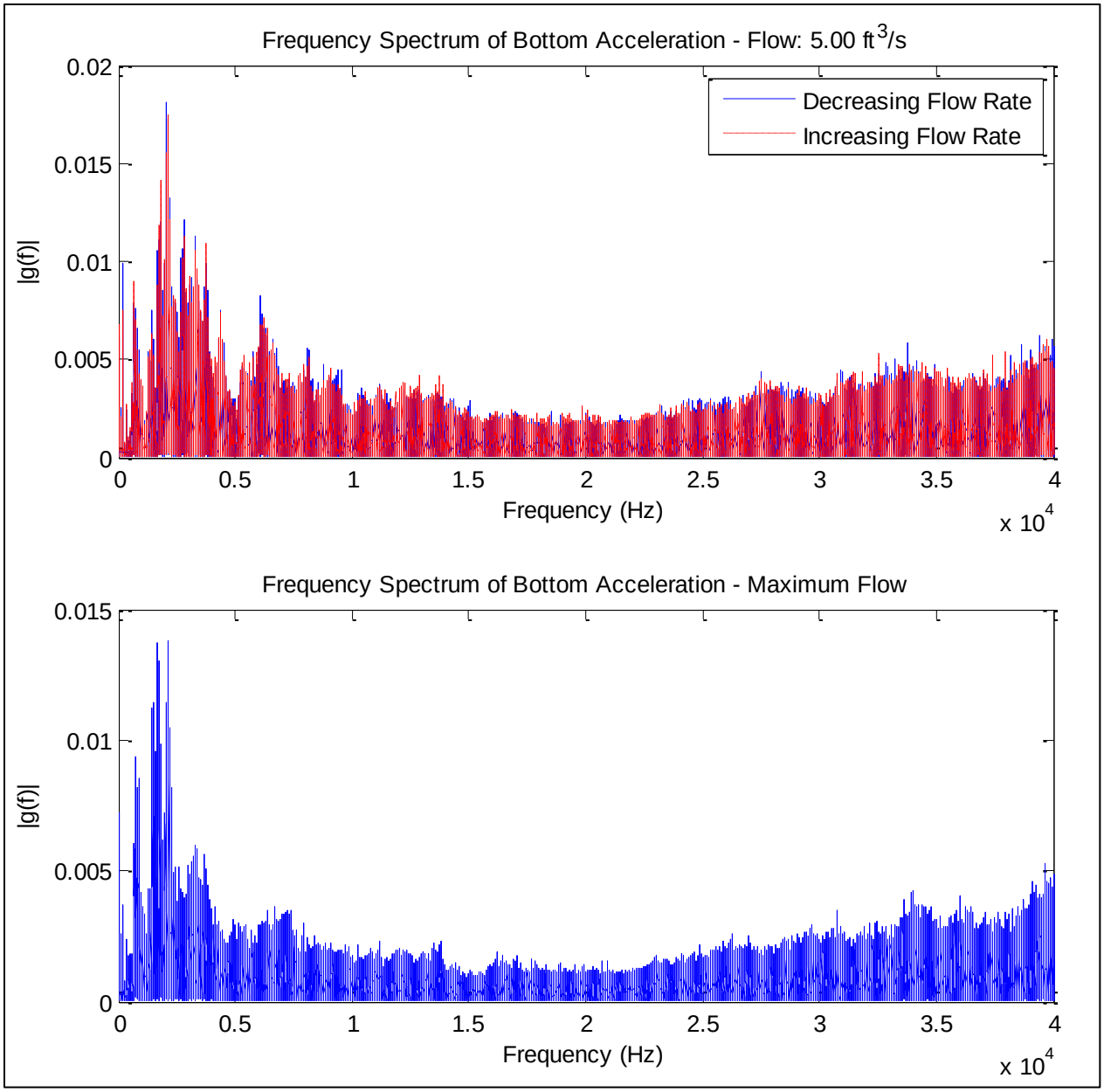

Figure N.10 Frequency Spectrum of Bottom Acceleration – Flow Range 5.00 – 5.25 ft^3/s

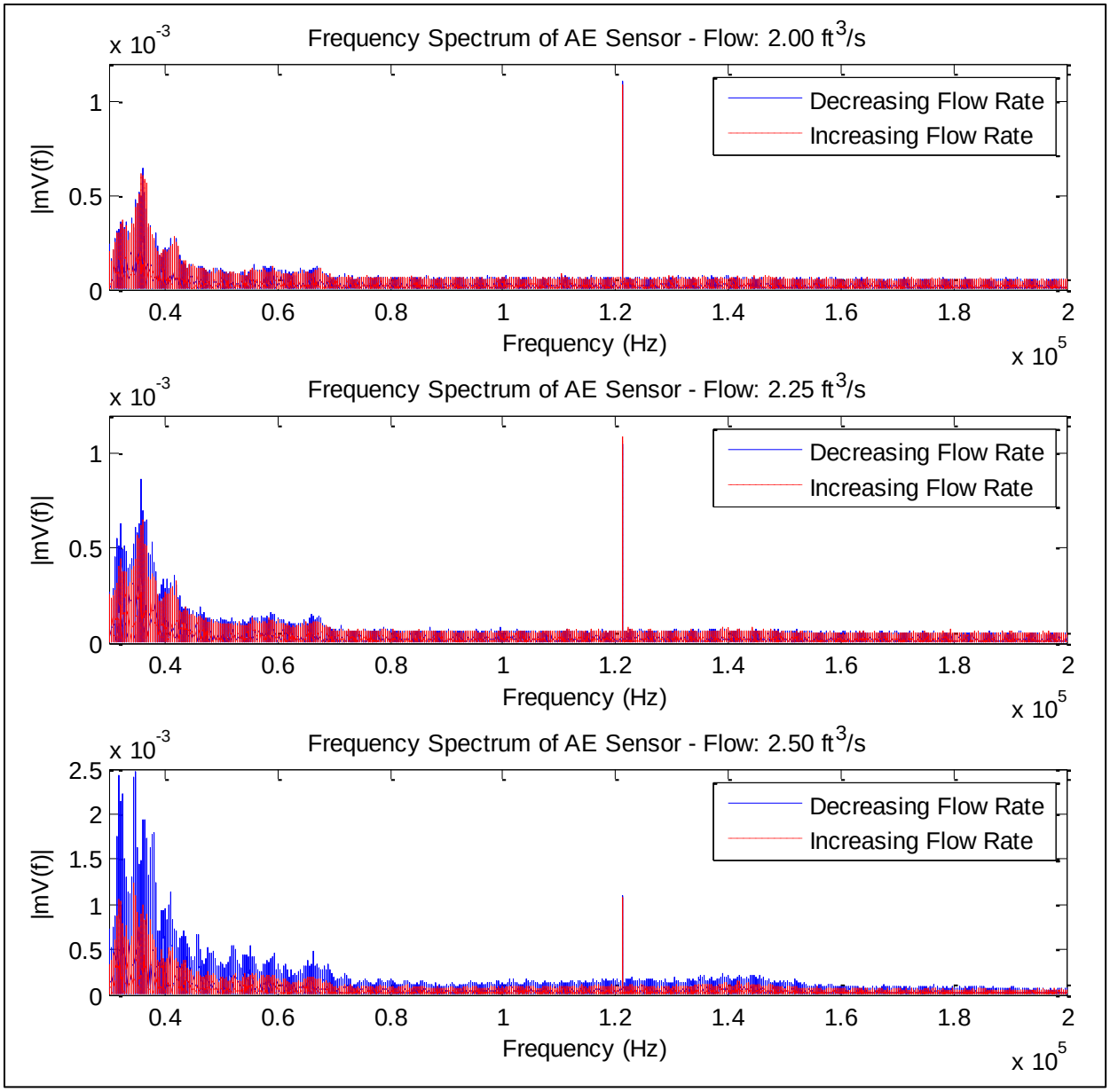

Figure N.11 Frequency Spectrum of Acoustic Emission – Flow Rates 2.00 – 2.50 ft^3/s

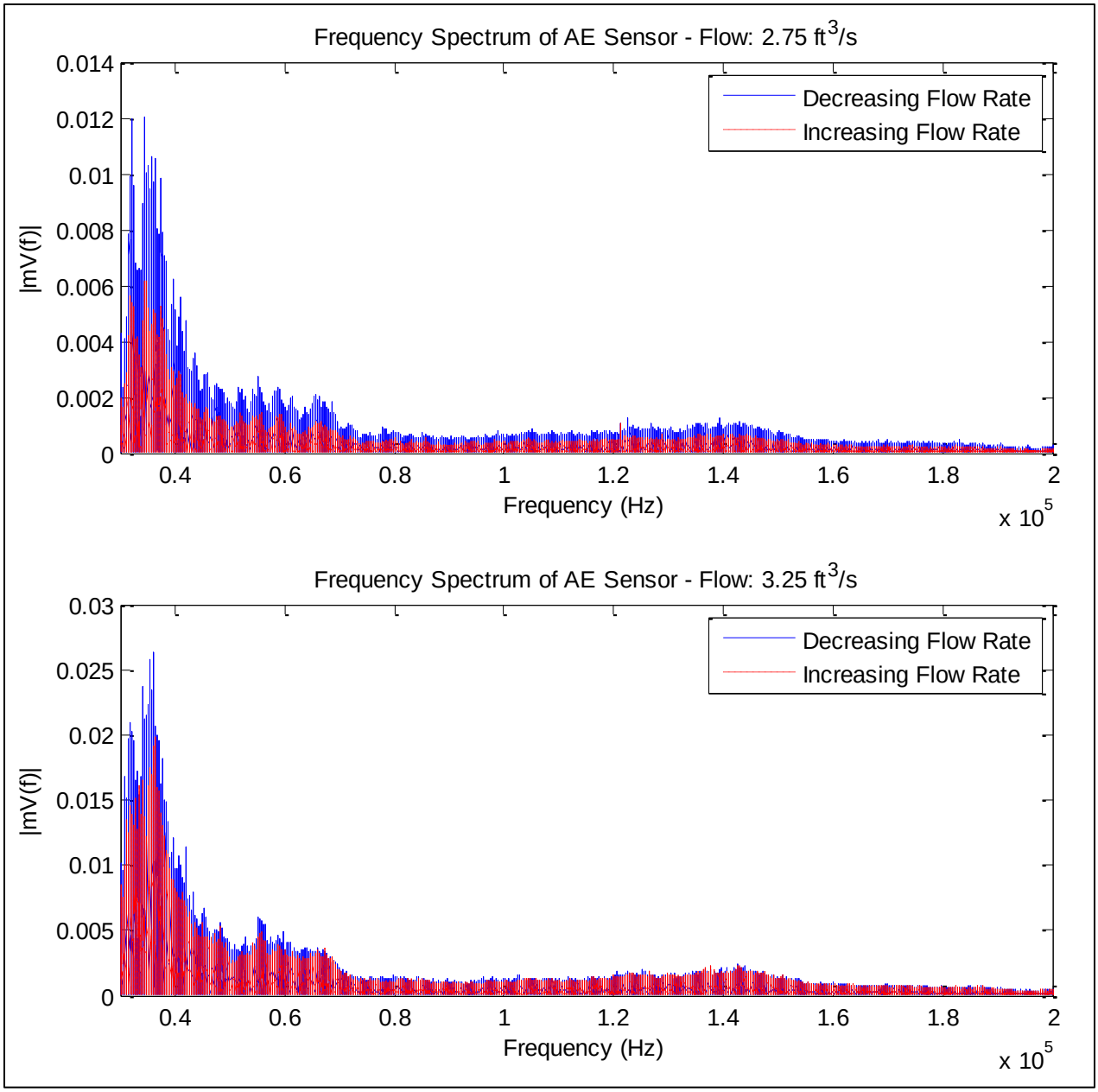

Figure N.12 Frequency Spectrum of Acoustic Emission – Flow Rates 2.75 – 3.25 ft^3/s

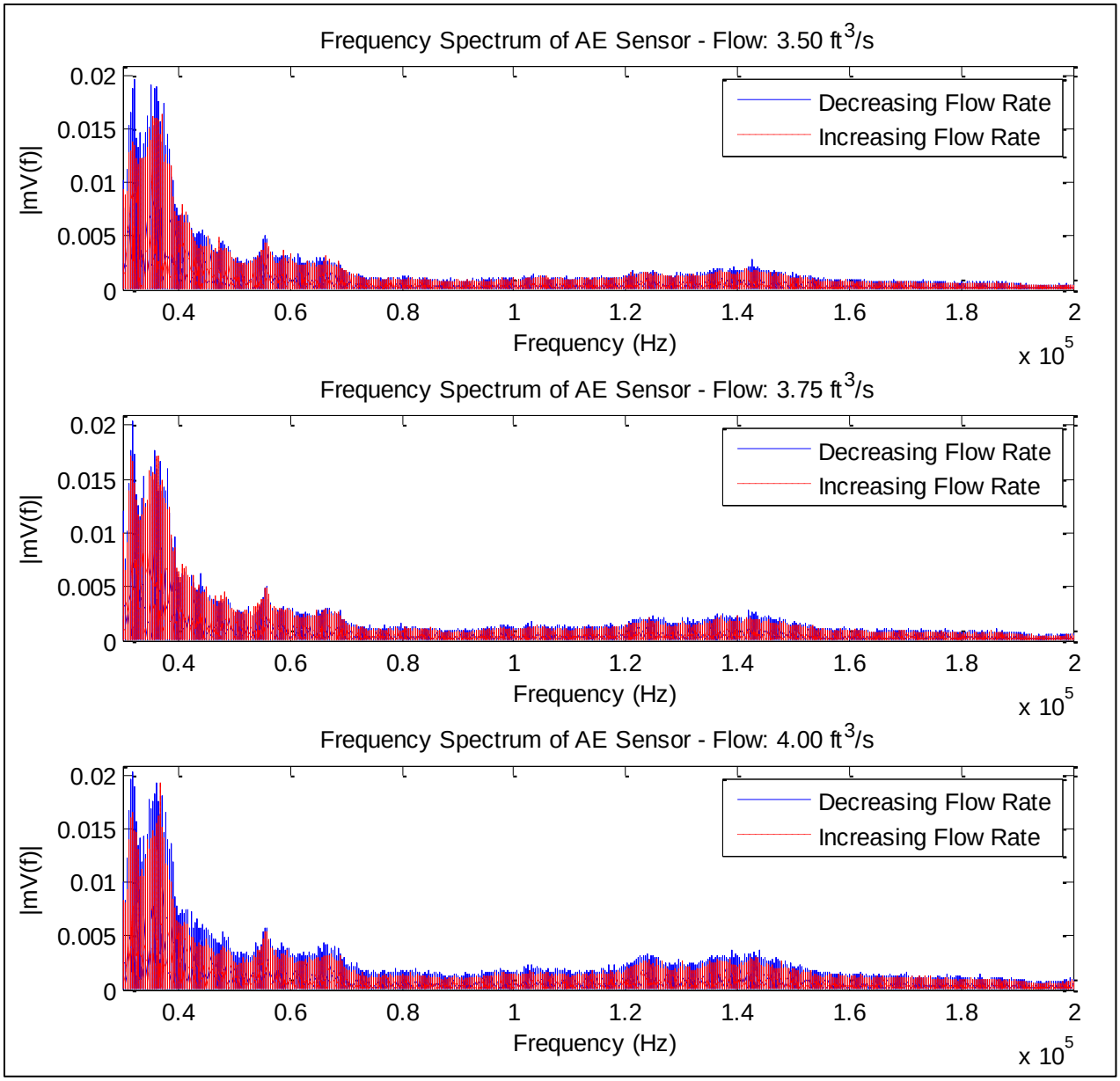

Figure N.13 Frequency Spectrum of Acoustic Emission – Flow Rates 3.50 – 4.00 ft^3/s

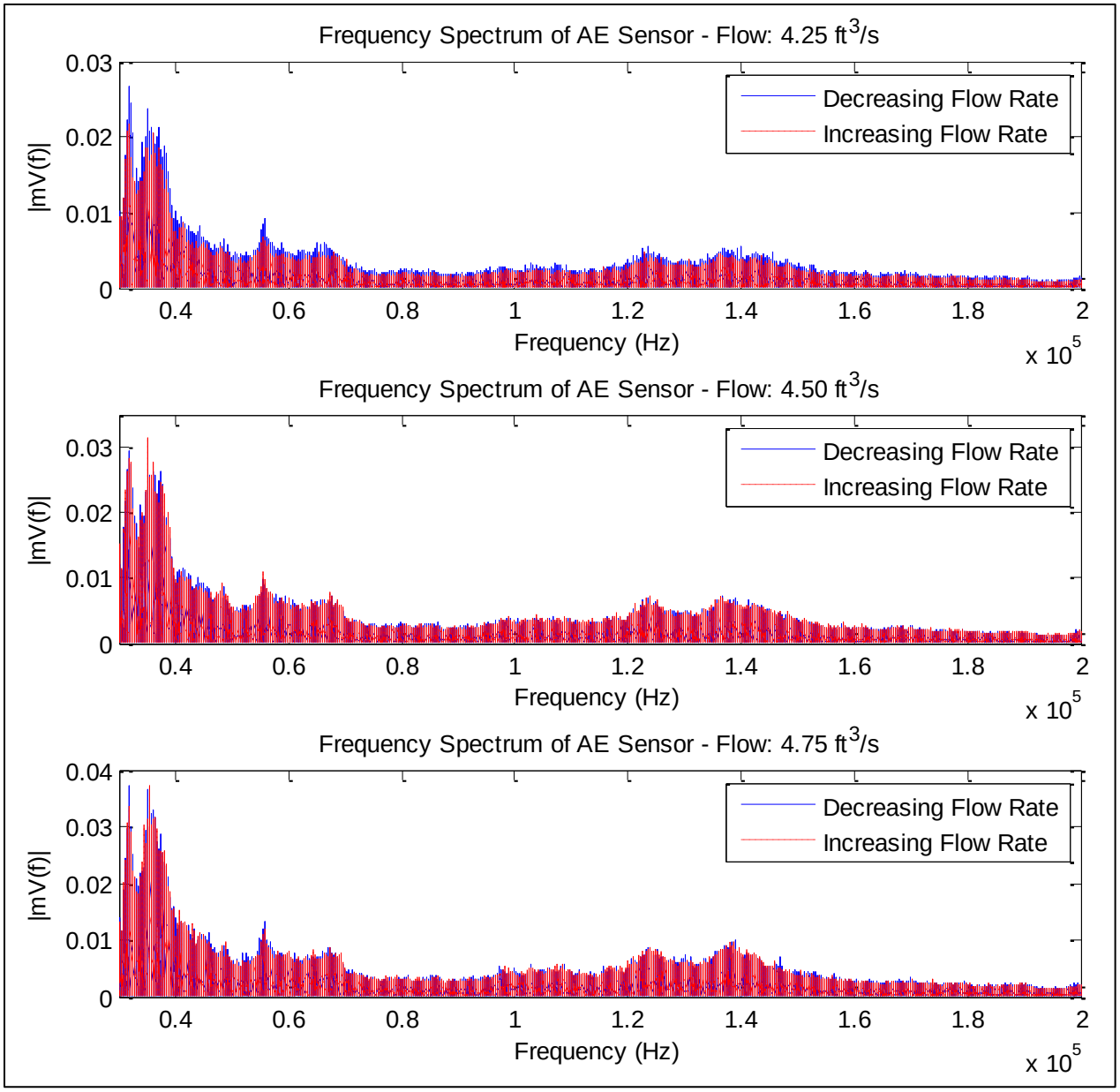

Figure N.14 Frequency Spectrum of Acoustic Emission – Flow Rates 4.00 – 4.75 ft^3/s

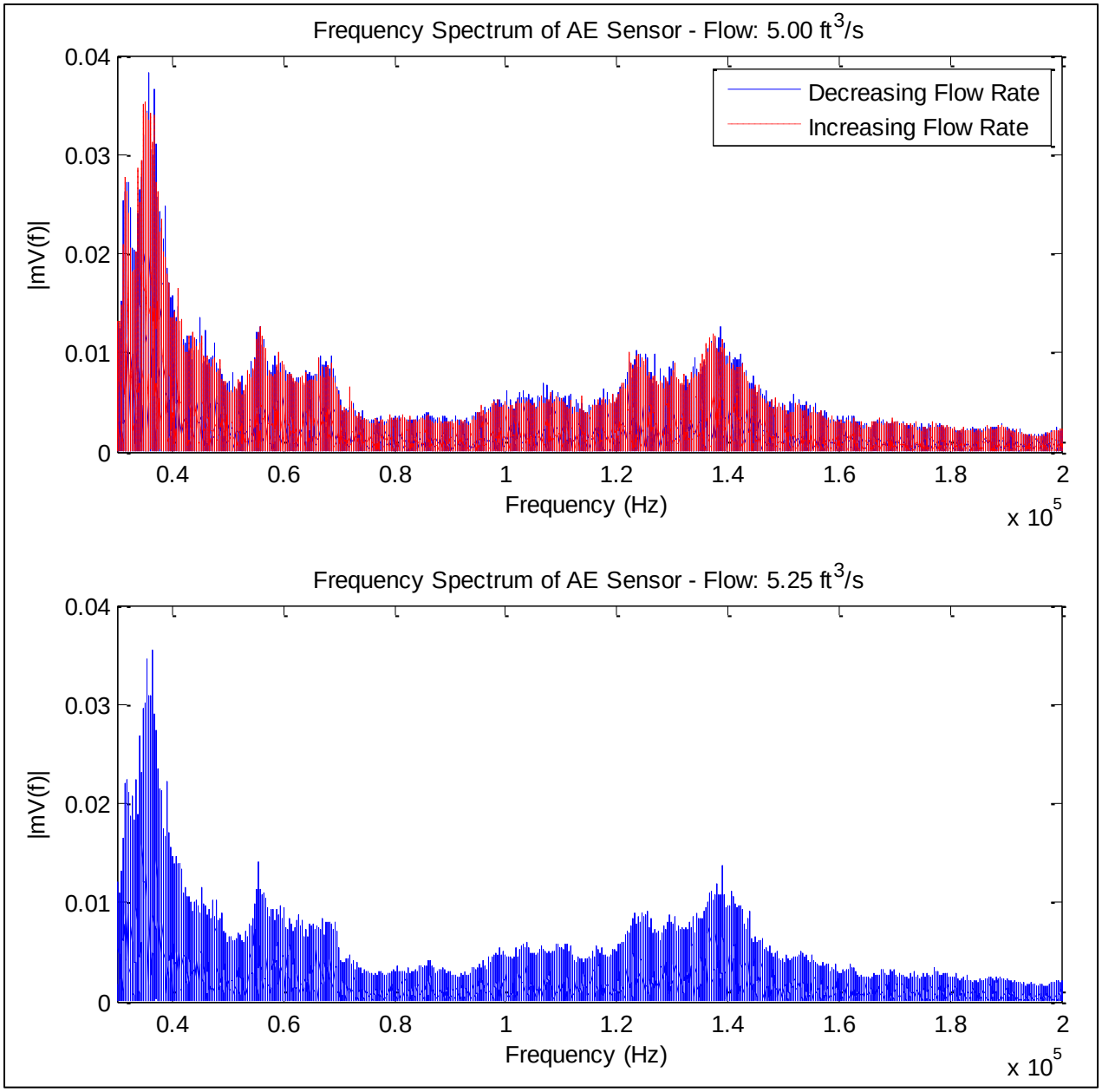

Figure N.15 Frequency Spectrum of Acoustic Emission – Flow Rates 5.00 – 5.25 ft^3/s

APPENDIX O

NORMALIZED FREQUENCY SPECTRUM BACKGROUND

The reference frequency spectrum, used to normalize all the frequency spectrums, was obtained by averaging together all frequency spectrums of flows below and equal to 2.25 ft^3/s. Figure O.1 provides a visual of the averaging using the bottom accelerometer as an example.

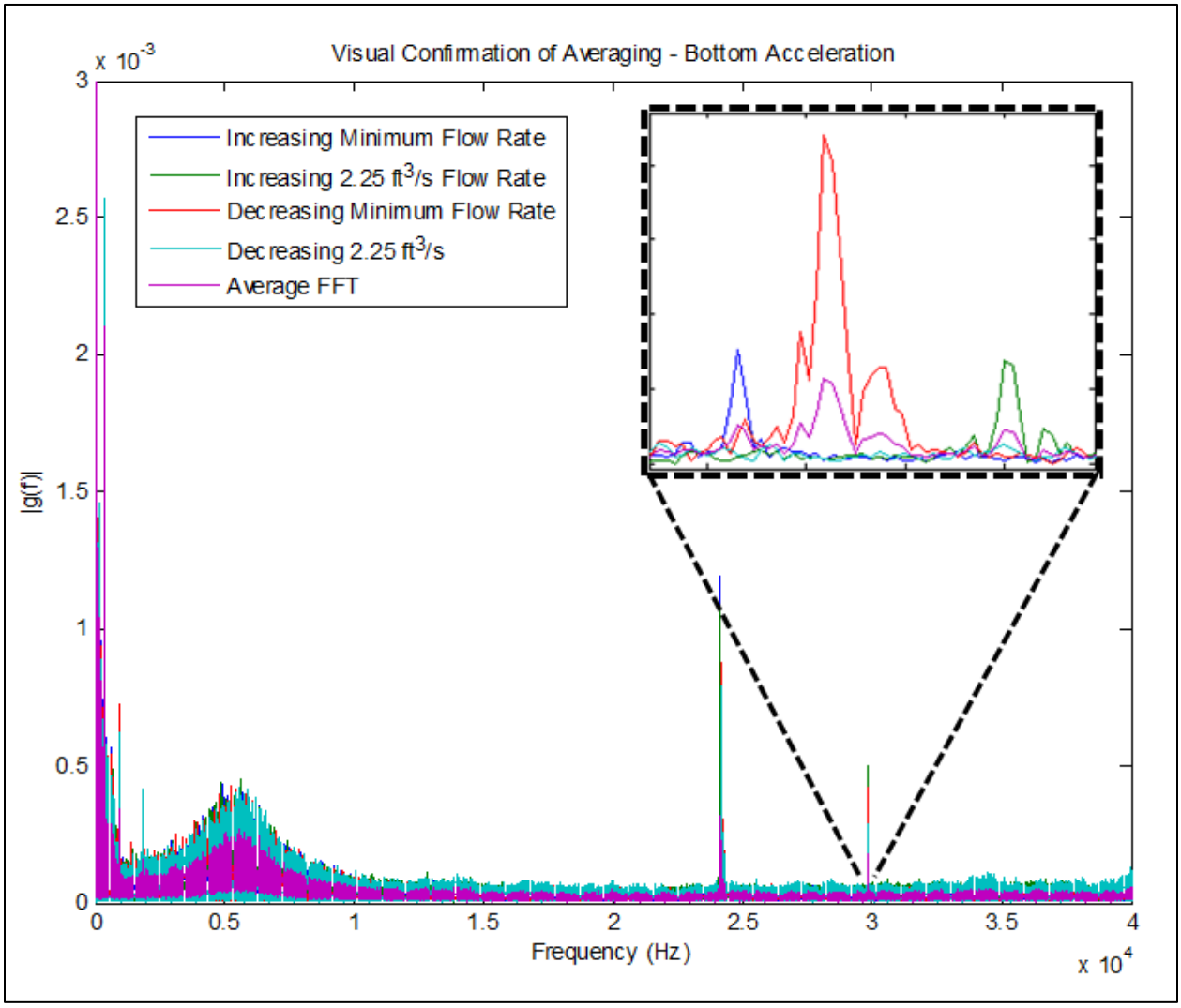

Figure O.1 Visual of Creating Reference FFT to be used to Normalize all FFTs

The supporting MATLAB© Code used to create the reference FFTs follows:

```
% Create Normalizing FFT for accels
clear, clc, close all

load Freq_Spectrum_Accels_205
B205 = freq_1;
T205 = freq_2;

load Freq_Spectrum_Accels_225
B225 = freq_1;
T225 = freq_2;

load Freq_Spectrum_Accels_down_170
B170d = freq_1;
T170d = freq_2;

load Freq_Spectrum_Accels_down_225
B225d = freq_1;
T225d = freq_2;

load Freq_Spectrum_Accels_XFREQ

B_FFT_norm = zeros(1,length(x_freq));
T_FFT_norm = zeros(1,length(x_freq));

for i = 1:1:length(x_freq)
    B_FFT_norm(i) = mean([B205(i),B225(i),B170d(i),B225d(i)]);
    T_FFT_norm(i) = mean([T205(i),T225(i),T170d(i),T225d(i)]);
end

% Check that the FFTs were averaged
 figure(1)
 plot(x_freq,B205,x_freq,B225,x_freq,B170d,x_freq,B225d,x_freq,B_FFT_norm)
 axis([0 40e3 0 3e-3]), title('Visual Confirmation of Averaging - Bottom
Acceleration')
 xlabel('Frequency (Hz)'), ylabel('|g(f)|')
 legend('Increasing Minimum Flow Rate', 'Increasing 2.25 ft^3/s Flow Rate',
'Decreasing Minimum Flow Rate', 'Decreasing 2.25 ft^3/s','Average FFT')
```

The same code was used for creating the reference FFT for the acoustic emission results.

APPENDIX P

SUPPLEMENTAL NORMAZLIED FREQUENCY SPECTRUM PLOTS

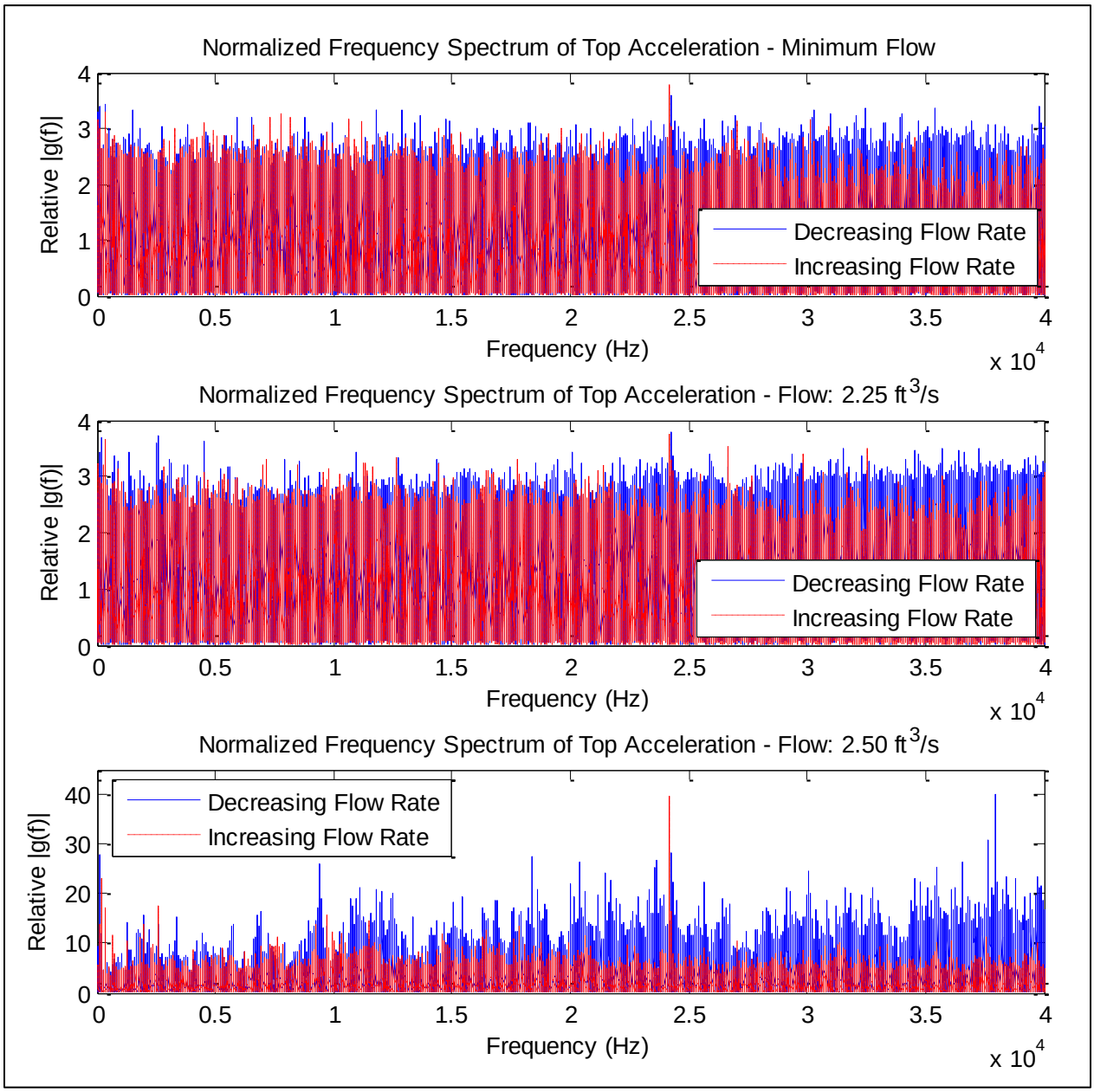

Figure P.1 Normalized Frequency Spectrum of Top Acceleration – Flow Rates 2.00 – 2.50 ft^3/s

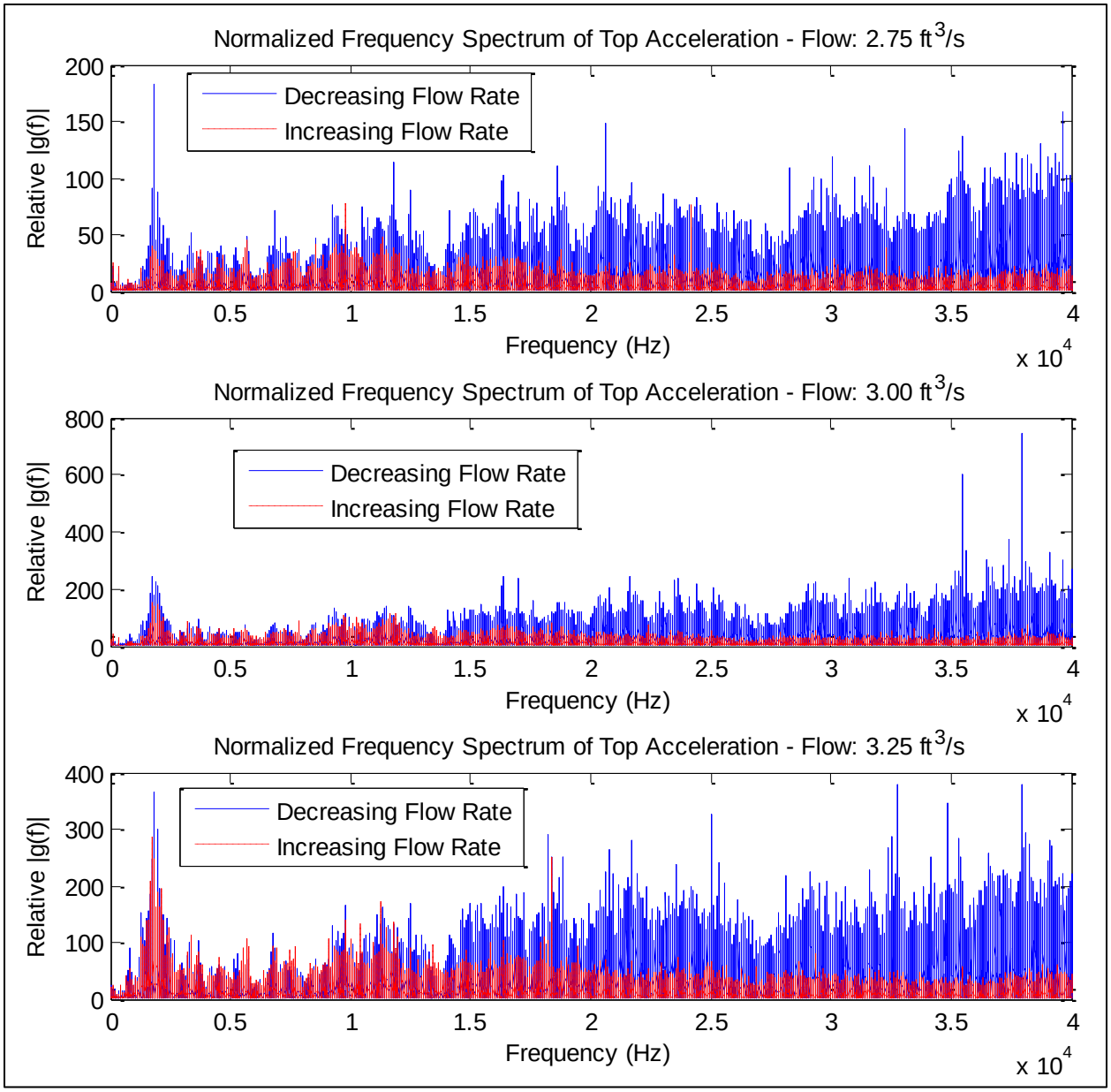

Figure P.2 Normalized Frequency Spectrum of Top Acceleration – Flow Rates 2.75 – 3.25 ft^3/s

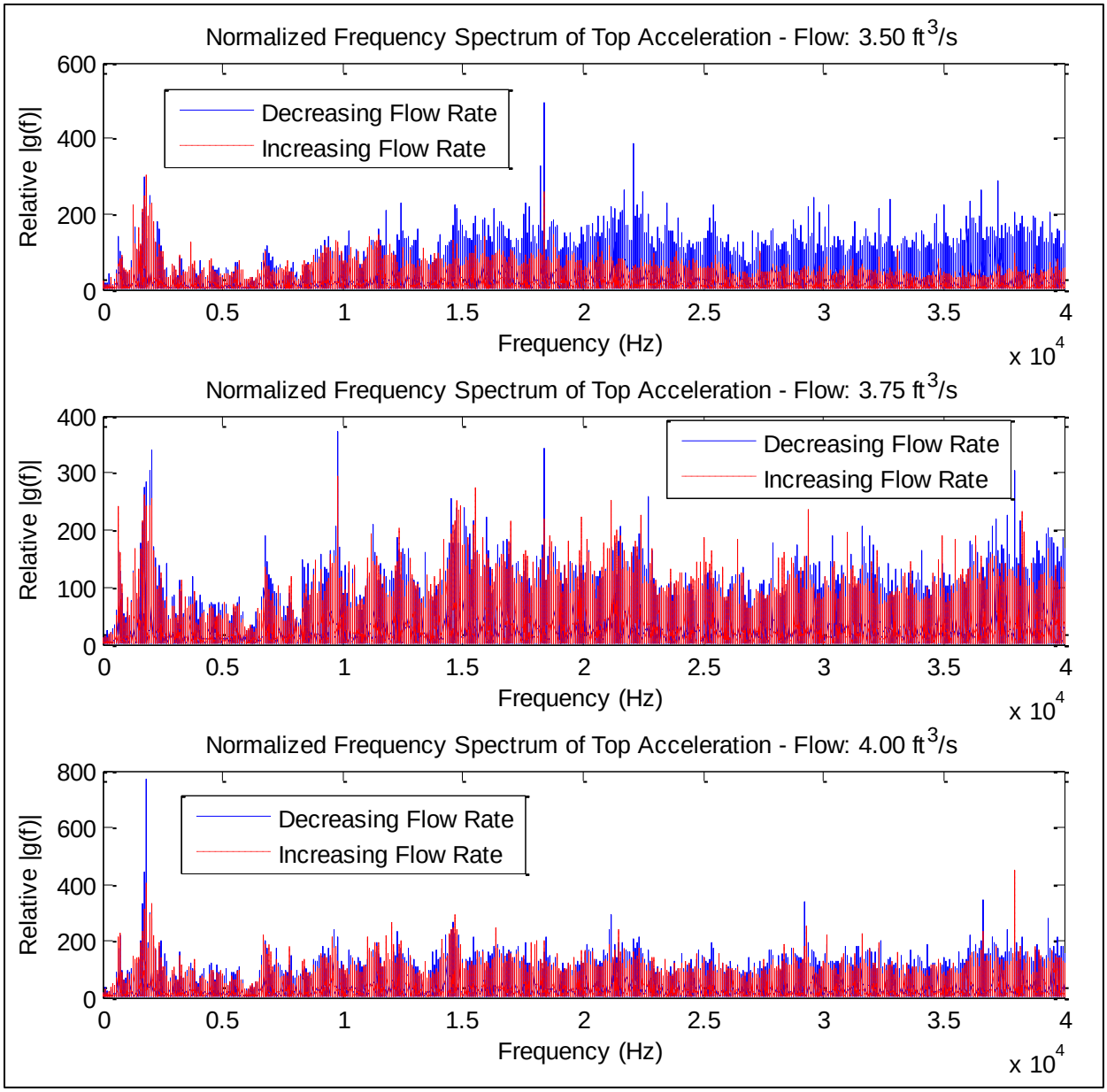

Figure P.3 Normalized Frequency Spectrum of Top Acceleration – Flow Rates 3.50 – 4.00 ft^3/s

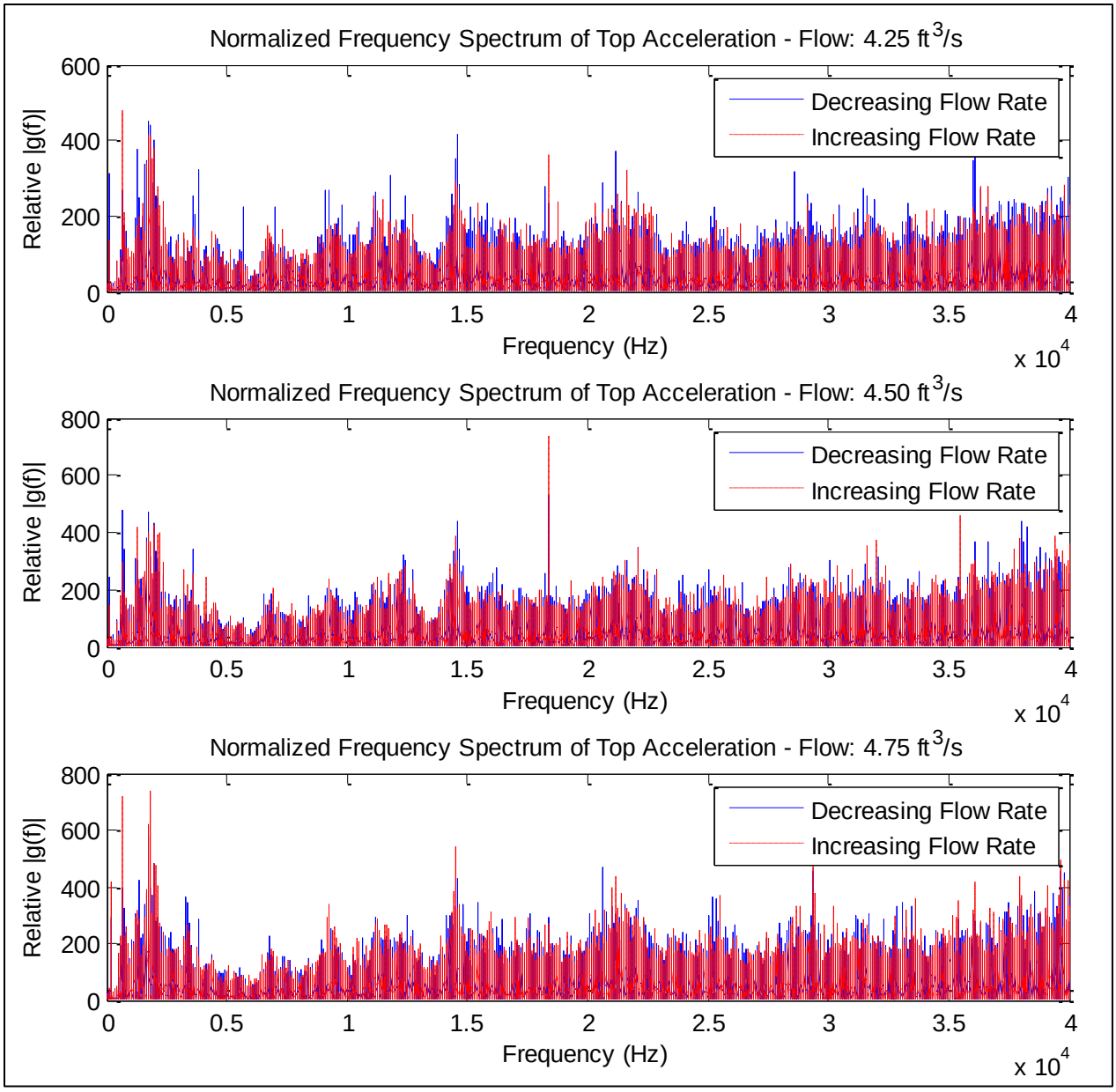

Figure P.4 Normalized Frequency Spectrum of Top Acceleration – Flow Rates 4.25 – 4.75 ft^3/s

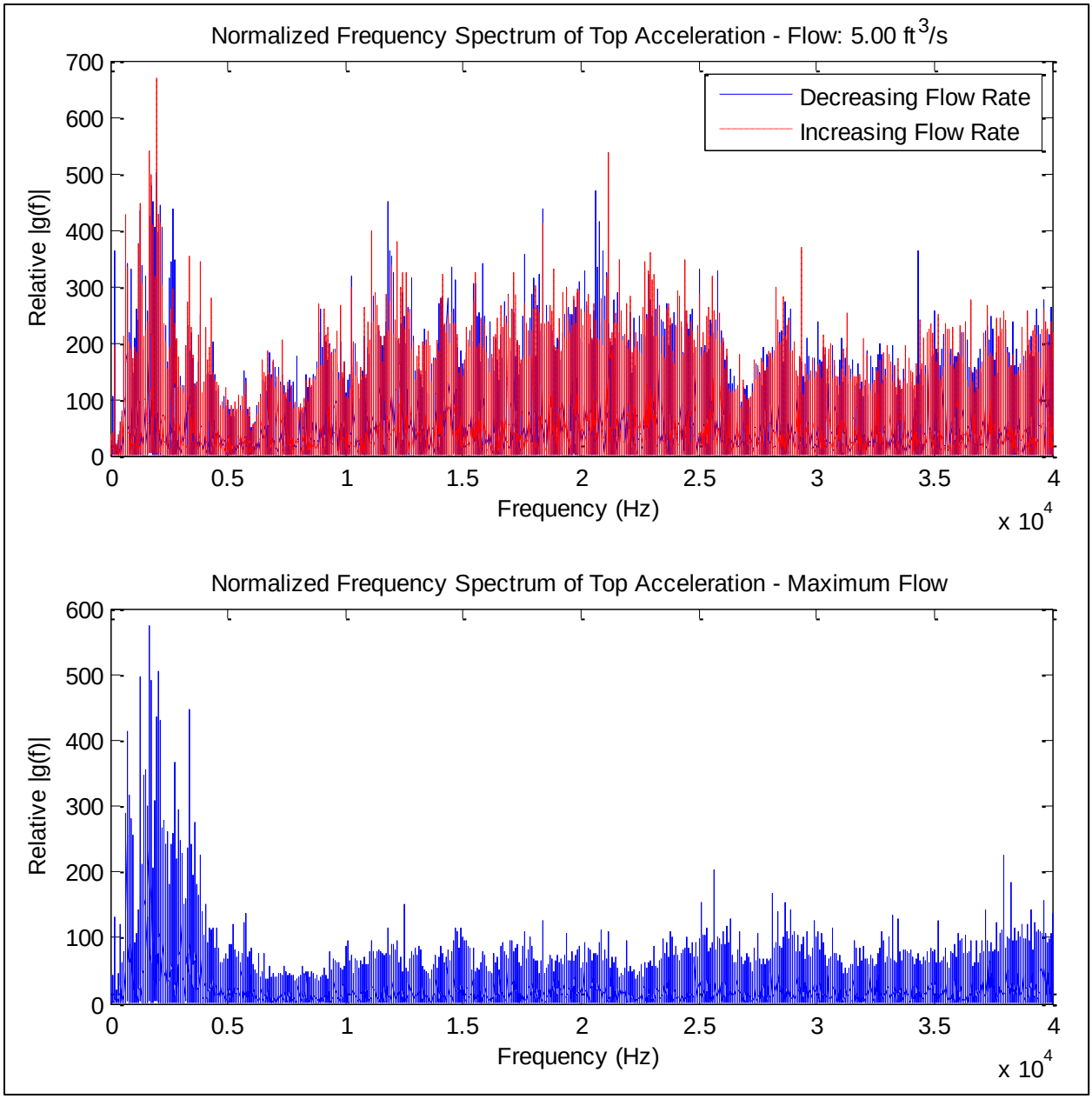

Figure P.5 Normalized Frequency Spectrum of Top Acceleration – Flow Rates 5.00 – 5.25 ft^3/s

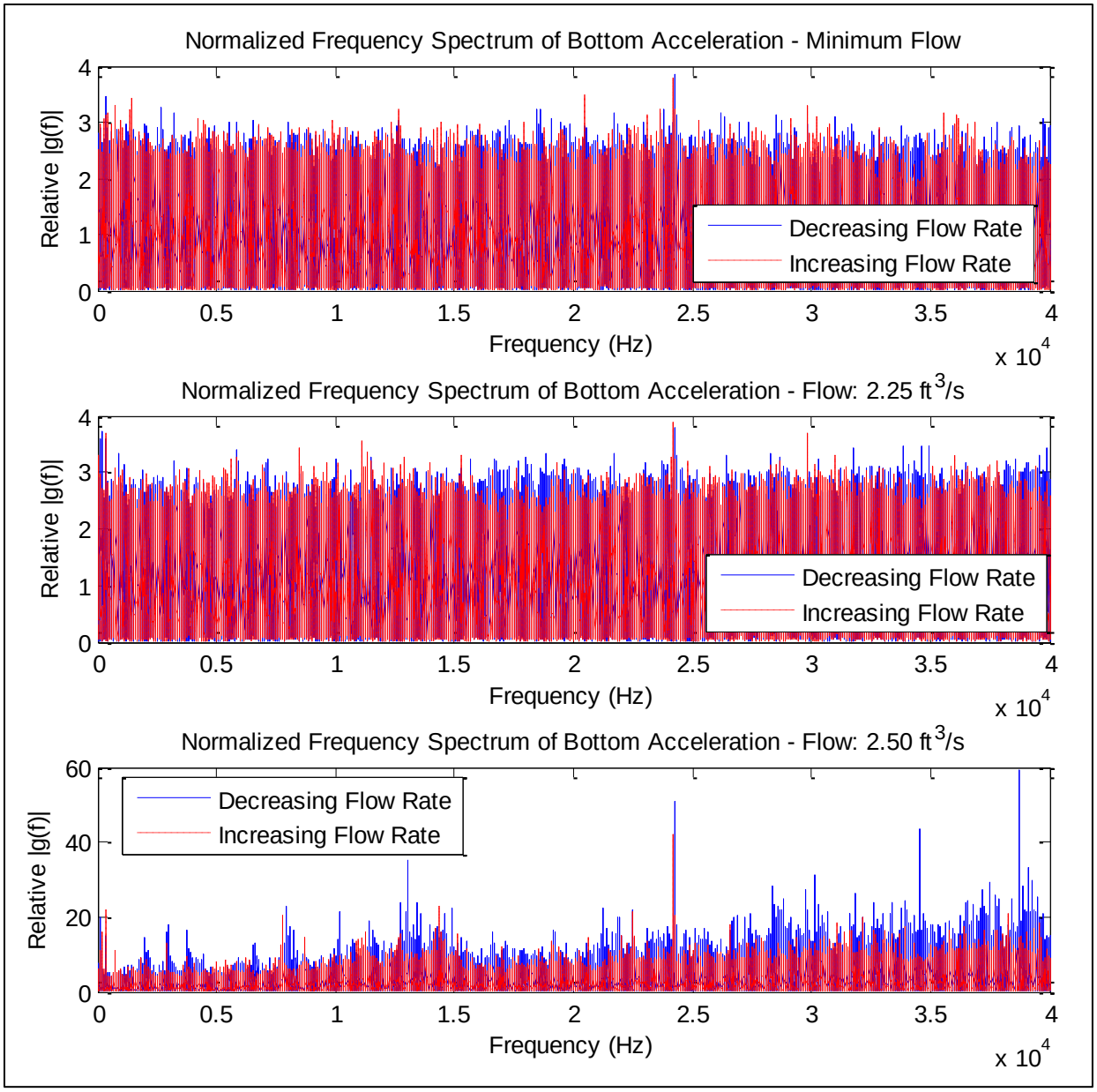

Figure P.6 Normalized Frequency Spectrum of Bottom Acceleration – Flow Rates 2.00 - 2.50 ft^3/s

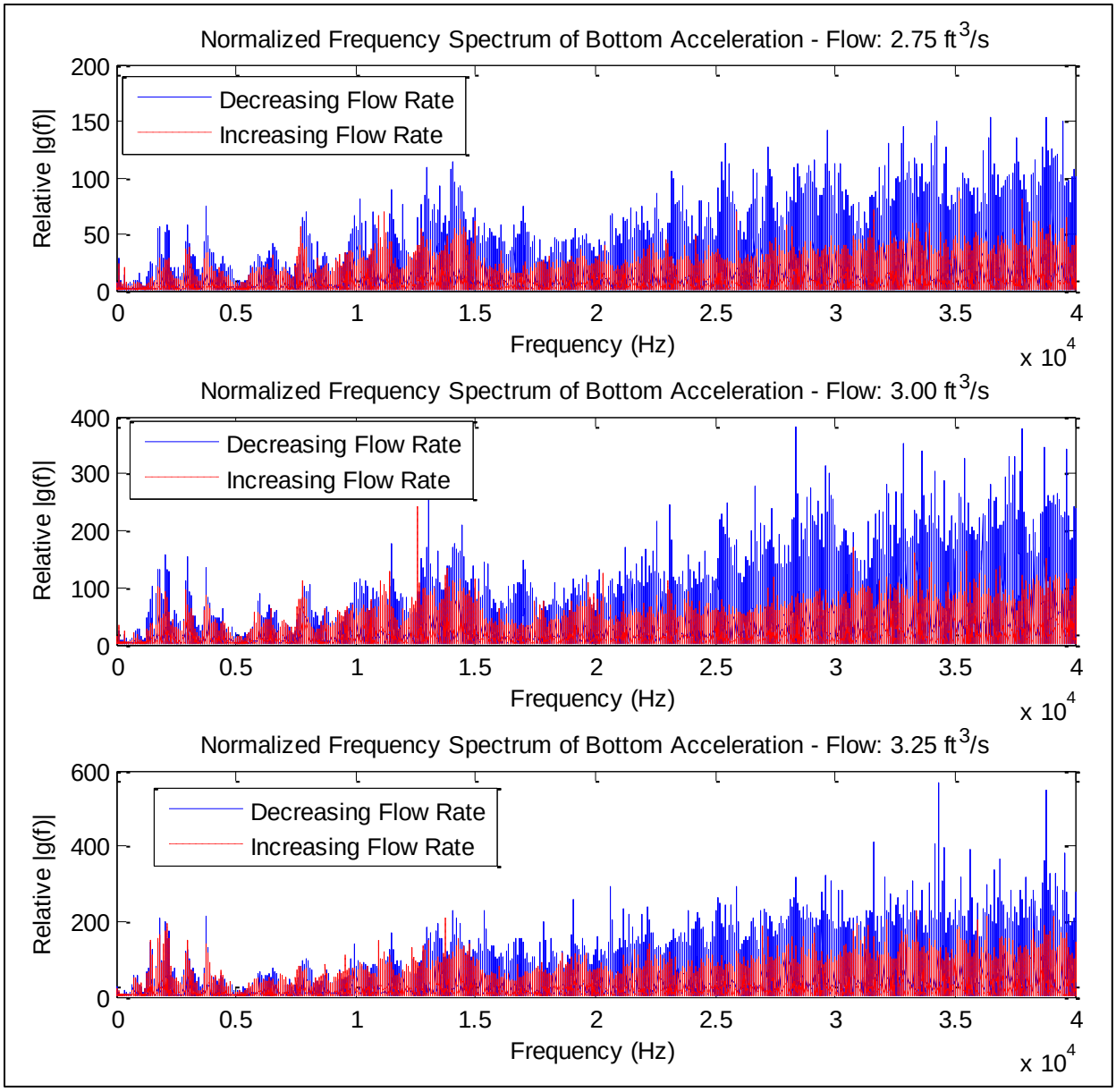

Figure P.7 Normalized Frequency Spectrum of Bottom Acceleration – Flow Rates 2.75 - 3.25 ft^3/s

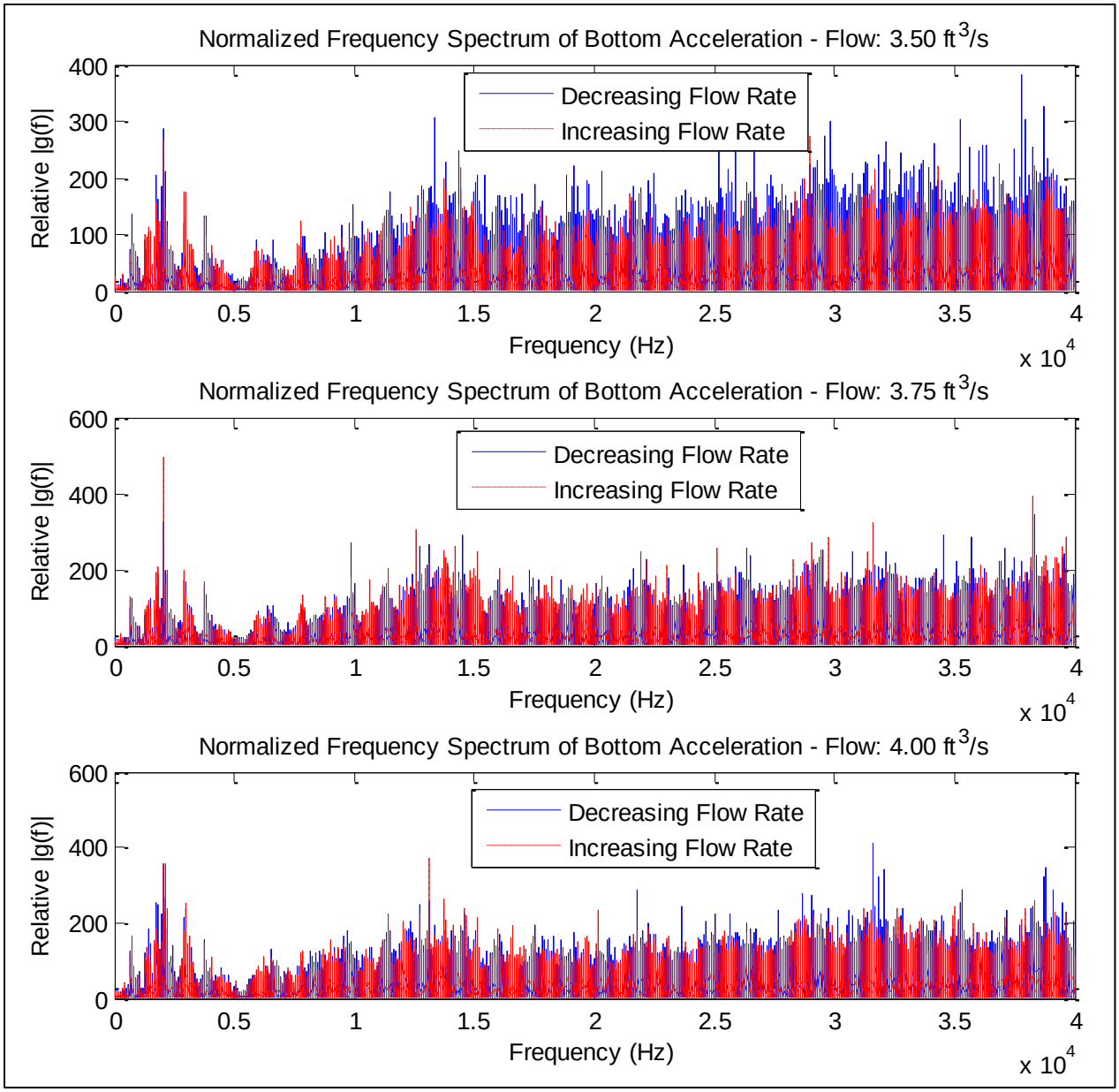

Figure P.8 Normalized Frequency Spectrum of Bottom Acceleration – Flow Rates 3.50 - 4.00 ft^3/s

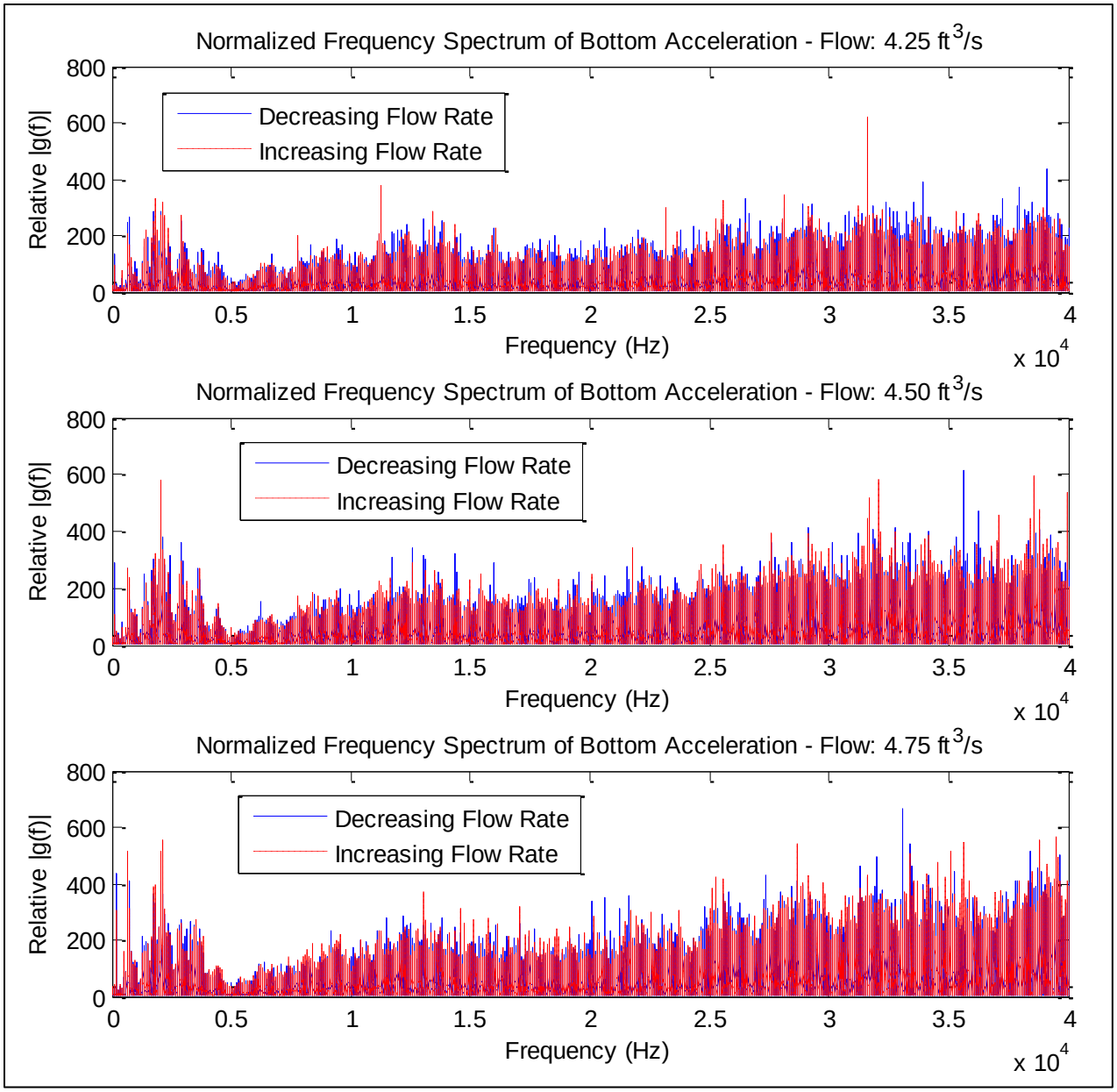

Figure P.9 Normalized Frequency Spectrum of Bottom Acceleration – Flow Rates 4.25 - 4.75 ft^3/s

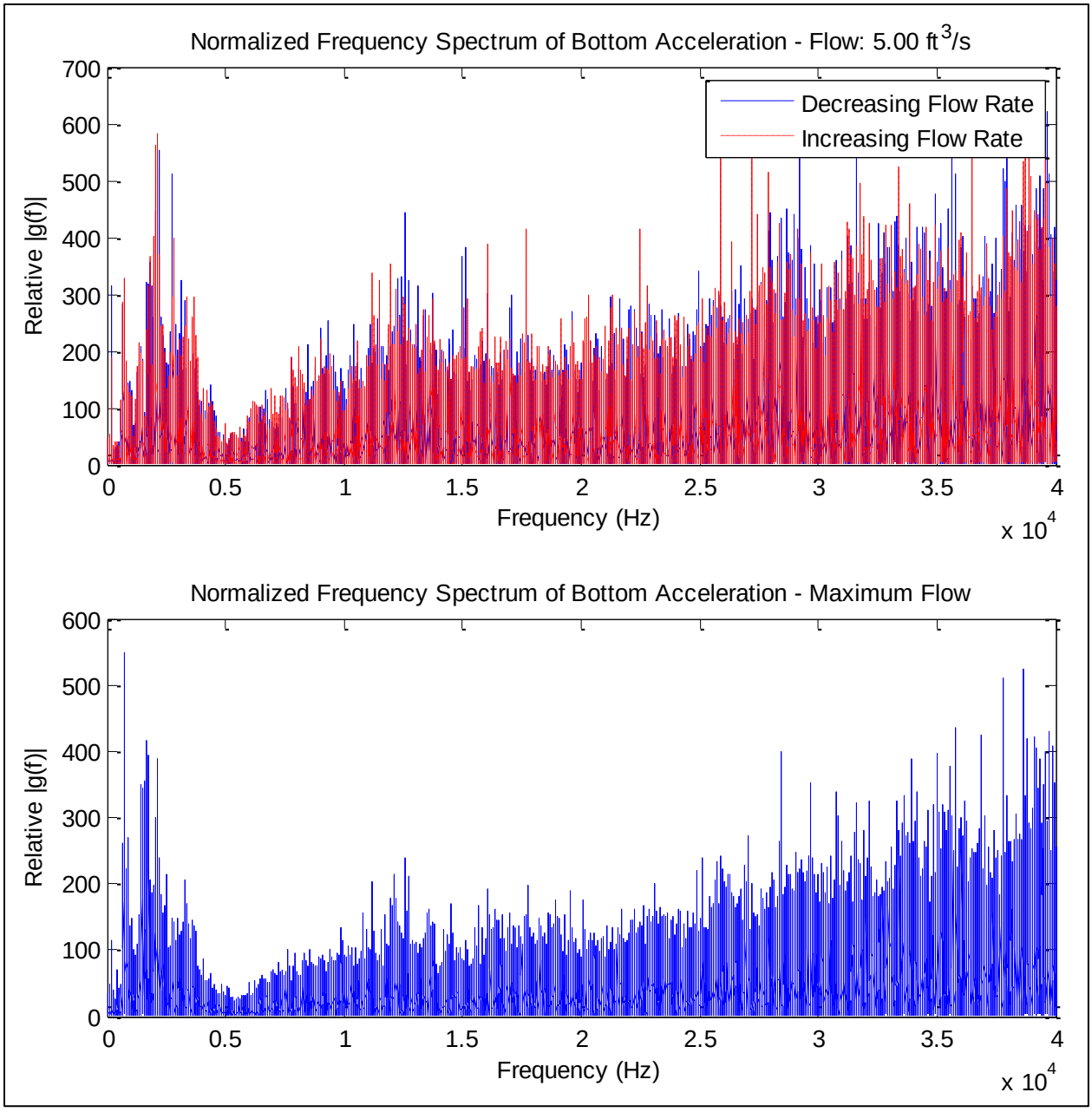

Figure P.10 Normalized Frequency Spectrum of Bottom Acceleration – Flow Rates 5.00 - 5.25 ft^3/s

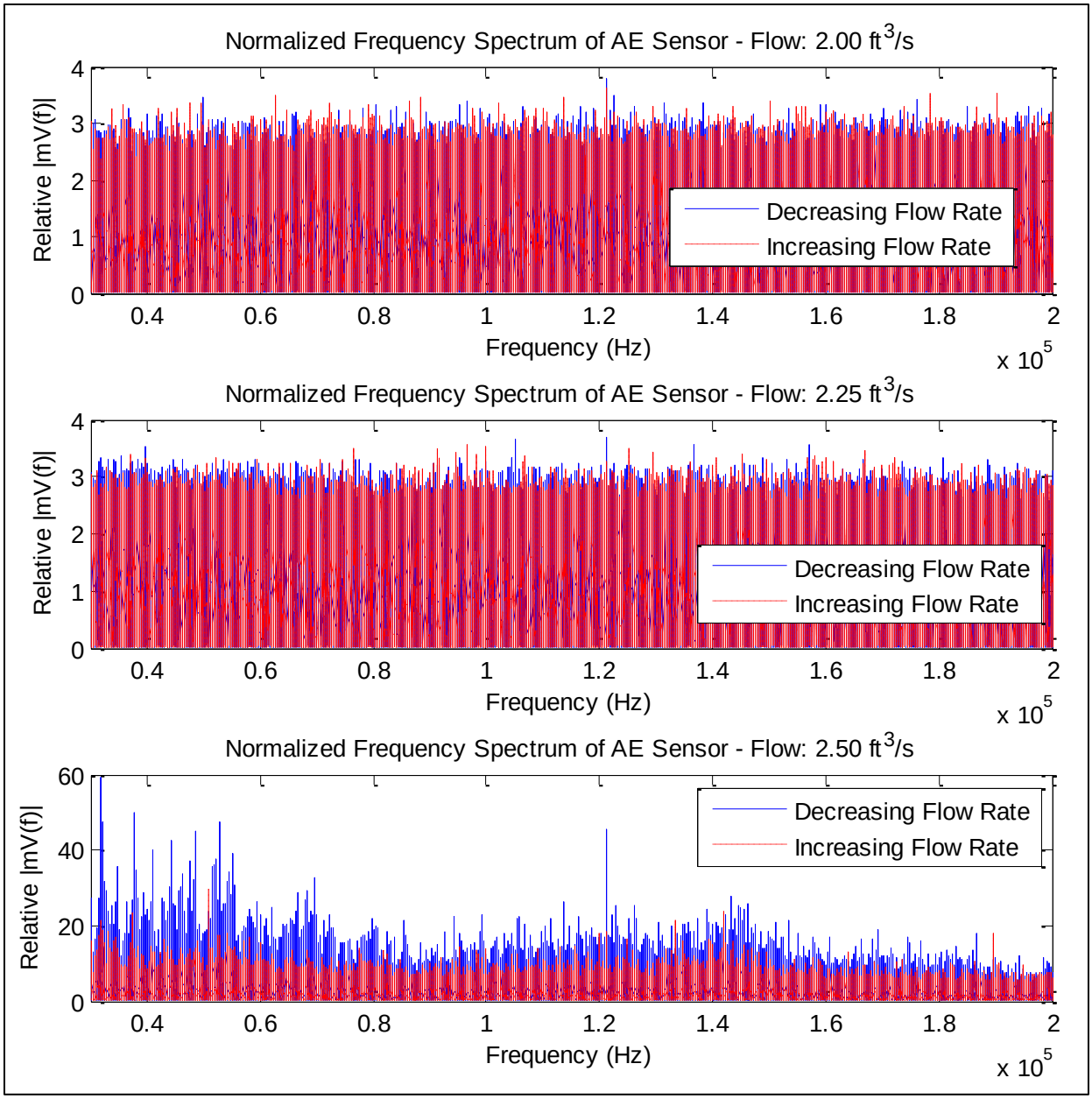

Figure P.11 Normalized Frequency Spectrum of Acoustic Emission – Flow Rates 2.00 - 2.50 ft^3/s

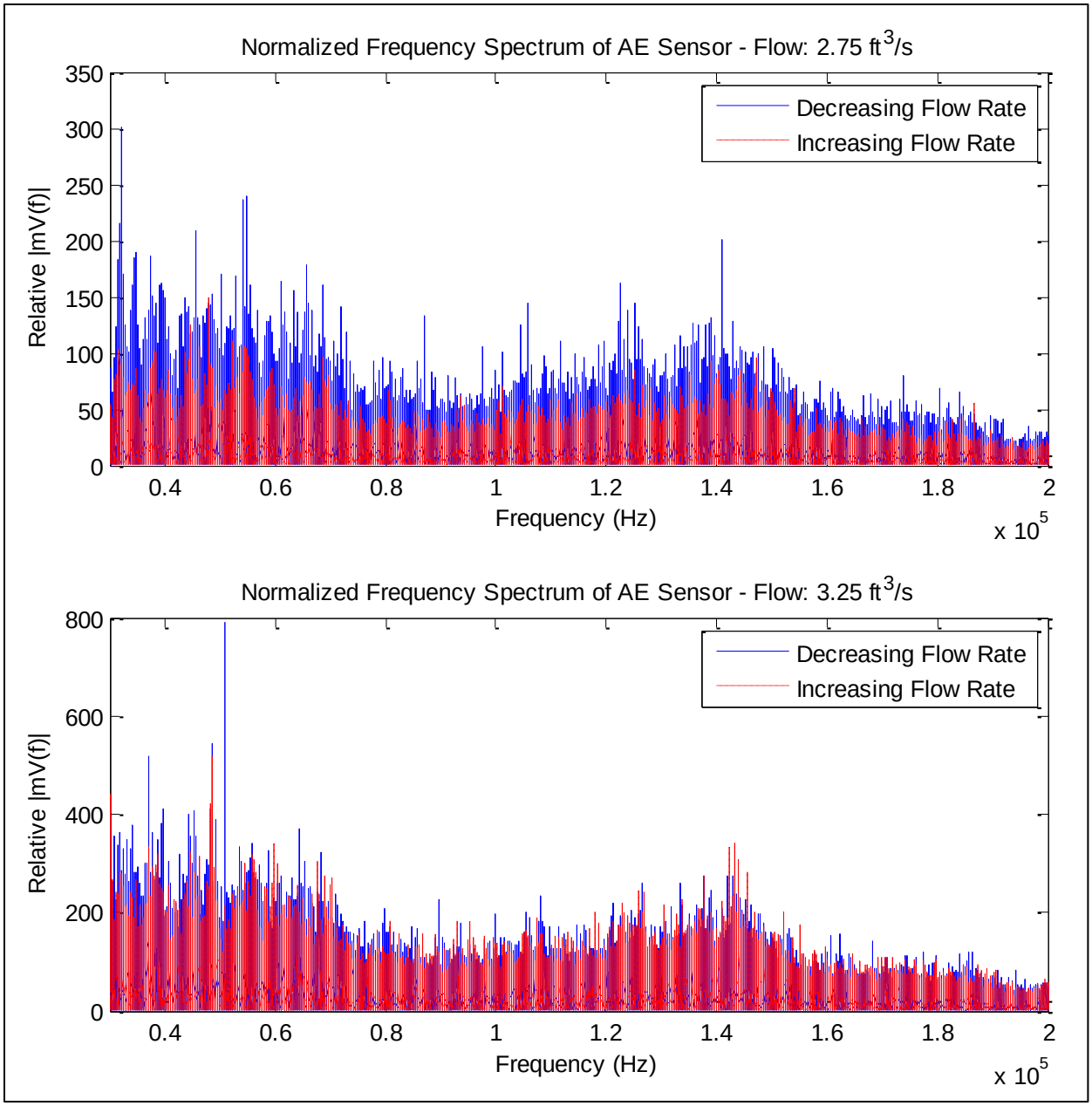

Figure P.12 Normalized Frequency Spectrum of Acoustic Emission – Flow Rates 2.75 - 3.25 ft^3/s

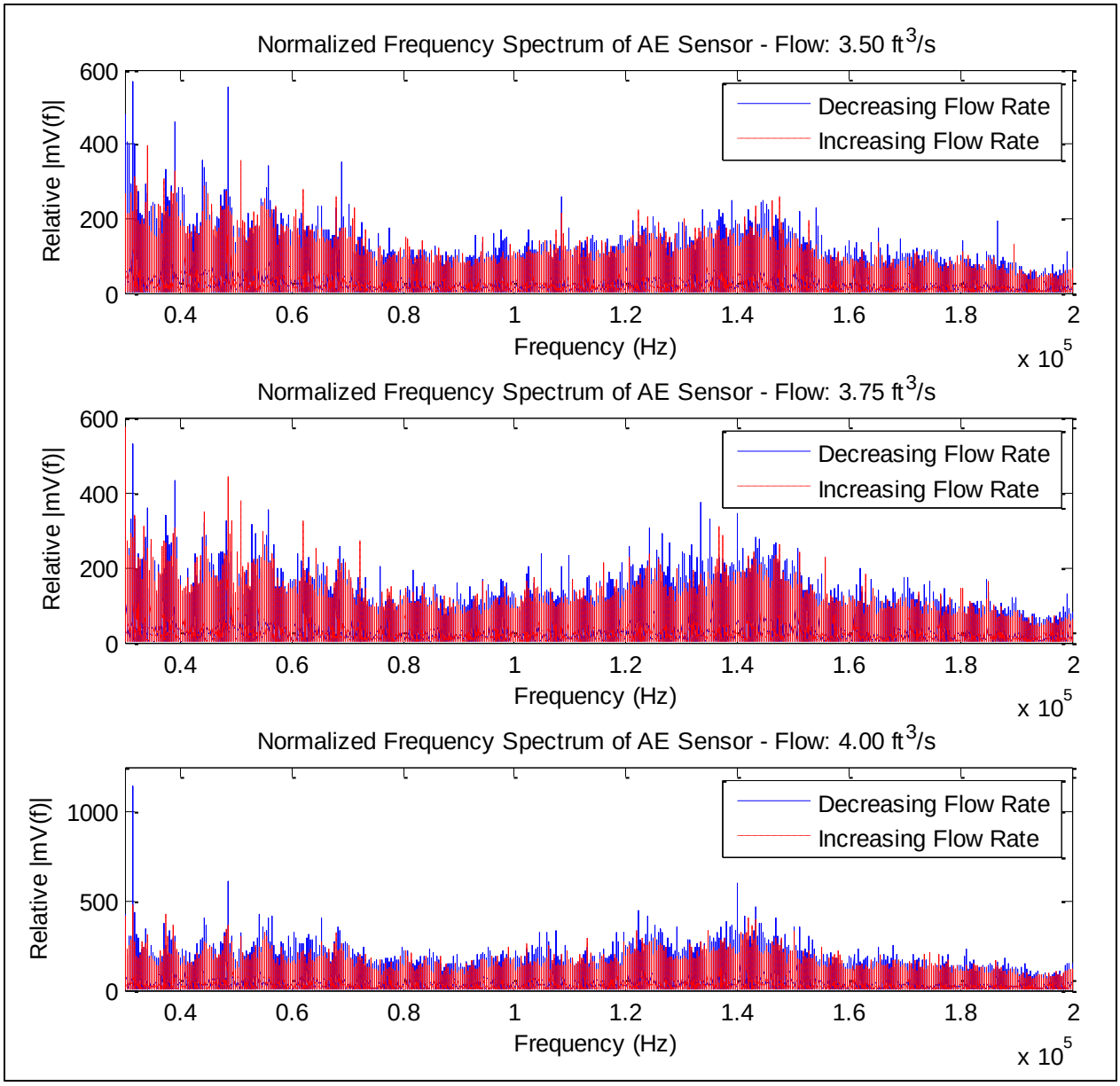

Figure P.13 Normalized Frequency Spectrum of Acoustic Emission – Flow Rates 3.50 - 4.00 ft^3/s

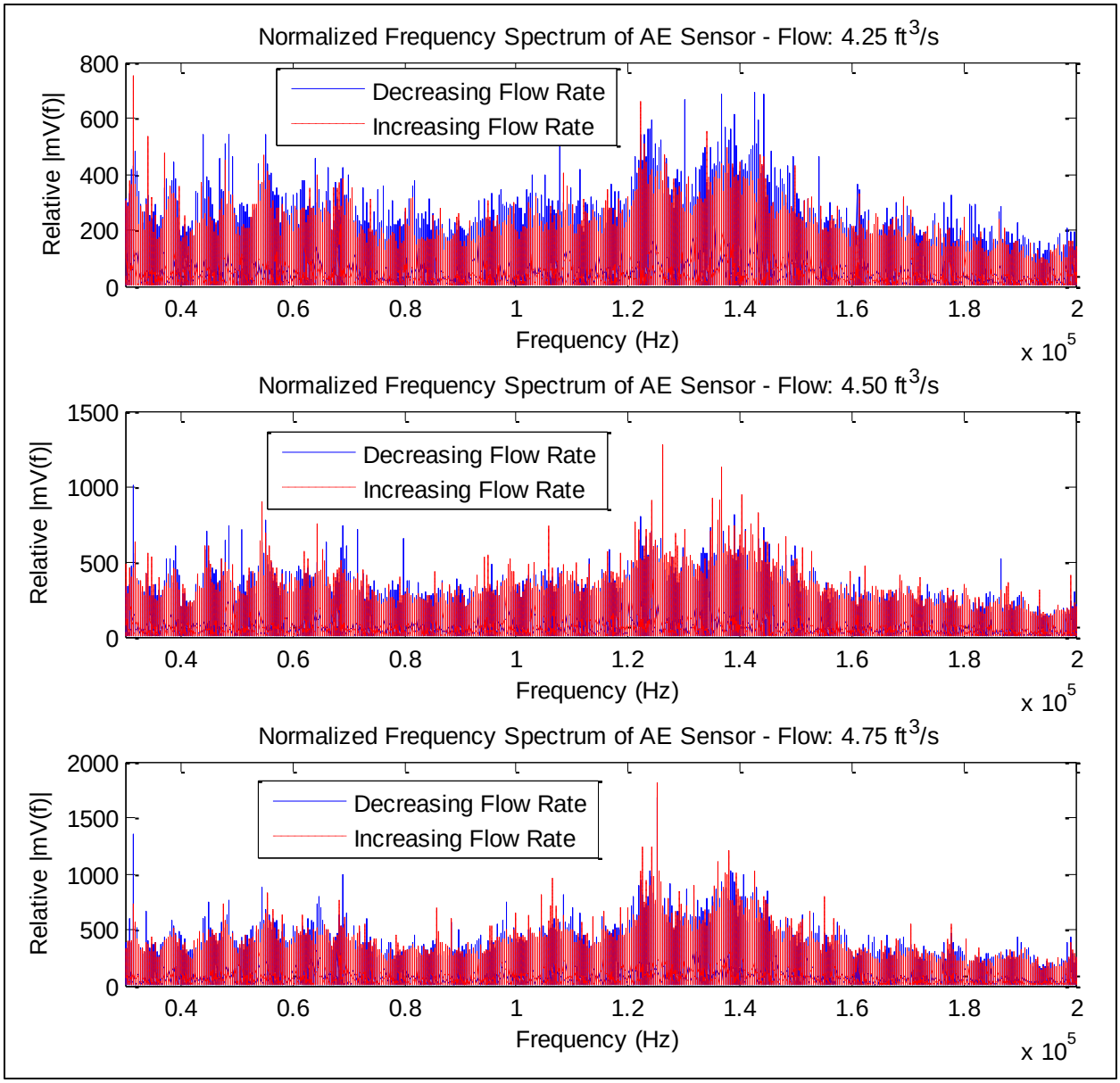

Figure P.14 Normalized Frequency Spectrum of Acoustic Emission – Flow Rates 4.25 - 4.75 ft^3/s

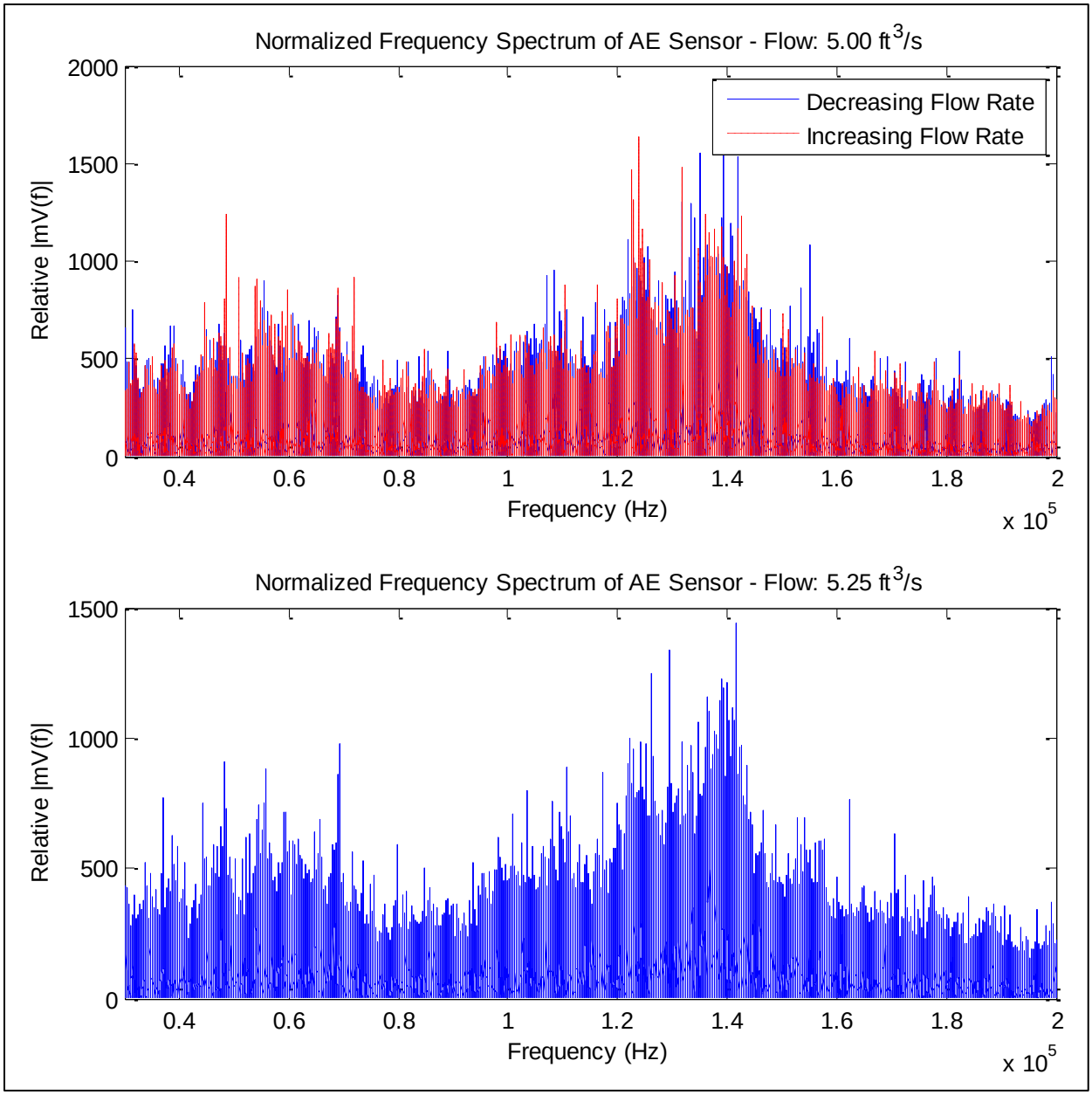

Figure P.15 Normalized Frequency Spectrum of Acoustic Emission – Flow Rates 5.00 - 5.25 ft^3/s

APPENDIX Q

COHERENCE FILTERING EFFECTS

Coherence is a function of frequency with a value between zero and one which indicates how well a signal corresponds to another signal at specific frequencies. Coherence calculations however can be noisy, and therefore pertinent information can be lost to erroneous noise. To dampen the noise, the two input signals are broken into specified windows and windowed with appropriate windows (i.e. Hanning). Computational costs however increases exponentially with smaller windows (i.e. signals are broken into more sections). In addition to specifying a window length, an overlap must be specified. The norm is to use a 50% overlap.

Before the final filter length of 2^{15} was chosen, filters with lengths 2^{16} - 2^{20} were considered. A Hanning window with length 2^{15} was decided upon for two reasons. First can be seen in Figure Q.1, where the computational time versus filter length is shown. A filter with length of 2^{15} took approximately 7.5 minutes to calculate using MATLAB©. By fitting all computational times of coherence calculations with filter lengths $2^{15} – 2^{20}$, it was predicted that a filter with length 2^{14} would take 15 minutes to calculate and a filter with length 2^{13} would take 33 minutes. Seven and a half minutes was the longest calculation time desired for coherence calculations.

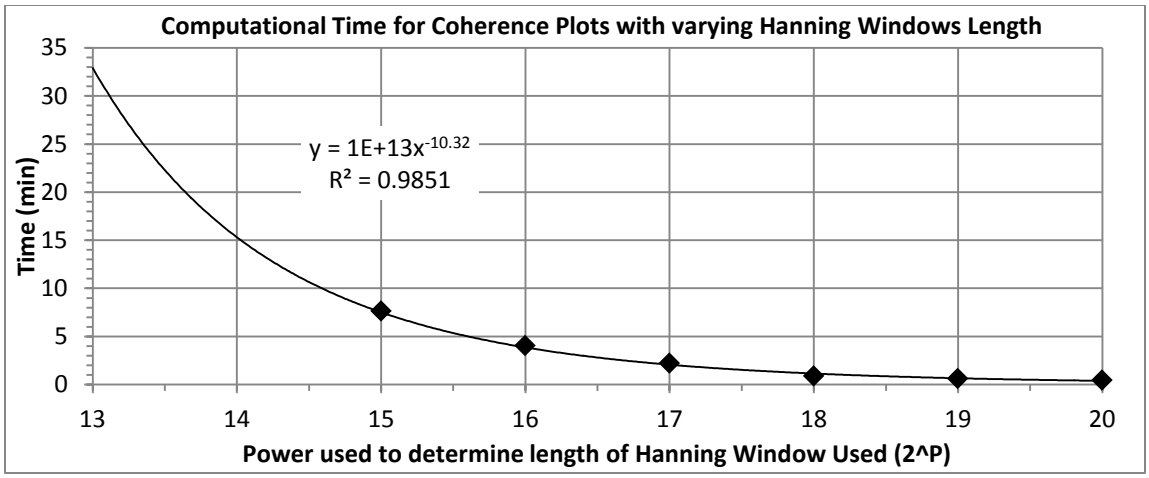

Figure Q.1 Computational Time for Coherence Plots with varying Hanning Window Length

The second reason was due to the acceptable clarity reached with a Hanning window of length 2^{15}. Figures Q.2 and Q.3 show the progression from using filters ranging from 2^{20} to 2^{15} and how the clarity is improved with each iteration. The combination of a filter of length 2^{15} took 7.5 minutes and provided acceptable clarity of the final, provided enough reasoning for the final filtering choice.

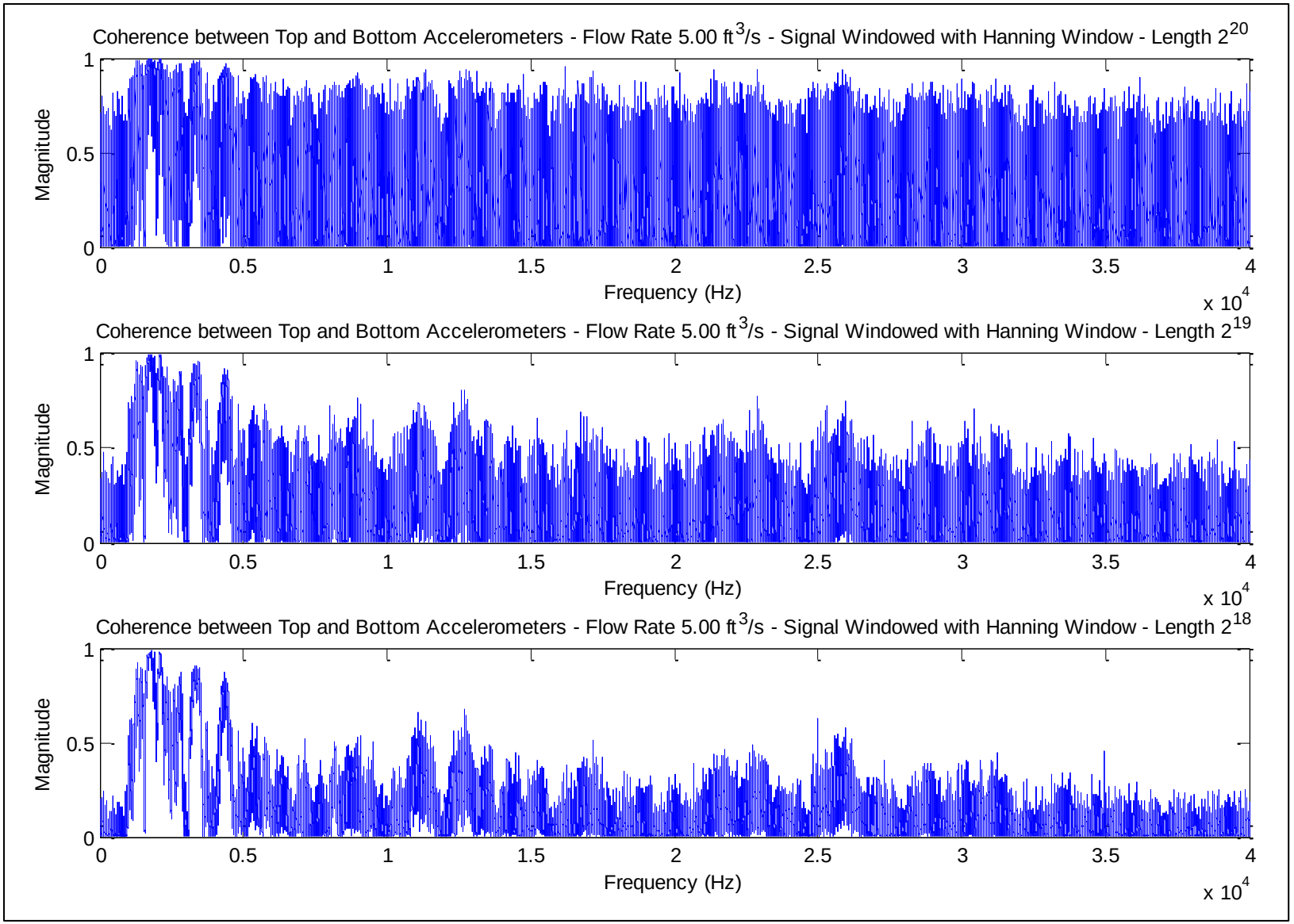

Figure Q.2 Coherence between Top and Bottom Acceleration with Hanning Window of varying Length $2^{20} - 2^{18}$

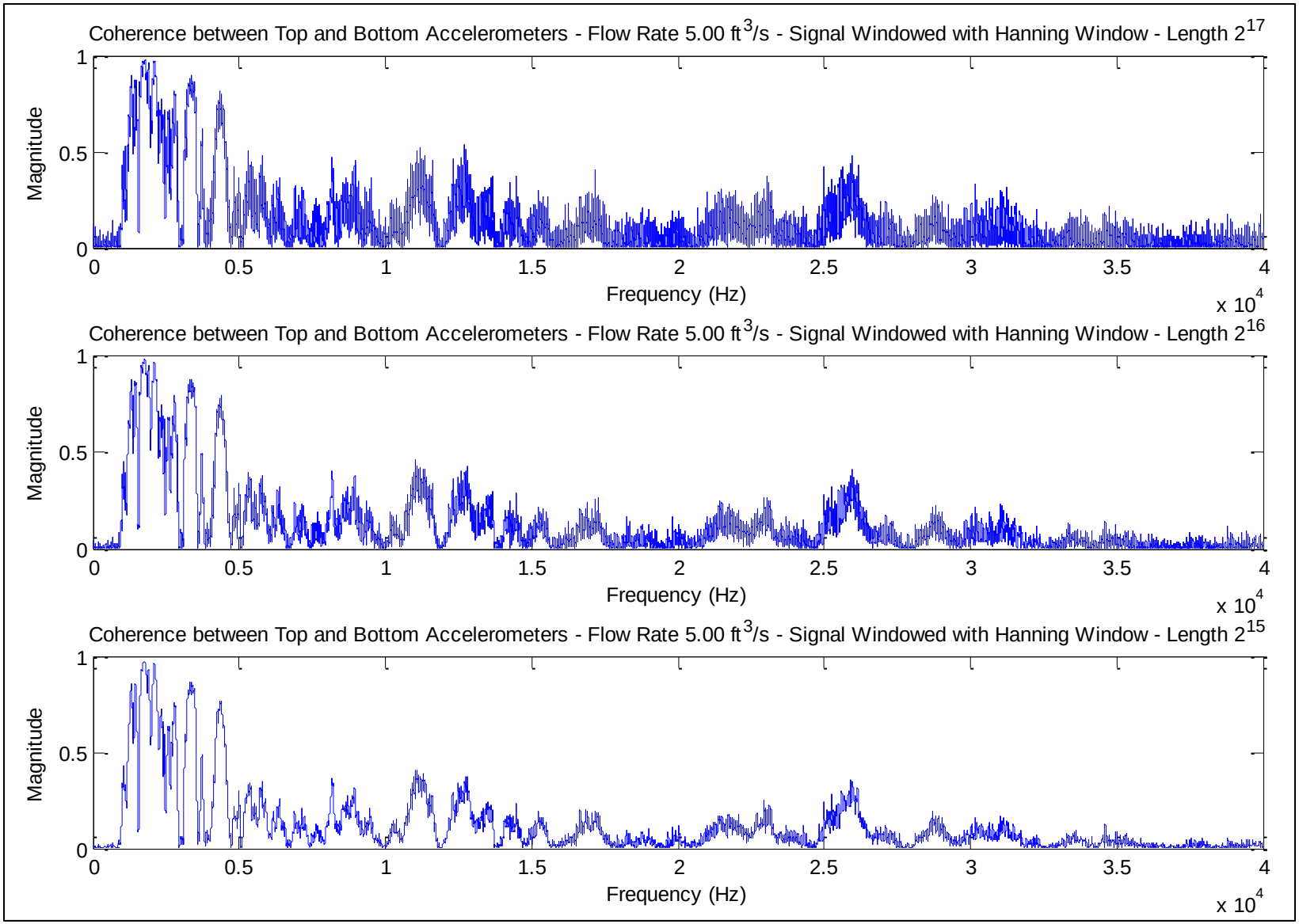

Figure Q.3 Coherence between Top and Bottom Acceleration with Hanning Window of varying Length $2^{17} - 2^{15}$

APPENDIX R

SUPPLEMENTAL COHERENCE PLOTS

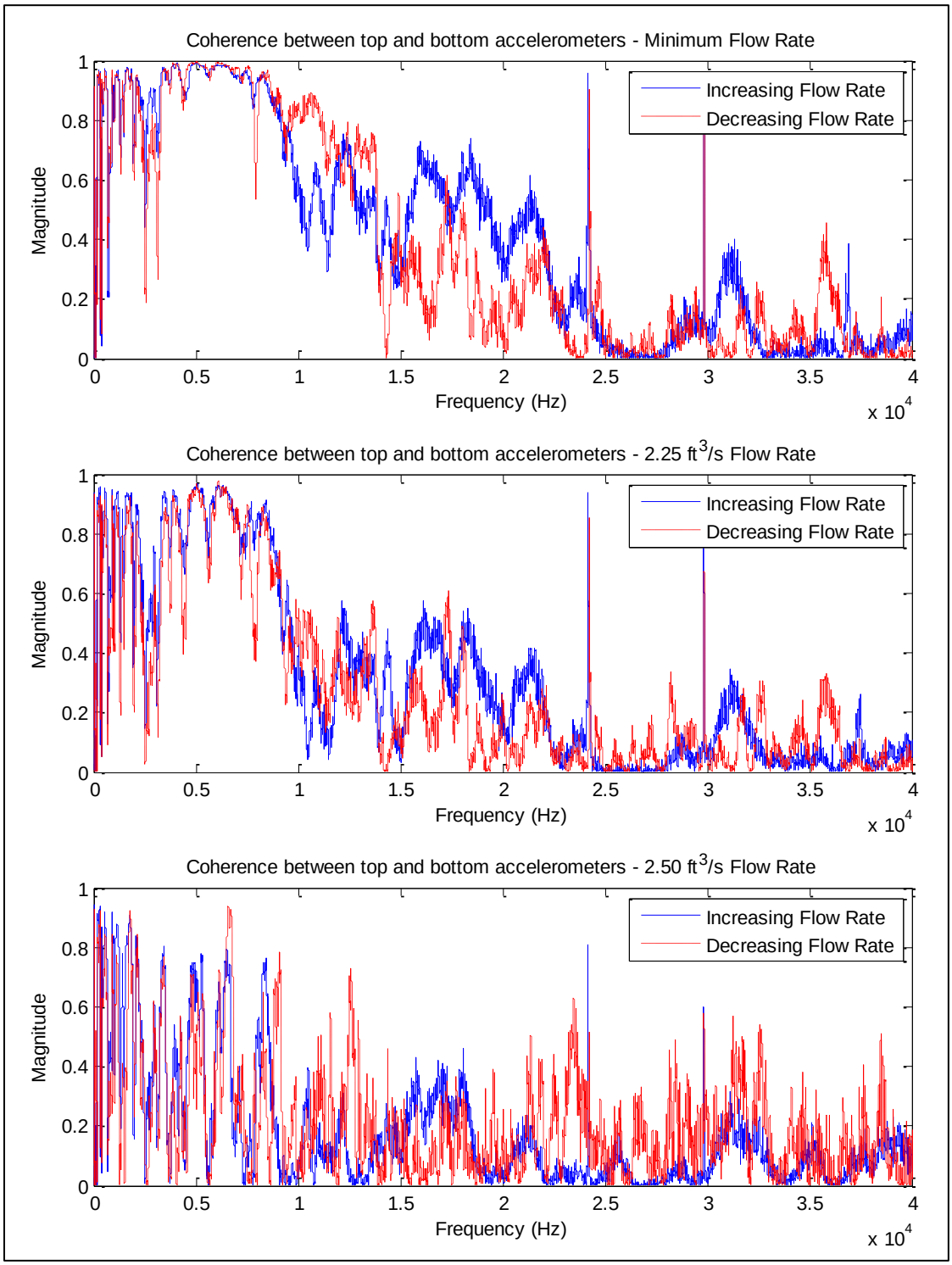

Figure R.1 Coherence between Top and Bottom Acceleration, Flow Range 2.00 – 2.50 ft^3/s

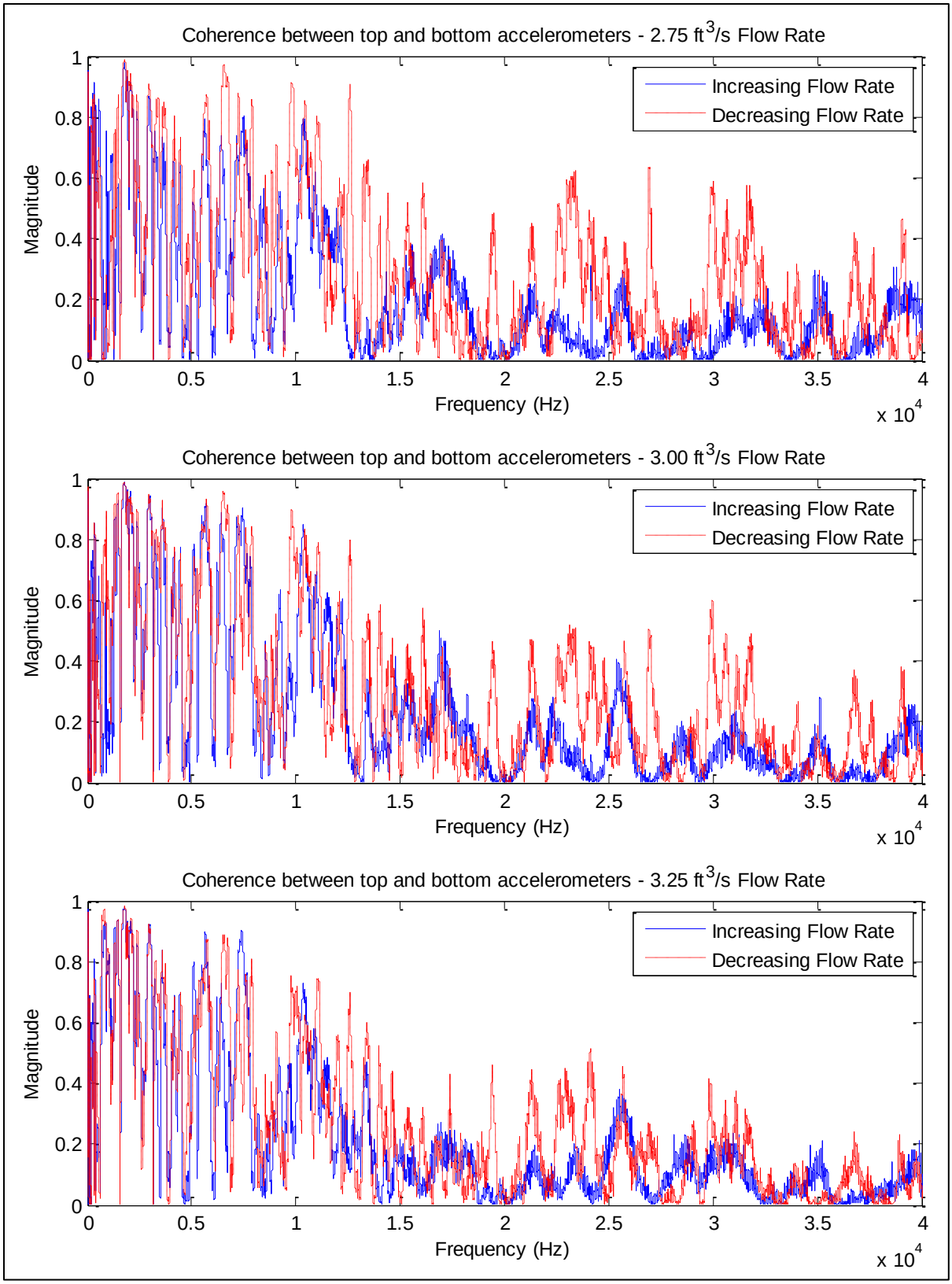

Figure R.2 Coherence between Top and Bottom Acceleration, Flow Range 2.75 – 3.25 ft^3/s

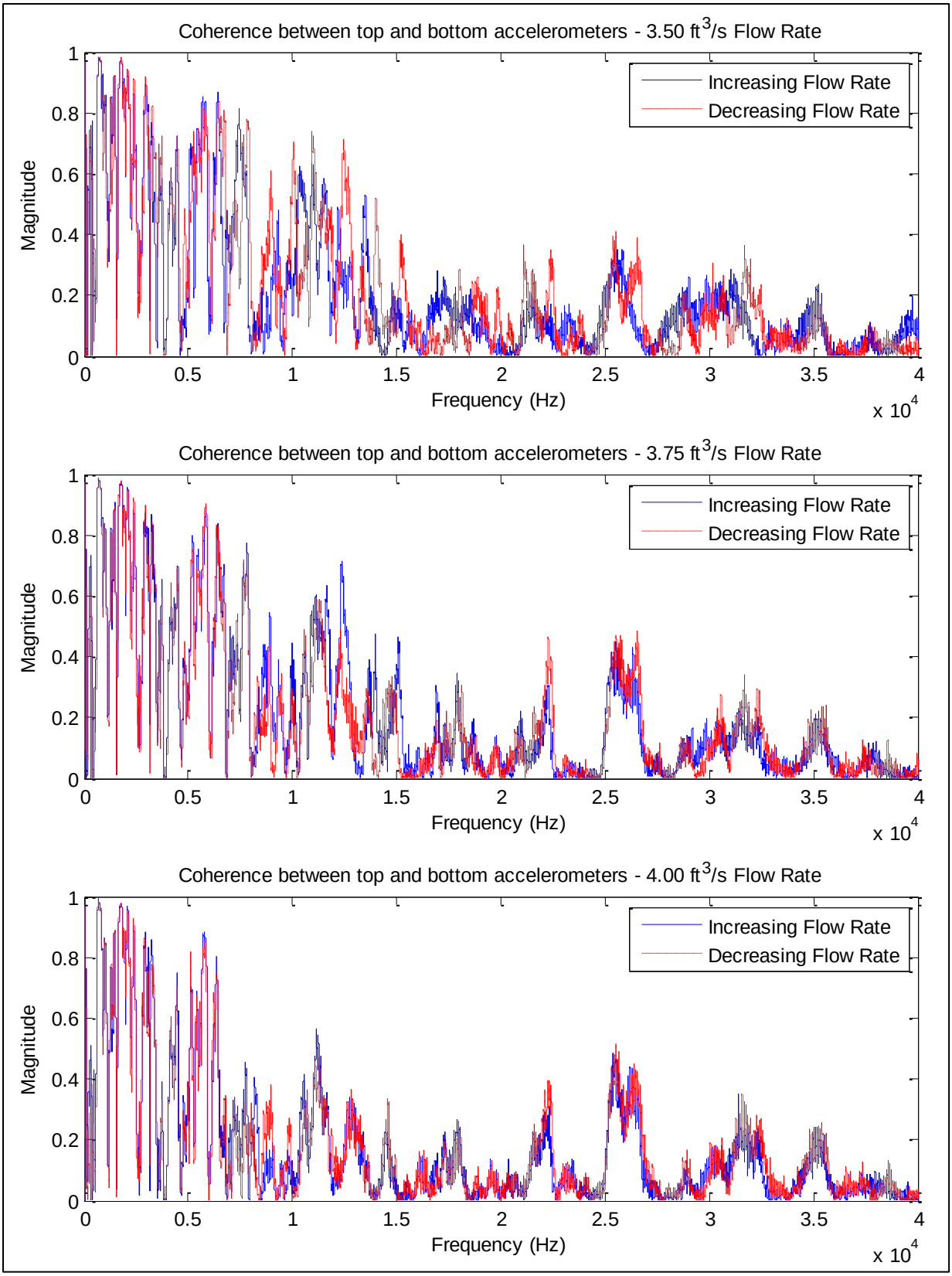

Figure R.3 Coherence between Top and Bottom Acceleration, Flow Range 3.50 – 4.00 ft^3/s

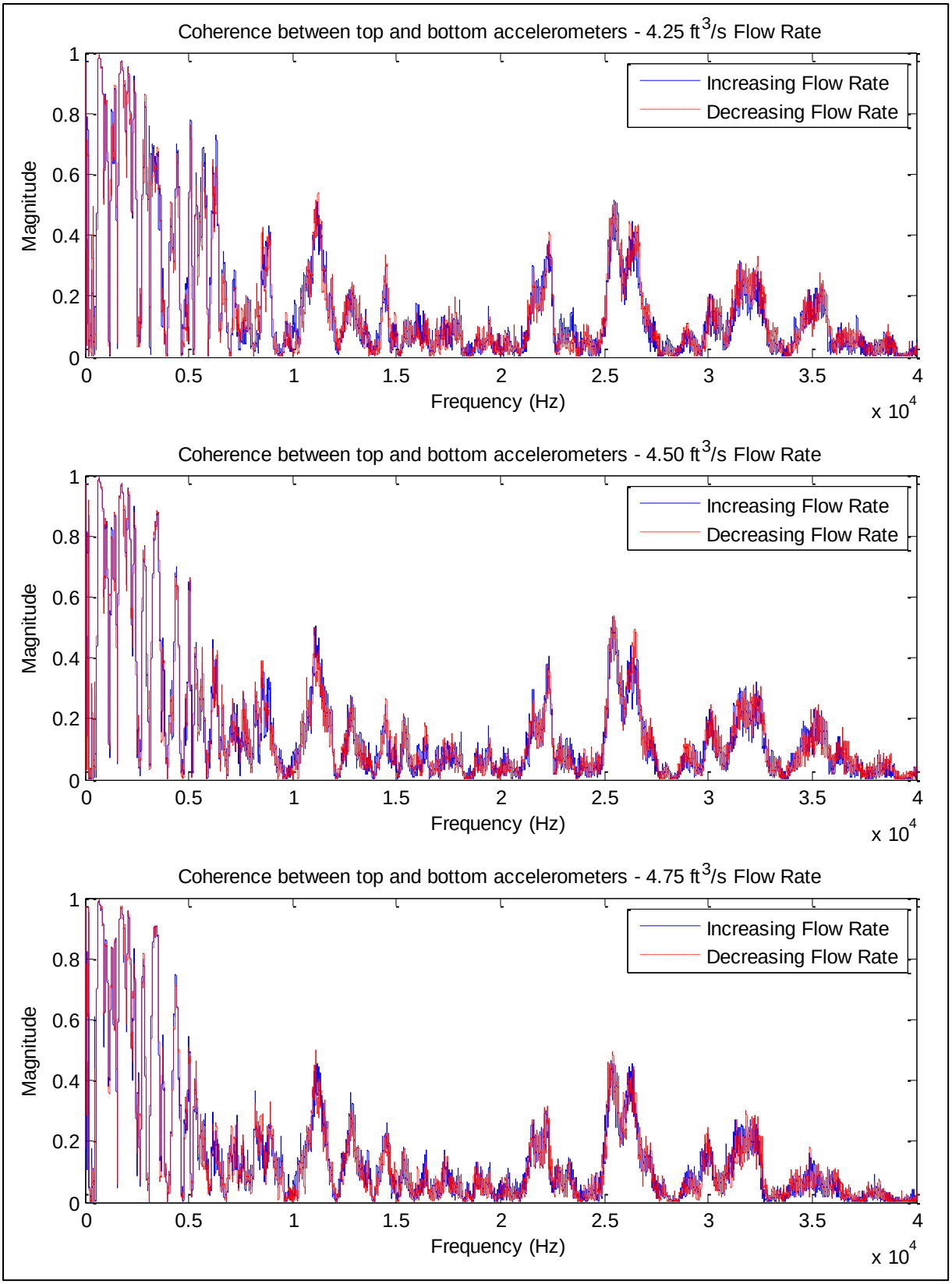

Figure R.4 Coherence between Top and Bottom Acceleration, Flow Range 4.00 – 4.75 ft^3/s

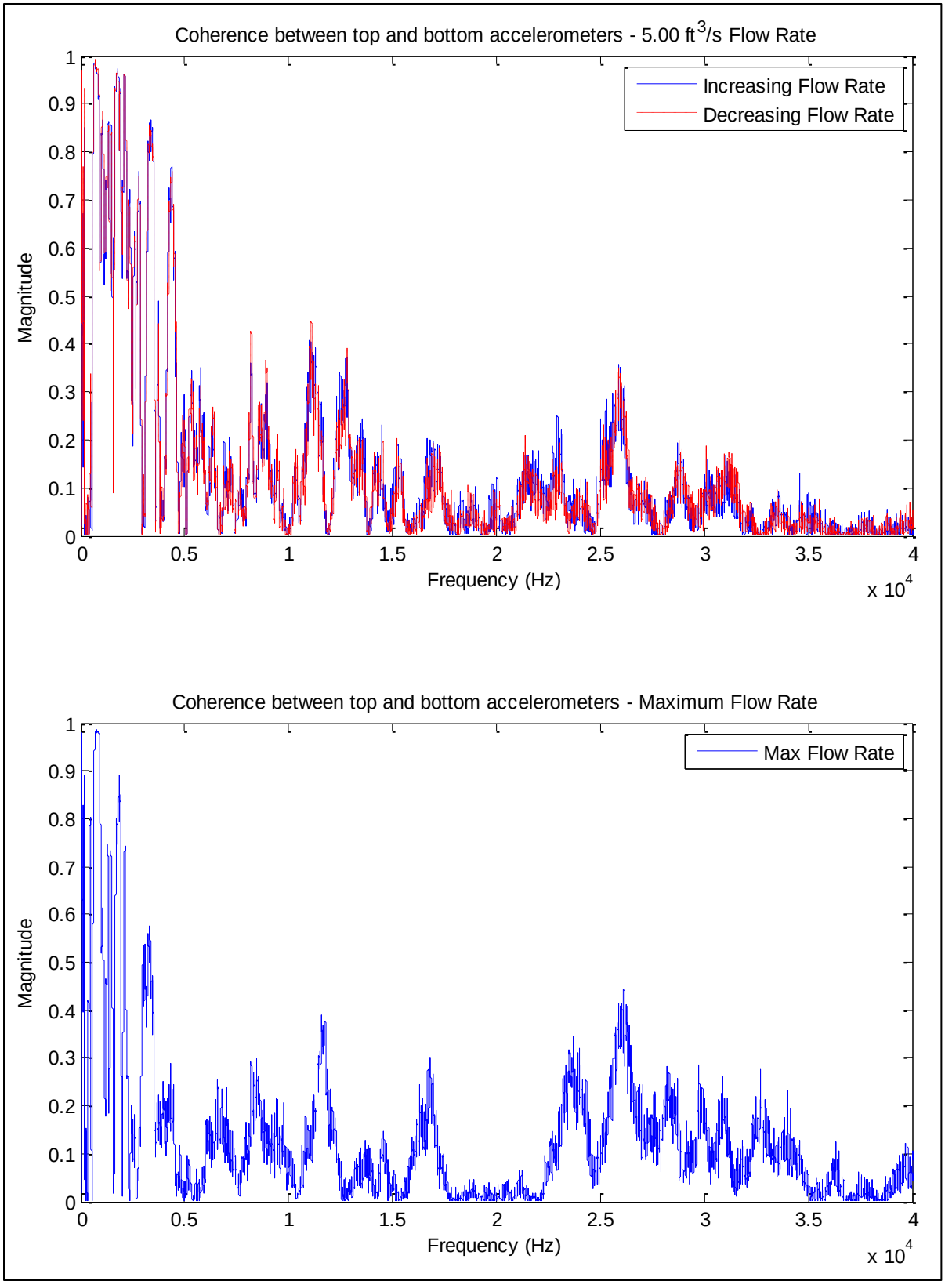

Figure R.5 Coherence between Top and Bottom Acceleration, Flow Range 5.00 – 5.25 ft^3/s

APPENDIX S

AVERAGE SPIKE ANALYSIS PLOTS

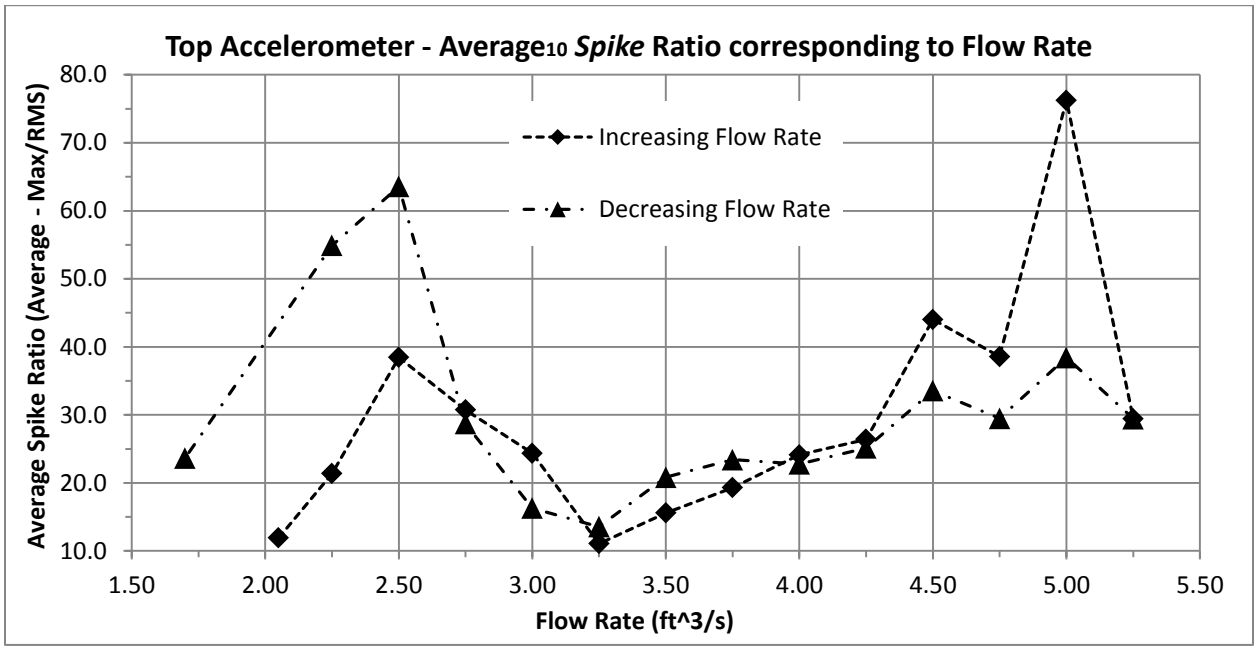

Figure S.1 *Average Spike* Analysis of Acceleration Signal Collected from Top of Cavitation Tunnel

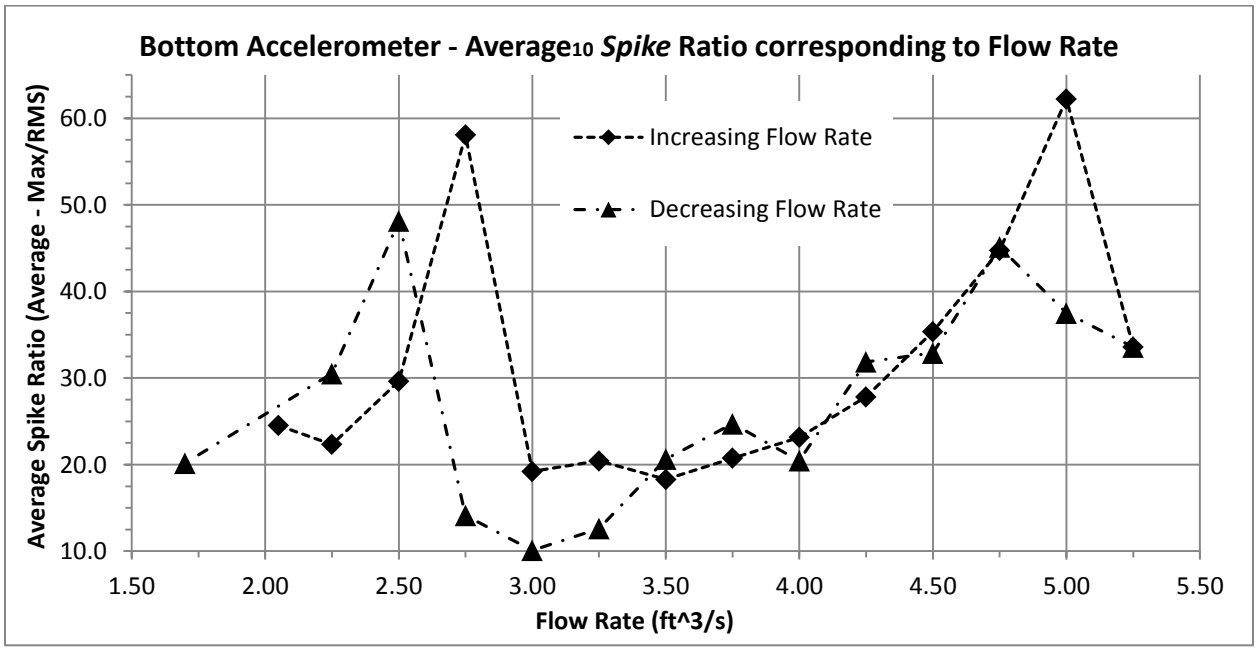

Figure S.2 *Average Spike* Analysis of Acceleration Signal Collected from Bottom of Cavitation Tunnel

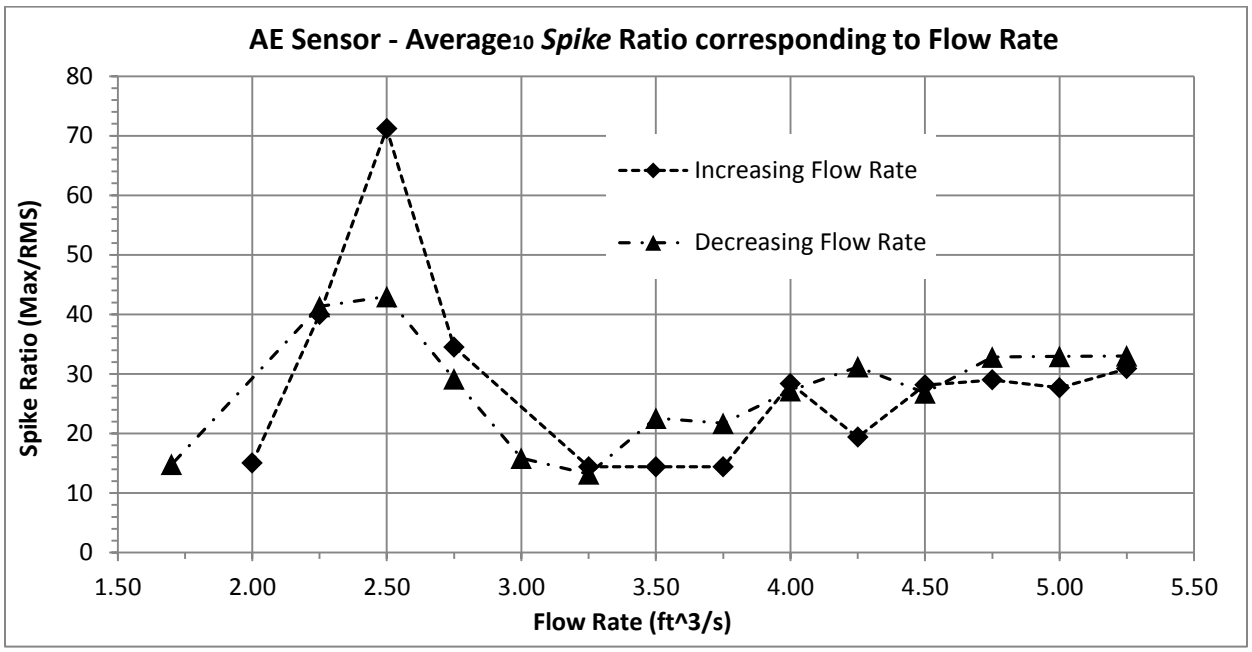

Figure S.3 *Average Spike* Analysis of Acoustic Emission Signal Collected from Bottom of Cavitation Tunnel

APPENDIX T

BURST ANALYSIS PLOTS AND NORMALIZATION BACKGROUND

Figures T.1 – T.15 present the plotted results of Burst Analysis completed on the top/bottom accelerometers and AE Sensor data at Burst thresholds 5x, 10x, 15x, 20x, and 25x the signals standard deviation.

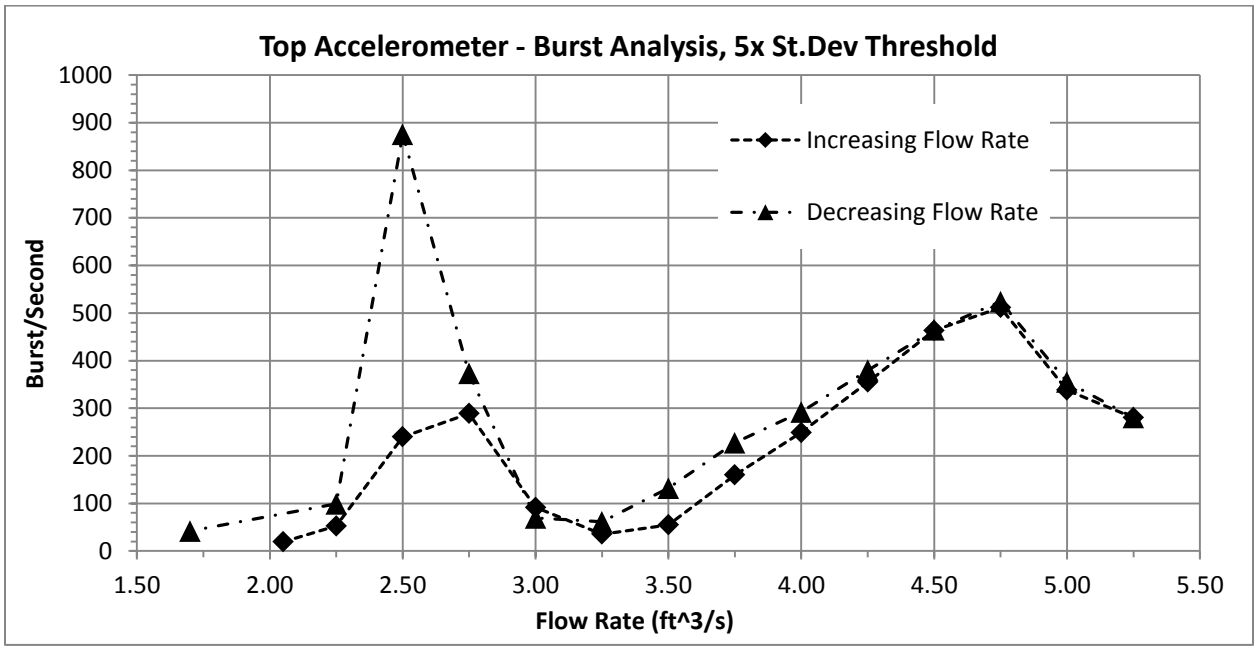

Figure T.1 Burst Analysis of Acceleration recorded from Top of Tunnel – 5x Standard Deviation Threshold

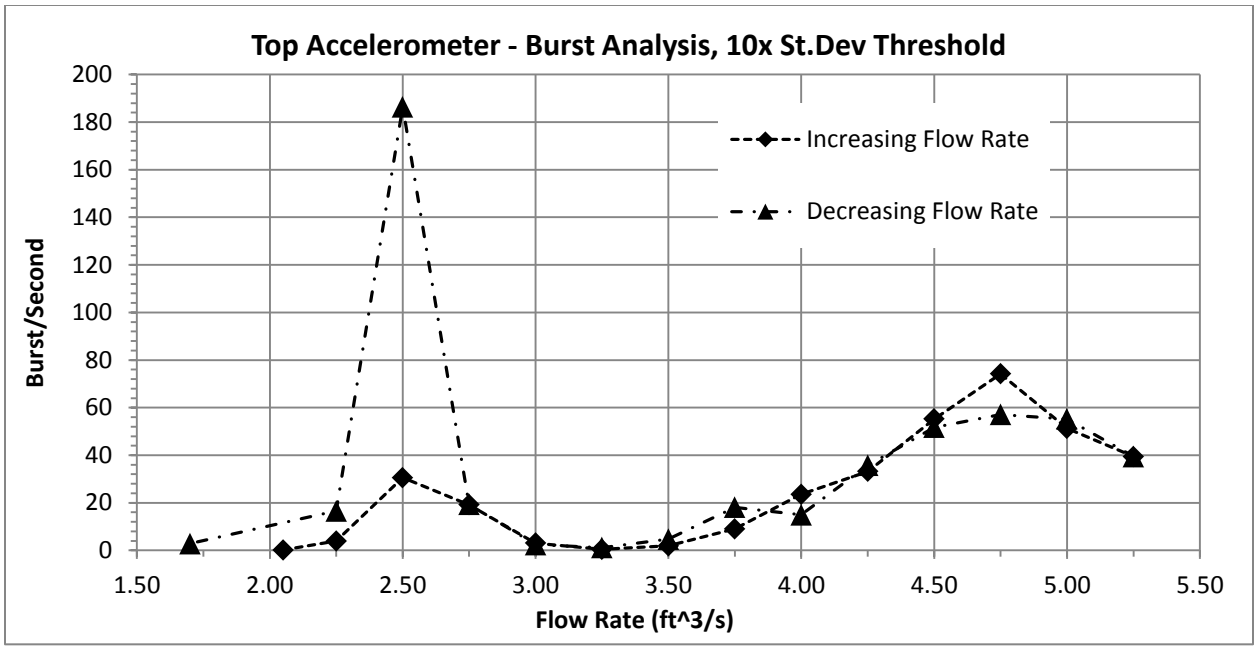

Figure T.2 Burst Analysis of Acceleration recorded from Top of Tunnel – 10x Standard Deviation Threshold

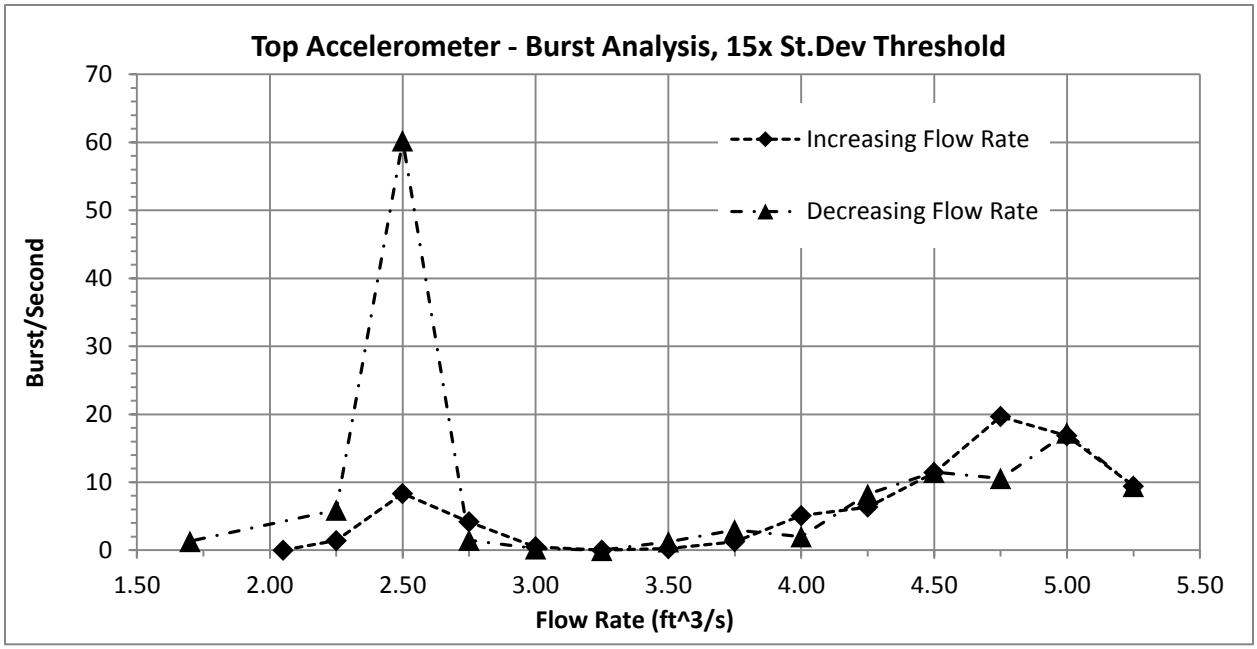

Figure T.3 Burst Analysis of Acceleration recorded from Top of Tunnel – 15x Standard Deviation Threshold

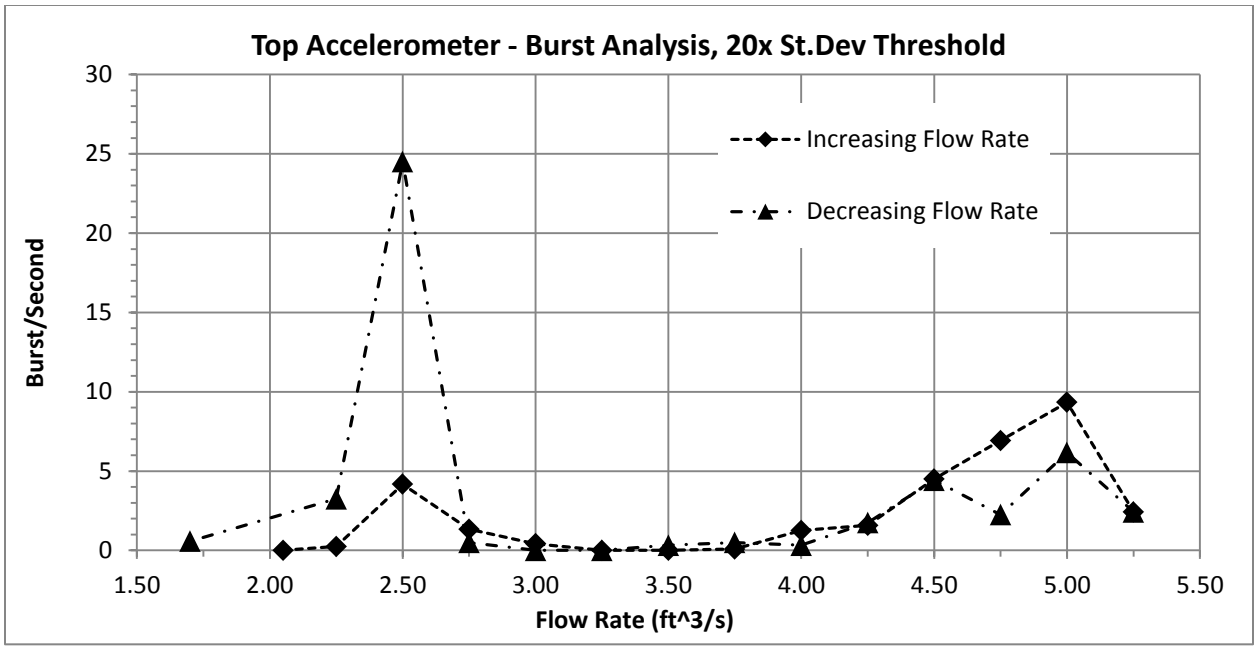

Figure T.4 Burst Analysis of Acceleration recorded from Top of Tunnel – 20x Standard Deviation Threshold

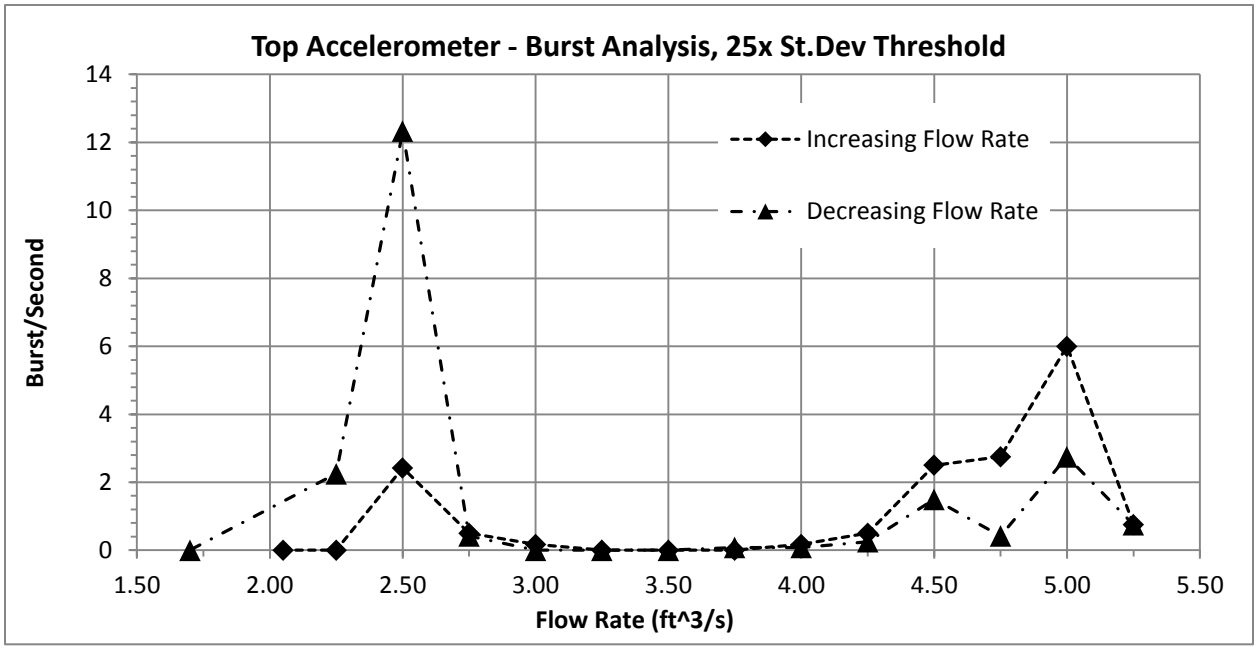

Figure T.5 Burst Analysis of Acceleration recorded from Top of Tunnel – 25x Standard Deviation Threshold

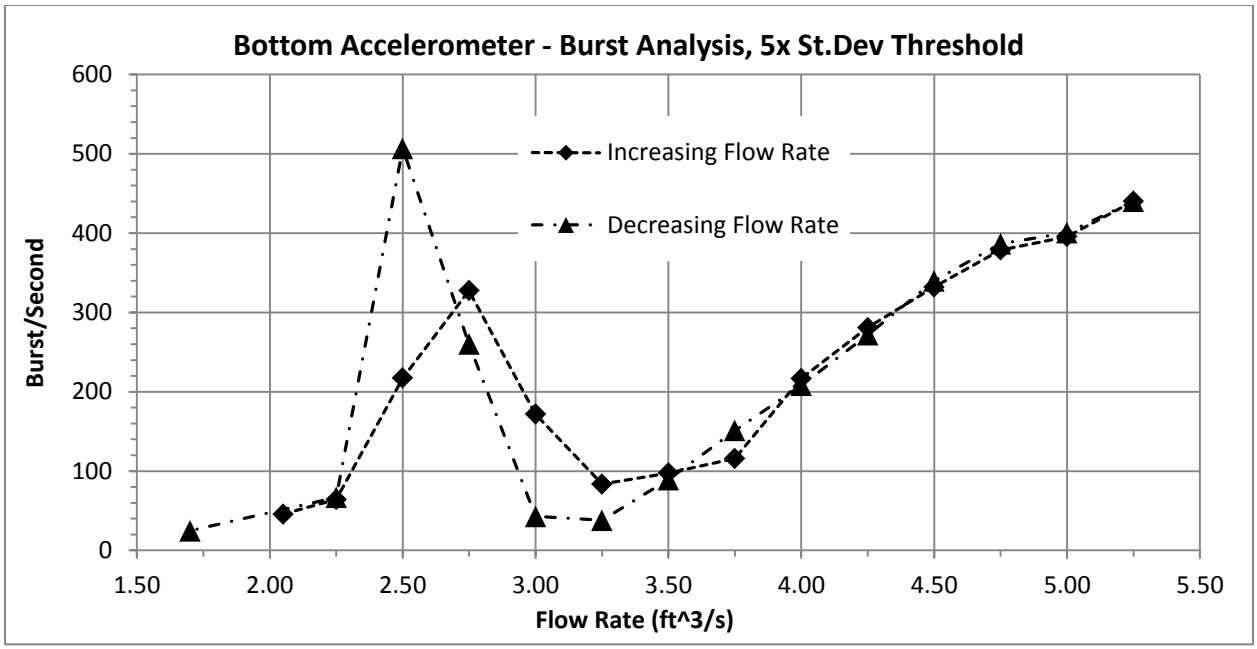

Figure T.6 Burst Analysis of Acceleration recorded from Bottom of Tunnel – 5x Standard Deviation Threshold

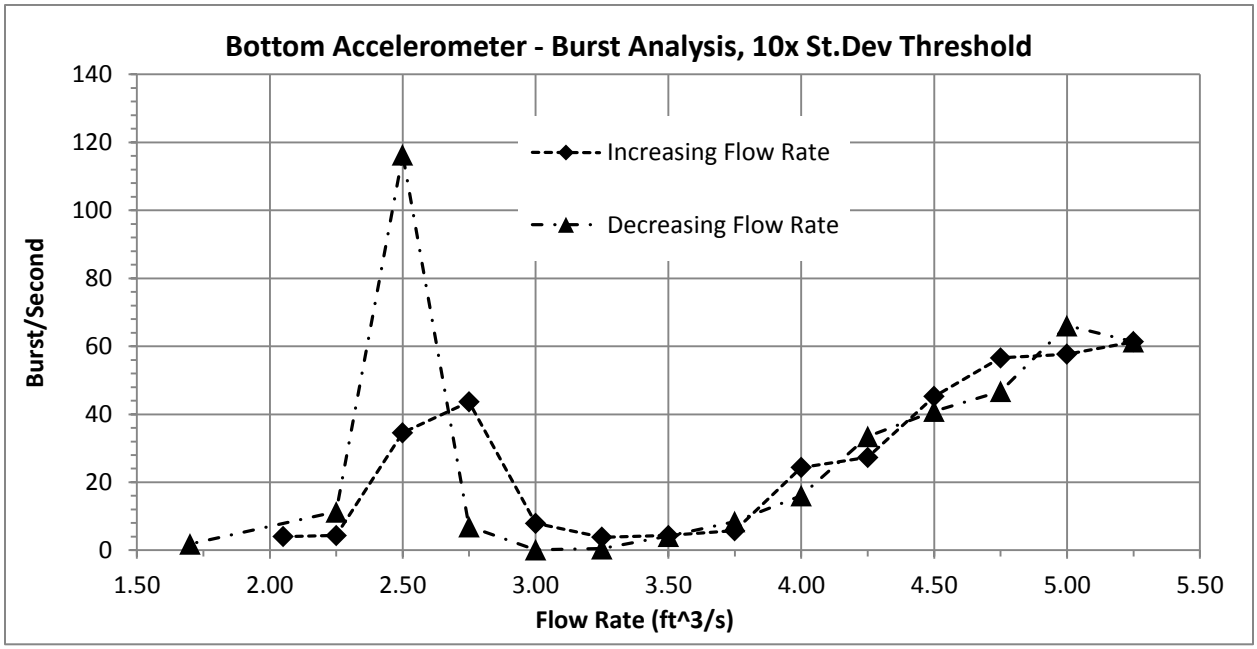

Figure T.7 Burst Analysis of Acceleration recorded from Bottom of Tunnel – 10x Standard Deviation Threshold

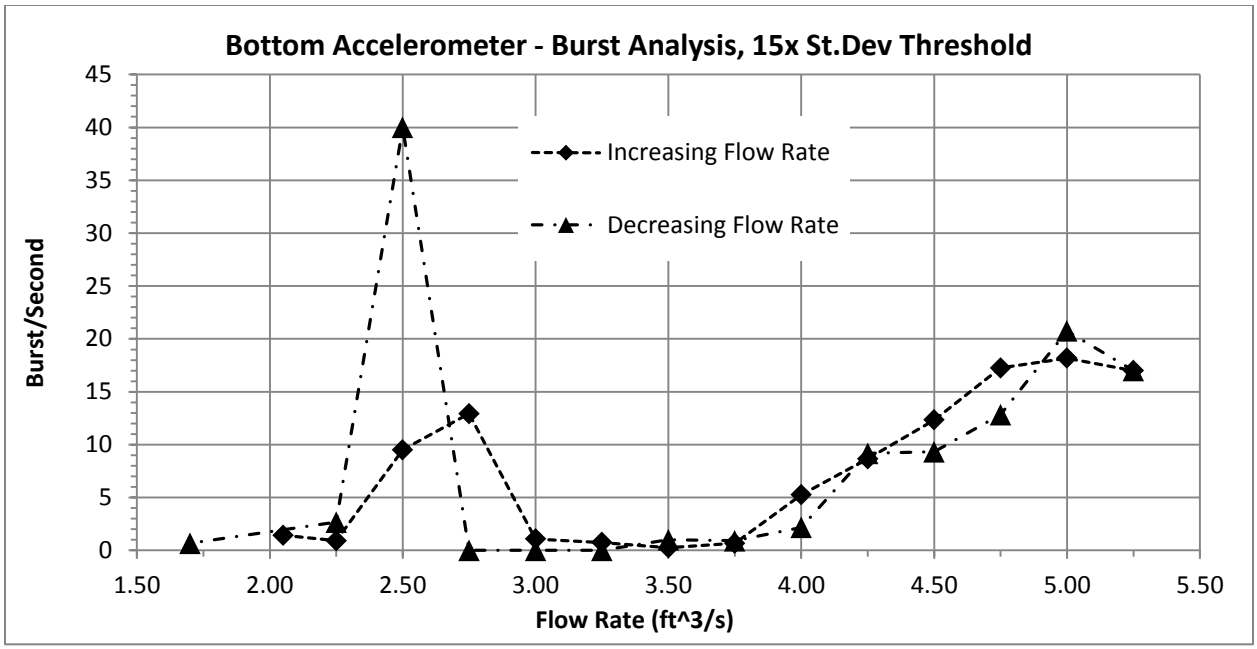

Figure T.8 Burst Analysis of Acceleration recorded from Bottom of Tunnel – 15x Standard Deviation Threshold

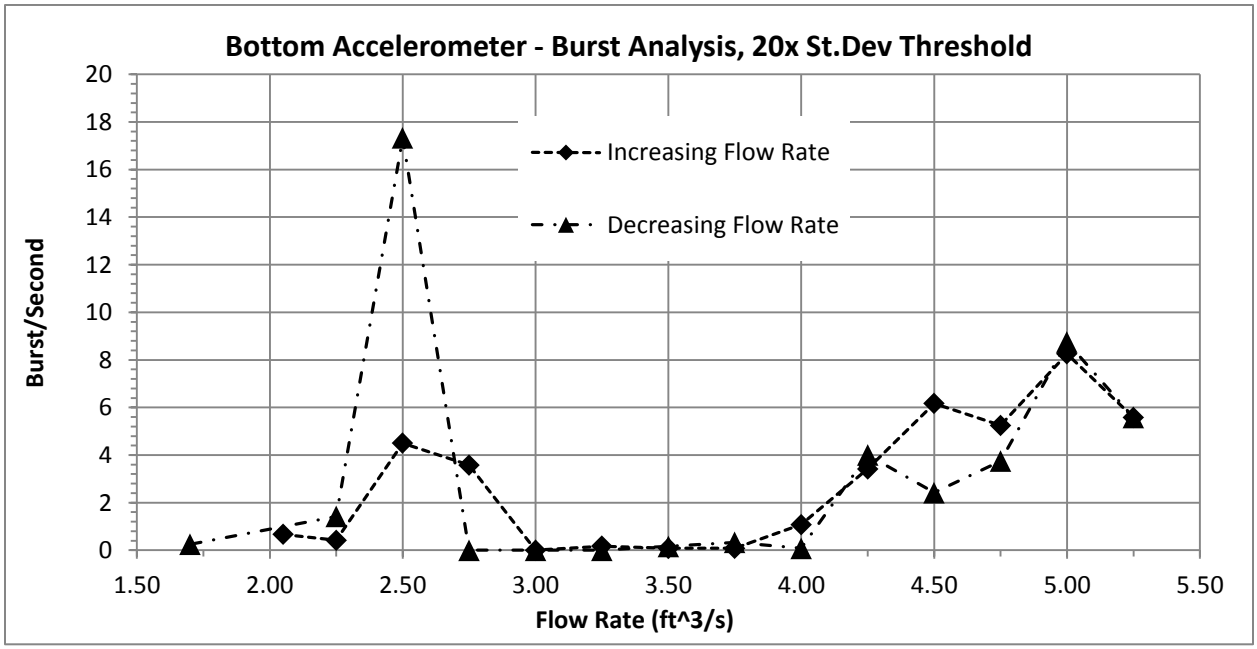

Figure T.9 Burst Analysis of Acceleration recorded from Bottom of Tunnel – 20x Standard Deviation Threshold

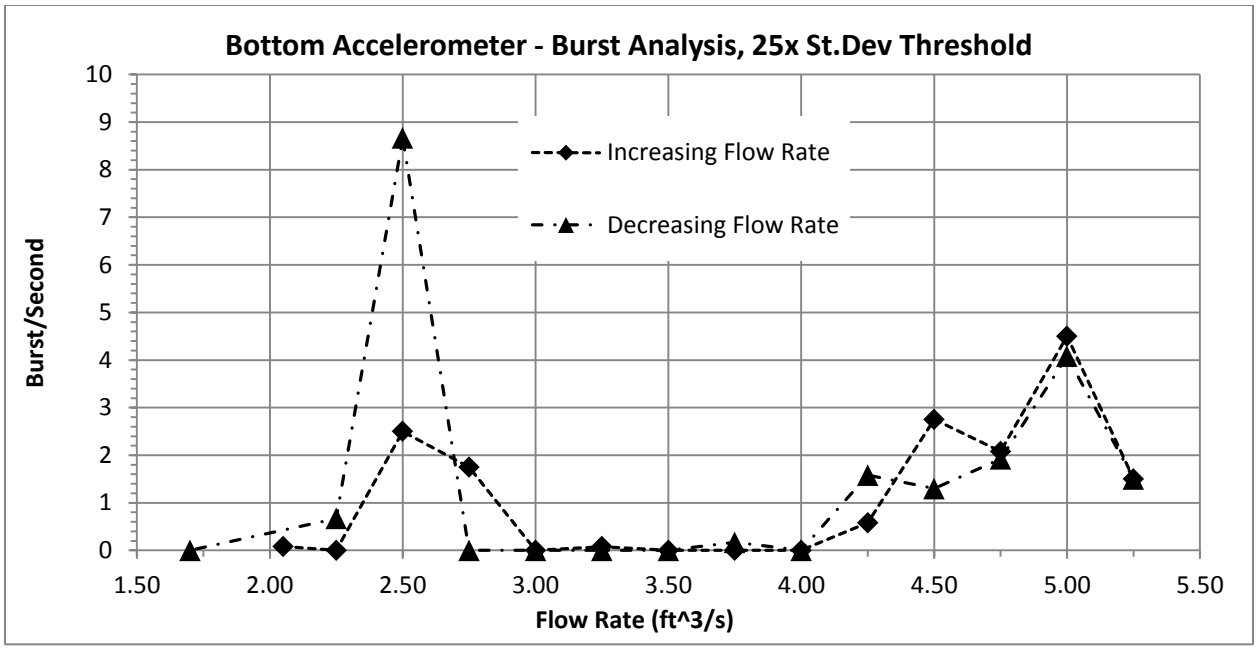

Figure T.10 Burst Analysis of Acceleration recorded from Bottom of Tunnel – 25x Standard Deviation Threshold

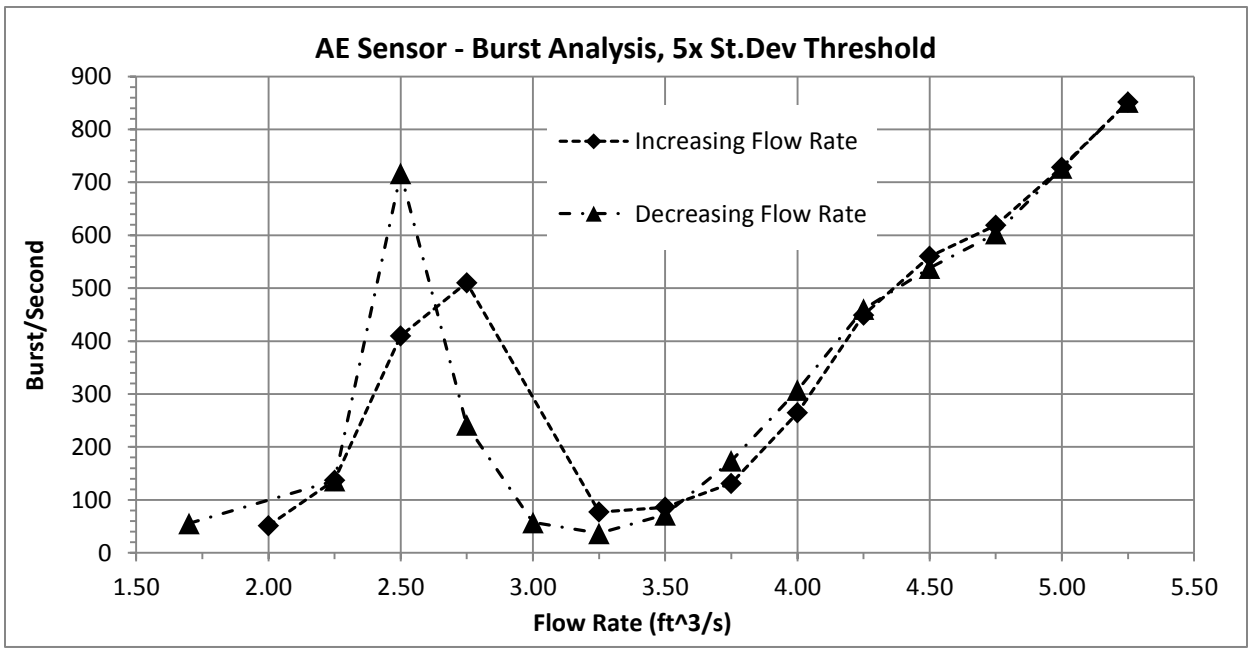

Figure T.11 Burst Analysis of Acoustic Emission Signals recorded from Bottom of Tunnel – 5x Standard Deviation Threshold

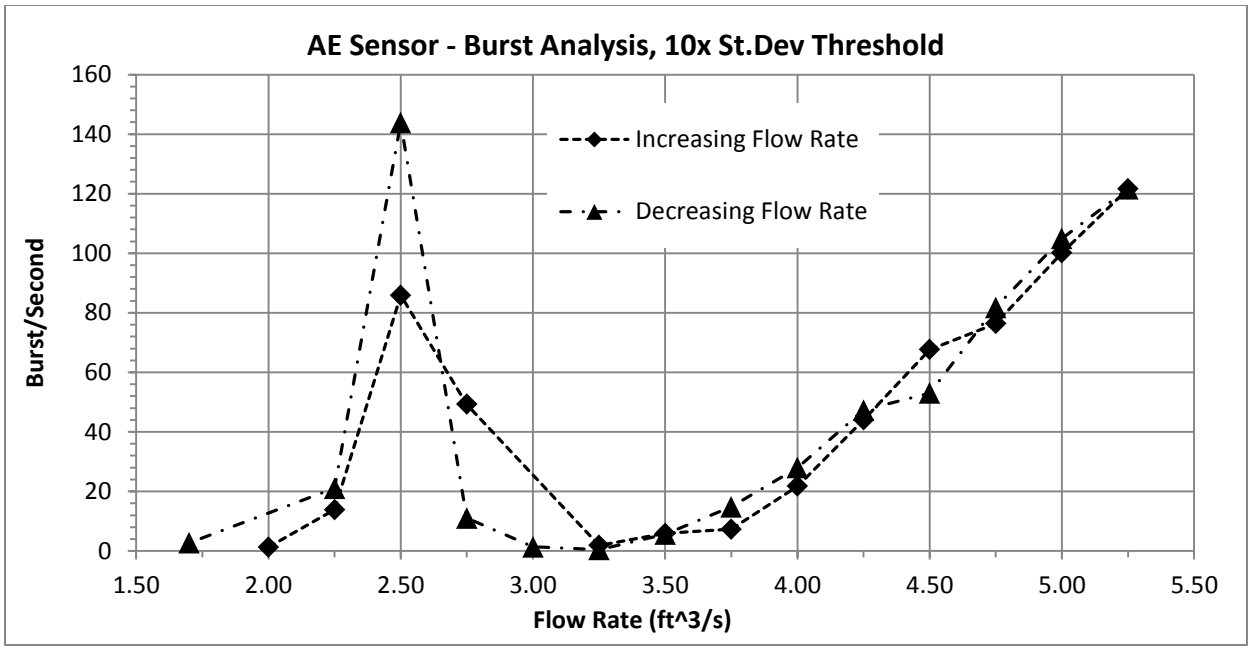

Figure T.12 Burst Analysis of Acoustic Emission Signals recorded from Bottom of Tunnel – 10x Standard Deviation Threshold

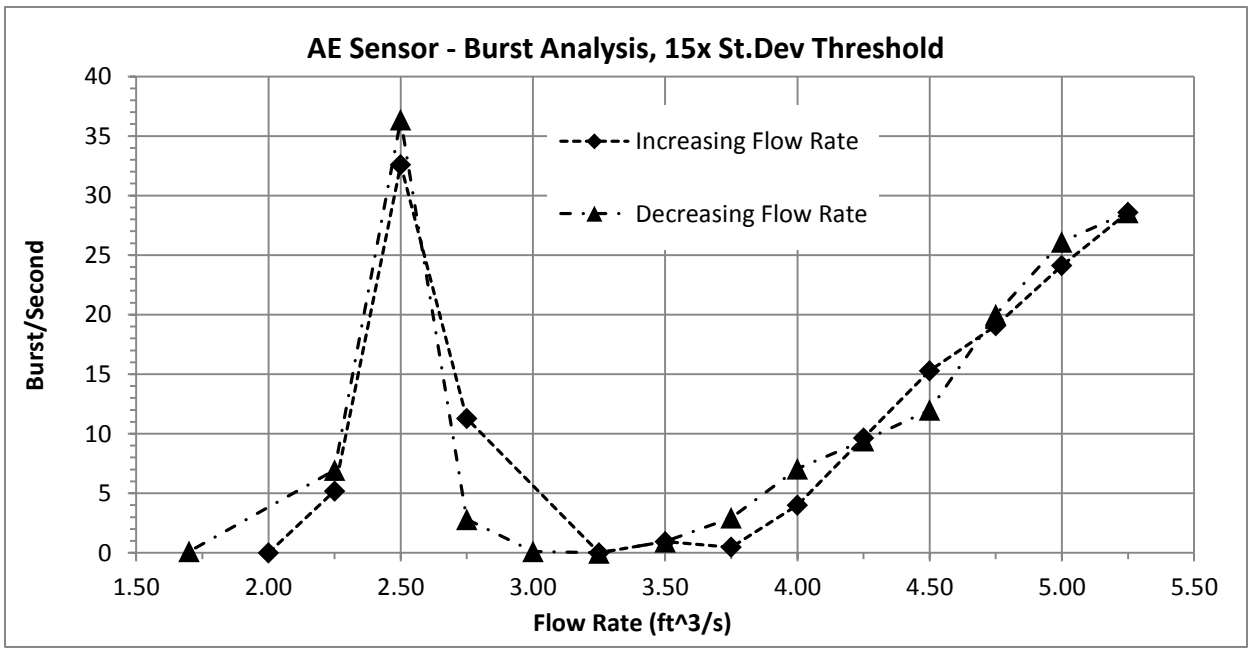

Figure T.13 Burst Analysis of Acoustic Emission Signals recorded from Bottom of Tunnel – 15x Standard Deviation Threshold

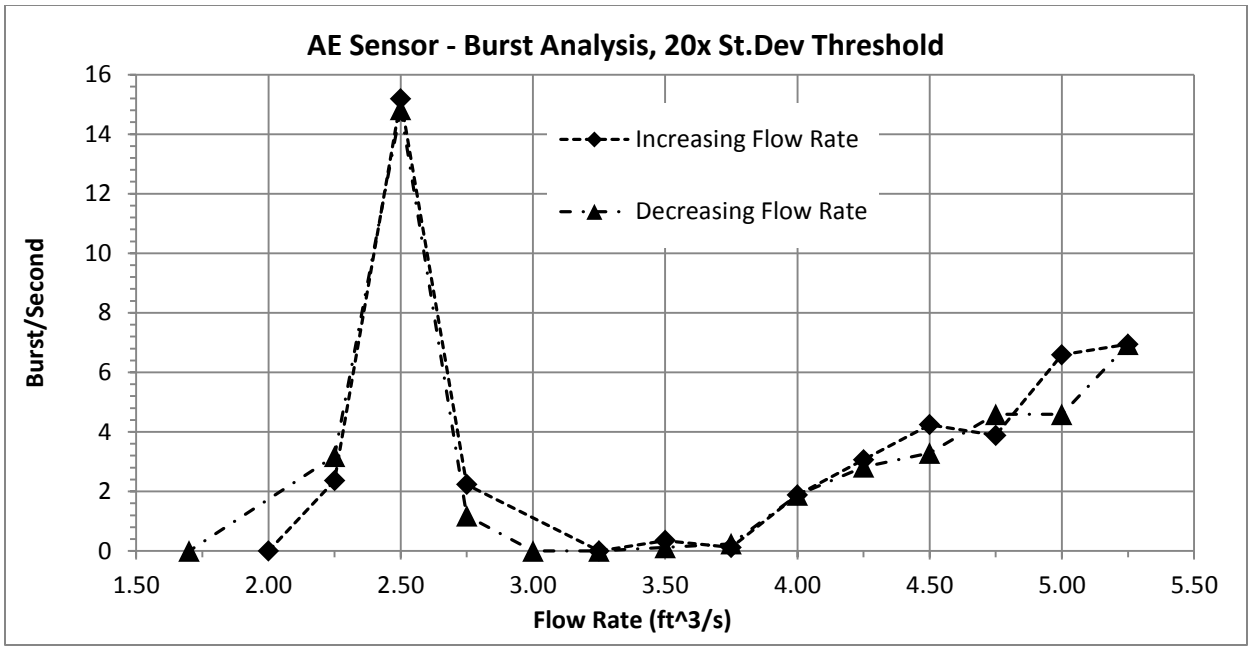

Figure T.14 Burst Analysis of Acoustic Emission Signals recorded from Bottom of Tunnel – 20x Standard Deviation Threshold

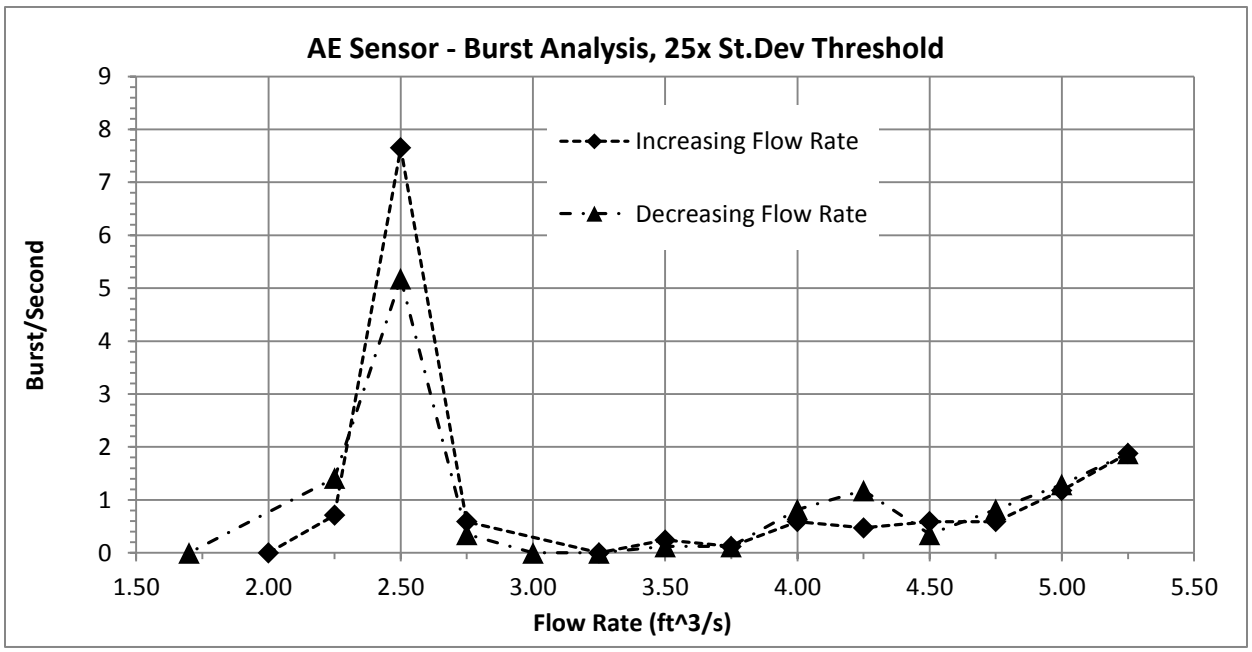

Figure T.15 Burst Analysis of Acoustic Emission Signals recorded from Bottom of Tunnel – 25x Standard Deviation Threshold

In the main body of this Thesis, the above fifteen figures were presented in a normalized/averaged manner to compress the information into three figures. This was achieved by normalizing all the Burst analyses by the same data point – decreasing flow rate: 2.75 ft^3/s. For the majority of the Burst analysis, this was the maximum value, hence why it was chosen. The normalization allowed all the Burst analyses to be represented in relative terms from zero to one. Any flow rates equal to one or close to it, represent the most volatile flow rates. Any flow rates equal to zero or close to it represent the least volatile flow rates. Once all the Burst analysis were normalized, the different thresholds (5x, 10x, 15x, 20x, 25x) were all averaged together. This normalization/averaging allowed for any anomalies to be removed from the data while maintaining the consistent trends found in all the Burst Analysis.